TUNING GEOMETRIC AND ELECTRONIC STRUCTURE OF NOBLE METAL WITH CORE-SHELL PLATFORM AS ENHANCED CATALYSTS

by

Zhenshu Wang (Stan)

M. S. Chemical Engineering Practice, Massachusetts Institute of Technology, 2017
Bachelor of Chemical Engineering, University of Minnesota-Twin Cities, 2015
Bachelor of Chemistry, University of Minnesota-Twin Cities, 2015
Bachelor of Math, University of Minnesota-Twin Cities, 2015

Submitted to the Department of Chemical Engineering
in partial fulfillment of the requirements for the degree of

Doctor of Philosophy in Chemical Engineering

at the

MASSACHUSETTS INSTITUTE OF TECHNOLOGY

September 2020

Author ....
Department of Chemical Engineering
May 26, 2020

Certified by...
Yuriy Román-Leshkov
Professor of Chemical Engineering
Thesis Supervisor

Accepted by ....
Patrick S. Doyle
Robert T. Haslam Professor of Chemical Engineering
Singapore Research Professor
Chairman, Committee for Graduate Students

Tuning Geometric and Electronic Structure of Noble Metals with Core-shell Platform as Enhanced Catalysts

by

Zhenshu Wang (Stan)

Submitted to the Department of Chemical Engineering on June 17, 2020 in partial fulfillment of the requirements for the degree of
Doctor of Philosophy in Chemical Engineering

ABSTRACT

The noble metals (NMs) are special materials satisfying the Sabatier principle which bind adsorbates neither too strongly nor too weakly. Along with the resistance to corrosion and bulk oxidation, this makes noble metals universal catalysts for many important industrial reactions. Despite the appealing chemical properties, noble metals are not the optimal catalysts for particular reactions based on theoretical calculations. Core-shell nanostructures are a versatile platform that has the potential to solve this problem. Recent advances have enabled the synthesis of platinum titanium tungsten carbide (Pt/TiWC) and platinum titanium tungsten nitride (Pt/TiWN) core-shell nanoparticles featuring superior Pt mass activity in oxygen reduction reaction (ORR) and CO tolerance during hydrogen oxidation reaction (HOR) which are the critical reactions to enable hydrogen fuel cell technologies. However, applications with these materials in thermal catalysis reactions and other adsorbates have not been shown. Furthermore, the use of tungsten carbide or nitride as the only backbone core material limits the tunability and core stability for the core-shell catalysts.

This thesis includes a combination of synthesis, characterization, and catalytic performance of new core-shell nanoparticles to provide a fundamental understanding of this versatile platform. Firstly, new core materials tantalum carbide (TaC) and niobium carbide (NbC) combining with platinum (Pt), rhodium (Rh), and iridium (Ir) shells will be introduced. The materials were analyzed by x-ray photoelectron spectroscopy (XPS) and x-ray absorption spectroscopy (XAS) to demonstrate the significant shell electronic and geometric structure alterations induced by the core. Next, these materials along with the conventional Pt/TiWC and Pt/TiWN materials were tested with thermal catalytic probe reactions, namely, carbon dioxide and acetylene selective hydrogenation. Core-shell catalysts featured superior selectivity towards the intermediate products compared to their parent NM catalysts owing to the modified geometric and electronic structures. Finally, the Pt/TaC core-shell nanoparticle was shown to outperform commercial Pt in methanol oxidation reaction (MOR) and methanol interfered ORR application due to the Pt shell electronic structure change which facilitates direct methanol fuel cell technologies. Overall, this work not only demonstrates methods to synthesize a broader spectrum of core-shell nanoparticles but also provides fundamental understandings of shell-core interactions in thermal-catalytic and electrochemical reactions.

Thesis Supervisor: Yuriy Román-Leshkov

Title: Professor of Chemical Engineering

ACKNOWLEDGEMENTS

This thesis was an ensemble of 1744 days of hard work and it would not have happened without the sincere help and support from numerous people. First and foremost, I need to thank my academic advisor, Yuriy Román-Leshkov, who has been a great teacher, supporter, and leader in helping me become the researcher I am today. I still remember that one time I was very frustrated that all the synthesis I had tried did not work in my first year and after talking with Yuriy, the encouragement I got from him pumped me up immensely. I always think a good teacher is a master of inspiring and encouraging, and Yuriy is certainly one of them by providing me the freedom to discover the fundamental science and allowing me to fail again and again and again. It's my great luck to be an advisee of Yuriy for my Ph.D.

Along with Yuriy's guidance, my thesis committee members, Prof. William Green and Prof. Karthish Manthiram also provided great help in my thesis. Bill was very good at asking critical questions to make me think which I have benefited a lot from those questions. Karthish was a great professor with tons of knowledge in electrochemistry which I have learned a lot for my Pt/TaC work. My collaborators contributed a lot to my work, namely, Prof. Rob Rioux, and his student Linxi Wang, Prof. Daniela Zanchet and her student Danielle Santos Gonçalves, Prof. Michael Janik and his student Haoran He. They taught me microcalorimetry, x-ray absorption spectroscopy, and density functional theory respectively which are critical for nowadays catalysis. I also want to thank Prof. Aditya Bhan and Dr. Wen-Sheng Lee who led me into the catalysis world during my undergrad time and taught me the microkinetic modeling.

As a people person myself, I enjoyed working with people from my group. I will not generate all the knowledge in this thesis without my colleagues' support. Dr. Sean Hunt taught me the synthesis of the great core-shell nanoparticles which laid the foundation of my thesis. Dr. Aaron Garg taught me about electronic interaction between the core and the shell. Dr. Bin Cai taught me the basic knowledge of electrochemistry and also being a good friend during his time in our group. Dr. Mark Sullivan, my Bhan's group legacy, helped me to revive all my kinetics knowledge accumulated from Bhan's group. Dr. Daniel Göhl worked with me to develop the Pt/TaC core-shell nanoparticles and was a typical German who had critical thinking and "great humor. Dr. Jin Soo Kang helped me a lot with the electrochemical measurement and provided wonderful discussion and encouragement for my last year of Ph.D. Last but not least, I also have to thank Kim. I am very happy we got to know each other during practice school and our friendship and jokeship have continued. Thank her for being a great friend that always thought about me, without

her secretary-like reminders, I would be past due for tons of academic / proposal deadlines. Kim was also a great gym partner, a joke sharer, a sane keeper, an XAS go-to partner, and a great photographer who had, probably still has, tons of my embarrassing pictures.

Besides my academic family members, I would like to thank my father and mother for all the love they gave me and being very supportive of my study-abroad decision. Although they have not got Bachelor's degrees, they are still the smartest and most determined people I have ever known. Their vision and openness provided me the opportunity to explore the world and shaped my personality.

TABLE OF CONTENTS

LIST OF FIGURES:

LIST OF TABLES:

CHAPTER 1 INTRODUCTION

The noble metals, including ruthenium (Ru), Osmium (Os), rhodium (Rh), iridium (Ir), palladium (Pd), platinum (Pt), silver (Ag), and gold (Au) are great catalysis metals given their unique d-band electronic structures. In this chapter, we will begin by talking about examples of noble metals in electrocatalysis, thermal-catalysis. Then, we will move into core-shell nanoparticles examples in catalysis, followed by constraints on core-shell particles. Lastly, we will reveal the outline of this thesis.

Noble metal in electrocatalysis

Electrocatalysis is a broad topic covering numerous reactions from the simpler ones such as hydrogen oxidation, hydrogen evolution, oxygen evolution, and oxygen reduction reactions (HOR, HER, OER, ORR) [1-4] to complicated ones, like methanol oxidation reaction (MOR), formic acid oxidation reaction, and even upgrading of biomass compounds.[5-7] In this section, we will only introduce the ORR and MOR reactions as these are the relevant reactions in the later chapters.

As the fuel-cell technology driving more attention, the ORR has become more and more important given that no matter what fuel will be used in the anode side, the cathode side will always be the ORR. Carbon supported Pt is the commonly used catalyst for ORR, while a second component (e.g., Ni, Co, Fe, Cu) is usually alloyed with Pt to enhance the stability and activity.[8-11] Researchers have demonstrated that Pd is another noble metal also active for ORR at both basic and acidic conditions, but the performances are not matching the state-of-the-art platinum alloy catalysts.[12-13] Due to the high cost and limited availability researchers have tried to replace the noble metals with non-precious metals (Ni, Fe) for ORR. The limitations, however, for the non-precious metals are the general inferior ORR performance and the instability in acidic media.[14-15] Even though Pt alloys have a superior activity in ORR compared to other noble metals, the slow kinetics, specifically, the large loss in the potential of 0.3-0.4 V limits the fuel-cell efficiency. In order to achieve required output, high Pt loading is necessary for the cathode side of the fuel cell which drives the cost up.[10]

Additionally, Pt alloy nanoparticles have decay in performance due to the second element dissolving under harsh acidic ORR conditions.[16] The nanoparticles regardless of composition will undergo Ostwald ripening which is a phenomenon to describe smaller particles dissolve and redeposit onto larger nanoparticles.[17-18] As the particle size increases, the electrochemically active surface area (ECSA) will decrease which hinders the ORR activity.

In addition to the most common fuel-cell, the proton-exchange membrane fuel-cell (PEMFC), direct methanol fuel cell (DMFC) is another alternative as it utilizes liquid fuel (methanol) in the anode part of the fuel-cell, allowing for easier transportation and a high volumetric energy density.[19] A liquid fuel would also allow for easier integration with existing infrastructure, foregoing the need to develop hydrogen refueling stations that can cost from \$2.5–5 million each, depending on the size.[20] Similar to the PEMFC, DMFC anode catalyst is also Pt-based. PtRu supported on carbon black is the state-of-the-art catalyst for the MOR.[21-22] PtRu alloy is better than the Pt nanoparticle is because MOR involves a carbon monoxide (CO) oxidation rate-limiting step that follows Langmuir-Hinshelwood kinetics in which adsorbed *CO reacts with neighboring adsorbed *OH to form CO_2.[23] Due to the intrinsic strong CO binding energy on the Pt surface, a relatively high onset potential is observed for MOR which decreases the DMFC efficiency even further compared to the PEMFC. Moreover, the PtRu alloy undergoes dynamic restructuring in reaction conditions which is hard to maintain the reactivity.[24-25]

Noble metal in thermal-catalysis

Noble metals Pt and Pd were firstly used as thermal-catalyst to catalyze burning of coal gas at room temperature back in 1817 by Humphry Davy.[26] Since then, noble metals have been used in various thermal-catalytic reactions, such as hydrogenation,[27-29] hydrodeoxygenation,[30] automotive exhaust treatment,[31] dehydrogenations,[32] and ammonia synthesis,[33] etc. We will focus on selective hydrogenation for this section as it is relevant for Chapter 3 and Chapter 4. As continuous developments of heterogeneous catalysts, researchers realize the material catalytic properties mainly depend on its surface electronic structure.[34] For instance, because of the unique electronic structure of Pt, H_2 can

be readily activated on Pt surface which enables Pt to do varies hydrogenation reactions.[35-36] However, Pt is not suitable for some selective hydrogenation reactions, such as hydrogenation of cycloocta-1,3-diene to cyclooctene and C_2H_2 to C_2H_4.[37-38] As we have increased our knowledge on why particular catalysts are good for certain reactions during the past a few decades, we would also want to use this knowledge as guidance to tune material electronic structures so that it can be more selective and active for given reactions.[34]

Noble metal mixing with a second metal, i.e., bimetallic system, has been an effective approach to modify the surface geometric and electronic structures of the parent noble metal which can enhance selectivity and stability in particular reactions.[39-42] Out of different bimetallic structures, alloying has received much attention due to its geometric and electronic synergetic effects.[39, 43-44] To be more specific, for the Pd-Ag system, Ag is observed to have charge transfer to the Pd;[43] for the Pd-Au alloy system, Pd active sites has been diluted by the less active Au atoms and Pd d-orbitals electron density varies upon alloying.[39] Unfortunately, because of the miscibility between the two metals in the alloy, the catalyst surface composition and structure will undergo dynamic rearrangements at a higher temperature which will change the catalytic behavior.[45-46]

Regards to the dynamic rearrangements, intermetallic Pd-Ga system and immiscible bimetallic Pt-Ag system have been reported to enhance stability.[47-48] In the Pd-Ga system, Pd is coordinated with Ga atoms which stabilize isolated active Pd sites and also greatly reduce the Pd density of states near the Fermi level.[47] While the Pt-Ag system is immiscible below 600 °C which provides a relatively stable Pt-Ag surface for low-temperature reactions.[42, 48]

Tuning the electronic structure will enable different adsorbate binding energies. For instance, Ru-Pt has a much lower d-band center compared to the pure Pt which enables a weaker CO binding and facilitates preferential oxidation of carbon monoxide in hydrogen (PROX).[24] Selective hydrogenation of C_2H_2 is another example where a weaker binding of the intermediate product, C_2H_4, will enhance the selectivity of the reaction. The selective hydrogenation of C_2H_2 to C_2H_4 is an important industrial step in the purification of ethylene feed for the polyethylene synthesis.[43, 47] Ethylene feed from thermal pyrolysis

will inevitably contain small amounts of acetylene which is a poison for the downstream Ziegler–Natta catalyst.[45]

Tuning the geometric structure will change reaction pathways. For instance, Rh with different ensemble sizes will have drastically different product distributions in CO_2 hydrogenation.[49] Another example in the bimetallic system, Pt-Au alloys have a dramatic difference in benzene hydrogenation activity as the Pt ensemble size changes. An Au-rich surface has a smaller Pt ensemble which is inactive for benzene hydrogenation while Pt-rich surface is much more active. The decrease of the pre-exponential term but relatively similar activation energy suggests geometric effect plays a major role in this reaction.[50]

Nevertheless, alloy and intermetallic systems would not be able to isolate geometric effects and electronic effects. A similar Ni-Cu alloy was studied by two groups and Ponec et al. attributed the reactivity difference towards the geometric effect while Sinfelt et al. attributed to electronic effect.[51-52] In general, alloy and intermetallic systems will inevitably have both effects where the electronic effect will show up in the exponential factor of the Arrhenius equation while the geometric effect will be in the pre-exponential term.[51]

Core-shell nanoparticle and its applications in catalysis

Core-shell structure offers more experimental knobs to vary compared to the alloy and intermetallic counterparts as one can change the core and shell compositions, particle size, particle shape, and shell thickness. In terms of the core-shell synthesis, the three main routes are as follow: [53]

1. Deposit a second metal onto the preformed metal seed.
2. Selectively remove one component from an alloy or intermetallic structure.
3. Treat an alloy so that one component segregates to surface or core in a thermodynamic fashion.

The three major routes can be extended to six specific methods shown in Figure 1-1.
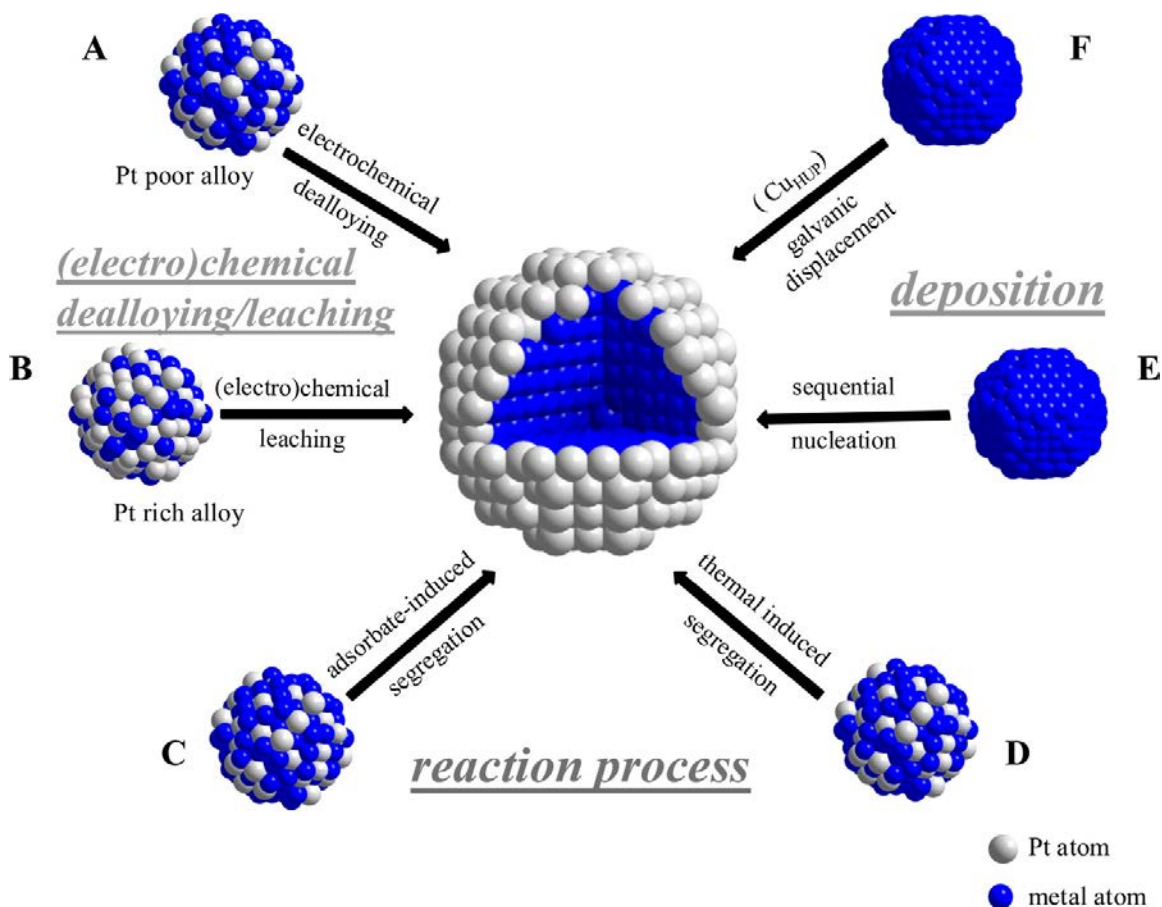
Figure 1-1. Core-shell synthesis routes.

A. Electrochemical dealloy; B. electrochemical or chemical leaching; C. adsorbate-induced segregation under reaction conditions; D. thermal annealing; E. wet synthesis, i.e., colloidal; F. underpotential deposition of the shell component.[53]

Reprinted with permission from (Oezaslan, M., Hasche, F., & Strasser, P. (2013). Pt-based core–shell catalyst architectures for oxygen fuel cell electrodes. *J. Phys. Chem. Lett.* 2013, 4, 19, 3273–3291). *Copyright © 2013, American Chemical Society.*

The difference between routes A and B is that the noble-metal-enriched surface is usually thicker for route A as the electrochemical way is less bounded by transport effect.[54] Route C is a unique method to induce a core-shell structure that can be applied to both thermal-catalytic reactions and electrochemical reactions. For instance, CO adsorption on CuPt alloy will pull Cu to the surface forming Cu enriched surface.[55] Another example is the Pd-Rh alloy in which oxidizing adsorbate like NO will bring Rh to surface and reducing adsorbate CO will bring Pd to surface to form the corresponding core-shell particles.[56]

Route D will be discussed in detail in 0. Route E is usually achieved in the colloidal synthesis where through minimizing the total surface energy, the shell will sit on top of the preformed seed.[57] The growth modes of core-shell structure through this method are governed by an ensemble term called "excess energy" which consists of surface energy, interfacial energy, lattice mismatch strain energy.[58] The three most common modes are the Layer-by-layer mode, island-on-wetting layer mode, and the island growth mode which are shown in Figure 1-2. For Route F, it is realized by the underpotential deposition of Cu onto the core material then replace the Cu with another noble metal through galvanic displacement. [59-61] Vapor deposition, a non-electrochemical way, is also used to make core-shell materials that one metal is vaporized and carried by an inert gas to flow to the second metal where it coats. However, this method bears a broader size distribution and the composition is hard to control.[62]

Core-shell nanoparticles have been reported in both thermal-catalytic reactions and electrochemical reactions. The reactions range from HOR, ORR to PROX, and benzyl alcohol oxidation.[2, 24, 63-65] Owing to the synergistic effects between the multi-component in core-shell structure, these catalysts often display better catalytic performance, either activity or selectivity, than their parent components. To be more specific, the synergistic effect consists of ligand effects, ensemble effects, and geometric effects. Ligand effect is usually involving charge transfer among the different components; ensemble effect governs adsorption property by having distinct atomic groups; geometric effect is commonly associated with the 3-D structural characteristics.[66] Nevertheless, these effects can also be found out in other platforms, yet, unlike the other multi-metallic systems (i.e., alloy and intermetallic), a core-shell structure can have well-tailored surface atoms to be the active sites for reactions which maximizes the atom efficiency especially the shell component is the more expensive part.[2-4]
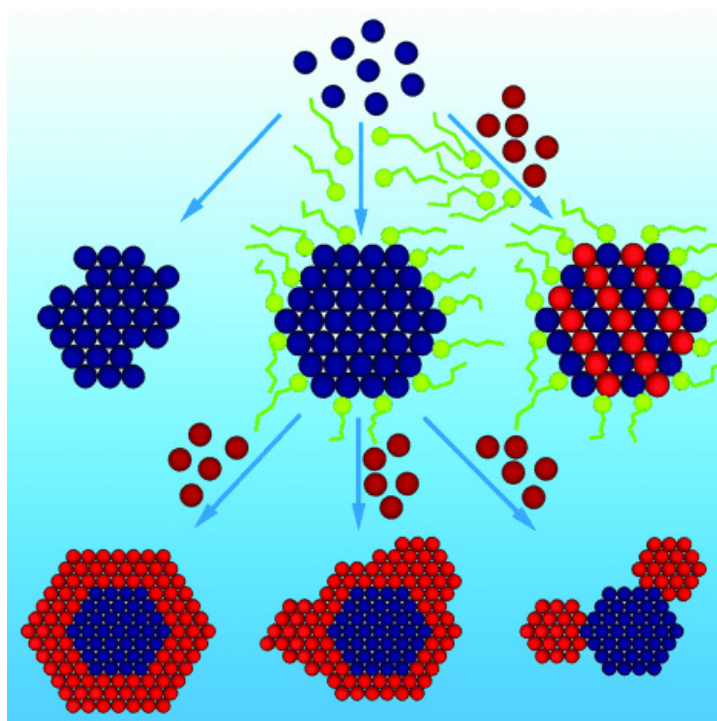
Figure 1-2. Core-shell growth modes.

Layer-by-layer mode, island-on-wetting layer mode, and island growth mode from left to right.[67]

From [Yang, Hong. "Platinum-Based Electrocatalysts with Core–Shell Nanostructures." *Angew. Chem.* 50.12 (2011): 2674-2676.]. Reprinted with permission from John Wiley & Sons, Inc. Web link as follow: https://doi.org/10.1002/anie.201005868

The most common examples lie in electrochemical reactions where the scarce noble metals Pt or Pd are the active sites for HOR or ORR. For instance, Hunt et al., has demonstrated 0.25 monolayer (ML) Pt/TiWC core-shell can outperform commercial Pt/CB nanoparticles by a factor of 13 in terms of Pt mass activity in HOR. The following technoeconomic analysis demonstrates that the 0.25 ML Pt/TiWC is 6 times cheaper than the state-of-the-art non-noble-metal catalyst, CoP, and 12 times cheaper than the commercial Pt/CB catalyst.[2] Kuttiyiel et al. used ammonia to nitridize the already-formed PtNi alloy which made the alloy undergo a structural and chemical change to form Ni_4N core and Pt thin layers. The resulting Ni_4N @ Pt core-shell nanoparticle exhibited more than 3 times higher Pt mass activity than the commercial Pt/CB. Moreover, the specific activity of the core-shell platform was 5 times higher than the conventional Pt

nanoparticles. Additionally, the Ni_4N core modified Pt shell through ligand and geometric effects. The core-shell Pt d-band center was downshifted compared to pure Pt resulting in a weaker oxygen binding energy (-3.94 eV vs. -4.09 eV) and also the Pt shell had -3.19% surface strain which was more than the conventional Pt (-3.04%).[68] Other examples like using Ag as the core material to host Pt in ORR,[69] or Ni as core to host Pt for MOR all demonstrated that ligand and geometric effects played critical roles in activity boost.[70]

Core-shell catalysts are also widely used in thermal-catalytic reactions. The applications are separated into two main categories. The first one is that core material facilitates the chemistry while shell components are porous material to resist sintering and gauge selectivity. For instance, Li et al., used Rh @ silica platform to catalyze the asymmetric transfer hydrogenation reaction where aromatic ketones were hydrogenated in aqueous medium with high enantioselectivity.[71] A similar core-shell platform was synthesized by Adijanto et al. in which Pd @ CeO_2 exhibited one order of magnitude higher methane oxidation rate from 210 °C to 290 °C than the conventional incipient wetness Pd/CeO_2 catalyst. Moreover, the new Pd @ CeO_2 platform featured a high thermal stability where it showed no sintering even after 850 °C calcination.[72-73]

The second category is the shell catalyzes reactions with the core modifying shell electronic and geometric structures of the shell. Humphrey et al. used the one-pot synthesis to synthesize Au @ Rh core-shell particles. The Au seeds were created by using $NaBH_4$ to reduce $HAuCl_4*H_2O$ in the presence of capping agent poly(vinylpyrrolidone) (PVP) in ethylene glycol medium followed by adding $RhCl_3*xH_2O$ to form the shell. The core-shell material was tested with cyclohexene hydrogenation where Au @ Rh demonstrated a much higher Rh mass activity than the Rh alone.[74] A similar approach was used to synthesize Au @ Pd core-shell nanoparticles and the material was tested by benzyl alcohol oxidation reaction. This work revealed that selectivity towards benzaldehyde and activity of benzyl alcohol could be tuned by Pd shell thickness. Additionally, Au core significantly tuned Pd which enabled selective oxidation of benzyl alcohol.[65] Same material, Au @ Pd, was also applied to Suzuki-Miyaura coupling reaction and the 2-5 ML of Pd shell demonstrated the best activity.[75-76]

Another unique advantage of core-shell structure is the possibility to separate geometric and electronic effect in multi-metallic system. The layer-by-layer nanostructure provides the opportunity to isolate the core-to-shell electronic effect from the geometric effect if the shell atom ensemble and bond distance remain the same.[77] In Chapter 4, we will discuss the acetylene selective hydrogenation over Pt/TiWC and Pt/TiWN core-shell systems where the ethylene selectivity is tuned only by the Pt electronic structure change while the Pt-Pt bond distance and Pt coordination number remain the same.

Transition metal carbides @ noble metal core-shell nanoparticles

Transition metal carbides (TMCs) with groups 4, 5, and 6 early transition metals are unique materials as they have both covalent and ionic bonding in their lattice which made them chemically and mechanically stable.[78] Additionally, the surface structure of TMCs has been investigated extensively since the 1970s when WC was found out to be able to catalyze the isomerization of 2,2-dimethylpropane to 2-methylbutane which was a typical Pt catalytic functionality.[79] Mo_2C was then found out to behave like Ru.[80] The hypothesis was the insertion of carbon atom into the transition metal lattice altered the d-band electronic structures which resembled noble metals.[79] However, the electronic structures between TMC and noble metals are not completely the same. As shown in Figure 1-3, the oxygen and carbon binding energies are dramatically different between TMCs and noble metals. TMCs have much stronger oxophilicity but less carbophilicity while noble metals like Pd and Pt have less oxophilicity.[81] These electronic structures difference can be used to explain why Pt can be poisoned easily by CO and H_2S but WC is much resistant to those compounds. [82-84] In addition to the poison resistance, TMCs can sometimes outperform noble metals in terms of reactivity. For instance, Porosoff et al., demonstrated that Mo_2C had a higher turnover frequency (TOF) in reverse water gas shift reaction ($CO_2+H_2\rightarrow CO+H_2O$) than the benchmark $PtCo/CeO_2$ catalyst. Additionally, the product was mainly CO (>90% selectivity) for the Mo_2C catalyst.[85] However, due to the strong oxiphilicity of the TMCs, once the TMCs are coated with oxide layers, the reactivity would drop dramatically. [86-87]

In this thesis, we will discuss the use of TMCs as the core material for the core-shell platform. The advantages of using TMCs as core materials are as follows: firstly, TMCs are earth-abundant and inexpensive compared to noble metals; secondly, the Tammann temperature of TMCs are extremely high (i.e., WC at 900 °C and TaC at 1300 °C) which provided TMCs great thermal stability; thirdly, TMCs are highly resistant to corrosion and leaching in acids;[88] fourthly, TMCs are conductive owing to ionic bonding in the structure; fifthly, noble metals are relatively hard to form carbides which prevent them to emerge into the TMC core lattice;[89] last but not least, noble metals have strong affinity to bind on TMCs which is ideal to form core-shell structure.[90-91]
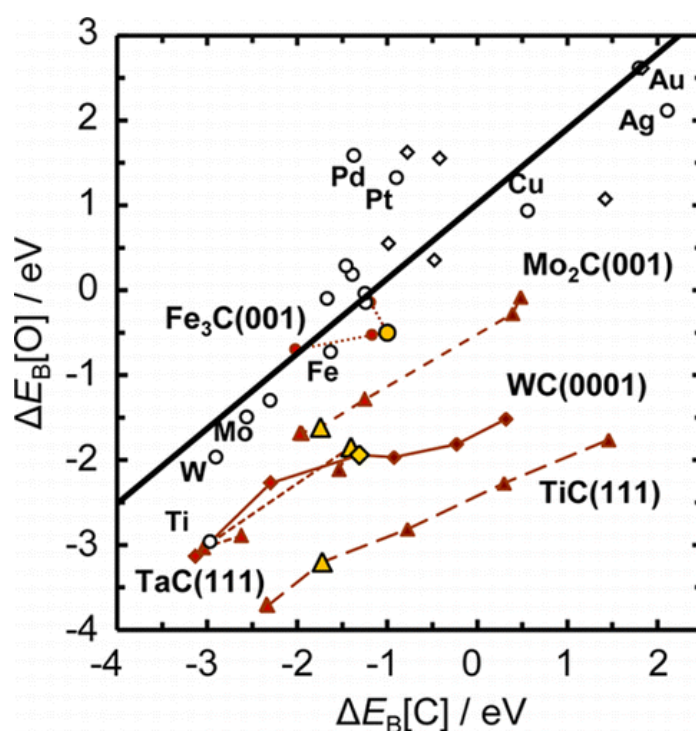
Figure 1-3. Details of the binding energies of carbon and oxygen on several carbide surfaces and their comparison to transition-metal surfaces.

The yellow symbols indicate the stoichiometric carbide surface, whereas the red symbols connected to this indicate the oxidized (typically weaker binding) and reduced (typically stronger binding) surfaces. The open symbols represent bonding on transition metal close-packed (diamonds) and stepped (circles) surfaces, taken from the literature. [92-94]

Reprinted with permission from (Michalsky, R., Zhang, Y. J., Medford, A. J., & Peterson, A. A. (2014). Departures from the adsorption energy scaling relations for metal carbide catalysts. *J. Phys. Chem. C* 2014, 118, 24, 13026–13034). *Copyright © 2014, American Chemical Society.*[81]

Using TMCs as the underlying material to host noble metals have been put forward by the Chen group. Specifically, they synthesized WC, W_2C, and Mo_2C thin films followed by the deposition of layers of Pt in an XPS set-up. The probe reaction HER was used to analyze the material and the Pt mass activity was 10 times higher than the commercial Pt.[95-96] However, all these atomic-layer-deposition (ALD) attempts were carried out by synthesizing the carbide first before depositing the noble metal which led to a non-conformal noble metal shell.[90-91, 95-98]

Recent advances from Garg et al. and Hunt et al. demonstrated that TiWC and TiWN core hosting Pt shell can be synthesized through one-pot synthesis where conformal Pt shell was demonstrated through the scanning transmission electron microscopes-energy dispersive x-ray spectroscopy (STEM-EDS) mapping. [2-4, 6] These nanoparticles featured high-temperature sintering resistance as shown in Figure 1-4 and Figure 1-5 where Pt nanoparticles would sinter under 600 °C to 700 °C while Pt/TiWC core-shell particles were not. Moreover, the strong interaction between Pt and TiWC and TiWN cores enabled the change of Pt electronic structure which changed CO, C_2H_2, and C_2H_4 adsorption energies.[3, 77, 99]
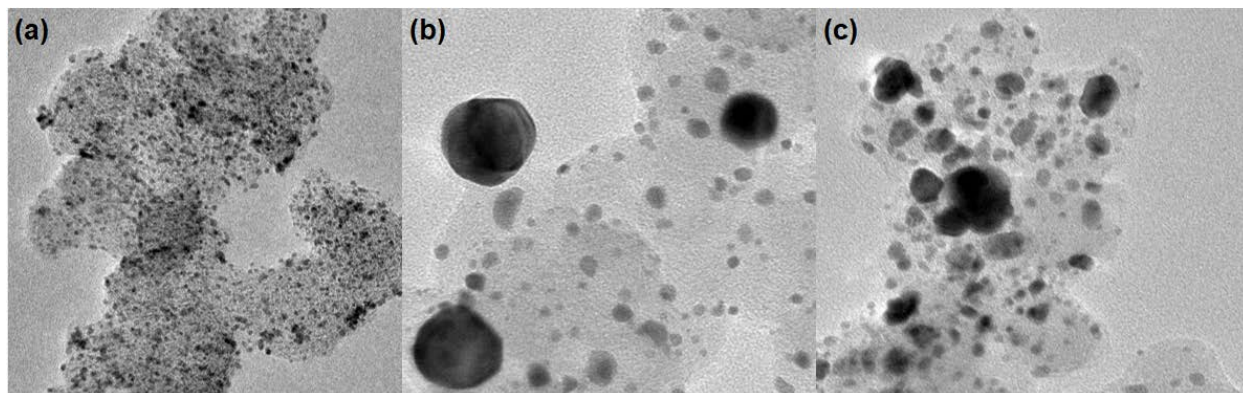
Figure 1-4. TEM analysis of commercial Pt nanoparticles before and after various heating treatment.

(a) as received; (b) after 4-hour N_2 treatment at 700 °C; (c) after 20-hour N_2 treatment at 600 °C.
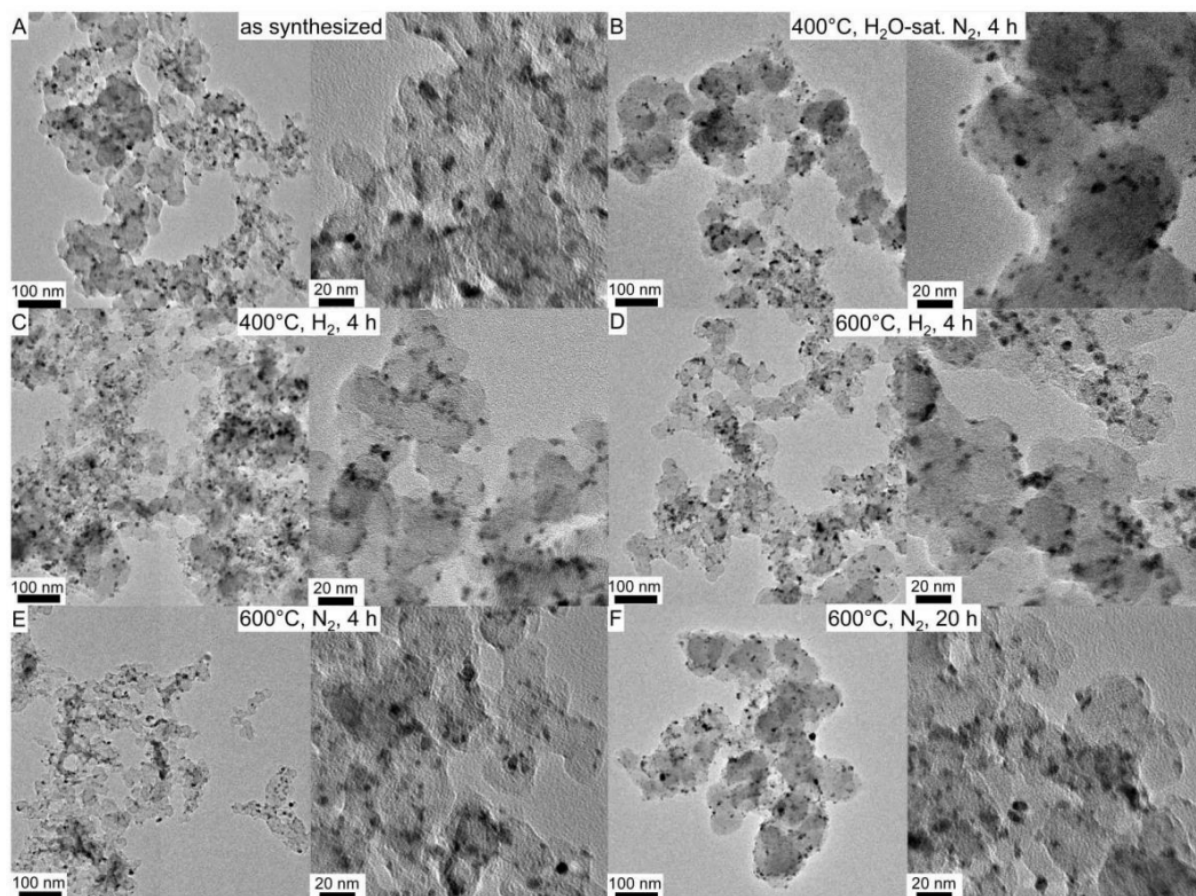
Figure 1-5. TEM analysis of sub-ML Pt before and after various heating treatment.

(A) Before heating treatment; (B) after 4-hour N_2 treatment at 400 °C; (C) after 4-hour H_2 treatment at 400 °C; (D) after 4-hour H_2 treatment at 600 °C; (E) after 4-hour N_2 treatment at 600 °C; (F) after 20-hour N_2 treatment at 600 °C;

From [Hunt, S. T., Milina, M., Alba-Rubio, A. C., Hendon, C. H., Dumesic, J. A., & Román-Leshkov, Y. (2016). Self-assembly of noble metal monolayers on transition metal carbide nanoparticle catalysts. *Science*, *352*(6288), 974-978.]. Reprinted with permission from AAAS. Web link as follow: https://science.sciencemag.org/content/352/6288/974/tab-pdf

While these breakthroughs enable a new class of core-shell materials, yet, TiWC and TiWN cores are not resistant to higher potential oxidation which limits the material capabilities in other reactions with harsher conditions. Specifically, Göhl and Garg et al. found out the Pt/TiWC core-shell nanoparticles would undergo core dissolution if the core-shell structure had disrupted shell.[4]

In order to achieve a better ORR stability, Lee et al. have demonstrated Ta-added WC had superior ORR activity and stability in acid electrolyte due to the possible W-Ta alloy formation.[87] Hunt et al. also have tried to synthesize TaWC using the reverse microemulsion method (RME). The mix-carbide composition was limited to $Ta_{0.3}W_{0.7}C$ due to the high temperature required for the pure TaC formation.[88, 100] One way to solve this issue is to introduce noble metal prior to the carburization step as noble metals have demonstrated to be able to catalyze CH_4 decomposition.[101-103] The methane decomposition mechanism is shown in Figure 1-6 as reprinted by Elsevier permission. With facile carbon access into the lattice, the TaC carburization temperature will be reduced.
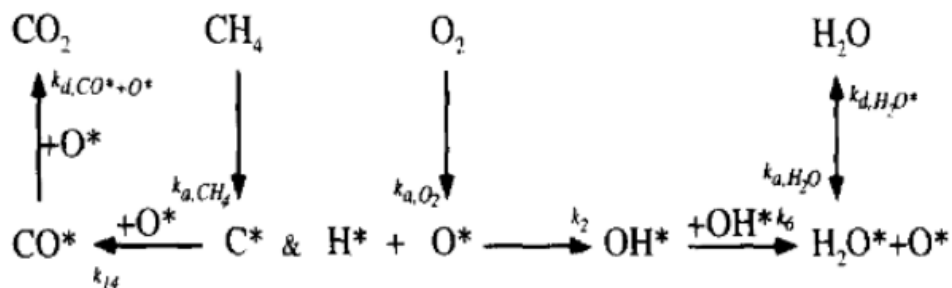
Figure 1-6. Results from reaction path analysis at ignition points.

Carbon and hydrogen formed upon methane decomposition, oxidize very fast to CO_2 and H_2O, respectively, in a surface rich oxygen environment.

Reprinted from Bui, P. A., Vlachos, D. G., & Westmoreland, P. R. (1997). Catalytic ignition of methane/oxygen mixtures over platinum surfaces: comparison of detailed simulations and experiments. *Surface science*, *385*(2-3), L1029-L1034. Copyright (1997), with permission from Elsevier.

The development of the new core materials will enable a broader library of the core-shell platforms which can provide opportunities to further optimize noble metal catalysts and study the fundamental impact from the core to shell.

Outline of the thesis

The results of this thesis are presented in four chapters (Chapter 2 to Chapter 5). Chapter 6 will provide Conclusions and Outlook for future core-shell studies. In Chapter 2, the synthesis of TaC and NbC core-based core-shell materials were introduced and the basic characterization technics, x-ray diffraction (XRD), transmission electron microscopy (TEM), and Inductively coupled plasma mass spectrometry (ICP-MS) were used to analyze the core-shell composition and particle sizes. Shell coverage was calculated by using the shell-to-core metal atomic ratio (from ICP-MS) and particle size (from TEM).

In Chapter 3, Rh/TiWC and Rh/NbC core-shell nanoparticles were synthesized and tested by using CO_2 hydrogenation as a probe reaction. Rh shell coverage was controlled by changing the shell-to-metal atomic ratio. Rh ensemble and electronic structures were modified by the TMCs cores which were characterized by X-ray absorption spectroscopy (XAS) and characterized by X-ray photoelectron spectroscopy (XPS) respectively. The Rh ensemble and electronic structure change enabled 10 times higher CO selectivity for the Rh/TiWC and Rh/NbC core-shell compared to the commercial Rh.

In Chapter 4, Pt/TiWC and Pt/TiWN with varied shell coverages were tested using C_2H_2 hydrogenation. XAS and XPS were used to analyze the Pt shell geometric, ensemble, and electronic structure changes. The superior selectivity of C_2H_4 for the core-shell particles (4 times higher) than commercial Pt was attributed only to electronic effect. Density functional theory (DFT) calculations and microcalorimetry measurements revealed that downshifted Pt d-band center weakened the C_2H_4 binding energy which enhanced the C_2H_4 selectivity. 1 monolayer Pt/TiWN core-shell demonstrated the best performance for the industrial relevant C_2H_2 selective hydrogenation with C_2H_4 co-feed.

In Chapter 5, Pt/TaC core-shell nanoparticles with varied Pt shell coverages were used for the methanol oxidation reaction (MOR) and methanol interfered oxygen reduction reaction (ORR). The 0.57 ML Pt/TaC exhibited the best MOR reactivity normalized by Pt mass. Additionally, Pt/TaC exhibited nearly twice as much methanol tolerance in ORR compared to the commercial Pt. A similar white-line intensity increase and Pt 4f peak binding energy shift were observed in Pt/TaC (by XAS and XPS) compared to the

previously reported Pt/TiWC and Pt/TiWN. Pt-Pt bond distance remained the same which indicating the electronic effect was the main reason for the enhanced performance.

In Chapter 6, main conclusions were summarized and other research directions in terms of new core-shell synthesis route, new industrial relevant reactions were proposed.

Chapter 3, 4, and 5 were written as separate publications that can be read independently.

Acknowledgement

CHAPTER 2 BROADEN THE CORE-SHELL SYNTHESIS LIBRARY

Introduction

About 18 years ago, On 9 January 2002, the US Secretary of Energy Spencer Abraham announced a new research partnership between the US Council for Automotive Research (USCAR) and the Department of Energy (DOE). This collaboration was specifically for the fuel cell technology development for automobiles and it was called Freedom CAR. The reason for the development of the fuel cell technology was because the United States was using 26% of the world's oil with only 9% of global oil production and a merely 2% of world's petroleum reserves which posed a great national security concern and brought back the nightmare from 1973. Thanks to the shale gas technology booming, U.S. exported nearly 9 million barrels of crude oil per day in June 2019 and surpassed Saudi Arabia becoming the largest oil exporter of the world.

It seems the Damocles Sword was removed because of the shale gas technology and there is no need to develop fuel cells. However, in early 2015, the State Department submitted a target to cut greenhouse house emissions to the United Nations Framework Convention on Climate Change (UNFCCC). The target was aiming to reduce emissions by 26-28% below 2005 level by 2025 which was around 1870.5 MMT (million metric ton) carbon dioxide equivalent reduction. Moreover, the transportation sector surpassed the electric power sector and became the largest CO_2 emission source in the U.S. starting in 2016.[104] Over 90 percent of the fuel used for transportation is petroleum-based, which includes primarily gasoline and diesel. The transportation CO_2 emission posed a challenge for the CO_2 sequestration due to the mobility of the vehicles. Thus, using the proton-exchange membrane fuel cells (PEMFCs) where no carbon source is involved will greatly alleviate this issue.

However, after nearly 2 decades of the Freedom CAR research initiative, the PEMFCs technology is still too expensive ($11,000 for each fuel cell stack) to be an economical alternative for the conventional combustion engines.[105] The costliest part of the fuel cell is the catalyst (~50% of the cost) which involves using noble metal platinum. The slow kinetics of the oxygen reduction reaction (ORR) at cathode induces loss of cell voltage, and therefore, high Pt loading is necessary to maintain decent PEMFC

performance. In addition to the sluggish kinetics, the stability of the Pt-based catalyst is also a challenge to overcome. The loss of reactivity during PEMFC cycles is mainly due to the loss of electrochemical surface area (ECSA) of catalyst nanoparticles. To solve these issues, the core-shell structure is put forward, where Pt is at the shell to maximize the accessibility.[106] Numerous core-shell structures have been synthesized where the core component is another noble metal, such as Pd,[64, 107] Ru,[24, 108], Au.[109-110] Even though the synthesis was uniform, the economic incentive is not as large. Moreover, these metal-metal core-shell structures are metastable due to the noble metal miscibility with the core component. Core-shell platforms with transition metal carbide (TMC) or nitride (TMN) as core are a promising type of materials that can be used in electrochemical reactions.[2-4, 6, 99] Specifically, the TMC and TMN cores have the following advantages, thermal and chemical stability, electrical conductivity, earth abundance, insolubility of noble metals in their lattice.

A recent study has shown Pt shell can stabilize TiWC cores even after 10,000 potential cycles under harsh ORR conditions.[4] However, this only limited to the fully covered TiWC core while the disrupted core-shell structure would not be able to survive the ORR potential cycles. Moreover, the incomplete Pt shell coverage would accelerate the dissolution of exposed TiWC core. This can be deemed as the electrochemical corrosion where the less noble part tends to corrode selectively while the noble part being protected. Another common example of this is using a thin Zn layer to protect the Fe from corrosion as Zn is less noble. The following Figure 2-1 demonstrated the Pt/TiWC core-shell structure would collapse with the core dissolving if the Pt shell was not fully covering the core.[4]
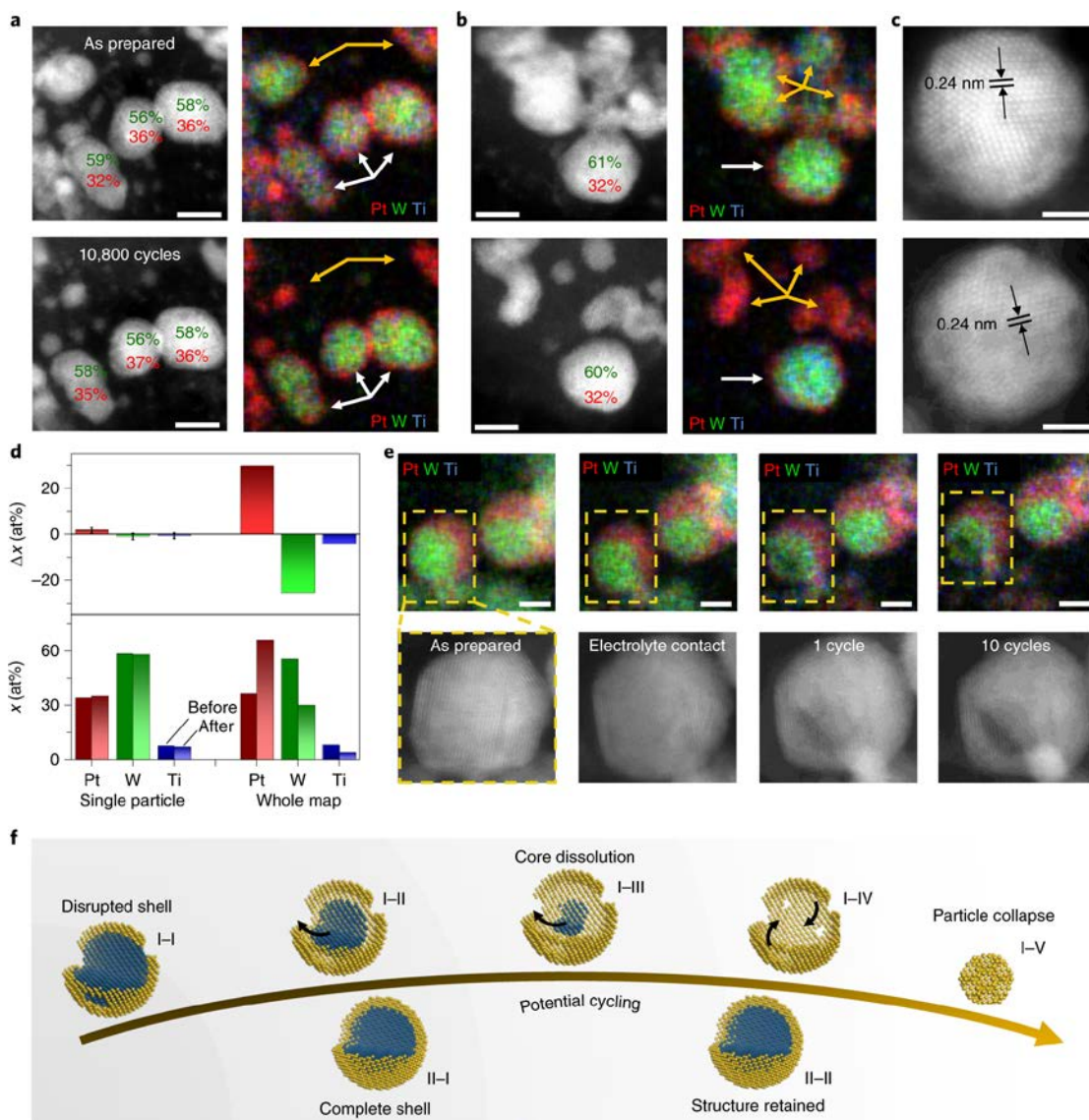
Figure 2-7. Structural stability during potential cycling.

a–c, Identical location STEM images and corresponding EDX elemental maps (IL–STEM–EDX) of 2 ML Pt/TiWC before (upper panel) and after (lower panel) ASTs showing particles with complete (white arrows) and incomplete (orange arrows) Pt shells. The AST consisted of 10,800 cycles between 0.4 and 1.0 V_{RHE} in Ar-sat 0.1 M HClO$_4$ at a scan rate of 1 V s^{-1}. Scale bars, 5 nm (a), 4 nm (b) and 2 nm (c). d, Change in elemental composition (x) measured by EDX of individual particles with complete Pt shells and the whole map after the AST. e, IL–STEM–EDX of 2 ML Pt/TiWC as prepared, after electrolyte contact, after one cycle and after ten cycles in 0.1 M HClO$_4$. Scale bars, 4 nm. f, Schematic showing the evolution of partially and fully coated core–shell particles during potential cycling.
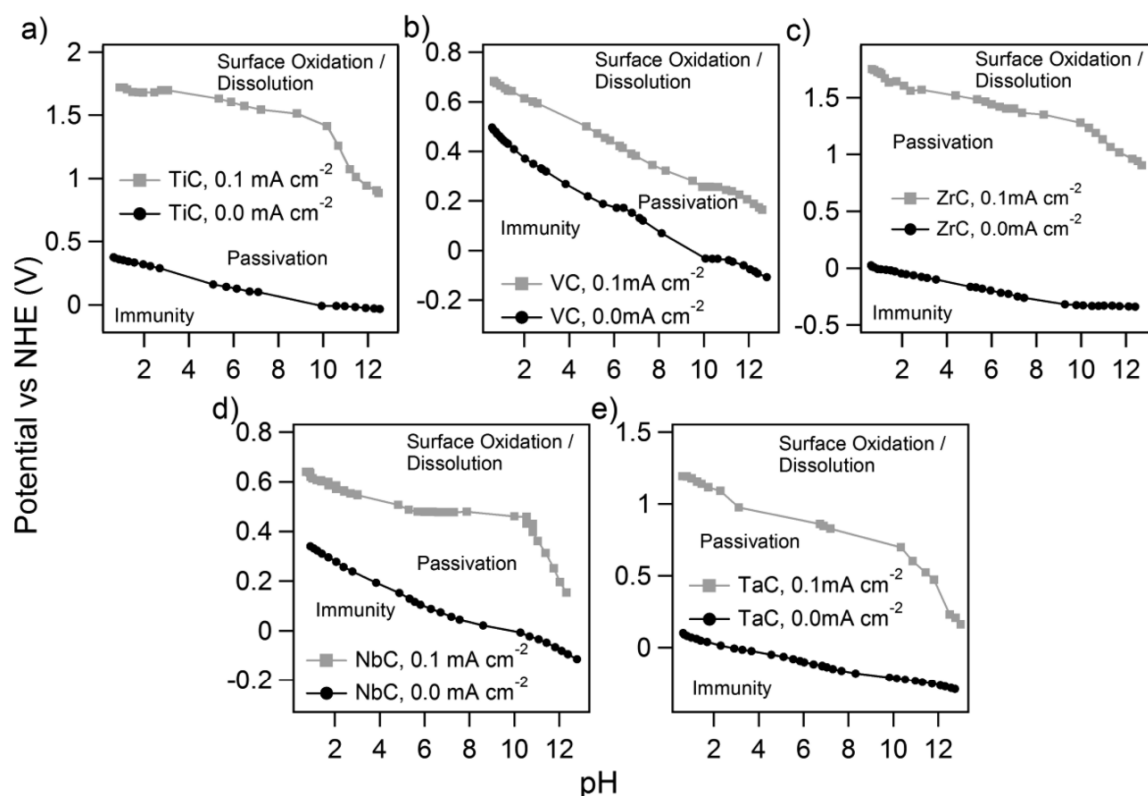
Figure 2-8. Chronopotentiometric (CP)-titration curves.

(a) TiC, (b) VC, (c) ZrC, (d) NbC, and (e) TaC. The uncertainty associated with the average variation in steady state potential is smaller than the size of the data points shown.[111]

Reprinted with permission from (*ACS Catal.* 2014, 4, 5, 1558-1562). *Copyright © 2014, American Chemical Society*.

As can be seen from Figure 2-1 (a) and (b), non-fully covered TiWC core before the potential cycles was stable under STEM-EDX mapping, however, after 10800 cycles, the core was dissolved and the Pt shell collapsed as shown in Figure 2-1 (f) cartoon.

In order to improve this core-shell catalyst, two routes can be taken. The first one is to fully cover all the TiWC cores by adding more Pt into the system. However, this defeats the purpose of reducing Pt loading and also pose a synthesis challenge. If more H_2PtCl_6 precursors were added into the reverse microemulsion (RME), the surfactant would not be able to hold the small water droplets and therefore result in Pt crash out. In addition, it is hard to control the coating under nanoscale especially with the dynamic movement of the Pt shell under ORR reaction conditions.

The second option is to replace the TiWC core with a stabler carbide core that the core itself will be able to withstand the harsh ORR condition.

A Pseudo-Pourbaix diagram is shown in Figure 2-2, where it demonstrated the transition metal carbide stabilities under different pH. The black dot line represented the immunity and passivation boundary, above which the carbide started to passivate and form an oxide layer. The grey dot line represented the dissolution and passivation boundary, if the potential was raised above the boundary, the transition metal carbide would start to dissolve in the electrolyte.[111] The data in Figure 2-2 can be further summarized in Figure 2-3 where the stability data was combined with the DFT calculated oxygen binding energy (OBE)
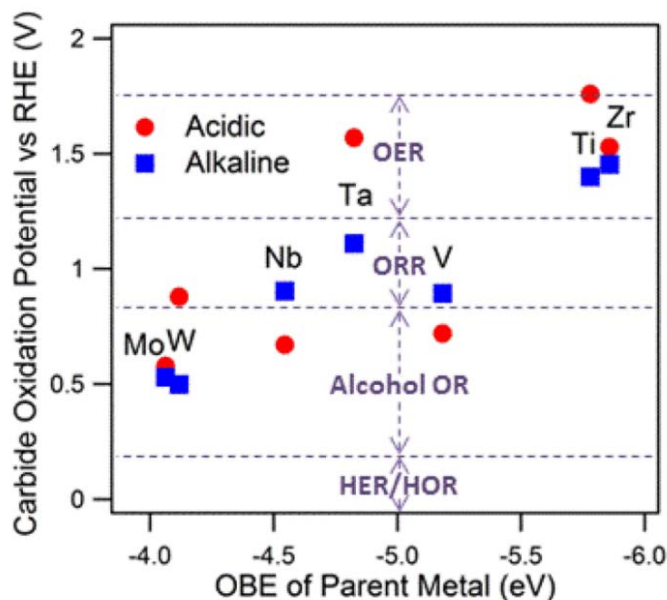
Figure 2-9. Oxidation potential of metal carbide as a function of DFT calculated oxygen binding energy (OBE) of the parent metal.

The dashed lines superimposed over the data represent the general operational potentials of common electrochemical reactions.[111]

Reprinted with permission from (*ACS Catal.* 2014, 4, 5, 1558-1562). *Copyright © 2014, American Chemical Society.*

The data in Figure 2-3 has demonstrated that the transition metal carbide stability under alkaline condition has a strong correlation with the metal-oxygen binding energy which the stronger the binding energy was, the more stable the carbide would be under

alkaline condition. For the acidic condition, the trend was not as clear with V being the outlier. Nevertheless, one can easily find out the WC is not stable under acidic conditions by cycling through 0.4-1.0 V for 10,000 times. Promising candidates under acidic ORR conditions are TaC, TiC, and ZrC. The TiC would require ~1550 °C to react between TiO_2 and C which surpasses our equipment limit.[112-113] A higher temperature (1550 °C~1700 °C) is required for ZrC synthesis which was not feasible to synthesize through the RME and carburization with methane route.[114-115] However, TaC carburization temperature is relatively lower compared to TiC and ZrC which is around 1000 °C.[116] This is achievable through the conventional method as the Pt or other noble metal adding into the system will facilitate the CH_4 decomposition which will lower the carburization temperature for the core-shell TaC.[102-103] Additionally, we also synthesized the NbC core-shell as the Nb carburization temperature is similar to TaC and achievable.[117-118]

Results and Discussion

The synthesis technic is very similar to the previously described method with the difference in carburization method.[2-4, 6, 99]

Synthesis Steps

Alkoxide precursors

Commercial niobium and tantalum isopropoxide (TaIPO and NbIPO, Alfa Aesar) were used as delivered. Tungsten isopropoxide (WIPO) was prepared by adding 20 mL anhydrous isopropanol (Sigma-Aldrich) into 5 grams of WCl_4 (Sigma-Aldrich) under constant stirring and continuous anhydrous N_2 flow which served as the carrier gas to purge out the HCl generated. The process can be heated to 333 K to accelerate the evaporation of residual isopropanol. This process was repeated 3 times with 20 mL isopropanol to avoid any HCl residue or unreacted WCl_4. After all the isopropanol residue drying out, 100 mL anhydrous isopropanol was added and then sonicated to make a well-dispersed mixture. The WIPO/isopropanol mixture was stored in a glovebox along with the other isopropoxide precursors. Titanium (IV) isopropoxide (TiIPO) was prepared by

diluting the commercial titanium (IV) isopropoxide (Sigma-Aldrich) to 5% w/v with anhydrous isopropanol.

Reverse microemulsion (RME) synthesis of oxide nanoparticles

The RME was prepared by mixing 240 mL n-heptane (VWR) with 54 mL Brij-L4® surfactant (Sigma-Aldrich), then stirred till transparent. 15 mg of NH_4Cl (Sigma-Aldrich) and 1.4 mL NH_4OH solution (Sigma-Aldrich) was added into 7.8 mL DI water (18.2 MΩ·cm), then injected into the previous described heptane-Brij mixture. If the noble metal shell is Pt only, then no NH_4Cl was added. The RME mixture was then sonicated for 10 minutes to ensure small aqueous phases to be well dispersed. Then the corresponding alkoxide precursors (8 mL WIPO& 0.2 mL TiIPO, or 1.5 mL NbIPO, or 1.5 mL TaIPO), diluted with 100 mL anhydrous heptane inside the glovebox, were injected into the RME as fast as possible to minimize hydrolysis in ambient air. The RME mixture was then left for 4 hours to ensure complete hydrolysis of the alkoxide precursors to form corresponding oxides.

A separate RME containing $RhCl_3$ or H_2PtCl_6 (depends on the noble metal shell component) precursor was prepared with 46 mL n-heptane (VWR), 7.2 mL Brij-L4® surfactant (Sigma-Aldrich) and 10-30 mg of $RhCl_3*xH_2O$ (Sigma-Aldrich) or 50~70 mg of H_2PtCl_6 (Strem) dissolving in 1 mL DI water (18.2 MΩ·cm). The small RME was sonicated 10 minutes before adding into the big RME. Tetraethyl orthosilicate (TEOS, Sigma-Aldrich) was added 4 hours after the Rh precursor added. The whole system was left stirring for 16.5 hours before precipitating out with 300 mL methanol (Sigma-Aldrich). The solid was recovered by decanting, centrifugation, washing with acetone and drying under vacuum.

Carburization

For the TiWC core-shell, the solid obtained in the previous step was heated in a tube furnace up to 900 °C at a ramping rate of 2 °C min^{-1} under 120 sccm H_2 and 30 sccm CH_4

flow. The temperature was held at 900 °C for 4.5 hours. The temperature was then dropped to 850 °C with only 120 sccm H_2 to do the H_2 scavenging step for 0.5 hours.

The system was then cooled to room temperature under a pure H_2 atmosphere. Encapsulated core-shell nanoparticles were passivated with 1% O_2/ 99%N_2 for 2 hours. The samples were measured by XRD to confirm the carbide phase formation then stored in a glovebox. For the NbC core-shell particles, the carburization was maintained at 970-990 °C for 4.5 hours then the H_2 scavenge step was operated at 1020 °C for 0.5 hours with a ramping rate 2 °C min^{-1}. For the TaC core-shell particles, the carburization was maintained at 970-990 °C for 7 hours then ramped to 1020-1090 °C with a ramping rate 2 °C min^{-1}. The H_2 scavenge step was operated at 1020-1090 °C for 1~3 hours. The rest procedures were the same as the TiWC core-shell (i.e., methane concentration, passivation procedure).

Dissolution of silica shell

For the TiWC core-shell nanoparticles, the procedure was as follows: 120 µL of 48 wt% aqueous HF solution (Sigma-Aldrich) was diluted with 5 mL degassed ethanol (VWR) to make the silica dissolving stock solution. 30 mg of the encapsulated core-shell nanoparticles were firstly mixed with 10 mg of acid-treated carbon black (Cabot, Vulcan® XC-72r) and then silica dissolving stock solution was added into the solid mixture. The whole system was sonicated for 1 minute then shaken for 18 hours to ensure fully dissolving the silica encapsulation. The core-shell nanoparticles were then recovered by centrifugation and washed thoroughly with degassed ethanol 4 times. The powders were dried under vacuum and tested by XRD to confirm the carbide phased remained before storing in a glovebox.

For the NbC and TaC core-shells, due to a higher carburization temperature and higher H_2 scavenge temperature, the silica encapsulation was more stable and contained less oxygen. Hence the HF concentration in the stock solution needed to be higher. For the NbC core-shell nanoparticles, the dissolving stock solution was prepared as follows: 150 µL of 48 wt% aqueous HF solution (Sigma-Aldrich) was diluted with 5 mL degassed ethanol (VWR). This stock solution was also applied to 30 mg of encapsulated NbC core-

shell with 10 mg acid-treated carbon black. For the TaC core-shell nanoparticles, the dissolving stock solution was prepared as follows: 210 µL or 270 µL of 48 wt% aqueous HF solution (Sigma-Aldrich) was diluted with 5 mL degassed ethanol (VWR). The choice of 210 µL or 270 µL depended on the oxidation of the encapsulated core-shell. To be noticed, the decapsulation process was able to diminish the metal oxide in the core-shell to some extent. Hence, if XRD crystallography demonstrated more TaO_x or NbO_x before the dissolution process, one may consider ramp up the HF concentration in the dissolving stock solution.

Characterization

The nanoparticles after the dissolution step were measured by XRD and the XRD crystallography was shown in Figure 2-4 for the Pt/NbC core-shell with different core-shell particle sizes; Figure 2-5 demonstrated the Pt/TaC core-shell with different core-shell particle sizes. The particle sizes were estimated through the Scherrer equation as follow:

$$\tau = \frac{K\lambda}{\beta cos\theta}$$

<div align="right">Equation 2-1</div>

τ can be deemed as the mean size of the nanoparticles; K is the shape factor and usually assigned as dimensionless number 0.9; λ is the x-ray wavelength 0.154 (given Cu Kα radiation source); β is the dominant peak full width at half maximum (FWHM); θ is the Bragg angle, or the dominant peak position. Thus, one can calculate the particle size based on XRD crystallography. The particle sizes can also be measured directly from TEM as shown in Figure 2-6. TEM images are the most straightforward way to identify the particle sizes, however, this technic is localized, meaning that one may not be able to capture the uniform / average particle sizes.

The core-shell particle sizes can be tuned by varying the Pt content, the carburization temperature and H_2 scavenge temperature and time. With a higher Pt content (thicker Pt shell), higher carburization temperature and higher H_2 scavenge temperature, and longer time would induce a larger core-shell particle. In a standard synthesis described above, adding less than 70 mg H_2PtCl_6 / mL would result in 4~7 nm particle size; 80 ~120 mg H_2PtCl_6 / mL would result in 7~16 nm particle size. The higher end of the particle size was

achieved by using 990 °C for carburization temperature and 3 hours of 1090 °C H$_2$ scavenge step.
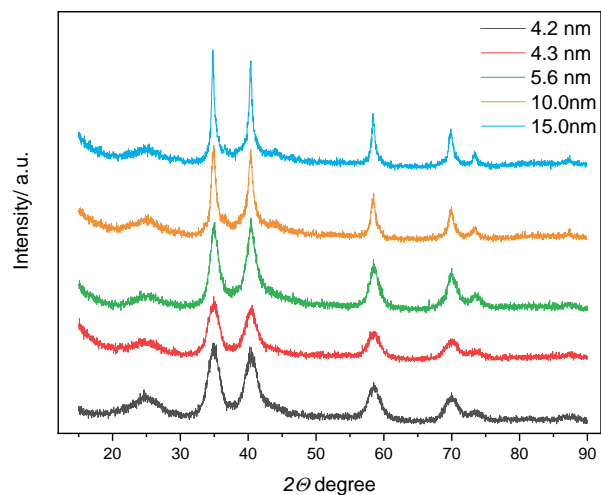
Figure 2-10. Pt/NbC core-shell XRD with different particle sizes.
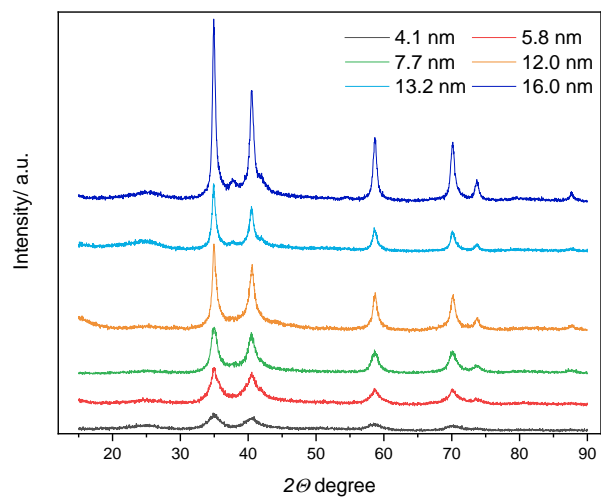
Figure 2-11. Pt/TaC core-shell XRD with different particle sizes.
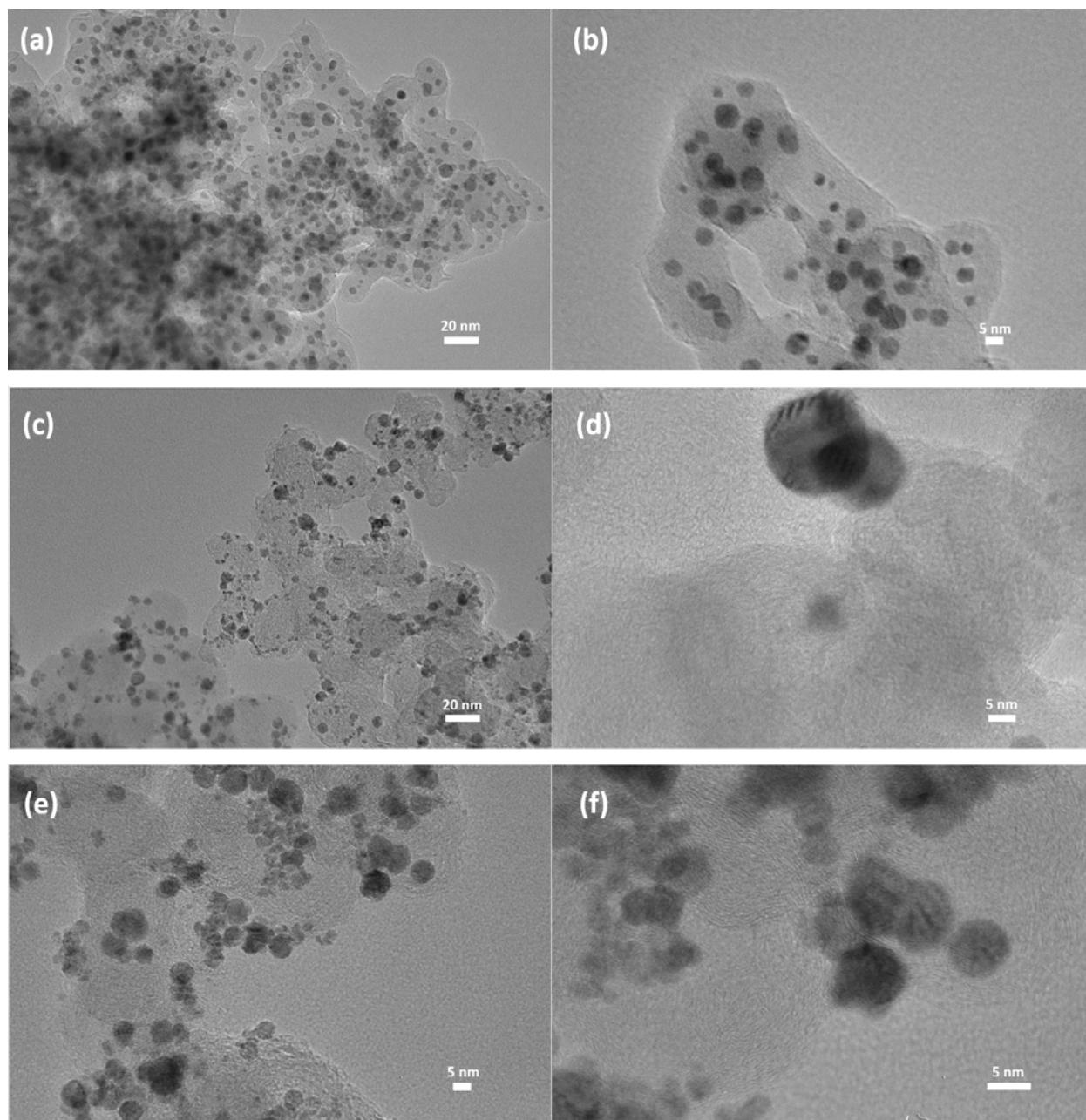
Figure 2-12. TEM of Pt/TaC core-shell before and after dissolutions with different sizes.

(a) silica encapsulated Pt/TaC nanoparticles with particle size ~6nm; (b) silica encapsulated Pt/TaC particles with particle size ~12nm; (c) carbon black supported Pt/TaC nanoparticles with particle size ~6nm; (d) carbon black supported Pt/TaC nanoparticles with particle size ~16nm; (e) carbon black supported Pt/TaC nanoparticles with particle size ~12nm; (f) carbon black supported Pt/TaC nanoparticles with particle size ~6nm.

Through a synthesis of Pt/TaC, Pt_2Ta phases were observed as shown in Figure 2-7. This was due to a long time of H_2 scavenge step (e.g., 4 hours). A patent on synthesizing Pt-

Ta alloy was documented in 1993 where they could synthesize Pt-Ta alloy by heating the Pt and Ta precursor mixtures under an inert atmosphere to 927 °C.[119] Interestingly, this patent described this Pt-Ta alloy as a carbon monoxide tolerant catalyst for the hydrogen oxidation reaction. We will mention a similar application in Chapter 5 which may be owing to the surface Pt-Ta alloy. However, the formation of Pt_2Ta alloy may not necessarily be an advantage as the Pt may sink into core losing the accessibility in reactions.
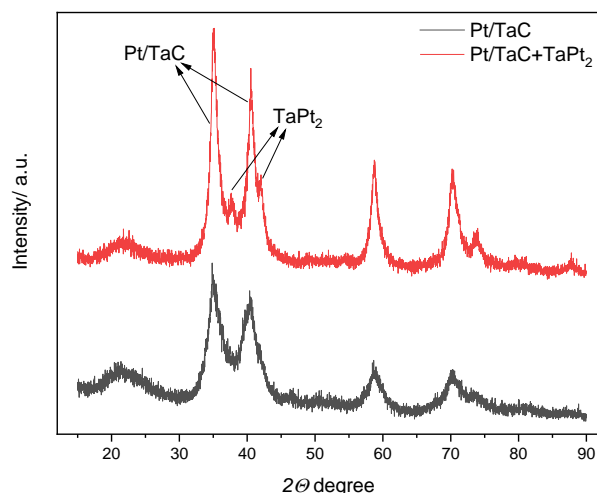
Figure 2-13. Pt/TaC core-shell and $TaPt_2$ XRD with different H_2 scanvage time.

Obtaining the particle size is a critical step to calculate the core-shell particle monolayer coverages and the next step is to measure the core to shell atomic ratio. This is measured by the inductively coupled plasma mass spectrometry (ICP-MS). The sample preparation method was described in experimental part. The data were shown in Table 2-1 for Pt/NbC core-shell and Table 2-2 for the Pt/TaC. To be noticed, the silica encapsulated uncarburized samples were measured rather than the carburized samples. The reason was because that TaC or NbC with well-defined crystallinity would form after carburization which was resistant to the dissolving stock solution (i.e., Aqua Regia and HF). A Ta ICP measurement of the carbon-supported carburized sample had been done which only showed 10% of the uncarburized sample which was another evidence to show how stable the TaC core was once it formed.

Table 2-1. ICP-MS results of encapsulated Pt/NbO$_x$ to calculate the core:shell metal ratio

Pt/NbO$_x$	Nb wt%	Stdev	Pt(wt%)	Stdev	Nb: Pt atomic ratio average	Nb: Pt atomic ratio stdev
Syn124	16.00%	0.40%	8.60%	0.20%	3.91	0.01
Syn125	16.40%	1.50%	6.50%	0.70%	5.28	0.16
Syn132	13.20%	1.50%	2.80%	0.20%	10.01	0.36
Syn135	14.80%	3.90%	3.60%	1.20%	8.7	0.61

Table 2-2. ICP-MS results of encapsulated Pt/TaO$_x$ to calculate the core:shell metal ratio

Pt/TaO$_x$	Ta wt%	Stdev	Pt(wt%)	Stdev	Ta: Pt atomic ratio average	Ta: Pt atomic ratio stdev
Syn123	11.60%	0.70%	4.90%	0.10%	2.57	0.09
Syn126	15.90%	0.40%	2.70%	0.10%	6.30	0.21
Syn131	14.60%	0.20%	2.10%	0.00%	7.56	0.05
Syn136	24.30%	1.00%	6.20%	0.30%	4.24	0.06
Syn137	17.20%	5.20%	5.80%	1.80%	3.22	0.00
Syn138	21.30%	3.70%	1.60%	0.30%	14.09	0.24
Syn139	19.40%	2.50%	1.80%	0.20%	11.47	0.02

Shell thickness calculation was done by assuming the nanoparticles are perfect spheres. This calculation was valid when the core-shell particle was at least 3 nm. Based on Alloyeau et al., 3 nm CoPt alloy was an isotropic truncated octahedron with 1289 atoms.[120] Barnard et al. also found out for gold nanoparticles the truncated octahedra was the most energetically favorable structure.[121] The truncated octahedron is usually constructed by removing 6 square pyramids from the regular octahedron. The square pyramids all have side lengths of a and the regular octahedron has a side length of 3a. The volume and the half-height were as follows:

$$V_{\text{trun-Octa}} = 8\sqrt{2}a^3 \qquad\qquad \textbf{Equation 2-2}$$

$$H = \sqrt{2}a \qquad\qquad \textbf{Equation 2-3}$$

At the same time, if we use the truncated octahedron half-height as the radius to construct the perfect sphere, the volume would be as follow:

$$V_{\text{sphere}} = \frac{4\pi}{3}(\sqrt{2}a)^3 = \frac{\pi}{3}8\sqrt{2}a^3 \approx 8\sqrt{2}a^3 \qquad\qquad \textbf{Equation 2-4}$$

There would be a 4.7% overestimate the real volume by assuming a perfect sphere which was acceptable given the measurement error was around 5%.

From the XRD, we would be able to know the particle size of the carbide core as the well-coated core-shell structure should not have noble metal peaks. The core volume was therefore calculated before converting to core mass by multiplying the core carbide density. The core mass was then divided by carbide molar mass to convert to moles. The number was divided by the atomic ratio measured by ICP-MS to get the noble metal moles which were then converted to shell mass and shell volume respectively. By adding the core and shell volume together we would be able to get the total volume of the core-shell which can then yield the total radius of the core-shell. Subtracting by the core radius would yield the shell thickness. The shell thickness divided by noble metal atomic diameter would yield the monolayer coverage.

After doing the calculation, one can find out the monolayer coverage is controlled by the shell to core metal ratio and carbide core sizes. By changing the shell to core precursor ratios while maintaining the same carburization and H_2 scavenge profile one can achieve the monolayer coverage control.

Conclusions

We have successfully synthesized core-shell platforms with NbC and TaC cores. The particle size and monolayer coverages can be tuned by changing the carburization and H_2 scavenge temperature or the shell to core precursor ratios. Besides, more than 4 hours of H_2 scavenge step is not recommended as it will induce Pt_2Ta peaks which may indicate

Pt sinks into core losing the accessibility in reactions. The superior Pt/TaC core-shell corrosive resistance and reactivity would be introduced in Chapter 5.

Experimental

Powder x-ray diffraction (PXRD)

Bruker D8 diffractometer using Cu Kα radiation source was used to measure the X-ray diffraction pattern for all the nanoparticles before and after the CO_2 hydrogenation reaction. The step size was 0.02° and step time was 0.3 s. Powder samples were placed onto zero background silicon crystal sample plate (MTI corp).

Transmission electron microscopy (TEM)

JEOL 2010 and JEOL 2010 F equipped with a field emission gun (FEG) were used to take TEM images on the core-shell Rh and Rh_{comm} nanoparticles. The accelerating voltage was at 200 kV and the magnifications ranged from 50,000× to 120,000×. Samples were dispersed in ethanol and deposited onto copper grids with carbon film.

Inductively coupled plasma mass spectrometry (ICP-MS)

Element corresponding loadings were measured on an Agilent 7900 ICP-MS. Samples with silica encapsulation was dissolved in aqua regia (concentrated HNO_3, HCl solutions from Sigma Aldrich) and 48 wt% aqueous HF solution (Sigma-Aldrich) overnight. The fully dissolved samples were diluted with 2% HNO_3 to a W or Nb concentration of ~100 ppb level (Rh would be a lower concentration. The monolayer coverage was calculated assuming the core-shell nanoparticles are perfect sphere. The sphere diameters were measured from TEM and XRD and the atomic ratio measured by ICP-MS.

Acknowledgement

CHAPTER 3 ENHANCEMENT OF CO SELECTIVITY BY TRANSITION METAL CARBIDE RHODIUM CORE-SHELL NANOPARTICLES IN CO$_2$ HYDROGENATION

Supported rhodium catalysts with a high Rh loading will normally catalyze CO$_2$ to CH$_4$. In this chapter, using partial CO$_2$ hydrogenation as a model reaction, we demonstrate how transition metal carbide (TMC) cores can modify both Rh shell electronic structure and Rh ensemble size to dramatically increase the selectivity for CO (~13 times) while at a high Rh loading. Charge transfer from Rh shell to cores were observed and the extended x-ray absorption fine structure (EXAFS) confirmed the Rh-W interaction for the Rh/TiWC core-shell structure. These results combining with the density functional theory (DFT) calculation have demonstrated that the enhanced CO selectivity is attributed to TiWC, NbC cores modification of the Rh shell through ligand and ensemble effects.

Introduction

Bimetallic systems have received much attention due to their unique catalytic properties that are different from those of the constituents.[24, 63, 122-124] The enhanced catalytic activity and selectivity can often be attributed to three effects, namely, strain, ligand, and ensemble effects.[125-126] These effects are induced mainly through constituents lattice mismatch, electronic interaction, and site coordination change respectively.[127-128] Due to the heterometallic nature, it is difficult to separate these three effects especially in alloy and intermetallic systems.[126, 129-130] Another bimetallic system, core-shell structures, can potentially offer the separation for these effects owing to the high degree of design flexibility.[64, 107] However, the conventional core-shell structures connected with metallic bonding suffer from dynamic restructuring under reaction conditions owing to the miscibility of the constituents.[56, 131-132]

We recently reported using TiWC and TiWN as core materials to host atomically thin Pt shell through one-pot synthesis and high-temperature self-assembly method which demonstrated superior activity and stability.[2-4, 6] The core-shell dynamic restructuring issue was overcome because the noble-metal shell was immiscible with the carbide or nitride core owing to its nobility of not forming corresponding carbide or nitride

compounds. Moreover, this platform was able to separate the ligand effect from ensemble and strain effects. From our previous study, Pt/TiWC and Pt/TiWN core-shell nanoparticles featured enhanced ethylene selectivity in acetylene hydrogenation reaction solely because of the ligand effect from Pt shell and underlying core interaction reduced intermediate ethylene binding energy.[77] While we envisaged this effect could extend to other noble-metal shells besides Pt and other reaction intermediates, a comprehensive study had not been performed.

Herein, we employed CO_2 hydrogenation reaction as a probe reaction, combining with density functional theory (DFT) calculations, X-ray photoelectron spectroscopy (XPS), and extended X-ray absorption fine structure (EXAFS) to elucidate the Rh ensemble and electronic structure change by interacting with the underlying TiWC and NbC core. Specifically, we demonstrated the enhanced CO selectivity of Rh for the CO_2 hydrogenation reaction using a core-shell platform. Rh typically will yield methane in CO_2 hydrogenation reactions due to a strong CO intermediate binding energy on the Rh surface.[27, 133-135] While CO selectivity can be changed by tuning CO binding energy through the ligand effect.[27] Additionally, nanoparticle ensemble size also plays a critical role in CO_2 hydrogenation selectivity.[49, 136-137] For instance, isolated Rh sites supported on TiO_2 are able to selectively hydrogenate CO_2 to CO rather than CH_4.[49] In this study, we demonstrated TiWC and NbC cores could modulate Rh shell through both ligand and ensemble effects. Both XPS and DFT calculation showed a change of Rh electronic structure in which Rh $3d_{5/2}$ peak binding energy was upshifted and Rh d-band center was downshifted respectively. The fitting of *in-situ* EXAFS spectra provided structural information, including Rh-Rh bond distance and coordination numbers. The unchanged Rh-Rh bond distance and nearly half of the Rh-Rh coordination number in the core-shell nanoparticles confirmed the Rh ensemble size reduction. Our work highlighted stark difference (~13 times) in CO selectivity by using core-shell platforms, providing valuable insights for the design of new catalysts for selective CO_2 hydrogenation reaction.

Results and Discussion

The CO_2 hydrogenation was investigated as a function of core composition and Rh shell coverage to demonstrate the reactivity trend. In order to study the ligand and ensemble effects induced by NbC and TiWC cores, commercial Rh nanoparticles supported on carbon black was used for comparison. The core-shell materials studied comprised nominal Rh shell coverages of 0.2 monolayers (ML) and 0.5 ML over NbC and TiWC cores (detailed synthetic and characterization descriptions were in SI and our previous work).[2-4, 6, 77, 99] Although the nominal coverages did not ensure each individual core-shell nanoparticle was covered by the exact monolayers of Rh shell as described, the materials with higher nominal Rh loading on average tended to have less exposed core as supported by the XPS measurement shown in **Table S3-1** which probed the surface atomic ratio. The materials were co-fed with CO_2 and H_2 (1:3 molar ratio) diluted with helium under 1 atm pressure. CO and CH_4 were the main hydrogenation products with minimal C_2H_6 detected which did not affect overall carbon balance. CO selectivity was compared at 543 K under iso-conversion of CO_2 by changing space velocity and catalyst rates normalized by Rh active sites and by overall catalyst weights were compared at 573 K as shown in Table 3-1.

Table 3-3. Catalysts selectivity and reaction rate at 543 K and 573 K.

	543 K		573 K			
	CO_2 conversion	CO selectivity	CO STY [hr^{-1}]	CH_4 STY [hr^{-1}]	CO Mass Rate [mmol/(hr*g_{Cat})]	CH_4 Mass Rate [mmol/(hr*g_{Cat})]
Rh/CB	1.2%	7.4%±0.4%	5.2±1.1	42.7±4.4	18.3±3.4	150.3±7.5
0.5ML Rh/NbC	0.9%	99.7%±0.1%	27.6±1.3	0.1±0.1	27.9±0.3	0.1±0.1
0.5ML Rh/TiWC	0.8%	96.3%±0.1%	29.9±3.6	0.6±0.1	21.0±0.6	0.4±0.1
0.2ML Rh/NbC	1.1%	97.4%±0.1%	85.6±5.0	3.5±0.2	79.1±2.9	3.1±0.1
0.2ML Rh/TiWC	1.2%	98.8%±0.1%	94.4±11.3	1.4±0.2	54.1±1.2	0.8±0.1
TiWC	N.A.	N.A.	N.A.	N.A.	2.1±0.2	0.1±0.1

Specifically, we observed more than 13 times enhancement in CO selectivity for all the core-shell nanoparticles with varied Rh coverages and different core compositions compared to a commercial carbon black supported Rh catalyst (~5 w-t%). Tungsten carbide had been reported as an effective catalyst for the reverse water gas shift reaction

(RWGS), [138-140] therefore, we also performed a control experiment where TiWC pure core was tested for the CO_2 hydrogenation and the mass activity was compared with the other catalysts at 573 K. As shown in Table 3-1, the TiWC mass activity in CO production was around one order of magnitude lower than the core-shell catalysts which indicated the enhanced CO rate in the RWGS reaction was not contributed solely by the pure core. To be noticed, even though the pure core had inferior mass activity than the Rh core-shell nanoparticles, the CO mass rate was still 36 times higher than the bulk unpromoted-tungsten carbide reported in literature owing to the increased surface area by nanostructure.[138] CO and CH_4 site time yield (STY) for Rh_{comm} and core-shell Rh catalysts were measured under the differential condition and normalized by the number of Rh active sites measured through electrochemical CO stripping method described in the supporting information. The CO STY values at 573 K were reported in Table 3-1 and 0.2 ML Rh/TiWC core-shell nanoparticles had the most CO STY which was more than 18 times higher than the Rh_{comm}. The CO site time yield of Rh/TiWC and Rh/NbC core-shell nanoparticles were comparable with similar Rh coverages which implied the TiWC and NbC cores affecting Rh shell with an analogous way. However, the CO rates were inversely proportional to Rh shell coverages for both TiWC and NbC cores which suggested CO_2 was adsorbed on the exposed core and Rh shell helped to split H_2 to facilitate the CO_2 hydrogenation.[141-143] Moreover, the Rh_{comm} had quite different kinetic parameters including apparent activation energy, CO_2, and H_2 reaction orders compared to the core-shell nanoparticles as shown in Table S3-8 to Table S3-10 which indicated the fundamental mechanisms were different for the Rh_{comm} and Rh core-shell. Additionally, the core-shell materials featured structure stability under reaction condition as shown in Figure S3-3 where XRD pattern of core-shell particles before and after reaction did not change while Rh_{comm} had increased particle size post-reaction. Similar stability for C_2H_2 hydrogenation reaction was reported before[77], and this was expected as the core-shell nanoparticles were synthesized through high temperature (>1173 K) self-assembly method, hence, reaction temperature at 573 K would not change the core-shell structure.

To find out the cause of the increased CO selectivity, we performed EXAFS and XPS measurements to gain insights into the Rh coordination, Rh bond distance, and Rh

electronic structure of the Rh_{comm} and Rh core-shell nanoparticles. Given the similar reactivity in the CO_2 hydrogenation probe reaction, we only performed the *in-situ* EXAFS measurement for Rh_{comm} and Rh/TiWC core-shell nanoparticles. As shown in Table 3-2, Rh_{comm}, 0.2 ML Rh/TiWC, and 0.5 ML Rh/TiWC nanoparticles were compared at 543 K with H_2 and CO_2 co-feeding at a ratio of 3:1. The Rh-Rh first coordination number of Rh_{comm} was around 9.3 which matched the TEM observed Rh_{comm} nanoparticles size 2.8 ± 0.6 nm as shown in Figure S3-2.[144-146] This Rh-Rh coordination number was twice as large as that of observed in Rh/TiWC which indicated the Rh ensemble size in the Rh/TiWC core-shell was smaller than Rh_{comm} which corroborated the enhanced CO selectivity observed in the CO_2 hydrogenation reaction for the Rh/TiWC nanoparticles. As Matsubu et al. pointed out that smaller Rh ensembles would be hard to complete an 8-electron reduction of CO_2 to CH_4, hence, featured a higher selectivity towards CO.[49] However, unlike other Rh alloy formation, the change of Rh ensemble was usually accompanied with the change of Rh-Rh bond distance,[147] Rh-Rh bond distances in Rh/TiWC core-shell nanoparticles were the same as the Rh_{comm} within uncertainty. This suggested that core modification of Rh shell through an ensemble effect but not strain effect. Moreover, W was also observed in the first Rh coordination neighbor which suggested there might be Rh-W interaction. The Rh carbon coordination was not found significant based on the EXAFS fitting which was discussed in detail in SI.

Table 3-4. Rh_{comm}, 0.2 ML Rh/TiWC and 0.5 ML Rh/TiWC Rh coordination number (CN) with Rh and W corresponding bond distances at 543 K with H_2 to CO_2 ratio 3 to 1.

	Rh-Rh CN	Rh-Rh Distance (Å)	Rh-W CN	Rh-W Distance (Å)
Rh_{comm}	9.33 ± 1.63	2.675 ± 0.009	-	-
0.2 ML Rh/TiWC	3.86 ± 0.81	2.669 ± 0.014	3.68 ± 0.89	2.748 ± 0.023
0.5 ML Rh/TiWC	5.11 ± 0.53	2.675 ± 0.008	3.64 ± 0.48	2.738 ± 0.015

The charge transfer from Rh to the core was revealed by the results of XPS. As shown in Figure 3-1 and Table S3-1, the commercial Rh $3d_{5/2}$ peak positioned at 307.1 eV which represented the metallic Rh^0, while Rh shells on TiWC core or NbC core were determined to be electron deficient metallic Rh with a $3d_{5/2}$ binding energy at 307.4~307.5 eV, 0.3~0.4 eV higher than that of the Rh_{comm} nanoparticles.[141, 148-149] We have also observed a

0.1~0.3 eV downshift in W $4f_{7/2}$ peak position on TiWC cores as Rh shell was placed on top of them which supported the hypothesis of Rh-W interaction existence that electron was withdrawn from the Rh shell and injected to the TiWC core.[2] However, a direct proof of Rh-Nb interaction was not observed in the Rh/NbC core-shell as Nb $3d_{5/2}$ peak positions were the same for pure NbC core and Rh/NbC core-shells as shown in Table S3-1, but Rh peak shifts were observed.
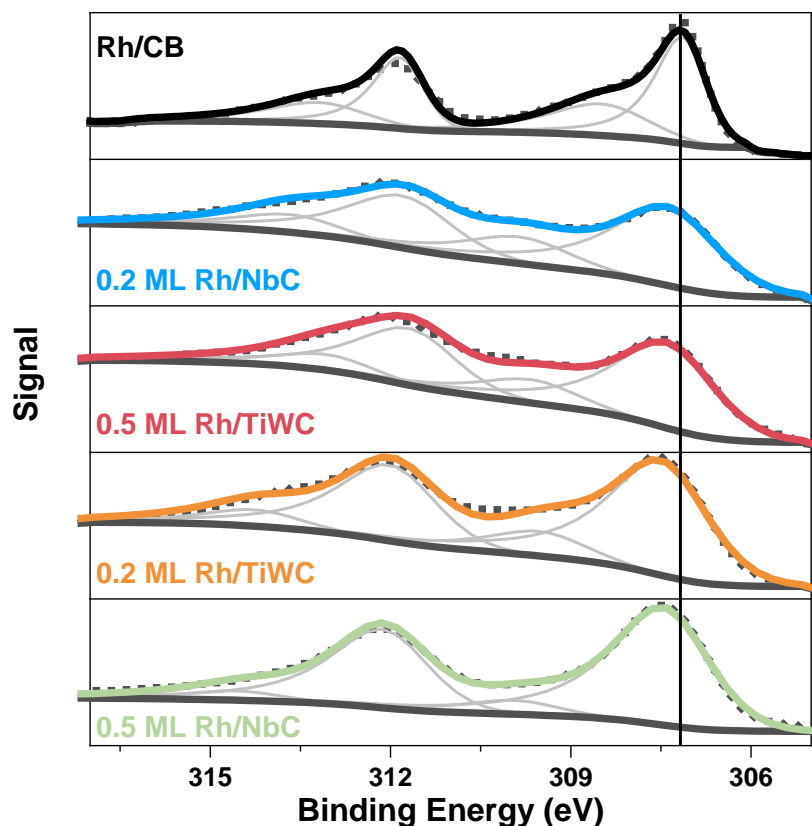
Figure 3-14. X-ray photoelectron spectroscopy (XPS) of Rh 3d orbitals.

The peaks were deconvoluted by Casa XPS.

DFT calculations were used to further probe the TiWC core impact on Rh shell and to explain the experimental observations. Rh/TiWC core-shell model was constructed through a heat, quench, and exfoliation (HQE) method which was described in detail in SI and previous works.[77, 99, 150] Given the observation of Rh-W coordination from EXAFS, W terminated TiWC core was constructed to host Rh shell. Previous DFT work from Liu et al. also supported this model construction as they found out that Rh on the W-

terminated surface was the most stable form.[149] However, for the exposed core, the C-terminated surface was more stable for tungsten carbide.[151] Therefore, the DFT model was separated into two parts where one section was Rh covered W-terminated TiWC and the other was the C-terminated exposed TiWC core. Rh (111) was used to represent the Rh$_{comm}$ catalyst in the DFT calculation.

DFT calculated CO_2 and CO adsorption energies over Rh (111), TiWC supported Rh and C-terminated TiWC core were shown in Table 3-3. The lower CO adsorption energy on Rh/TiWC and the bare core than Rh (111) was consistent with the enhanced CO selectivity observed in the CO_2 hydrogenation as the CO binding energy was an important descriptor of CO selectivity.[152-153] The CO_2 adsorption energies over Rh (111) surface and Rh/TiWC were similar and both were much weaker than CO_2 binding to the C-terminated TiWC core. A similar result was reported by Koverga et al. where a strong CO_2 adsorption on C-terminated tungsten carbide was observed.[154] This suggested the CO_2 would preferentially bind to the uncovered C-terminated TiWC core than to the Rh shell in the Rh/TiWC which corroborated the higher reaction rates observed for low Rh coverage core-shell particles shown in Table 3-1. The existence of Rh shell improved H_2 splitting as there was nearly no barrier for H_2 activation for Rh$_{comm}$ and Rh shell but a 0.2 eV barrier for the bare TiWC core. This was consistent with the Rh/TiWC core-shell exhibited a CO production rate that was one order of magnitude higher than that of the pure TiWC core. A similar mechanism was reported where CO_2 chemisrobed onto Mo$_2$C and form *CO by breaking one of the C=O bonds while the *CO was able to desorb directly but the oxygen atom had to be removed by activated H_2 to complete the catalytic cycle.[85, 139, 155]

Table 3-5. DFT calculated CO_2 and CO adsorption energies and over Rh (111), Rh/TiWC and pure TiWC core

	CO$_2$ E$_{ads}$ (eV)	CO E$_{ads}$ (eV)	H$_2$ dissociation barrier (eV)
Rh (111)	-0.3	-2.5	0
Rh/TiWC	-0.2	-2.0	0
TiWC	-1.1	-1.5	0.2

DFT calculations of the projected density of states (PDOS) were performed to further reveal the electronic structure difference between the Rh core-shell compared to the

Rh$_{comm}$. As shown in Figure 3-2, the Rh d-band was broadened in the Rh/TiWC compared to the Rh (111) surface. The Rh-Rh bond distance calculated from the DFT model were nearly the same between Rh (111) and Rh/TiWC which was consistent with the EXAFS analysis shown in Table S3-2 to Table S3-4. This suggested the change of the Rh d-band electronic structure was not from the strain effect. Thus, we propose this broadening was a result of the hybridization of W and Rh d states (through ligand effect).[99] Rh and W have different coupling matrix elements and the coupling matrix element is a measure of the extent of transition metal d states which increases down through the groups and decreases to the right in the periodic table.[156] Thus, W has a larger coupling matrix element than Rh which results in d orbital overlap increasing for Rh when hybridizing with W. Based on the Hammer- Nørskov model, d orbital overlapping would result in the d-band broadening and it correlated to a downshifted d-band center relative to the Fermi level.[157] The downshifted Rh d-band center was indeed observed. As shown in Figure 3-2, the d-band center downshifted from -1.53 eV to -1.95 eV which explained the lower CO adsorption energy calculated for Rh/TiWC.[3, 24, 77, 99]
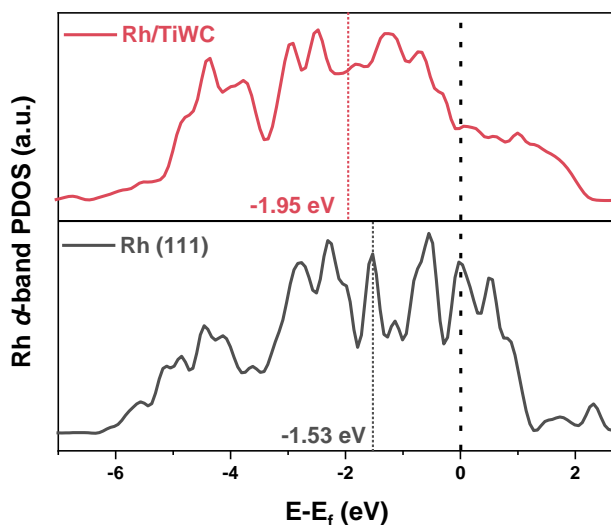
Figure 3-15. Calculated Rh valence d-band projected density of states (PDOS) and Rh d-band centers relative to the Fermi level.

Conclusion

Through a combination of experimental and computational technics, we have demonstrated Rh shell was modified by the NbC and TiWC cores through ligand and ensemble effects. The downshifted Rh d-band center and decreased Rh ensemble size featured facile desorption of the CO intermediate and barrier of further hydrogenation of CO to CH_4 which led to a remarkable enhancement in CO selectivity in the CO_2 hydrogenation reaction. More generally, we used the core-shell platform to provide a versatile way of tuning material properties to control reaction selectivity.

Experimental Section

A detailed experimental description can be found in the Supporting information.

Sample Preparation. Rh_{comm} was purchased from Sigma-Aldrich and core-shell Rh nanoparticles were synthesized through the previously reported high temperature self-assembly method with modified carburization profiles.[6]

Catalytic Reactions. CO_2 hydrogenation reactions were performed in a single-pass-plug-flow reactor. The reactor temperature was maintained constant to obtain steady-state reactivity data. The total flow rate was 80 mL/min (CO_2 = 10 mL/min, H_2 = 30 mL/min, He = 40 mL/min or CO_2=0.125 atm, H_2=0.375 atm, and He=0.5 atm) at 1 atm with a gas hourly space velocity (GHSV) varied from 6100 to 73000 hr^{-1} to obtain the iso-conversion CO selectivity comparison. The reaction temperature was varied from 523 K to 593 K to obtain the activation energy. An Agilent 6890 FID & TCD gas chromatography was used to analyze product distribution. The system was free of mass and heat transfer limitations with details shown in the SI.

Sample Characterization. Rh_{comm} and core-shell Rh nanoparticle particle before and after reaction were measured by powder x-ray diffraction (PXRD, Bruker D8) using Cu Kα radiation source to monitor the crystal structure changes. JEOL 2010 and JEOL 2010 F equipped with a field emission gun (FEG operating at 200 kV) were used to take TEM images for particle size analysis. PHI Versaprobe II with a monochromatic Al anode X-

ray source was used to analyze the binding energy shifts of surface Rh, NbC and TiWC cores. Rh, Nb, Ti, and W element loadings were measured on an Agilent 7900 ICP-MS. The Rh number of sites were measured by electrochemical CO stripping method. XAS was performed at the National Synchrotron Light Source II (NSLS-II) at Brookhaven National Laboratory with Inner-Shell Spectroscopy (8ID-ISS) where Rh K-edge (23219.9 eV) and W L3-edge (10206.8 eV) were measured for Rh_{comm}, Rh/TiWC with two shell coverages and corresponding standards.

DFT Calculation. Vienna ab initio simulation package (VASP) was used for the Rh electronic structure calculations.[158] The Rh/TiWC core-shell model was constructed through heat, quench and exfoliation (HQE) method.[150] A detailed description was included in the Supporting Information.

Code Availability. The corresponding codes for the density functional theory calculations are available upon request.

Acknowledgements

Supporting Information

Results

TEM of Core-shell Rh and Rh$_{comm}$
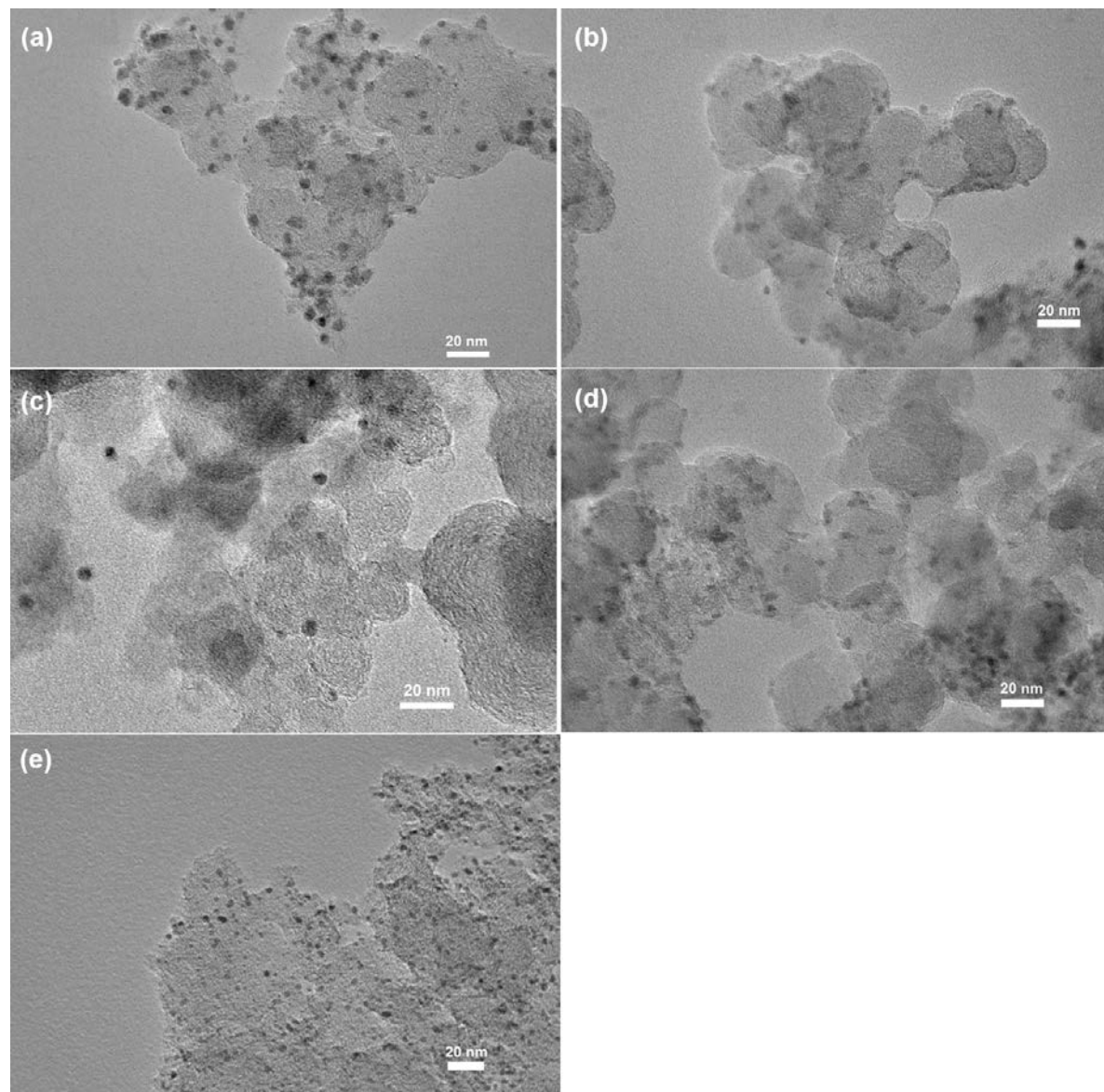
Figure S3-16. Transmission electron microscopy (TEM) of the Rh/TiWC, Rh/NbC, and Rh commercial (Rh$_{comm}$) nanoparticles.

(a) 0.2 ML Rh/TiWC nanoparticles; (b) 0.2 ML Rh/NbC nanoparticles; (c) 0.5 ML Rh/TiWC nanoparticles; (d) 0.5 ML Rh/NbC nanoparticles; (e) Rh/carbon black commercial nanoparticles.

TEM of Core-shell Rh and Rh$_{comm}$ Particle Size Histogram
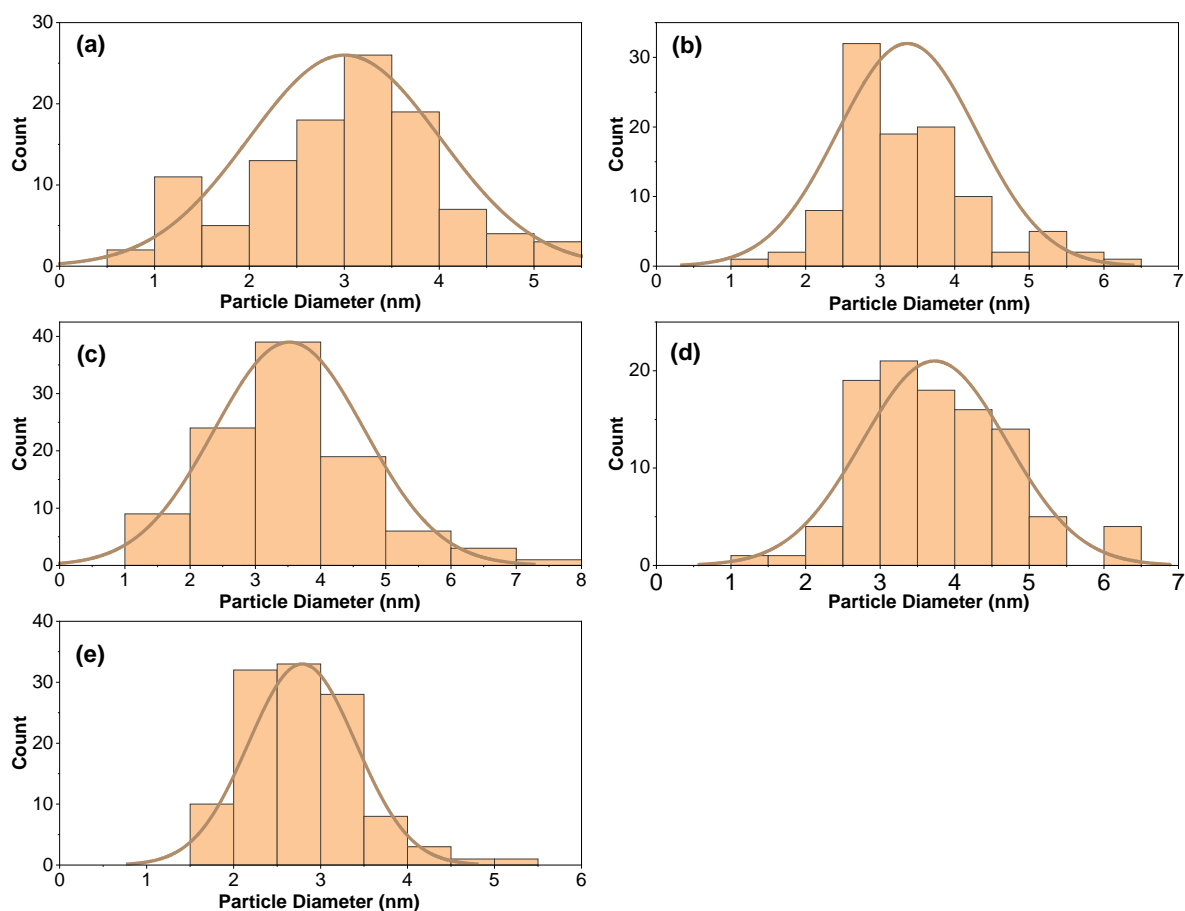
Figure S3-17. TEM histogram of the Rh/TiWC, Rh/NbC, and Rh$_{comm}$ nanoparticles.

(a) 0.2 ML Rh/TiWC nanoparticles, 3.0 ± 1.0 nm; (b) 0.2 ML Rh/NbC nanoparticles, 3.4 ± 0.9 nm; (c) 0.5 ML Rh/TiWC nanoparticles, 3.5 ± 1.2 nm; (d) 0.5 ML Rh/NbC nanoparticles, 3.7 ± 1.0 nm; (e) Rh/carbon black commercial nanoparticles, 2.8 ± 0.6 nm.

XRD before and post CO₂ hydrogenation reaction
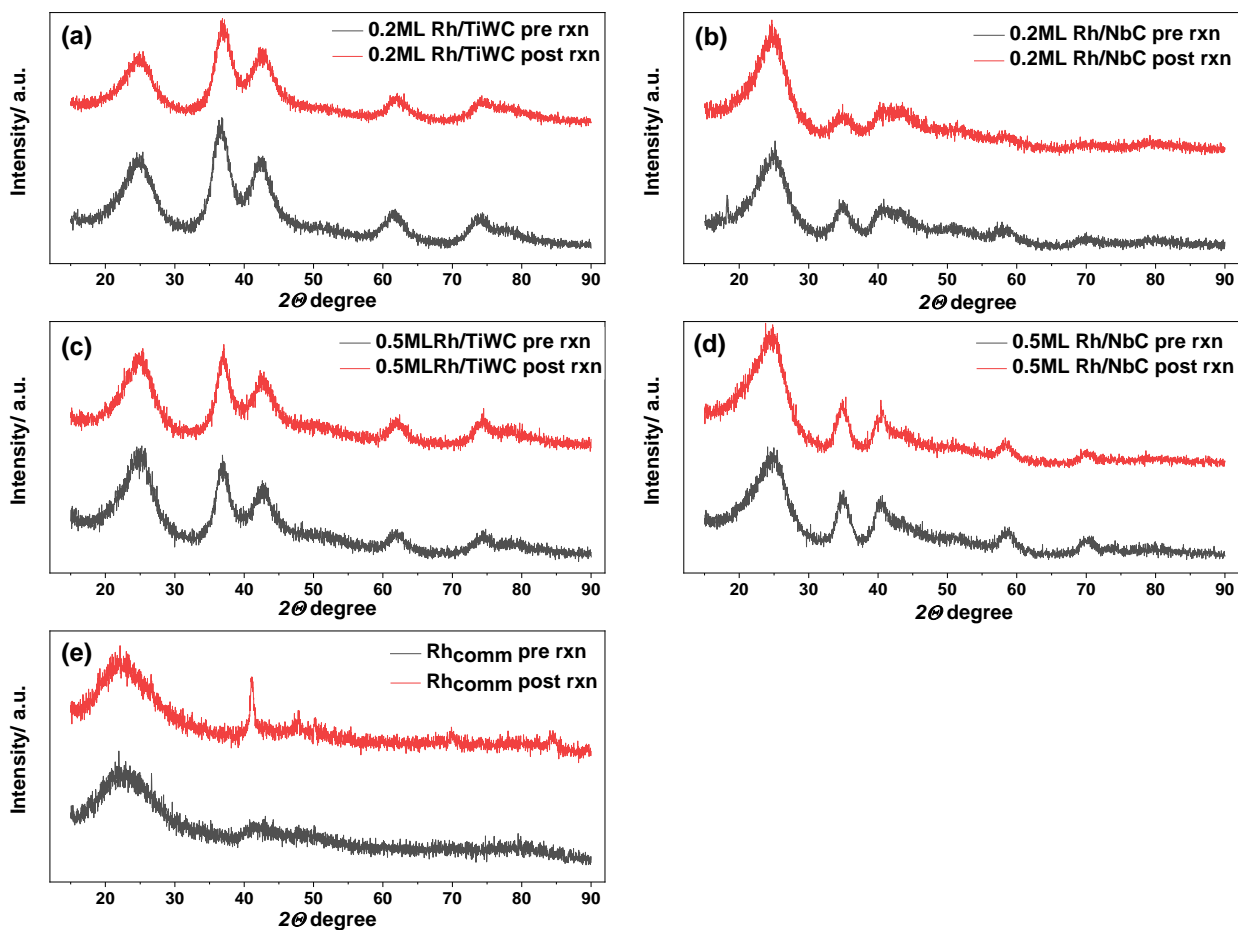
Figure S3-18. X-Ray diffraction patterns of core-shell Rh catalysts and Rh_{comm} before and after the reaction.

(a) Combined diffractograms for 0.2 ML Rh/TiWC before and after reaction; (b) combined diffractograms for 0.2 ML Rh/NbC before and after reaction; (c) combined diffractograms for 0.5 ML Rh/TiWC before and after reaction; (d) combined diffractograms for 0.5 ML Rh/NbC before and after reaction; (e) combined diffractograms for Rh_{comm} before and after reaction; The structure of the core-shell particles remained intact through the CO₂ hydrogenation reaction, however, Rh_{comm} had sharp Rh (111) peak indicating the Rh_{comm} nanoparticles size increased after the reaction condition.

XPS of nanoparticles before reaction

Table S3-6. Core-shell Rh 3d$_{5/2}$ binding energy and bulk and surface shell to core atomic ratio

	Shell : Core (Surface XSP, atomic)	Shell : Core (Bulk ICP, atomic)	Rh 3d$_{5/2}$ Binding Energy (eV)	W 4f$_{7/2}$ Binding Energy (eV)	Nb 3d$_{5/2}$ Binding Energy (eV)
Rh/CB	N.A.	N.A.	307.1	-	-
0.5ML Rh/NbC	0.86	0.26	307.5	-	204.1
0.5ML Rh/TiWC	0.90	0.26	307.4	31.9	-
0.2ML Rh/NbC	0.47	0.15	307.4	-	204.1
0.2ML Rh/TiWC	0.36	0.14	307.5	32.1	-
TiWC	-	-	-	32.2	-
NbC	-	-	-	-	204.1
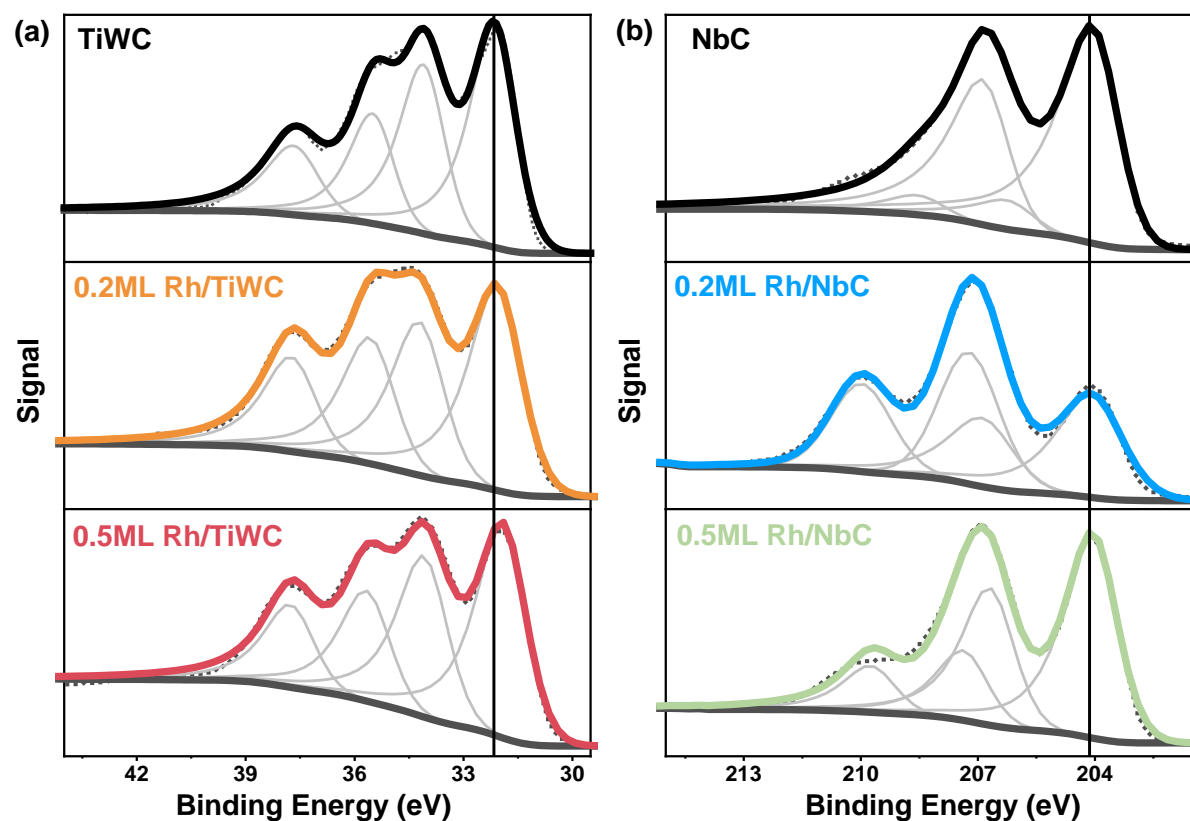
Figure S3-19. X-ray photoelectron spectroscopy (XPS) of W 4f and Nb 3d orbitals.

(a) W 4f orbitals were compared among the pure TiWC core, 0.2 ML Rh/TiWC and 0.5 ML Rh/TiWC core-shell nanoparticles; (b) Nb 3d orbitals were compared among the pure NbC core, 0.2 ML Rh/NbC and 0.5 ML Rh/NbC core-shell nanoparticles; The peaks were deconvoluted by Casa XPS.

Description

Core-shell Nanoparticles Synthesis

Alkoxide precursors

Commercial niobium isopropoxide (NbIPO, Alfa Aesar) was used as delivered. Tungsten isopropoxide (WIPO) was prepared by adding 20 mL anhydrous isopropanol (Sigma-Aldrich) into 5 grams of WCl_4 (Sigma-Aldrich) under constant stirring and continuous anhydrous N_2 flow which served as the carrier gas to purge out the HCl generated. The process can be heated to 333 K to accelerate the evaporation of residual isopropanol. This process was repeated 3 times with 20 mL isopropanol to avoid any HCl residue or unreacted WCl_4. After all the isopropanol residue drying out, 100 mL anhydrous isopropanol was added and then sonicated to make a well-dispersed mixture. The WIPO/isopropanol mixture was stored in a glovebox along with the other isopropoxide precursors. Titanium (IV) isopropoxide (TiIPO) was prepared by diluting the commercial titanium (IV) isopropoxide (Sigma-Aldrich) to 5% w/v with anhydrous isopropanol.

Reverse microemulsion (RME) synthesis of oxide nanoparticles

The RME was prepared by mixing 240 mL n-heptane (VWR) with 54 mL Brij-L4® surfactant (Sigma-Aldrich), then stirred till transparent. 15 mg of NH_4Cl (Sigma-Aldrich) and 1.4 mL NH_4OH solution (Sigma-Aldrich) was added into 7.8 mL DI water (18.2 MΩ·cm), then injected into the previous described heptane-Brij mixture. The RME mixture was then sonicated for 10 minutes to ensure small aqueous phases to be well-dispersed. Then the corresponding alkoxide precursors (8 mL WIPO& 0.2 mL TiIPO, or 1.5 mL NbIPO), diluted with 100 mL anhydrous heptane inside the glovebox, were injected into the RME as fast as possible to minimize hydrolysis in ambient air. The RME mixture was then left for 4 hours to ensure complete hydrolysis of the alkoxide precursors to form corresponding oxides.

A separate RME containing $RhCl_3$ precursor was prepared with 46 mL n-heptane (VWR), 7.2 mL Brij-L4® surfactant (Sigma-Aldrich) and 10-30 mg of $RhCl_3*xH_2O$ (Sigma-Aldrich) dissolving in 1 mL DI water (18.2 MΩ·cm). The small RME was sonicated 10 minutes

before adding into the big RME. Tetraethyl orthosilicate (TEOS, Sigma-Aldrich) was added 4 hours after the Rh precursor added. The whole system was left stirring for 16.5 hours before precipitating out with 300 mL methanol (Sigma-Aldrich). The solid was recovered by decanting, centrifugation, washing with acetone and drying under vacuum.

Carburization

For the Rh/TiWC, the solid obtained in the previous step was heated in a tube furnace up to 1173 K at a ramping rate of 2 K min^{-1} under 120 sccm H_2 and 30 sccm CH_4 flow. The temperature was held at 1173 K for 4.5 hours. The temperature was then dropped to 1123 K with only 120 sccm H_2 to do the H_2 scavenging step for 0.5 hours. The system was then cooled to room temperature under a pure H_2 atmosphere. Encapsulated core-shell nanoparticles were passivated with 1% O_2/ 99%N_2 for 2 hours. The samples were measured by XRD to confirm the carbide phase formation then stored in a glovebox. For the Rh/NbC particles, the carburization temperature was maintained at 1203 K for 4.5 hours then the H_2 scavenge step was operated at 1253 K for 0.5 hours. The rest procedures were the same as the Rh/TiWC core-shell.

Dissolution of silica shell

120 µL of 48 wt% aqueous HF solution (Sigma-Aldrich) was diluted with 5 mL degassed ethanol (VWR) to make the silica dissolving stock solution. 30 mg of the encapsulated core-shell Rh nanoparticles were firstly mixed with 10 mg of acid-treated carbon black (Cabot, Vulcan® XC-72r) and then silica dissolving stock solution was added into the solid mixture. The whole system was sonicated for 1 minute then shaken for 18 hours to ensure fully dissolving the silica encapsulation. The core-shell nanoparticles were then recovered by centrifugation and washed thoroughly with degassed ethanol 4 times. The powders were dried under vacuum and tested by XRD to confirm the carbide phased remained before storing in a glovebox.

Materials Characterization

The equipment was the same for the previous paper and the measurements were done in a similar manner.[77]

Transmission electron microscopy (TEM)

JEOL 2010 and JEOL 2010 F equipped with a field emission gun (FEG) were used to take TEM images on the core-shell Rh and Rh$_{comm}$ nanoparticles. The accelerating voltage was at 200 kV and the magnifications ranged from 50,000× to 120,000×. Samples were dispersed in ethanol and deposited onto copper grids with carbon film.

Powder x-ray diffraction (PXRD)

Bruker D8 diffractometer using Cu Kα radiation source was used to measure the X-ray diffraction pattern for all the nanoparticles before and after the CO_2 hydrogenation reaction. The step size was 0.02° and step time was 0.3 s. Powder samples were placed onto zero background silicon crystal sample plate (MTI corp).

X-ray photoelectron spectroscopy (XPS)

PHI Versaprobe II with a monochromatic Al anode X-ray source was used to analyze the binding energy shifts of surface Rh, NbC and TiWC cores. The X-ray source was operated at 50 W and 15 kV. Due to the high conductivity of the sample, no charge correction was applied. The Rh/TiWC, Rh/NbC and Rh$_{comm}$ samples were loaded into a U-tube set-up where pure H_2 (50 sccm) flowed through and heated up to 623 K for 1 hour to imitate the normal activation condition during CO_2 hydrogenation. The recarburization condition was carried out at 873 K for 8 hours with 20% CH_4 and 80% H_2 cofeed. After the activation, the U-tube set-up was isolated by two on-off valves and transferred into a glove box. XPS samples were prepared by mounting powders onto conductive copper tape inside the glove box. Samples were transferred into XPS side chamber using a transferring vessel to minimize the air exposure.

X-ray absorption spectroscopy (XAS)

XAS was performed at the National Synchrotron Light Source II (NSLS-II) at Brookhaven National Laboratory with Inner-Shell Spectroscopy (8ID-ISS). Rh K-edge (23219.9 eV) and W L3-edge (10206.8 eV) were measured for the Rh_{comm}, core-shell Rh/TiWC nanoparticles and standards (e.g. Rh foil, Rh_2O_3, W metal, WO_2, WO_3, WC, W_2C) in fluorescence mode. For the Rh K-edge measurement, samples were measured with a Rh foil serving as a reference spectrum. The extended x-ray absorption fine structure (EXAFS) parameters were fitted with Athena and Artemis software from the Demeter package. The Rh_{comm}, 0.2 ML, and 0.6 ML Rh/TiWC Rh environment under reaction conditions were shown in Table S3-2, Table S3-3 and Table S3-4.

Table S3-7. Rh_{comm} Rh coordination number (CN) with Rh and O and corresponding bond distances under room temperature (RT) and different reaction conditions.

Rh_{comm}	CN Rh-Rh	Distance Rh-Rh (Å)	CN Rh-O	Distance Rh-O (Å)
No flow RT	4.14 ± 0.94	2.673 ± 0.010	3.19 ± 0.47	1.993 ± 0.017
H_2 RT	8.89 ± 0.82	2.678 ± 0.004	-	-
H_2 623 K	8.89 ± 1.00	2.668 ± 0.006	-	-
CO_2 573 K	9.26 ± 1.44	2.678 ± 0.008	-	-
$3H_2$ + CO_2 573 K	9.38 ± 1.21	2.667 ± 0.007	-	-
$3H_2$ + CO_2 543 K	9.33 ± 1.63	2.675 ± 0.009	-	-

Table S3-8. 0.2 ML Rh/TiWC Rh coordination number (CN) with Rh, O, and W and corresponding bond distances under room temperature (RT) and different reaction conditions.

0.2 ML Rh/TiWC	CN Rh-Rh	Distance Rh-Rh (Å)	CN Rh-O	Distance Rh-O (Å)	CN Rh-W	Distance Rh-W (Å)
No flow RT	4.42 ± 1.15	2.593 ± 0.016	1.76 ± 0.70	2.002 ± 0.031	6.15 ± 1.58	2.675 ± 0.018
H$_2$ RT	3.36 ± 0.45	2.689 ± 0.006	1.39 ± 0.25	1.908 ± 0.018	2.70 ± 0.60	2.799 ± 0.010
H$_2$ 623 K*	3.71 ± 1.38	2.663 ± 0.029	-	-	2.72 ± 1.18	2.701 ± 0.048
CO$_2$ 573 K*	5.57 ± 1.42	2.682 ± 0.023	1.07 ± 0.58	1.970 ± 0.044	4.91 ± 1.70	2.697 ± 0.027
3H$_2$ + CO$_2$ 573 K	4.28 ± 1.02	2.659 ± 0.018	-	-	4.33 ± 0.94	2.708 ± 0.024
3H$_2$ + CO$_2$ 543 K	3.86 ± 0.81	2.669 ± 0.014	-	-	3.68 ± 0.89	2.748 ± 0.023

*χ(k) truncated at 10

Table S3-9. 0.5 monolayer (ML) Rh/TiWC Rh coordination number (CN) with Rh, O, and W and corresponding bond distances under room temperature (RT) and different reaction conditions.

0.5 ML Rh/TiWC	CN Rh-Rh	Distance Rh-Rh (Å)	CN Rh-O	Distance Rh-O (Å)	CN Rh-W	Distance Rh-W (Å)
No flow RT	5.16 ± 1.19	2.680 ± 0.016	1.15 ± 0.49	1.976 ± 0.040	2.73 ± 1.05	2.743 ± 0.038
H$_2$ RT	5.68 ± 1.18	2.689 ± 0.017	-	-	2.81 ± 1.02	2.760 ± 0.043
H$_2$ 623 K	4.91 ± 0.76	2.675 ± 0.013	-	-	3.39 ± 0.63	2.735 ± 0.024
CO$_2$ 573 K	4.78 ± 0.35	2.661 ± 0.005	-	-	3.74 ± 0.34	2.734 ± 0.010
3H$_2$ + CO$_2$ 573 K	5.29 ± 0.73	2.686 ± 0.012	-	-	3.43 ± 0.67	2.756 ± 0.023
3H$_2$ + CO$_2$ 543 K	5.11 ± 0.53	2.675 ± 0.008	-	-	3.64 ± 0.48	2.738 ± 0.015

Inductively coupled plasma mass spectrometry (ICP-MS)

Element loadings were measured on an Agilent 7900 ICP-MS. Samples with silica encapsulation was dissolved in aqua regia (concentrated HNO_3, HCl solutions from Sigma Aldrich) and 48 wt% aqueous HF solution (Sigma-Aldrich) overnight. The fully dissolved samples were diluted with 2% HNO_3 to a W or Nb concentration of ~100 ppb level (Rh would be a lower concentration). The ICP-MS results were shown in Table S3-5. The monolayer coverage was calculated assuming the core-shell nanoparticles are perfect sphere. The sphere diameters were measured from TEM and XRD and the atomic ratio measured by ICP-MS.

Table S3-10. Rh core-shell material compositions

	Core wt%	Rh wt%	Rh:Core (Atomic Ratio)
0.2 ML SiO$_2$/Rh/TiWC	11.0%±0.6%	1.1%±0.1%	0.14±0.05
0.5 ML SiO$_2$/Rh/TiWC	11.7%±1.1%	1.8%±0.2%	0.26±0.04
0.2 ML SiO$_2$/Rh/NbC	14.0%±1.5%	3.9%±0.4%	0.15±0.03
0.5 ML SiO$_2$/Rh/NbC	13.0%±0.4%	2.2%±0.1%	0.26±0.02

Heat and Mass Transfer Limitation Calculation

The calculation was performed in a similar manner as the previous work.[77]

External Transport Limitations

Mear's criteria were used to estimate the external mass transfer.[159]

$$\frac{r_{obs}\rho_b R n}{k_c C_b} < 0.15$$

Equation S3-5

where r_{obs} is the observed rate of reaction in mol/(kg$_{cat}$*s); ρ_b is the catalyst bed density in kg/m^3 (the total weight of the catalyst bed and the volume taken up in the reactor was measured, hence void fraction was not used in this calculation); R is the catalyst particle

radius in m; n is the reactant reaction rate order; k_c is the external mass transfer coefficient in m/s; C_b is the reactant bulk concentration in mol/m³.

k_c was calculated by assuming the Sherwood number equals to 2 and D_{AB} is the diffusivity.

$$Sh(Sherwood\ Number) = \frac{2Rk_c}{D_{AB}} = 2 \qquad \textbf{Equation S3-6}$$

Mear's external heat transfer was shown as follow.[159]

$$\frac{|\Delta H| r_{obs} \rho_b R E_a}{h R_g T_0^2} < 0.15 \qquad \textbf{Equation S3-7}$$

where ΔH is the enthalpy of reaction in kJ/mol; E_a is the reaction activation energy in kJ/mol; h is the external heat transfer coefficient in W/(m²-K); R_g is the gas constant (8.314 J/(mol-K)); T_0 is the reaction temperature (543K was used).

h was calculated by assuming the Nusselt number equals to 2.

$$Nu(Nusselt\ Number) = \frac{2Rh}{D_{AB}} = 2 \qquad \textbf{Equation S3-8}$$

Table S3-11. Tabulation of Parameters for the Mear's Criteria Calculation

Symbol	Meaning & Unit	Value
r_{obs}	reaction rate (mol/(kg$_{cat}$-s)) (highest)	1.34×10^{-3}
Re	Reynold's number	1.35
Q	flow rate (ml/min)	80
u	superficial velocity (m/s)	0.08
D	reactor inner diameter (m)	0.0046
A	reactor inner area (m^2)	1.6×10^{-5}
ρ_{gas}	gas density (kg/m^3)	0.159
ρ_b	catalyst bed density (kg/m^3)	1198
μ	gas viscosity (Pa-s)	2.09×10^{-5}
P	total pressure of the gas (Pa)	1.01×10^5
R	particle size (m)	7.5×10^{-5}
k_c	external mass transfer coefficient (m/s)	1.93
C_b	reactant bulk concentration (mol/m^3)	2.41
E_a	activation energy (kJ/mol)	79
ΔH	$CO_2 + 4H_2 \rightarrow CH_4 + 2H_2O$ enthalpy (kJ/mol)	-165.3
n	reaction order (use H$_2$, the largest one)	1.0
h	heat transfer coefficient (W/m^2-K)	1050
Mear's criterion (Mass) 2.6×10^{-5} << 0.15		
Mear's criterion (Heat) 5.5×10^{-4} << 0.15		

Internal Transport Limitations

Internal mass transfer limitation was checked by using the Weisz-Prater criterion.[159]

$$\eta\phi^2 = \frac{r_{obs}R^2\rho_c}{D_e C_{AS}}$$

Equation S3-9

η is the dimensionless effectiveness factor; ϕ is the Thiele modulus; D_e is the effective gas-phase diffusivity in m²/s; C_{AS} is the reactant gas concentration at the catalyst surface in mol/m³ which was assumed to be the same as C_b due to no external mass transfer limitation; ρ_c is the crystallite density in kg/m³; if ϕ <<1, then $\eta \approx 1$ and ϕ can be calculated. D_e was calculated using the following equation, where D is the diffusivity, ε is the porosity; δ is the constrictivity; τ is the tortuosity. (ε =0.6, δ =0.8, τ =1.8) [160]

$$D_e = \frac{D\varepsilon\delta}{\tau}$$ **Equation S3-10**

Table S3-12. Tabulation of Parameters for the Weisz-Prater's Criteria Calculation

Symbol	Meaning & Unit	Value
r_{obs}	reaction rate (mol/(kg$_{cat}$-s))	1.34×10^{-3}
R	particle size (m)	7.5×10^{-5}
D_e	effective diffusivity (m²/s)	1.81×10^{-7}
ρ_c	catalyst particle density (kg/m³)	2000
C_{AS}	reactant concentration at the catalyst surface (mol/m³)	2.41
Calculated Weisz-Prater's criterion ($\eta\phi^2$)		**3.5×10^{-2} <<1**

In addition to the Mear's criteria and Weisz-Prater's criterion, GradientCheck for Heterogeneous Catalysis was used.

(https://engineering.purdue.edu/~catalyst/gradientcheck/grad_index.html)

Reactants and products physical properties were obtained from the NIST websites.

Reaction kinetics

Table S3-13. Activation energy data for core-shell Rh and Rh_{comm} nanoparticles. Reaction conditions: $CO_2 = 0.125$ atm $H_2 = 0.375$ atm, He = 0.5 atm, and temperature varied from 523 K to 573 K.

Activation Energy	Based on CO rate (kJ/mol)	Based on CH₄ rate (kJ/mol)	Based on total rate (kJ/mol)
Rh_{comm}	82.5±10.7	76.6±3.9	76.7±6.8
0.2ML Rh/TiWC	53.4±5.6	71.8±15.8	53.7±5.8
0.5ML Rh/TiWC	63.1±3.2	78.1±5.7	60.4±7.7
0.2ML Rh/NbC	47.8±2.8	61.3±7.9	48.2±3.1
0.5ML Rh/NbC	45.6±2.8	68.4±5.5	46.4±2.5

Table S3-14. CO_2 reaction order data for core-shell Rh and Rh_{comm} nanoparticles. Reaction conditions: $CO_2 = 0.038$ atm to 0.575 atm; $H_2 = 0.375$ atm, balanced with He to make the total pressure 1atm and temperature was at 543 K.

CO₂ Reaction Order	Based on CO rate	Based on CH₄ rate	Based on total rate
Rh_{comm}	0.99±0.07	0.02±0.02	0.13±0.02
0.2ML Rh/TiWC	0.43±0.03	0.06±0.03	0.43±0.03
0.5ML Rh/TiWC	0.45±0.01	0.02±0.02	0.44±0.01
0.2ML Rh/NbC	0.45±0.01	-0.04±0.01	0.43±0.01
0.5ML Rh/NbC	0.42±0.01	0.00±0.06	0.42±0.01

Table S3-15. H_2 reaction order data for core-shell Rh and Rh_{comm} nanoparticles. Reaction conditions: $CO_2 = 0.125$ atm; $H_2 = 0.063$ atm to 0.825 atm, balanced with He to make the total pressure 1atm and temperature was at 543 K.

H₂ Reaction Order	Based on CO rate	Based on CH₄ rate	Based on total rate
Rh_{comm}	0.02±0.02	0.78±0.02	0.66±0.02
0.2ML Rh/TiWC	0.41±0.03	0.83±0.05	0.41±0.03
0.5ML Rh/TiWC	0.40±0.04	0.96±0.05	0.41±0.04
0.2ML Rh/NbC	0.33±0.02	1.36±0.07	0.35±0.01
0.5ML Rh/NbC	0.40±0.02	0.97±0.03	0.40±0.02

Experimental measurement of the number of Rh active sites CO stripping measurements

BASI RDE-2 rotating disk electrode combining with a CH Instruments 627 E potentiostat were used for the CO stripping measurement at room temperature. Ag/AgCl was used as the reference electrode and Pt coil was used for the counter electrode. Stock solution (DI water, isopropanol, Nafion ® 117 solution) was prepared to disperse samples. The ink concentration was 6 mg sample / mL stock solution. The working electrode was prepared by dropping 6 µL of the ink on freshly polished 3 mm glassy carbon disk electrodes, followed by drying. Each catalyst sample measurements were made with at least triplicates.

The samples were pretreated in argon saturated 0.1 M $HClO_4$ solution with 100 cyclic voltammetry (CV) conditioning scans from -0.252 V to 0.722 V at 0.2 V/s scan rate with a 2500 rpm ration rate; after conditioning, the samples were purged with CO for 7 minutes followed by purging with Ar for 7 minutes to make sure no residue CO was in the solution. Then 6 cyclic voltammetry scans from -0.259 V to 0.898 V at 0.05 V/s scan rate without rotation were performed to strip off CO for Rh_{comm} and Rh/NbC samples. For Rh/TiWC samples, 6 cyclic voltammetry scans from -0.259 V to 0.798 V at 0.05 V/s scan rate without rotation were performed. The higher potential may lead to TiWC core dissolving. The voltammetry scans were shown in Figure S3-5 and the number of sites for each sample was shown in Table S3-11. The TiWC core did not have the CO stripping peak as shown in previous studies. [3, 6, 161]
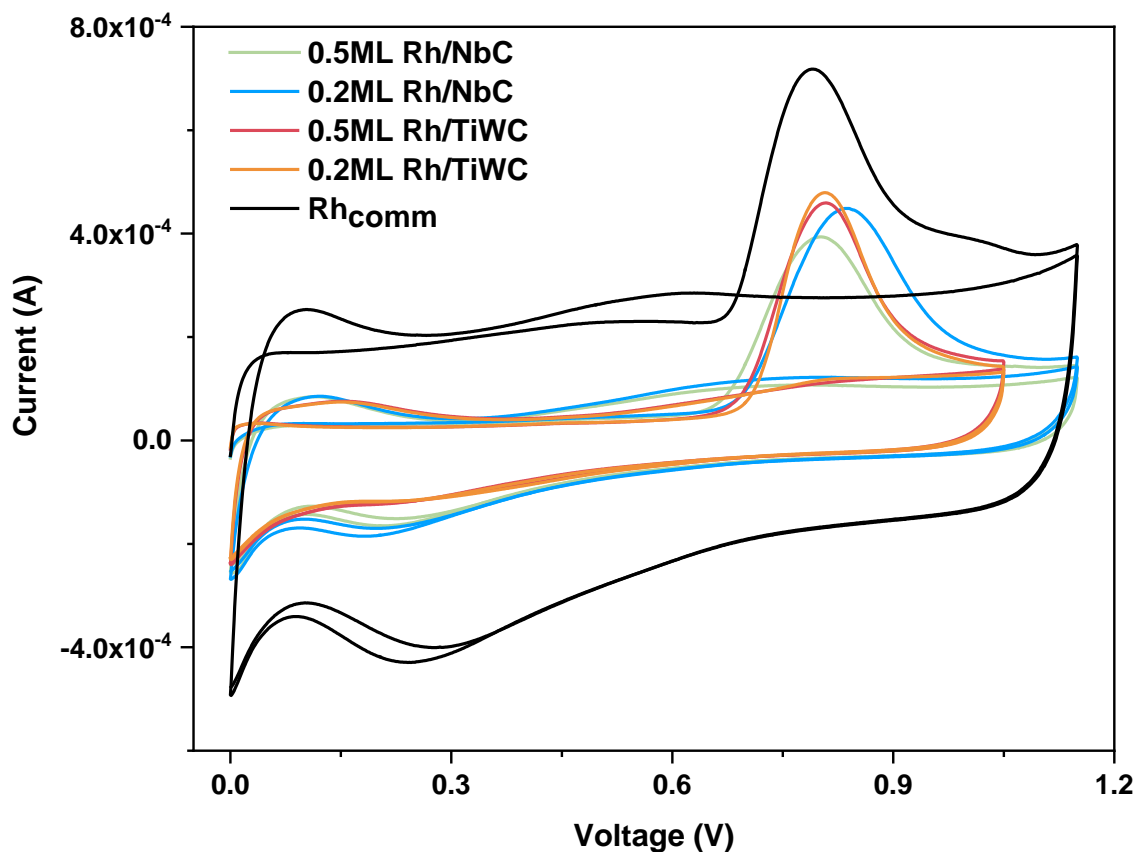
Figure S3-20. Two-cycle of cyclic voltammetry (CV) curve.

The peak areas were integrated.

After obtaining the data, the area was integrated for the CO peak between 0.6 V to 1.1 V. The mathematical meaning of the area was shown in the following equation.

$$Area = IV = \frac{QV}{t}$$

<div align="right">

Equation S3-11

</div>

The area divided by the scan rate provided the total charge transferred. In order to convert the charge into a mole basis, the total charge transferred was divided by F, Faraday's constant.

$$\text{Total Charge Transfer} = \frac{Area}{ScanRate} = \frac{QV}{t} / \frac{V}{t}$$

<div align="right">

Equation S3-12

</div>

$$\text{Mole Basis} = \frac{\text{Total Charge Transfer}}{F}$$

For Rh, the factor of the net charge due to oxidation and desorption of the CO adlayer was 385 µC cm^{-2}. [162-163] This factor was used to convert total charge to the Rh active surface area.

Table S3-16. Site Number Count from CO stripping integration method and CO chemisorption method for Pt$_{comm}$, core-shell and core materials.

	CO stripping area (m^2/g$_{Rh}$)	Number of Sites (mmol/g$_{Rh}$) or (mmol/g$_{core}$)
Rh$_{comm}$ (TEM size estimate)	173.3	N.A.
Rh$_{comm}$(CO stripping)	178.6±15.9	3.5±0.3
0.5 ML Rh/NbC	191.2±7.3	3.8±0.1
0.2 ML Rh/NbC	232.9±10.9	4.6±0.2
0.5 ML Rh/TiWC	231.0±26.4	4.5±0.5
0.2 ML Rh/TiWC	255.5±29.7	5.0±0.6

Stability of Core-Shell Rh and Rh$_{comm}$ under Reaction Condition
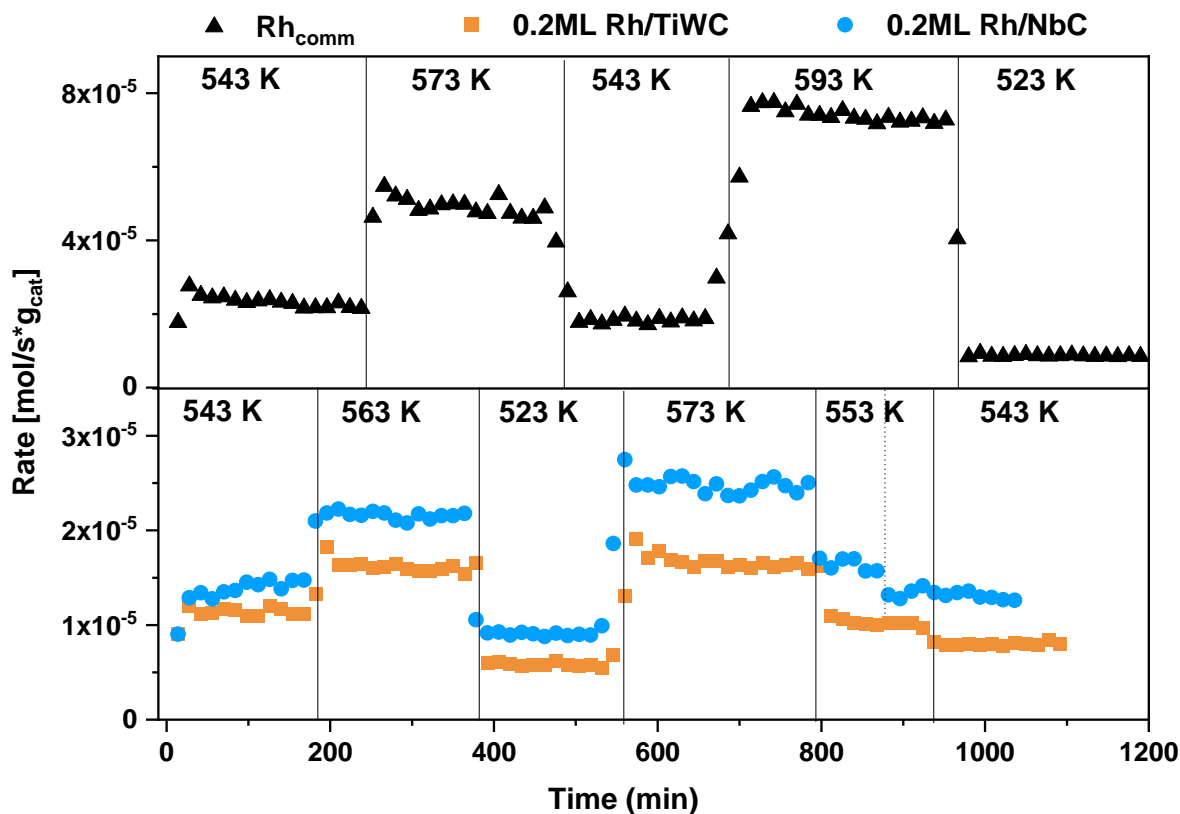
Figure S3-21. Steady-state reaction rates of 0.2 ML Rh/TiWC, 0.2 ML Rh/NbC core-shell and Rh$_{comm}$ particles collected at different temperatures for 20 hours.

The total flow rate was 80 mL/min (CO$_2$ = 10 mL/min, H$_2$ = 30 mL/min, He = 40 mL/min at 1 atm)

Gas-Phase Reactivity Testing

General Set-up

The hydrogenation experiments were carried out with CO$_2$ (Airgas, UHP grade), H$_2$ (Airgas, UHP grade 5), He (Airgas, UHP grade 5). CO (Airgas, UHP), CH$_4$ (Airgas, research grade) combined with CO$_2$ were used in the GC calibration.

The CO$_2$ hydrogenation reaction was performed in a packed-bed, downflow reactor. A K-type thermocouple (Omega, model SCAXL-020G-12) was set inside a 1/4-inch stainless

tube (inner diameter 0.180 inches). (~40-50 mg) Quartz wool was used as a physical support of the catalyst bed. A single-zone furnace (Applied Test Systems, Series 3210, 850W/115V) was used to heat up the reactor and the temperature was controlled by a temperature controller (Digi-Sense, model 68900-10). The gases were controlled by the Brooks mass flow controllers (GF40). Catalysts were activated by a reduction in pure H_2 (50 mL/min) and ramped from room temperature to 623 K over 1.5 h and maintained at 623 K for 1 h. The catalysts were then cooled to the reaction temperature under H_2. For the CO_2 hydrogenation reaction, the total flow rate was 80 mL/min (CO_2 = 10 mL/min, H_2 = 30 mL/min, He = 40 mL/min at 1 atm), reaction temperature was varied from 503 K to 593 K. CH_4 was analyzed with an Agilent 6890 gas chromatography FID column, CO generation was analyzed by a TCD column.

CHAPTER 4 ENHANCEMENT OF ALKYNE SEMI-HYDROGENATION SELECTIVITY BY ELECTRONIC MODIFICATION OF PLATINUM

We demonstrate that atomically-thin Pt shells deposited on transition metal carbide or nitride cores induce up to a four-fold enhancement in C_2H_4 selectivity during the partial hydrogenation of acetylene compared with commercial carbon-supported Pt (Pt_{comm}) nanoparticles. While Pt typically catalyzes the complete hydrogenation of alkynes to alkanes, a catalyst comprising a nominal one monolayer (ML) Pt shell on titanium tungsten nitride cores (Pt/TiWN) is capable of net C_2H_4 generation under industrial front-end reaction conditions featuring a large excess of C_2H_4 and H_2. Microcalorimetry measurements were consistent with a change in the Pt electronic structure that decreases C_2H_4 binding strength, thus increasing partial hydrogenation selectivity. Density functional theory (DFT) calculations and X-ray absorption near edge structure (XANES) both indicate broadening of the Pt d-band and concomitant down-shifting of the d-band center. The ability to control shell coverage and core composition opens up extensive opportunities to modulate the electronic and catalytic properties of noble metal-based catalysts.

Introduction

Modulation of the electronic structure of supported metal nanoparticles enables an effective strategy for improving catalyst activity and selectivity.[24] This can be achieved by synthetic means to influence factors such as strong metal-support interactions,[40] number and type of under-coordinated sites (e.g., by synthesizing single atoms, nanoclusters, or

particles with shapes that expose specific facets),[164-171] and synergies within heterometallic architectures, including alloys, intermetallics, and core-shells[24, 63-64, 107, 172]. Core-shell structures offer a high degree of design flexibility given that the nanoparticle can be tuned by the size, shape, heterometallic core and shell composition, and shell coverage extent.[173] Unfortunately, most core-shell nanoparticles suffer from dynamic alloying and restructuring during operation given the high miscibility of the elements in the structure.[4, 56, 99, 132]

Recently, we reported that these challenges can be overcome by using transition metal carbides (TMCs) and nitrides (TMNs) as ideal core materials to host atomically-thin late transition metal shells.[2-3, 6] Specifically, our prior work reported the synthesis and characterization of such materials through a high-temperature exsolution methodology, where it was demonstrated that the Pt shells bonded strongly with and wetted the surface of the metal-terminated TMC and TMN cores. Additionally, dynamic restructuring was eliminated because Pt is insoluble in the carbide and nitride lattices. These Pt/TMC and Pt/TMN core-shell nanoparticles featured enhanced CO tolerance during electro-oxidation reactions, an effect we hypothesized resulted from strong electronic interactions between the shell and the underlying ceramic core that altered the binding energy of the surface Pt-CO adsorbates.[3, 6] While we envisaged this effect could influence other reactions over Pt catalysts for which the surface coverage of reactant-specific adsorbates in competitive reactions dictates selectivity, a fundamental study demonstrating this effect had not been performed.

Here, through a combination of rigorous reactivity studies, microcalorimetry, density functional theory (DFT) calculations, and X-ray absorption spectroscopy (XAS) measurements, we demonstrate the electronic structure (and thus catalytic performance) of Pt can be effectively tuned by depositing atomically-thin shells onto titanium tungsten carbide or nitride cores. Specifically, we demonstrate the chemoselectivity of Pt for the partial hydrogenation of alkynes can be drastically enhanced using a core-shell architecture. Indeed, during polyethylene production, trace acetylene (C_2H_2) impurities (~1.5%) in the ethylene (C_2H_4) feed need to be removed in order to avoid poisoning of the downstream polymerization catalysts. This requires a chemoselective catalyst

capable of hydrogenating alkynes without saturating olefinic components. The binding energies of C_2H_2 and C_2H_4 on the catalyst surface play an important role in determining the C_2H_2 hydrogenation selectivity.[174-175] Several studies have shown Ag and Ga promoters in bimetallic Pd-Ag or Pd-Ga nanoparticles alter Pd through geometric and electronic effects to attain the desired binding energies of intermediates that maximize C_2H_4 selectivity.[47, 176-177] While Pt is a remarkable hydrogenation catalyst, it is unselective for this reaction because it binds both C_2H_2 and C_2H_4 strongly, resulting in over hydrogenation to ethane (C_2H_6) at high C_2H_2 conversion. [177-179] In this study, we show that, unlike the combined geometric and electronic effects that change the catalytic activity of metal alloys, the TMC and TMN cores modulate the binding energies of alkynes and alkenes on Pt surfaces to achieve high selectivity towards partial alkyne hydrogenation mainly by an electronic effect. DFT and X-ray absorption spectroscopy (XAS) demonstrate a down-shift of the Pt d-band center, implicating changes in the electronic structure as the cause for the weakened adsorption of the C_2H_4. This effect was further confirmed by microcalorimetry measurements coupled with reactivity studies under industrial front end conditions. The altered binding energy of the core-shell catalysts resulted in drastically higher selectivity values when compared to a control Pt catalyst. Ultimately, an optimized 1ML Pt/TiWN catalyst achieved net ethylene generation during simulated front-end industrial reaction conditions featuring C_2H_2 in a large excess of C_2H_4 and H_2.

Results and Discussion

The partial hydrogenation of pure acetylene was investigated as a function of Pt shell coverage and core composition in order to gain insight into reactivity trends. Given that the aim of this work is to demonstrate the impact that the changes in the electronic structure of Pt have on selectivity in a series reaction, a commercial Pt supported on carbon was used for comparison. The materials studied comprised nominal Pt shell coverages of 0.5, 1, and 2 ML over TiWC and TiWN cores (synthetic and characterization details found in the SI and references; more detailed characterization studies confirming the core-shell structure before reaction can be found in our previous work).[3, 6] Although all samples feature some degree of imperfect shell coverage, on average, materials with

lower nominal Pt loadings tended to have a greater extent of the exposed core compared to core-shell catalyst samples with a greater content of Pt as indicated by scanning transmission electron microscopy (STEM) imaging and energy-dispersive X-ray spectroscopy (EDS) mapping. [4]Importantly, the core-shell structure remained intact after the reaction as confirmed by STEM-EDS mapping shown in the Figure S4-1. Additionally, the PXRD patterns (Figure S4-2) and XPS spectra (Figure S4-3) collected before and after the reaction suggest the core-shell architecture remained unaltered. These results are expected given the core-shell structure is assembled at high- temperatures under hydrocarbon/H_2 atmospheres and remains stable under re-carburization conditions (600 °C, 80% CH_4, 20% H_2) as confirmed by in-situ *extended X-ray absorption fine structure* (EXAFS) analyses.[99] C_2H_4 and C_2H_6 were the main hydrogenation products, with minimal contribution of C_2+ species to the overall carbon balance. As shown in Figures 1a and S4-4, for all Pt coverages and core materials studied, we observed significant improvements in C_2H_4 selectivity compared to a commercial 5 w-t% carbon-supported Pt catalyst (Premetek). Specifically, core-shell materials generated C_2H_4 selectivity values ranging from 60-80% across a range of shell coverages and temperatures while the commercial Pt catalyst was ~20% regardless of acetylene conversion level (i.e., either 5% or 71%, Figure 4-1a, S4-4). These values compared favorably to C_2H_4 selectivity values obtained with state-of-the-art Pd-based catalysts, albeit under slightly different experimental conditions.[180]

Interestingly, the Pt coverage did not significantly affect the C_2H_4 selectivity while the core composition did, with Pt/TiWN materials reaching 77% C_2H_4 selectivity compared to the 60% obtained with Pt/TiWC. We note that due to the wide range of activities across samples, the reaction temperature was varied between 345~388 K in order to compare C_2H_4 selectivity values at near isoconversion levels. C_2H_4 selectivity for core-shell particles was independent of acetylene conversion for data collected at either different space velocity or reaction temperature. Conversely, Pt_{comm} featured higher C_2H_4 selectivity at higher temperatures (see Figures S5-S7), likely because acetylene outcompetes ethylene for adsorption sites at these conditions.[179] The reaction likely follows the Horiuti-Polanyi mechanism with a strong acetylene adsorption step, in agreement with the kinetic analysis by Vincent, et al. [181]
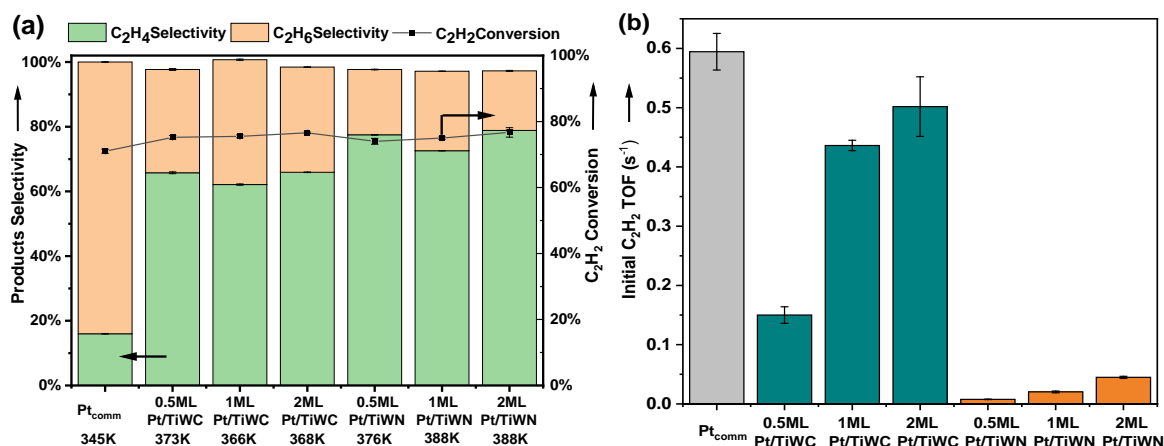
Figure 4-22. C_2H_2 hydrogenation results over different Pt-based catalysts. (a) Selectivity and conversion values measured at different temperatures to achieve ca. 75% conversion; (b) Turnover frequency of C_2H_2 hydrogenation collected at differential conditions and constant temperature (Reaction condition for Figure 4-1 (b): constant temperature at 353 K, C_2H_2 = 0.05 atm, H_2 = 0.20 atm, CH_4 = 0.08 atm internal standard and He = 0.67 atm with a gas hourly space velocity (GHSV) ~1800 hr^{-1}). Error bar indicated the propagated error (standard deviation during the number of site measurements and reactivity).

The activity, quantified by the turnover frequency (TOF, defined as C_2H_2 molecules consumed per surface Pt atom per second), varied significantly with Pt coverage and choice of core material (Figure 4-1b). The rates were calculated under differential conditions at a reaction temperature of 353 K in the absence of mass transfer limitations and were normalized by the number of Pt surface sites as quantified by hydrogen underpotential deposition (Hupd) (see SI for more details). Neither the bare TiWC nor TiWN cores were active for acetylene hydrogenation under these conditions (Figure S4-4(c)). For submonolayer Pt coverages, note that the Hupd method does not count exposed core sites, as shown in Table S4-3. [3, 6] We observed similar acetylene hydrogenation rates on the 1 ML and 2 ML samples, while 0.5 ML samples featured much lower TOF values. These results suggest contiguous surface Pt atoms are more reactive than Pt-core interfacial sites. It appears that increasing core coverage had a positive effect on TOF without jeopardizing selectivity; the origin of this effect is currently unknown. The core material also drastically affected C_2H_2 TOF values: Pt/TiWN exhibited 10-70 times lower TOF values than Pt$_{comm}$, while Pt/TiWC only exhibited 1.2-3.5 times lower

activity, which is consistent with activity-selectivity tradeoffs in bulk metals and alloys that result from scaling relations between adsorbate binding energies.[175] The reactivity difference among Pt_{comm}, Pt/TiWC, and Pt/TiWN exemplifies the strong influence of the core material on the activity and reaction kinetics of the Pt shell. Since hydrogenation of C_2H_2 is a structure-insensitive reaction[48, 182-183], the observed altered reaction rates and product selectivity cannot be ascribed to changes in catalyst morphology or size. Denhartog et al. reported similar C_2H_4 selectivity for acetylene hydrogenation over Pt nanoparticles with sizes ranging from 2 nm to 20 nm.[183] In addition, our previous study indicated the Pt-Pt coordination numbers and Pt-Pt distances are very similar for Pt_{comm} and 2 ML core-shell particles reduced in H_2 at 300°C (shown in Table S4-4).[99]

We compared the hydrogenation activity of Pt_{comm} and the core-shell nanoparticles using a C_2H_4 feed (full experimental details in SI) to assess if our catalysts could be used under industrial acetylene hydrogenation conditions in which C_2H_2 has to be hydrogenated in an excess of C_2H_4. The TOF values for C_2H_4 hydrogenation decreased in the order Pt_{comm} > Pt/TiWC >Pt/TiWN (Figure S4-8). Importantly, all catalysts featured C_2H_4 hydrogenation rates nearly an order of magnitude faster than those measured for C_2H_2, which immediately poses a selectivity challenge for industrial C_2H_2 hydrogenation conditions unless there are drastic differences in adsorption strength on the catalyst surface between these molecules. We, therefore, investigated the effects of adsorbate binding energies on reaction rates and selectivity as a function of the catalyst composition. Microcalorimetry measurements showed markedly different results during the adsorption of C_2H_4 and C_2H_2 on the core-shell catalysts as compared to Pt_{comm} shown in Table 4-1. The Pt-normalized uptake of C_2H_2 and C_2H_4 on 2 ML Pt/TiWC and 2 ML Pt/TiWN were more than an order of magnitude reduced compared to Pt_{comm}, which is surprising given that Hupd measurements showed a similar number of active sites for the materials (Table S4-3). This difference suggests drastic changes in heat of adsorption of C_2H_2 and C_2H_4 on the core-shell particles compared to Pt_{comm}. Given that our microcalorimeter features a measurement limit of ca. 20 kJ mol^{-1}, these data suggest that a small amount of C_2H_2 binds strongly to a few sites and that most of the C_2H_2 is bound to the core-shell surface so weakly that it could not be captured by the microcalorimetry measurement. More significantly, the ratios of adsorbed C_2H_2 to C_2H_4 increased in the order Pt_{comm} < Pt/TiWC

< Pt/TiWN, in agreement with the observed selectivity trend. Indeed, the heat of adsorption (ΔH_{ads}) measurements showed marked differences across samples. At 298 K, the ΔH_{ads} for C_2H_2 and C_2H_4 on Pt_{comm} was 200 kJ mol^{-1} and 190 kJ mol^{-1}, respectively, consistent with literature values.[179, 184-186] The maximum uncertainty in the calorimetry measurements is estimated to be 10 kJ mol^{-1} through previous experiments with a similar set-up.[187] In stark contrast, C_2H_4 adsorption on the core-shell nanoparticles was much less exothermic, measuring 125 kJ mol^{-1} for 2 ML Pt/TiWC and below instrumental detection limits (~20 kJ mol^{-1}) for 2 ML Pt/TiWN as would be expected from the differences in amounts of C_2H_4 adsorption and reactivity trends. Although C_2H_2 appeared to adsorb more strongly on the core-shell nanoparticles than on Pt_{comm} (260-290 kJ mol^{-1} vs. 200 kJ mol^{-1}), the number of adsorbed C_2H_2 molecules was an order of magnitude lower. In Table S4-3, the reduced number of adsorbed C_2H_2 was not due to fewer available Pt exposed sites, given that the dispersion is similar between the core-shell carbide, nitride and commercial Pt catalysts (as measured by hydrogen underpotential deposition in Table S4-3). These results can possibly be reconciled by acetylene dehydrogenation. The experimental procedure adopted for the microcalorimetry measurements without a H_2 co-feed could have overestimated the C_2H_2 ΔH_{ads} value due to the exothermicity of initial coke formation via C_2H_2 dehydrogenation upon adsorption.[179, 188-189] Regardless, the measured difference in binding for the alkyne and the olefin is consistent with the reactivity trends.

Table 4-17. Microcalorimetry Data for Core-shell Particles and Pt_{comm}.

	Pt_{comm}	2ML Pt/TiWC	2ML Pt/TiWN
C_2H_2 adsorption amount (mol C_2H_2 / mol Pt site)	>0.206	0.006	0.018
C_2H_4 adsorption amount (mol C_2H_4 / mol Pt site)	0.109	0.002	0
C_2H_2 ΔH_{ads} (kJ mol^{-1})	-200	-260	-290
C_2H_4 ΔH_{ads} (kJ mol^{-1})	-190	-125	N.A[a]

[a] Adsorption of C_2H_4 at room temperature was below instrumental detection limits. (Indicating the absolute value of the heat of adsorption was less than ~20 kJ mol^{-1})

We performed XAS and XPS measurements to gain insight into the electronic structure changes between Pt_{comm} and the Pt in the core-shell materials. Pt L_2 edge (13.27 keV) spectrum was taken rather than Pt L_3 edge (11.56 keV) due to overlap with the W L_2 edge (11.54 keV). X-ray absorption near edge structure (XANES) experiments showed greater white line intensities for Pt/TiWN than for Pt/TiWC, while the Pt foil showed almost no white line features (Figure 4-2). Given that the samples are fully reduced and do not feature significant Pt-O bonding as measured by extended X-ray absorption fine structure (EXAFS) (Table S4-5), these data indicate a change in the electronic structure of metallic Pt resulting from d-band broadening accompanied by a down-shift of the d-band center, as further confirmed by Garg et al with detailed follow-up in-situ characterization studies.[99] In addition, Table S4-5 also demonstrates the Pt-Pt bond distances are within 0.03 Å across bulk and core-shell samples, which indicates the cores do not induce a strong strain effect. XPS was used to characterize the formation of the core-shell nanoparticles following prior analysis protocols.[3] The Pt $4f_{7/2}$ peaks for Pt/TiWN and TiWC (71.8 eV and 71.5 eV respectively) were centered at higher energies than those of metallic Pt (71.2 eV) (Figure S4-7c)—an effect known to correlate with the down-shifting of the d-band center.[3, 24, 96, 190]
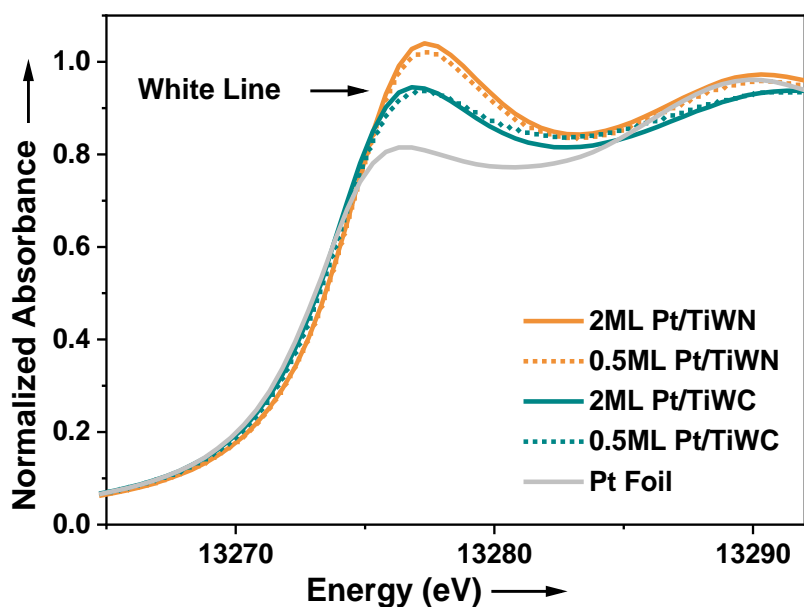
Figure 4-23. XANES of Pt and Core-shell Pt. Pt foil, and Pt core-shell L_2 edge (13.27 keV) XANES spectra. Pt L_3 edge (11.56 keV) spectrum was not taken due to overlap with the W L_2 edge (11.54 keV).

A similar Pd $3d_{5/2}$ core-level shift was reported in the Pd catalyst for the alkyne hydrogenation that was associated with the creation of a Pd-C surface phase. [191] However, such phenomenon was observed in our system as the Pt $4f_{7/2}$ core-level shift for the core-shell particles existed prior to feeding the reactant gases and remained in the same position after the reaction, as shown in the Figure S4-3. In addition, unlike Pd, the formation of Pt carbide is thermodynamically unfavorable under our reaction conditions.[89] Furthermore, our previous DFT calculation showed that the interactions between Pt-W are much more energetically favored than the Pt-C interaction, which rules out the formation of PtC_x species during the reaction.[6] The XPS data show that the Pt in the shell and the W in the core had reverse core electron binding energy shifts, which is indicative of strong Pt-W bonding interactions and is in agreement with prior studies on this system. [3] The core-hole/final state effects have little influence on the observed binding energy shift. Therefore, these results are strong evidence that the carbide and nitride cores significantly alter the electronic structure of the Pt overlayers.

DFT calculations confirmed the experimentally observed differences in adsorption energies and electronic structures among Pt_{comm} and the core-shell nanoparticles. The binding energies of C_2H_2 and C_2H_4 on the core-shell materials are nearly 1 eV weaker compared to Pt (111) (Table S4-6). This result is consistent with the drastic differences in achievable total C_2H_x coverages on Pt/TiWC and Pt/TiWN compared to Pt_{comm} shown in Table 4-1. Indeed, experimental measurements directly probe the adsorption energy of reactive sites, but averaging the heats of adsorption over all sites, most of which do not adsorb C_2H_2 or C_2H_4, would produce similar results as those predicted by DFT. Notably, the C_2H_2 TOF has the trend of Pt>Pt/TiWC>Pt/TiWN, which is consistent with activity-selectivity tradeoffs in bulk metals and alloys resulting from scaling relations between adsorbate binding energies.[175] In addition, the integral binding energies (IBEs) of the second Pt layer were positive for both Pt/TiWC and Pt/TiWN core-shells at 0.035 eV/Å^2 and 0.016 eV/ Å^2, respectively, which indicated the second Pt 2D-layer is less stable relative to 3D Pt growth (see SI for details). Hence the 1ML Pt/TiWC and Pt/TiWN models were chosen to compare with the experimental data.

Analysis of the d-band structure showed that the Pt d-band center energy, relative to the Fermi level, changed from -1.97 eV for Pt (111) surface to -2.82 eV for 1ML Pt/TiWC and -2.95 eV for 1ML Pt/TiWN (Table S4-7). Prior reports on early transition metal nitride @Pt core-shell structures for the oxygen reduction reaction similarly featured downshifted d-band centers that affected the binding energy of surface oxygen species. [68, 192] In light of these results, we investigated the C_2H_2 hydrogenation pathway through DFT calculations over Pt (111), 1 ML Pt/TiWC and 1 ML Pt/TiWN surfaces. We calculated adsorption energies on multiple hollow, bridge, and atop sites, and selected the strongest adsorption configuration from which to determine C_2H_2 hydrogenation barriers. Specifically, C_2H_2 adsorbed in a hollow site was chosen for both Pt (111) and core-shell particles; the C_2H_4 atop site configuration chosen for core-shell particles; and the bridge site configuration chosen for Pt (111). As shown in Figure 4-3, the energy profile for C_2H_2 hydrogenation over 1 ML Pt/TiWC and 1 ML Pt/TiWN indicates that both surfaces are highly active to C_2H_2 hydrogenation, with activation barriers of 0.35 eV and 0.19 eV, respectively. Notably, the C_2H_4 hydrogenation barrier on Pt (111) is significantly lower than the desorption energy, with a 0.35 eV difference, indicating high activity of Pt (111) for C_2H_4

hydrogenation. In contrast, the C_2H_4 hydrogenation barriers on the core-shell structure are comparable to the desorption energies (0.07 eV of difference for 1ML Pt/TiWC and 0.12 eV of difference for 1ML Pt/TiWN), implying these materials should exhibit better C_2H_4 selectivity than Pt (111). The difference between C_2H_4 desorption energy and further hydrogenation to the C_2H_5 barrier has been used to predict ethylene selectivity.[175] From the DFT perspective, it is difficult to predict overall selectivity differences between the 1ML Pt/TiWC and 1ML Pt/TiWN surfaces, as each surface Pt atom is not identical to each other considering the local subsurface environment and each has different ethylene desorption and activation energies. C_2H_4 adsorption is significantly weakened on the core-shell structures, which is the key factor for improving C_2H_4 selectivity.[175] The hydrogneation energitics in Figure 4-3 were based on the strongest adsorption configuration; Pt/TiWN has stronger *C2H2 binding energy than the Pt/TiWC, yet other stable adsorption configurations could contribute to the observed difference in the acetylene TOF data in Figure 4-1(b) between Pt/TiWN and Pt/TiWC. Additionally, differences in reaction rates could also arise from differences in H_2 binding energies. As it can be seen in Figure 4-3, for the C_2H_2*+H* step, both Pt/TiWC and Pt decreased in total free energy from the previous step which indicated the H_2 adsorption was favored on Pt/TiWC and Pt. However, for Pt/TiWN, the C_2H_2*+H* total free energy increased from the C_2H_2* step which indicated H_2 adsorption to Pt/TiWN surface was unfavorable and hence limited C_2H_2 turnover frequency on Pt/TiWN as shown in Figure 4-1 (b).
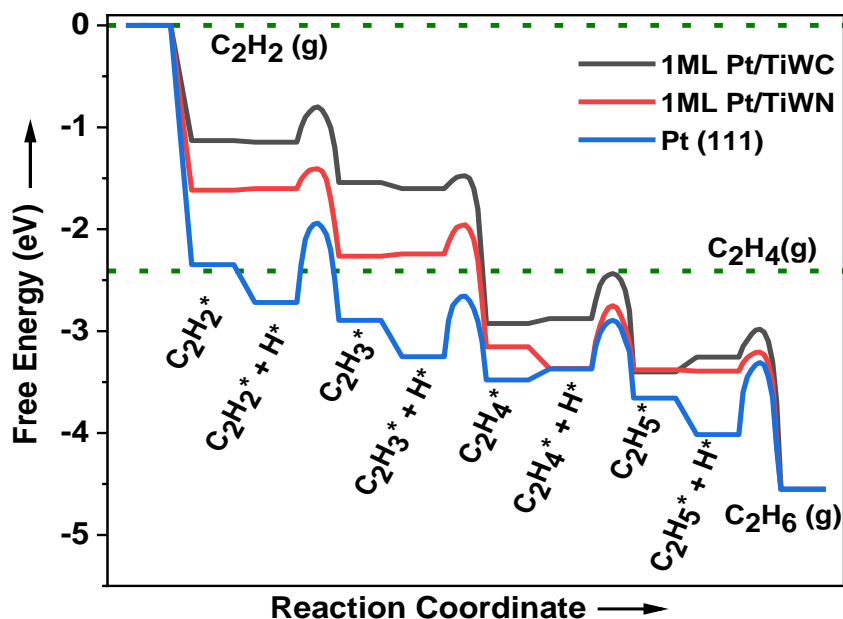
Figure 4-24. C_2H_2 Hydrogenation Energy Diagram.
1ML Pt/TiWC (Black), 1ML Pt/TiWN (Red) and Pt (111) (Blue).

Inspired by the promising results on pure feeds, we investigated the C_2H_2 partial hydrogenation under industrially-relevant conditions.[43, 193] Simulating front-end conditions, we performed test reactions with a $C_2H_2 : C_2H_4 : H_2$ ratio of 1 : 20 : 15, a gas hourly space velocity (GHSV) ~1800 hr^{-1} at ambient pressure under and temperatures ranging from 348 K to 378 K to maintain isoconversion of C_2H_2 (80%) (see SI for full experimental details). Note that catalyst performance can be assessed by tracking C_2H_4 consumption, but a selective catalyst that generates more C_2H_4 that it consumed would result in a "negative" C_2H_4 conversion value when using the traditional definition of conversion (Equation 4-1).

$$C_2H_4 \text{ conversion} = \frac{C_2H_{4\,(\text{feed})} - C_2H_{4\,(\text{effluent})}}{C_2H_{4\,(\text{feed})}} \qquad \textbf{Equation 4-14}$$

As shown in Table 4-2, Pt$_{comm}$ had the highest C_2H_4 consumption values of ~16% of the feed, followed by Pt/TiWC (ca. 5% of the feed) and finally Pt/TiWN (ca. 0-2% of the feed). The 1ML Pt/TiWN demonstrated a modest net generation of C_2H_4 (i.e., a -0.3% C_2H_4

conversion) under these conditions. As the core-shell nitride nanoparticles demonstrated less C_2H_4 consumption at ~80% C_2H_2 conversion, C_2H_4 disappearance was further measured at a C_2H_2 conversion of ~95%, as shown in Table S4-8. As shown in Figure S4-9, 1ML Pt/TiWN featured high stability with no activity decay for more than 10 h at acetylene conversion levels with a turnover number of 22400, that was comparable to that obtained Pt_{comm} under similar conditions. The 1 ML Pt/TiWN featured higher C_2H_4 selectivity than the 0.5 ML Pt/TiWN material. In our prior DFT study [150] focusing on the effect of Pt coverage over early transition metal carbide underlayers, we showed that a 1 ML had a lower d-band center than a 0.75 ML for the Pt/TiWC system. Therefore, lower Pt loadings were not pursued in the present study.

Table 4-18. Front-end Condition Core-shell Particles and Pt_{comm} Reactivity.

C_2H_2=0.02 atm, H_2=0.23 atm, C_2H_4=0.31 atm CH_4=0.15 atm (internal standard) and He=0.29 atm with a gas hourly space velocity (GHSV) ~1800 hr^{-1}.

	Temperature (K)	C_2H_2 Conversion	C_2H_4 Conversion
Pt_{comm}	371	83.1%	15.9% ± 0.2%
1ML Pt/TiWC	354	81.5%	5.4% ± 0.1%
2ML Pt/TiWC	348	82.1%	5.0% ± 0.1%
0.5ML Pt/TiWC	353	81.5%	4.7% ± 0.2%
2ML Pt/TiWN	378	85.9%	2.1% ± 0.1%
0.5ML Pt/TiWN	378	81.4%	1.0%± 0.1%
1ML Pt/TiWN	368	83.0%	-0.3%±0.1%[a]

[a] A negative C_2H_4 conversion meant that there was C_2H_4 net generation.

In order to understand the origin of C_2H_6 over-hydrogenated products as related to the intrinsic and net ethylene selectivity, defined in Equations 2 and 3 below, we performed hydrogenation experiments in a recirculating batch reactor with isotopically-labeled $^{13}C_2H_4$ and $^{12}C_2H_2$ to track specific $^{12}C_2H_4$, $^{12}C_2H_6$ and $^{13}C_2H_6$ generation for the 1ML Pt/TiWN catalyst (detail set-up in SI).[41, 194]

$$\text{Intrinsic } C_2H_4 \text{ Selectivity} = \frac{{}^{12}C_2H_4}{\Delta \, {}^{12}C_2H_2} \qquad \textbf{Equation 4-15}$$

$$\text{Net } C_2H_4 \text{ Selectivity} = \frac{{}^{12}C_2H_4 - {}^{13}C_2H_6}{\Delta \, {}^{12}C_2H_2} \qquad \textbf{Equation 4-16}$$
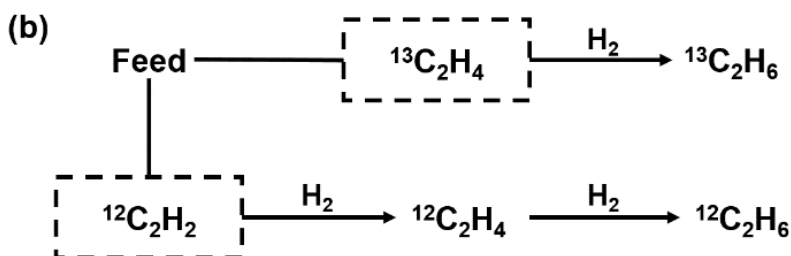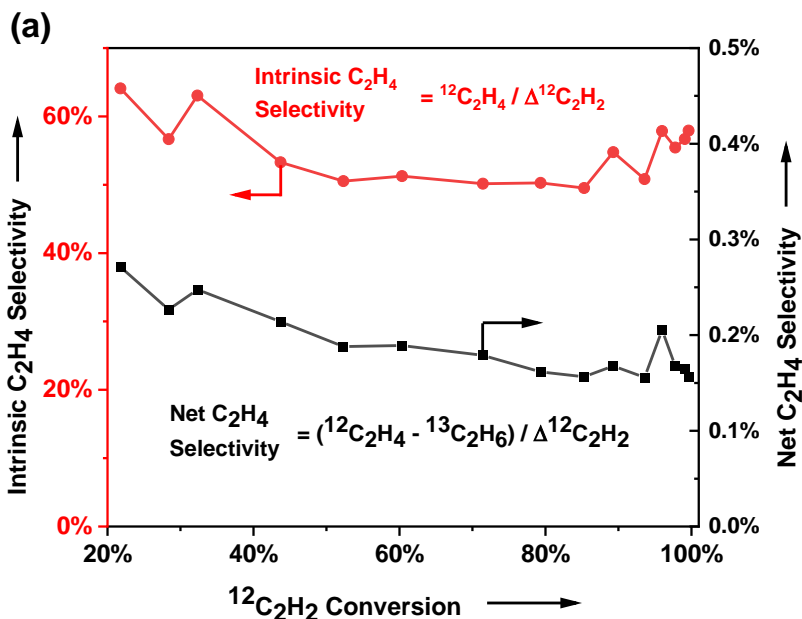
Figure 4-25. Isotopic Study of C_2H_4 Selectivity vs. C_2H_2 Conversion and Reaction Network Schematic.

(a) Variation of intrinsic ${}^{12}C_2H_4$ selectivity and net C_2H_4 selectivity (see the formula for definitions) with the ${}^{12}C_2H_2$ conversion (x-axis) are illustrated by red and black lines respectively; (b) The schematics of the isotopic study.

A batch reactor was charged initially with 6 Torr ${}^{12}C_2H_2$ 120 Torr ${}^{13}C_2H_4$ and 90 Torr H_2 to maintain a similar $C_2H_2 : C_2H_4 : H_2 = 1 : 20 : 15$ ratio to that used in the flow reactor front-end condition. The net C_2H_4 selectivity defined in Equation 4-3 was positive as shown in Figure 4-4 (a), which is consistent with a net generation of C_2H_4 observed under the flow

reactor industrial condition. Based on the definition of Equation 4-2 & 4-3 and the data shown in Figure 4-4 (a), we calculated that ca. 88% C_2H_6 was generated from the hydrogenation of $^{13}C_2H_4$. Thus, for the unwanted overhydrogenation, $^{13}C_2H_6$ formation was from the hydrogenation C_2H_4 rather than from the sequential hydrogenation of bound $^{12}C_2H_2$ intermediates.

Conclusion

Through a combination of reactivity, characterization and computational studies, we demonstrated the Pt electronic structure was modified by interactions with the underlying transition metal carbide or nitride core, leading to a modulation of the relative adsorption energies of C_2H_2 and C_2H_4 and a remarkable enhancement in C_2H_4 selectivity in the industrially important hydrogenation of C_2H_2. More generally, our core-shell nanoparticle platform represents a general means by which the electronic properties of noble metals can be tuned for the enhancement of their catalytic properties. These results motivate further exploration of accessible combinations of shell coverages and core materials to control reactivity and selectivity for a wide range of reactions, while also unearthing structure-property relationships that extend our fundamental understanding of core-shell nanoparticle catalysis.

Experimental Section

A comprehensive description of the experimental methods is documented in the Supporting Information.

Sample Preparation. Core-shell carbide particles were synthesized through carburizing mixtures of H_2PtCl_6 and tungsten oxides encapsulated in removable silica templates.[6] Core-shell nitride samples were obtained through nitridation of the core-shell carbide sample.[3] Platinum nanoparticle supported on tungsten carbide was synthesized through the incipient wetness impregnation (IWI) method and commercial Pt on carbon black was purchased from Premetek. Inc.

Catalytic Reactions. Catalytic reactions were performed in a single-pass-plug-flow reactor. Catalyst (~2-70 mg) was well mixed with α-alumina (4.0 g, 100-200 mesh) to enhance heat transfer. The reactor temperature was kept constant with an ATS furnace. For the acetylene hydrogenation reaction, the total flow rate was 60 mL/min (C_2H_2 = 3 mL/min, H_2 = 12 mL/min, CH_4 = 5 mL/min (internal standard), He = 40 mL/min or C_2H_2=0.05 atm, H_2=0.20 atm, CH_4=0.08 atm (internal standard) and He=0.67 atm) at 1 atm with a gas hourly space velocity (GHSV) of 1800 h^{-1}, reaction temperature was varied from 343 K to 388 K. For acetylene hydrogenation at industrial condition, the total flow rate was 65 ml/min (5% C_2H_2/He = 20 mL/min, H_2 = 15 mL/min, C_2H_4 = 20 mL/min CH_4 = 10 mL/min (internal standard) or C_2H_2=0.02 atm, H_2=0.23 atm, C_2H_4=0.31 atm CH_4=0.15 atm (internal standard) and He=0.29 atm), reaction temperature was varied from 348 K to 378 K. For C_2H_4 hydrogenation, the total flow rate was 60 ml/min (C_2H_4 = 5 mL/min, H_2 = 5 mL/min, CH_4 = 5 mL/min, He = 45 mL/min or C_2H_4=0.08 atm, H_2=0.08 atm, CH_4=0.08 atm (internal standard) and He=0.75 atm), the reaction temperature was set to be 318 K. Product distribution was analyzed by Agilent 6890 FID gas chromatography. Industrial reaction condition with co-fed $^{13}C_2H_4$ and $^{12}C_2H_2$ was carried out in a batch reactor equipped with a pump to recirculate the reactant gases within the reactor. The effluent was analyzed with a Shimadzu QP 2010 Ultra GC-MS fitted with an Rt-Alumina BOND/KCl column. The system was free of heat and mass transfer limitations analyzed with Mear's and Weisz-Prater's criteria (shown in the SI).[195-196]

Sample Characterization. Nanoparticle particle sizes before and after the reaction were measured with transmission electron microscopy (TEM, JEOL 2010) with a field emission gun (FEG) operating at 200 kV. Crystal structures before and after the reaction were measured by powder x-ray diffraction (PXRD, Bruker D8) using Cu Kα radiation source. Pt, Ti and W contents were measured by inductively coupled plasma mass spectrometry (ICP-MS, Agilent 7900) and thermogravimetric analysis (TGA, TA-Q500). The number of sites for the control Pt$_{comm}$ catalyst was measured electrochemically through H$_{upd}$ method and the conventional CO chemisorption while core-shell particles were measured only electrochemically. Microcalorimetry was carried out in a combined home-made breakthrough reactor (BTR)-differential scanning calorimetry (DSC)-mass spectrometer (MS) instrument. Ex-situ x-ray absorption fine structure (XAFS, APS, Argonne National

Lab, Pt L_2-edge 13,273 eV) was measured for core-shell samples, Pt foil, and PtO_2. A PHI Versaprobe II spectrometer with a monochromatic aluminum anode X-ray source was used to perform the photoemission spectra before and after the reaction to analyze the catalyst surface composition.

DFT Calculation. Electronic structure calculations were performed using the Vienna ab initio simulation package (VASP) [158]. The projector augmented-wave (PAW) method was used to represent the ion-core electron interactions [197]. Nonlocal gradient corrections to the total energy were calculated using the Perdew-Burke-Ernzerhof revised for solid (PBE sol) exchange correlation functional [198]. The heat, quench and exfoliation (HQE) method was used to construct the core-shell model.[150] A detailed description of the construction of the Pt overlayer model, including analysis of the optimal Pt density and stability in the monolayer structure, is included in the Supporting Information.

Code Availability. The corresponding codes for the density functional theory calculations are available upon request.

Acknowledgements

Supporting Information

STEM and EDS mapping for the core-shell structure after C_2H_2 hydrogenation reaction
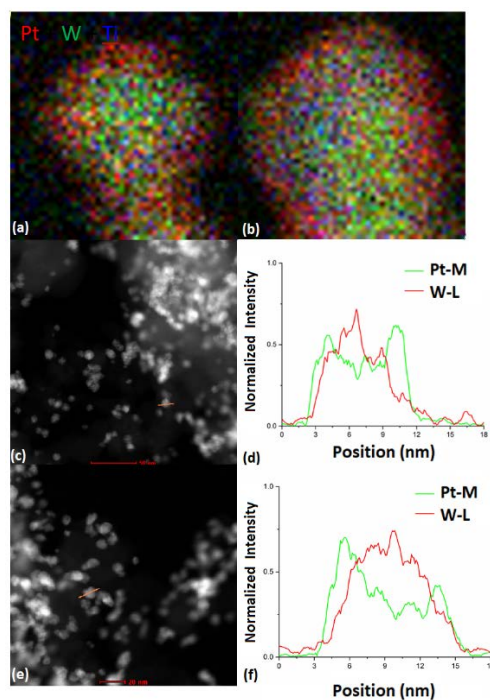
Figure S4-26. Scanning transmission electron microscopy (STEM) and energy-dispersive X-ray spectroscopy (EDS) mapping of the core-shell structure post C_2H_2 hydrogenation reaction for the Pt/TiWC.

(a) EDS mapping of Pt/TiWC particle after C_2H_2 hydrogenation with an overlay of all three elements Pt, W, Ti; (b) EDS mapping of the Pt/TiWN particles after C_2H_2 hydrogenation with an overlay of all three elements Pt, W, Ti; (c) STEM image for line scan for Pt/TiWC; (d) line scan to show the composition of the Pt/TiWC core-shell structure; (e) STEM image for line scan for Pt/TiWN; (f) line scan to show the composition of the Pt/TiWN core-shell structure

XRD before and post C$_2$H$_2$ hydrogenation reaction

(a)

Stand alone
Pt 10.2%

Stand alone
Pt 9.7%

graphite
WC
Stand alone
Pt

2ML Pt/TiWC fitting post rxn

2ML Pt/TiWC fitting before rxn

Intensity/ a.u.

2Θ degree

(b)

Stand alone
Pt 15.7%

Stand alone
Pt 16.0%

graphite
W$_2$N
Stand alone
Pt

2ML Pt/TiWN fitting post rxn

2ML Pt/TiWN fitting before rxn

Intensity/ a.u.

2Θ degree
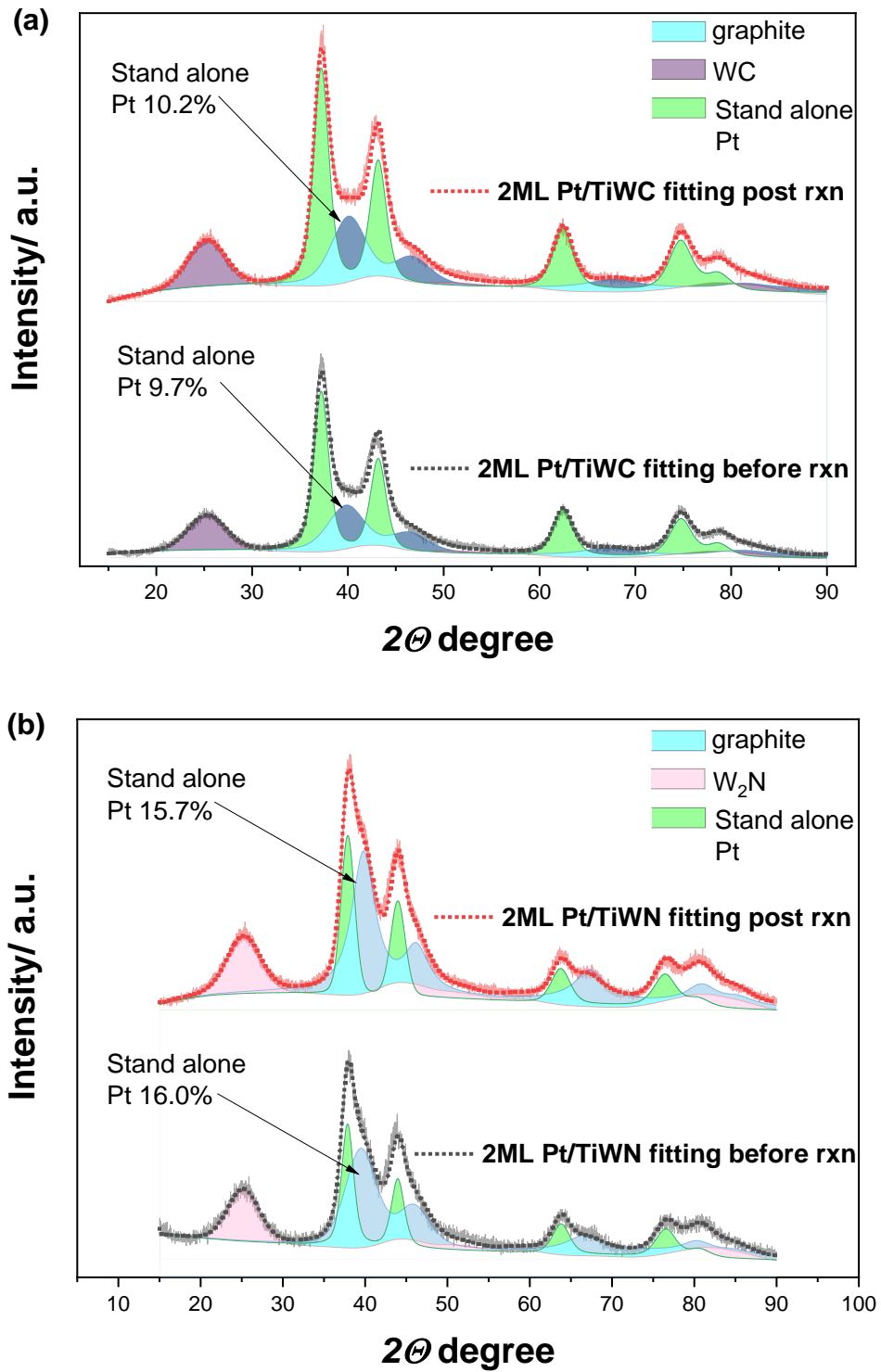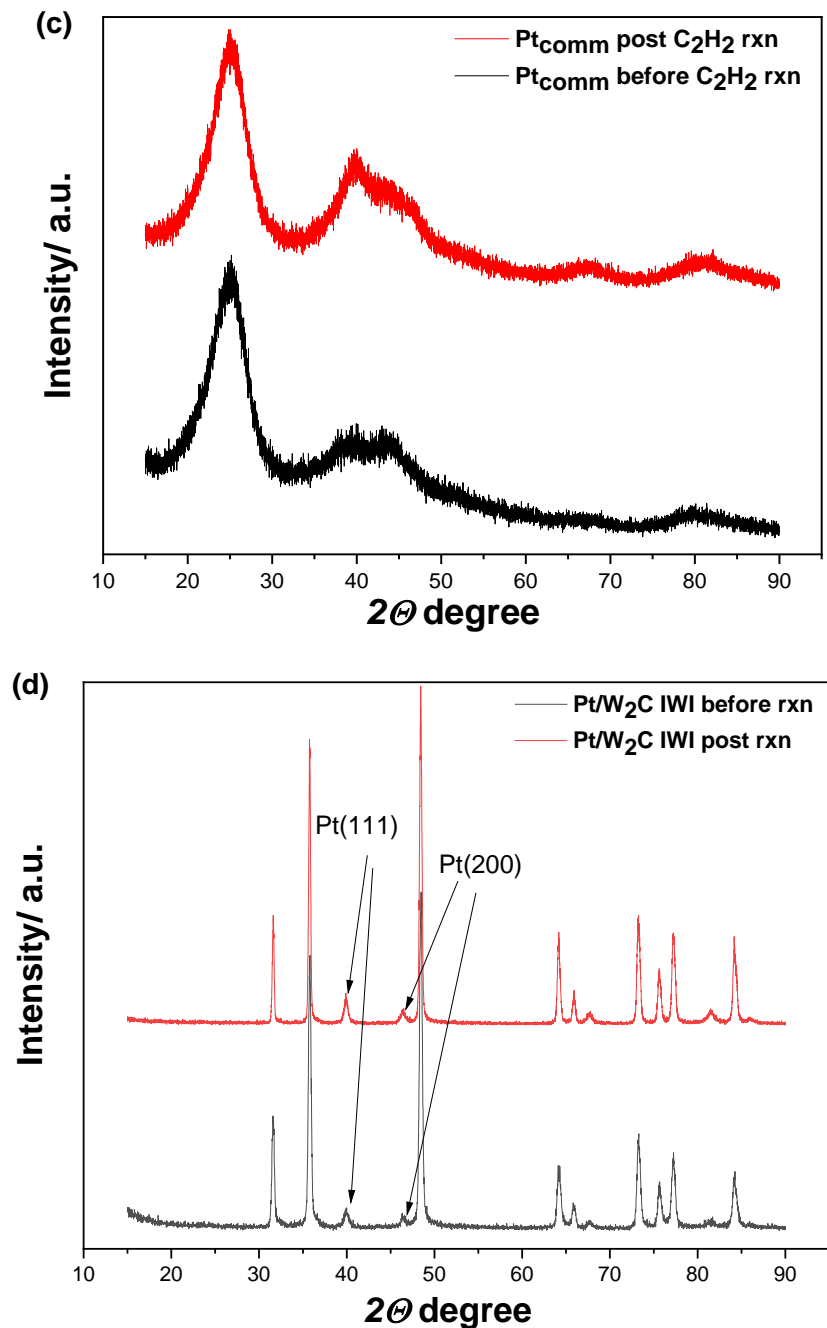
Figure S4-27. X-Ray diffraction patterns of core-shell catalysts analyzed before and after reaction deconvoluted using Rietveld refinement.

(a) Combined diffractograms for 2ML Pt/TiWC and the Rietveld fitting using HighScore Plus (b) Combined diffractograms for 2ML Pt/TiWN and the Rietveld fitting using HighScore Plus. (c) Combined diffractogram for Pt_{comm} before and after C_2H_2 hydrogenation reaction. (d) Combined diffractogram for Pt/W$_2$C incipient wetness impregnation samples before and after the C_2H_2 hydrogenation reaction. The structure of the core-shell particles remained intact through the C_2H_2 hydrogenation reaction condition.

XPS before and post C$_2$H$_2$ hydrogenation reaction

(a) 2ML Pt/TiWC before rxn — 2ML Pt/TiWC post rxn

C 1s
284.4 eV

Pt 4f$_{7/2}$
71.5 eV

W 4f$_{7/2}$
31.9 eV

Intensity (A.U.)

Binding Energy (eV)

(b) 2ML Pt/TiWN before rxn — 2ML Pt/TiWN post rxn

C 1s
284.4 eV

Pt 4f$_{7/2}$
71.8 eV

W 4f$_{7/2}$
32.1 eV

Intensity (A.U.)

Binding Energy (eV)
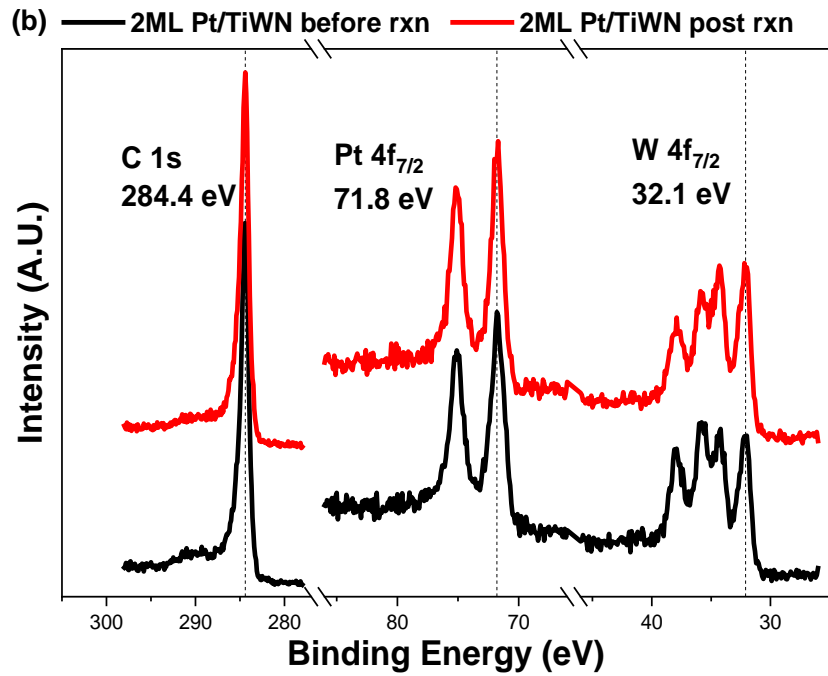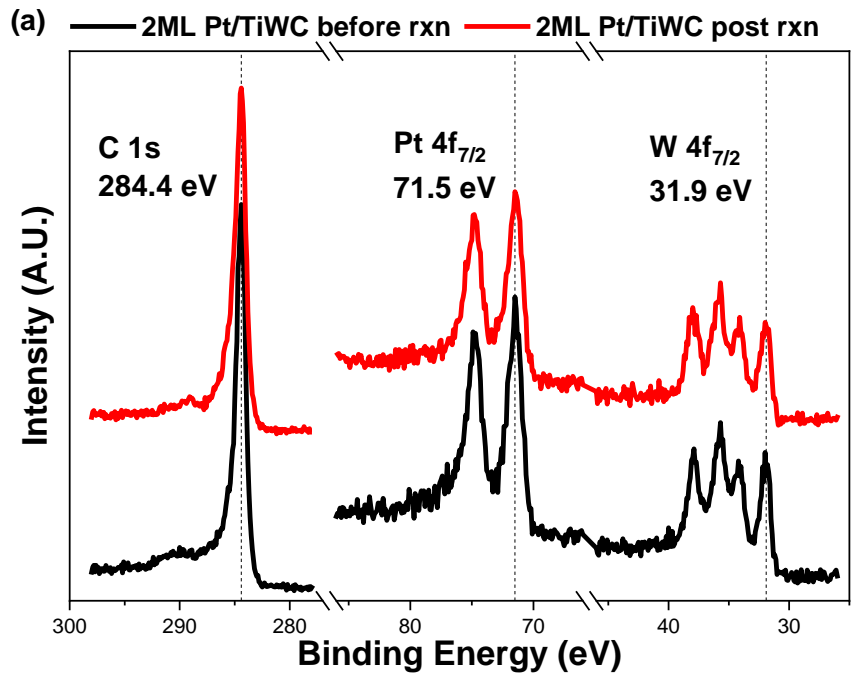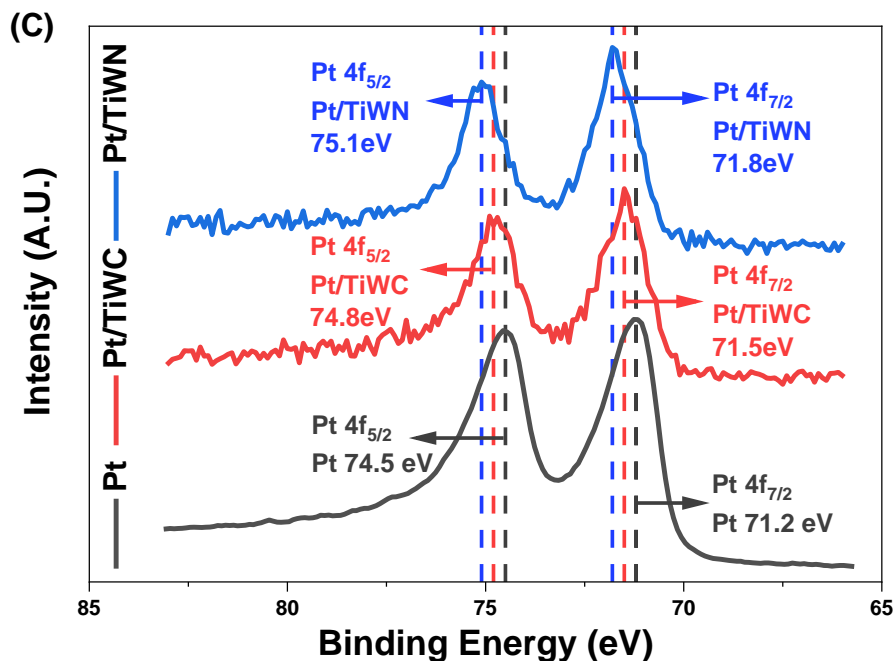
Figure S4-28. X-ray photoelectron spectroscopy (*XPS*) measurements for different catalysts for Pt 4f, W 4f and C 1s. (a) 2ML Pt/TiWC sample before and after C_2H_2 hydrogenation reaction; (b) 2ML Pt/TiWN sample before and after C_2H_2 hydrogenation reaction; (c) Characterization of the core-shell materials as the Pt $4f_{7/2}$ energy shifts indicating the Pt shell formation.

C_2H_2 hydrogenation reactivity
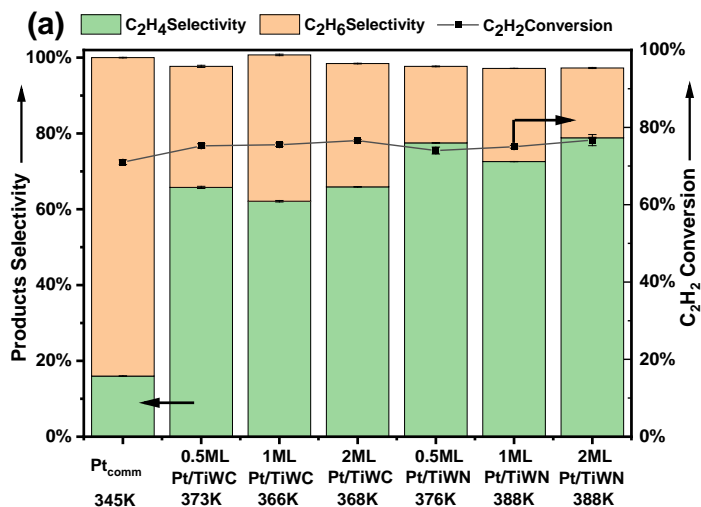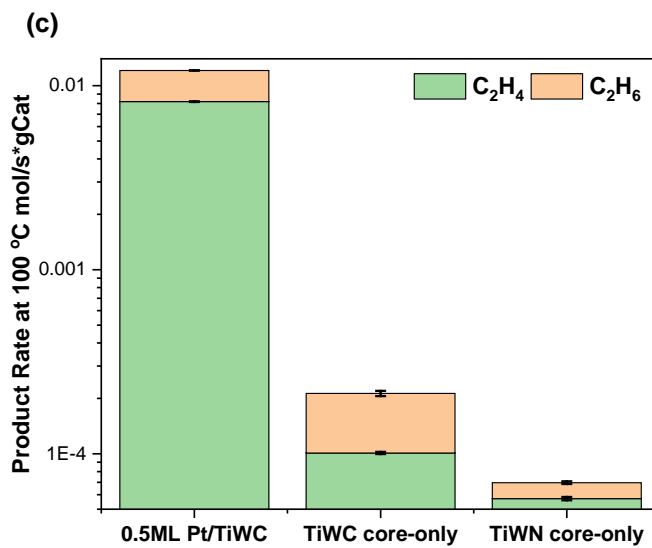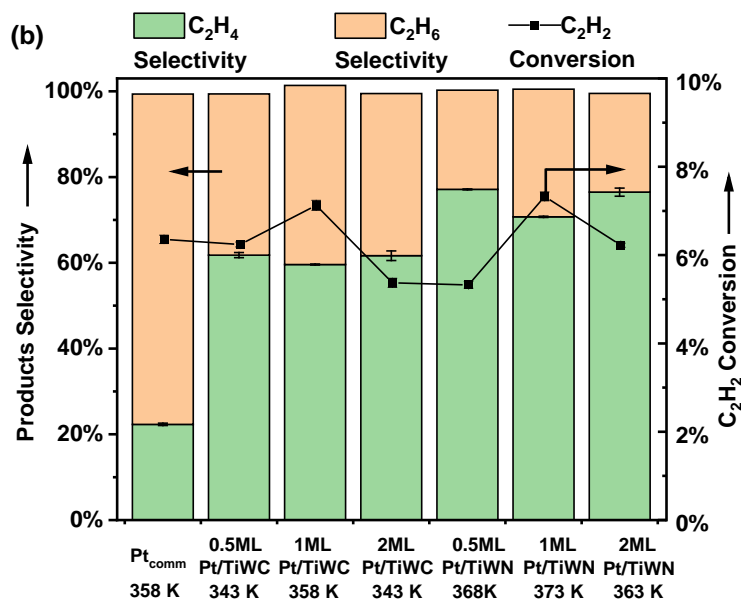
Figure S4-29. C_2H_2 hydrogenation results for different catalysts.

(a) Selectivity and conversion for different catalysts at different temperatures to achieve ~75% acetylene conversion;

(b) Selectivity and conversion for different catalysts at different temperatures to achieve ~7% acetylene conversion; (c) weight normalized (based on the core-shell total weight) reactivity comparison between 0.5ML Pt/TiWC, TiWC and TiWN cores at 100ºC.

Selectivity to C_2H_4 at different conversion and temperature

Here we showed that Pt_{comm} selectivity of C_2H_4 varied only on the temperature but not the conversion (induced by different space velocity) in Figure S4-5, while Pt/TiWC and Pt/TiWN core-shell particles selectivity of C_2H_4 were independent of conversion or temperature in Figure S4-6 and Figure S4-7.

Depending on how one changes the conversion (gas hourly space velocity, GHSV or temperature), the selectivity can be different, simply because GHSV approaches can be conducted under constant coverage, while temperature-dependent approaches are done under variable coverage. At high temperatures, it is not surprising the selectivity on the commercial catalyst goes up. Hydrogen coverage decreases (confirmed by the increase in apparent hydrogen reaction order with temperature, Table S4-2). However, the selectivity with temperature for the core-shell doesn't change. This is related to the similar temperature dependency of the adsorption energy, such that the ratio of coverage ($\theta_{C2H4}/\theta_{H2}$) doesn't change considerably with temperature.
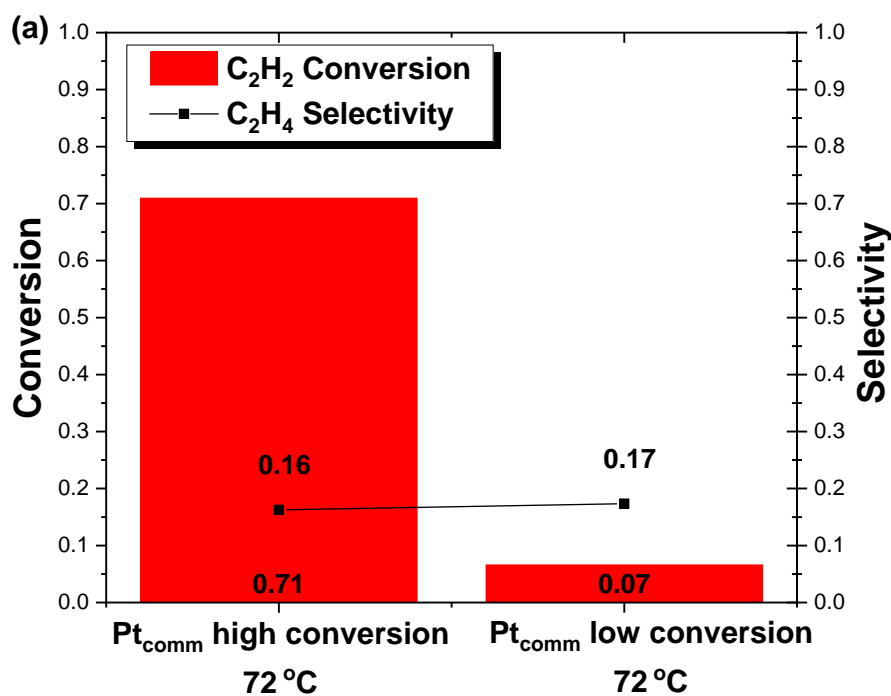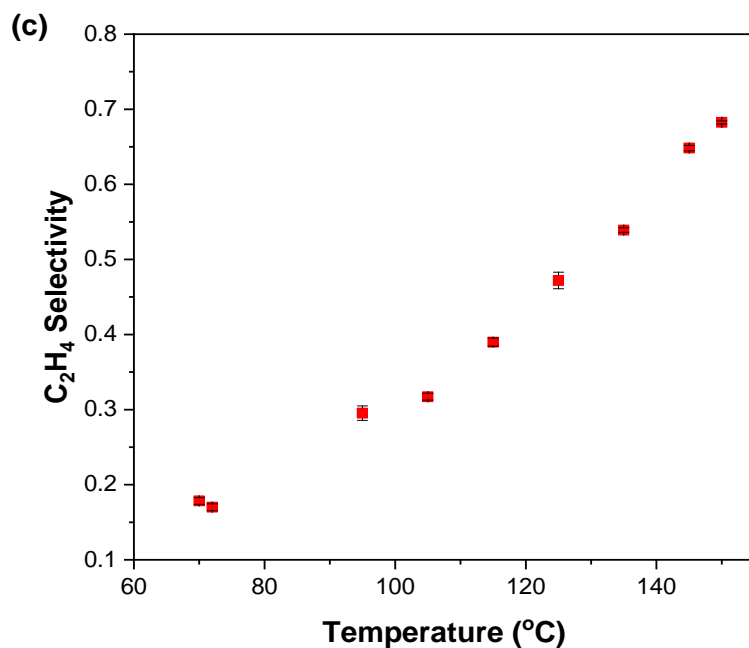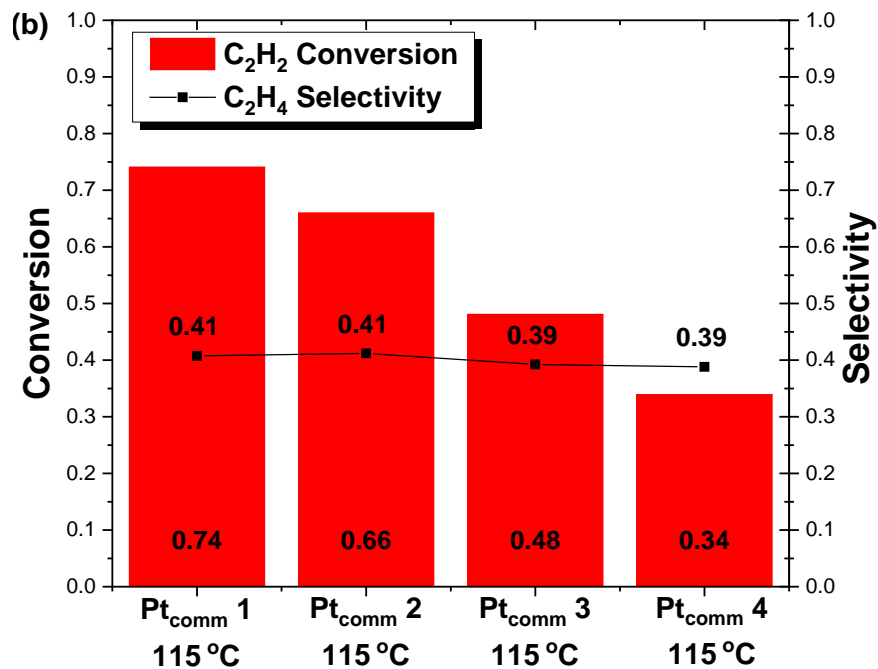
Figure S4-30. C_2H_4 selectivity of Pt_{comm} at different conversions and temperatures for the C_2H_2 hydrogenation reaction. (a) C_2H_2 conversion vs. C_2H_4 selectivity at 72 °C with varied GHSV; (b) C_2H_2 conversion vs. C_2H_4 selectivity at 115 °C with varied GHSV; (c) C_2H_4 selectivity vs. temperature.

(a)

(b)

(c)

(d)

(e)

(f)
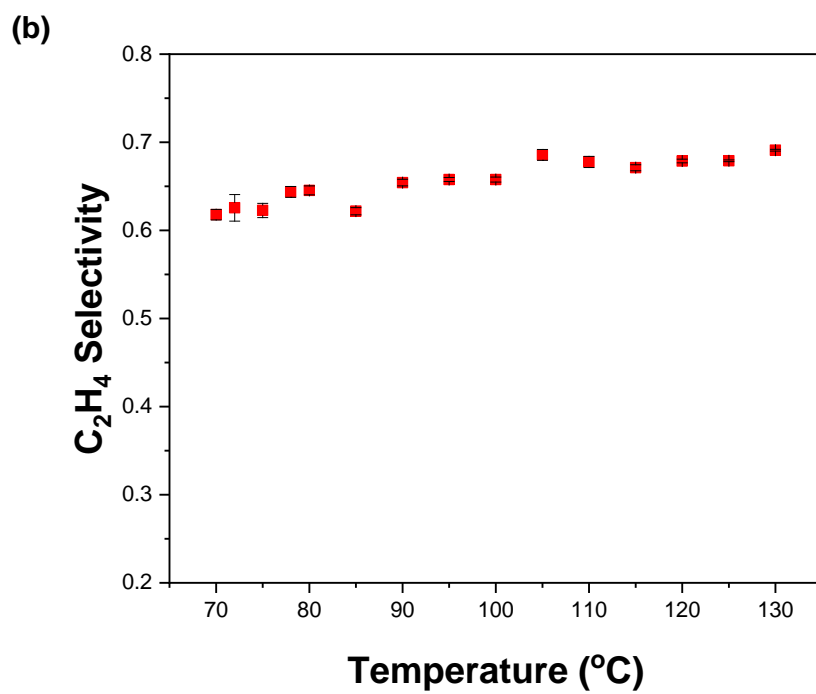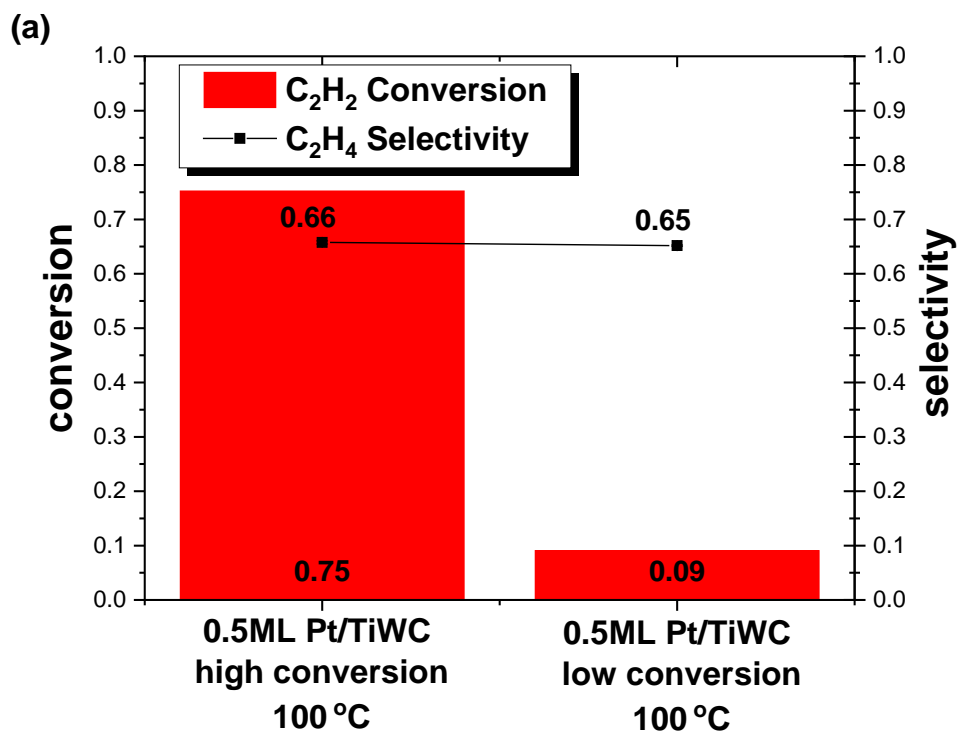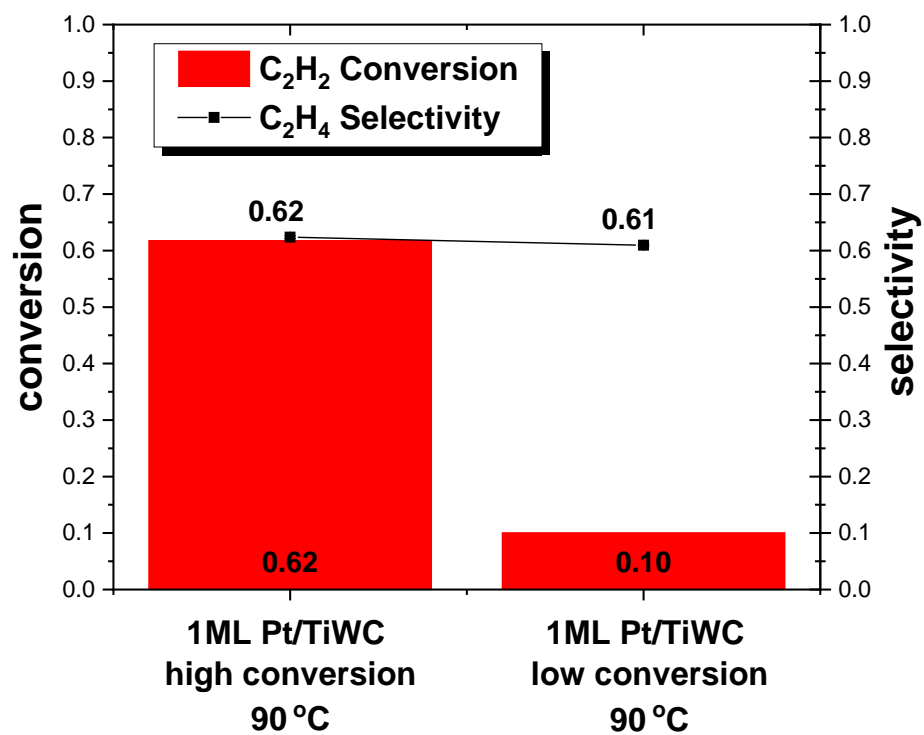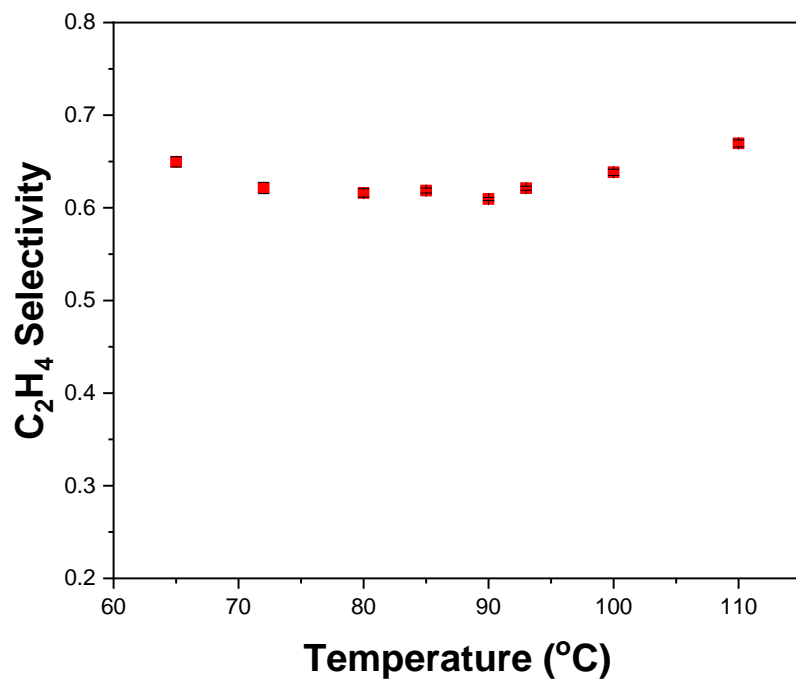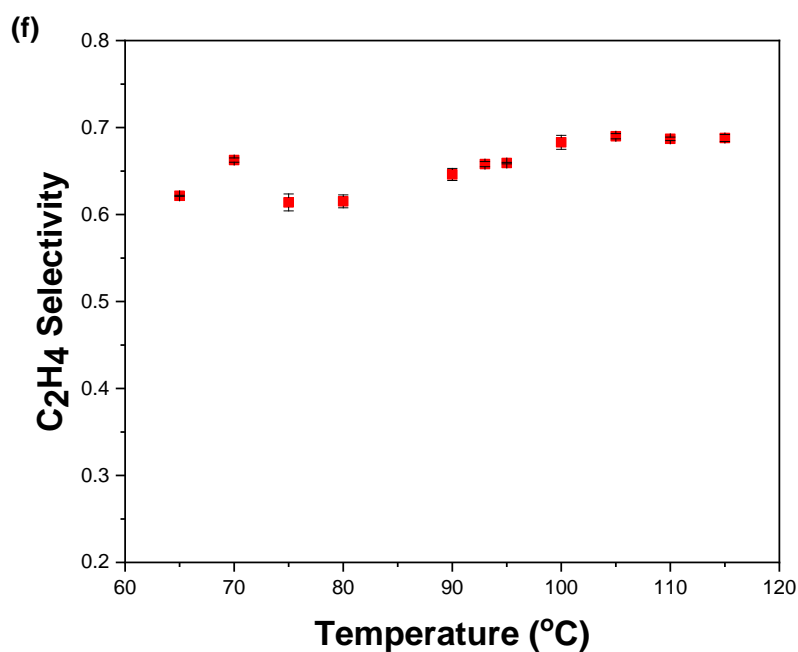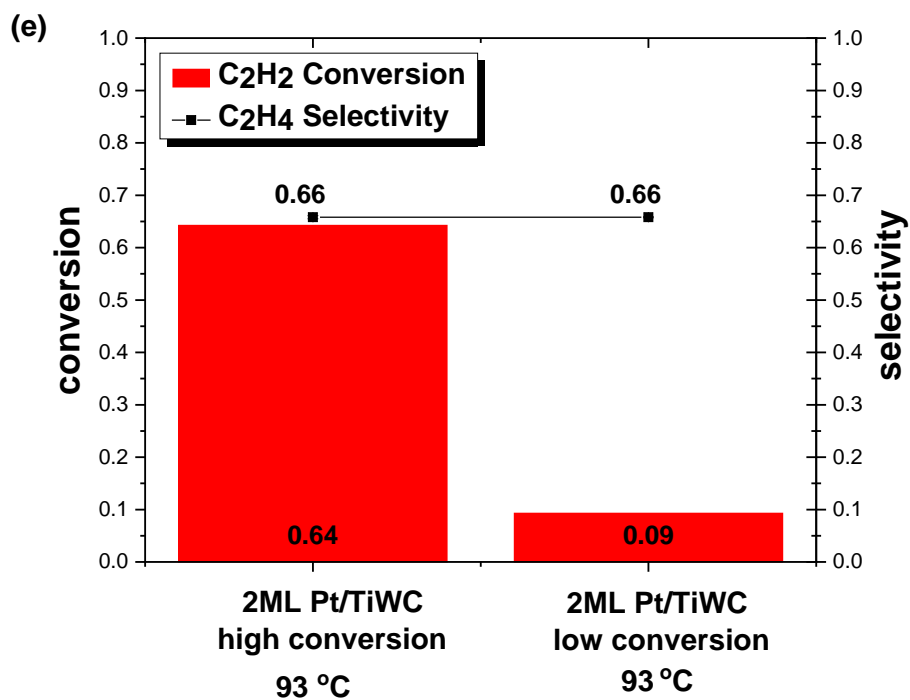
Figure S4-31. C_2H_4 selectivity of Pt/TiWC at different conversions and temperatures for the C_2H_2 hydrogenation reaction

(a) C_2H_2 conversion vs. C_2H_4 selectivity at 100 °C for 0.5 ML Pt/TiWC with varied GHSV; (b) C_2H_4 selectivity vs. temperature for 0.5 ML Pt/TiWC; (c) C_2H_2 conversion vs. C_2H_4 selectivity at 90 °C for 1 ML Pt/TiWC with varied GHSV;

(d) C_2H_4 selectivity vs. temperature for 1 ML Pt/TiWC; (e) C_2H_2 conversion vs. C_2H_4 selectivity at 93 °C for 2 ML Pt/TiWC with varied GHSV; (f) C_2H_4 selectivity vs. temperature for 2 ML Pt/TiWC.

(a)

(b)

(c)

(d)

(e)

(f)
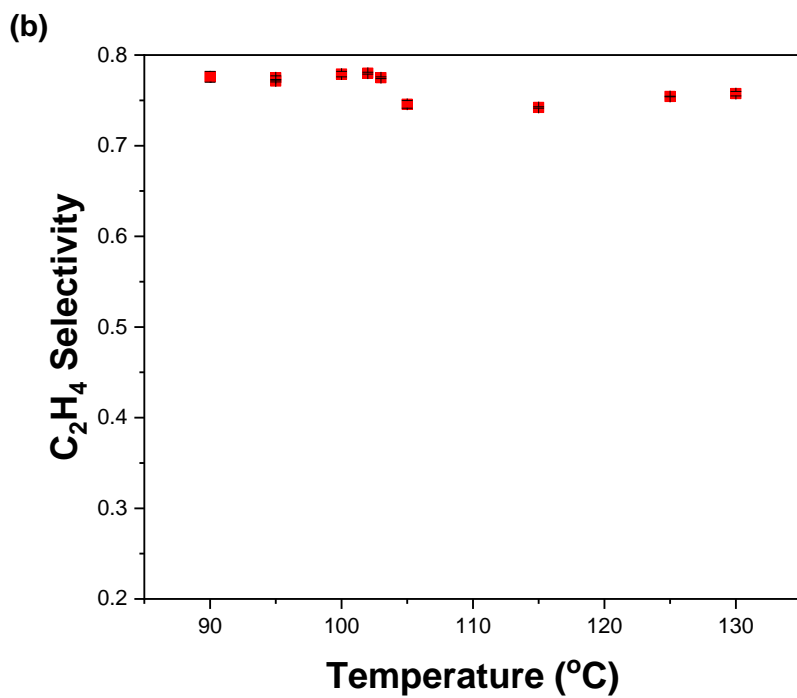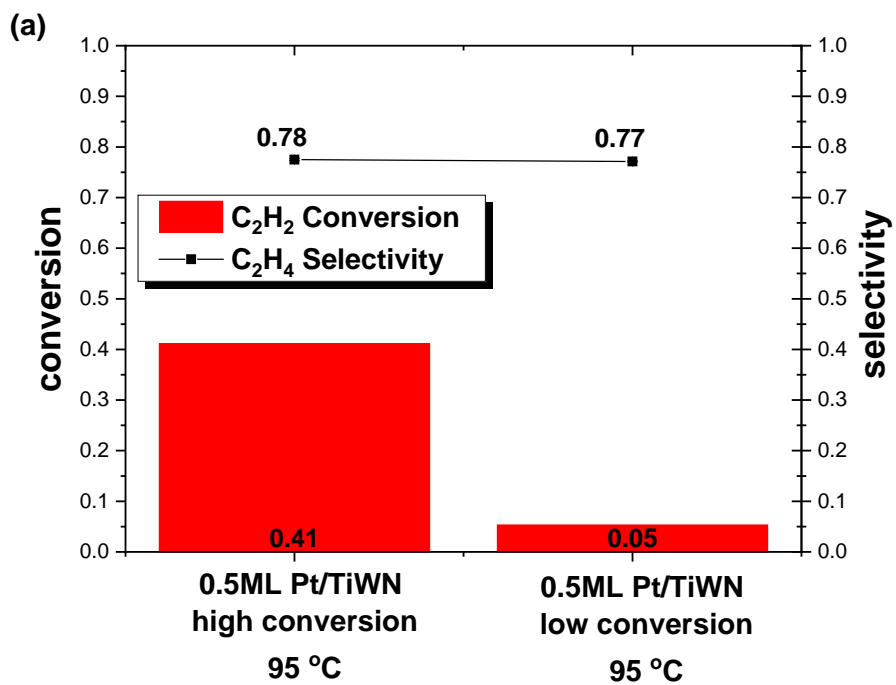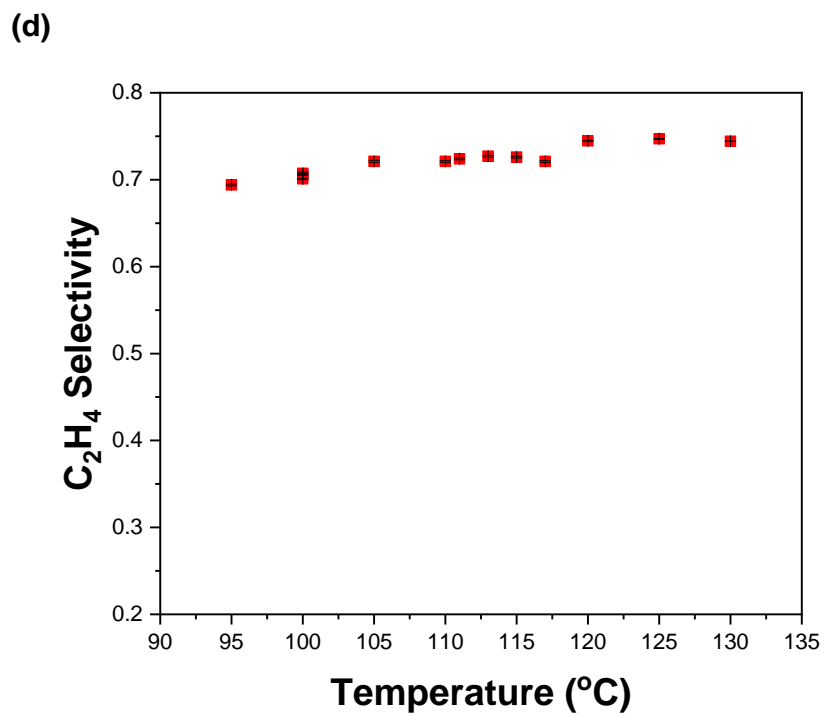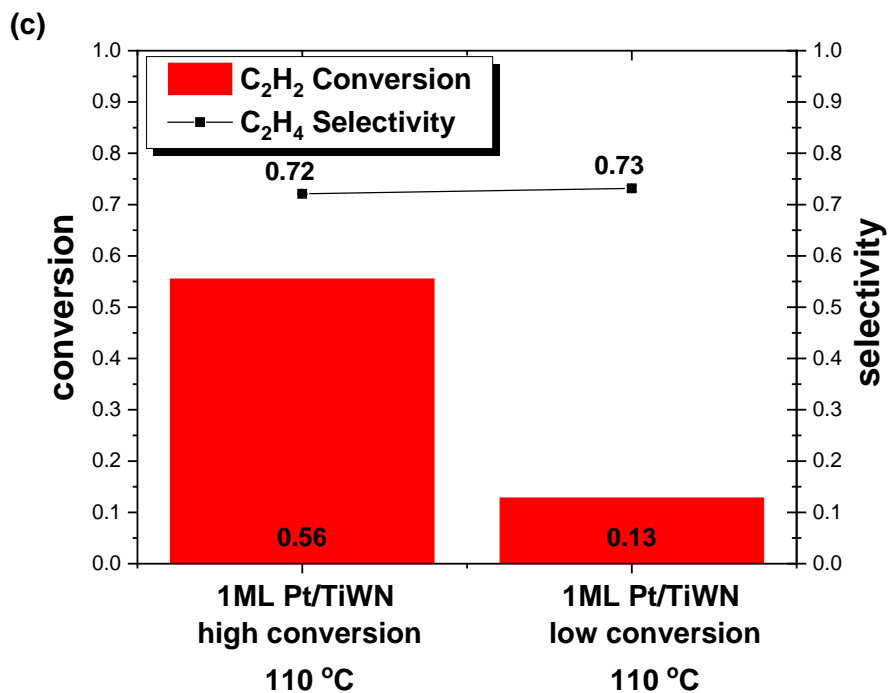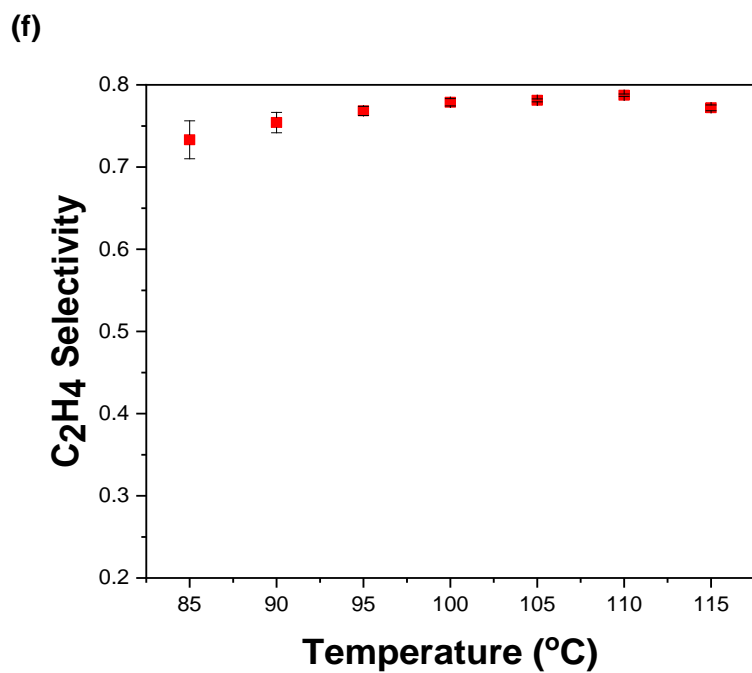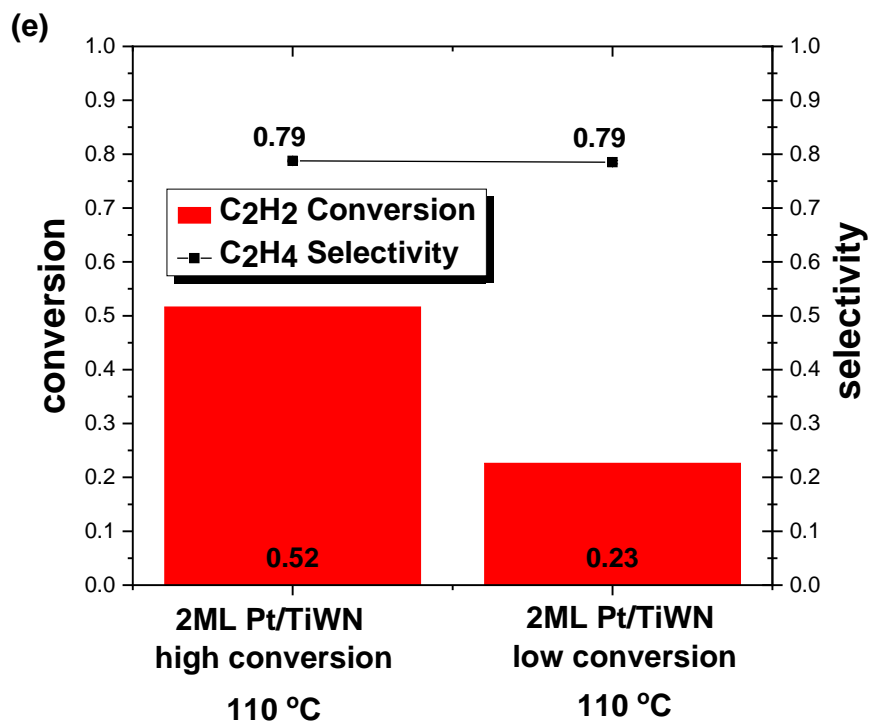
Figure S4-32. C_2H_4 selectivity of Pt/TiWN at different conversions and temperatures for the C_2H_2 hydrogenation reaction.

(a) C_2H_2 conversion vs. C_2H_4 selectivity at 95 °C for 0.5 ML Pt/TiWN with varied GHSV; (b) C_2H_4 selectivity vs. temperature for 0.5 ML Pt/TiWN; (c) C_2H_2 conversion vs. C_2H_4 selectivity at 110 °C for 1 ML Pt/TiWN with varied GHSV; (d) C_2H_4 selectivity vs. temperature for 1 ML Pt/TiWN; (e) C_2H_2 conversion vs. C_2H_4 selectivity at 110 °C for 2 ML Pt/TiWN with varied GHSV; (f) C_2H_4 selectivity vs. temperature for 2 ML Pt/TiWN.

Reaction order studies

Table S4-19. Temperature-dependent C_2H_2 reaction order for C_2H_2 hydrogenation.

Reaction conditions: C_2H_2 = 0.03 atm - 0.07 atm, H_2 = 0.20 atm, CH_4 = 0.08 atm (internal standard) and He = 0.67 atm, with a gas hourly space velocity (GHSV) of ~1800 hr^{-1} and temperature varied from 323 K to 358 K.

C_2H_2 Order	Pt_{comm}	2ML TiWC	2ML TiWN
323 K	--	-0.43±0.02	--
338 K	--	-0.39±0.01	--
348 K	-0.24±0.03	-0.47±0.03	-0.55±0.06
358 K	-0.17±0.02	-0.48±0.03	-0.63±0.07

Table S4-20. Temperature-dependent H_2 reaction order for C_2H_2 hydrogenation.

Reaction conditions: C_2H_2 = 0.05 atm, H_2 = 0.15 atm - 0.25 atm, CH_4 = 0.08 atm (internal standard) and He = 0.67 atm with a gas hourly space velocity (GHSV) of ~1800 hr^{-1} and temperature varied from 323K to 358K.

H_2 Order	Pt_{comm}	2ML Pt/TiWC	2ML Pt/TiWN
323 K	--	1.02±0.04	--
338 K	--	1.10±0.02	--
348 K	1.12±0.04	1.09±0.04	1.13±0.14
358 K	1.01±0.03	1.15±0.02	1.19±0.15

Experimental measurement of the number of Pt active sites

Table S4-21. Site Number Count from Hupd integration method and CO chemisorption method for Pt_{comm}, core-shell and core materials.

	Hupd Area (m^2/g_{Pt}) or (m^2/g_{core})	Number of Sites (mmol/g_{Pt}) or (mmol/g_{core})
Pt_{comm}(Chemisorption)	96.0±1.6	1.99±0.03
Pt_{comm}(Hupd)	94.8±7.0	2.06±0.15
2ML Pt/TiWC (Hupd)	62.2±6.2	1.35±0.14
2ML Pt/TiWN (Hupd)	58.5±1.8	1.27±0.04
1ML Pt/TiWC (Hupd)	113.2±2.2	2.46±0.05
1ML Pt/TiWN (Hupd)	137.5±9.7	2.99±0.21
0.5ML Pt/TiWC (Hupd)	88.5±8.2	1.93±0.18
0.5ML Pt/TiWN (Hupd)	114.0±3.8	2.48±0.08
TiWN (Hupd)	0.88	0.02
TiWC (Hupd)	2.57	0.06

Catalysts geometry comparison

Table S4-22. EXAFS parameters determined under 300°C H_2 reduction condition[99]

	Pt_{comm}	Pt_{2ML}/TiWC	Pt_{2ML}/TiWN
ΔE_0 (eV)	6.9 ± 0.9	6.9 ± 0.8	7.2 ± 1.0
N_{Pt-Pt}	10.4 ± 1.2	9.2 ± 1.0	9.5 ± 1.3
r_{Pt-Pt} (Å)	2.770 ± 0.002	2.773 ± 0.002	2.781 ± 0.003
s^2_{Pt-Pt} (Å^2)	0.006 ± 0.001	0.009 ± 0.001	0.008 ± 0.001
R-factor	0.013	0.014	0.022

Table S4-23. EXAFS parameters of Pt-Pt shell and Pt-O

	2 ML Pt/TiWN	0.5ML Pt/TiWN	2 ML Pt/TiWC	0.5ML Pt/TiWC	Pt-foil
Coordination Number (Pt-Pt)	8.2 ± 0.9[3]	6 ± 2[3]	9 ± 3	8 ± 3	12[3]
r (Å) (Pt-Pt)	2.777 ± 0.002[3]	2.77 ± 0.01[3]	2.742 ± 0.004	2.744 ± 0.007	2.753 ± 0.008[3]
$\sigma^2(Å^2)\times10^{-3}$ (Pt-Pt)	8 ± 1[3]	8 ± 3[3]	13 ± 4	14 ± 5	5 ± 0[3]
ΔEo (eV) (Pt-O)	-	11 ± 1[3]	-	11 ± 1	-
Coordination Number (Pt-O)	0.6 ± 0.1[3]	1.2 ± 0.3[3]	1.0 ± 0.4	1.2 ± 0.4	-
r (Å) (Pt-O)	-	2.11 ± 0.06[3]	-	2.11 ± 0.06	-
$\sigma^2(Å^2)\times10^{-3}$ (Pt-O)	-	8 ± 2[3]	-	8 ± 2	-
R-factor	0.015[3]				

C_2H_4 hydrogenation reactivity

C_2H_4 hydrogenation reactivity had different trend from the C_2H_2 hydrogenation, a hypothesis is that the exposed WC surface can also be active for the C_2H_4 hydrogenation (based on literature) [199-201] but not active for the C_2H_2 hydrogenation.
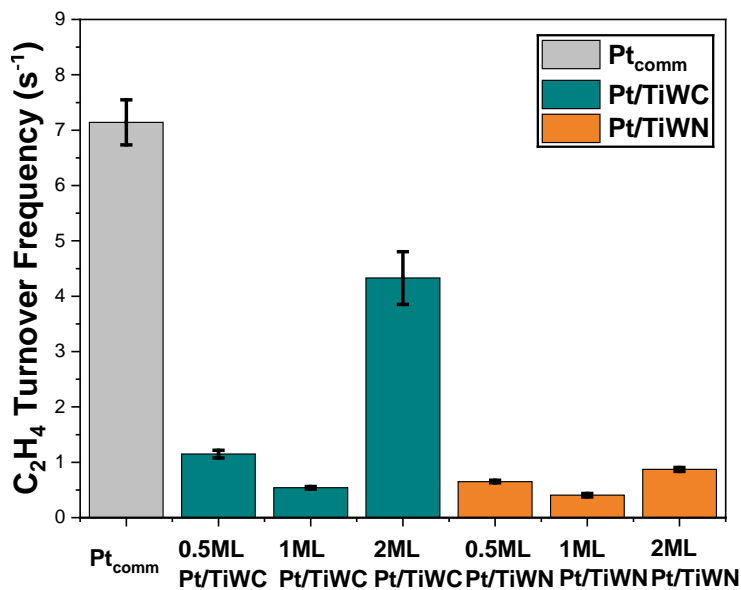
Figure S4-33. Turnover frequency of C_2H_4 hydrogenation at 318 K.

Error bar indicated the propagated error (standard deviation during the number of site measurements and mole of C_2H_4 consumed)

DFT C_2H_2 and C_2H_4 binding energy calculations

Table S4-24. Acetylene and ethylene adsorption energies on 1ML Pt/TiWC and 1ML Pt/TiWN

C$_2$H$_2$ on 1ML Pt/TiWC		C$_2$H$_4$ on 1ML Pt/TiWC		C$_2$H$_2$ on 1ML Pt/TiWN		C$_2$H$_4$ on 1ML Pt/TiWN	
site	E_{ads} (eV)	site	E_{ads} (eV)	site	E_{ads} (eV)	site	E_{ads} (eV)
Hollow1	-1.13	Bridge1	-0.21	Hollow1	-1.42	Bridge1	-0.41
Hollow2	-1.16	Bridge2	-0.37	Hollow2	-1.57	Bridge2	-0.57
Hollow3	-0.79	Bridge3	-0.20	Hollow3	-1.62	Bridge3	-0.38
Hollow4	-1.04	Bridge4	-0.40	Hollow4	-1.26	Atop1	-0.74
Bridge1	-0.88	Atop1	-0.51	Bridge1	-1.39	Atop2	-0.46
Bridge2	-0.79	Atop2	-0.49	Bridge2	-1.49	NA	NA
NA	NA	Atop3	-0.39	Bridge3	-0.96	NA	NA

DFT d-band center calculations

Table S4-25. d-band center of Pt atoms on 1ML Pt/TiWC, 1ML Pt/TiWN and Pt (111)
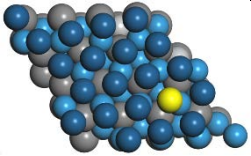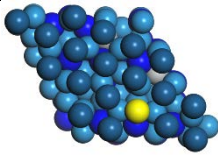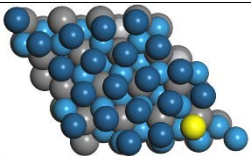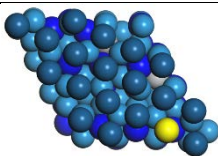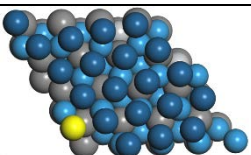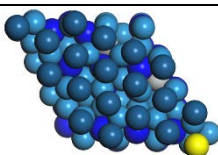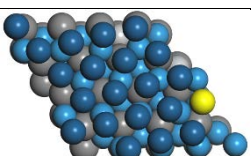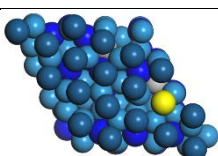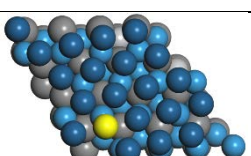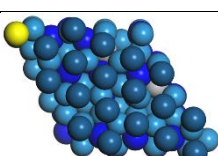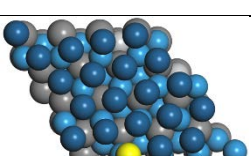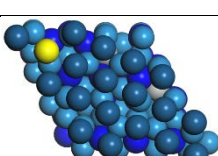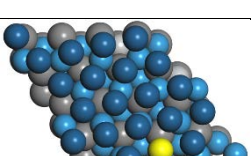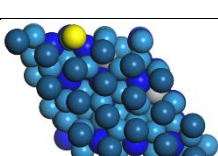
Pt #	1ML Pt/TiWC d-band center (eV)	Surface Pt position on TiWC (marked as yellow)	1ML Pt/TiWN d-band center (eV)	Surface Pt position on TiWN (marked as yellow)
1	-2.79		-3.10	
2	-2.77		-2.96	
3	-2.80		-3.01	
4	-2.85		-3.00	
5	-2.78		-3.03	
6	-2.82		-2.96	
7	-2.81		-2.81	
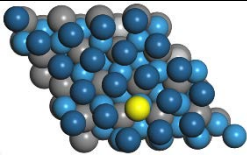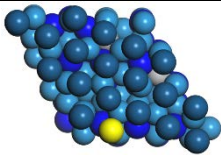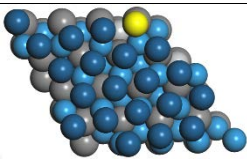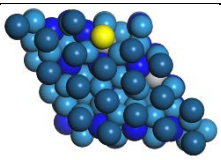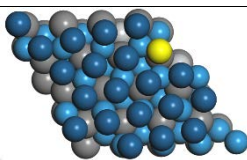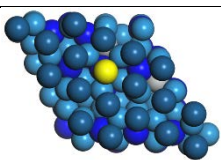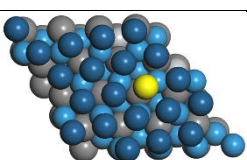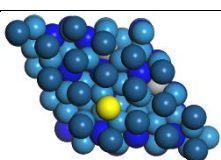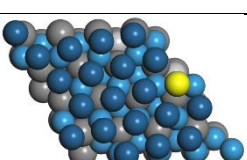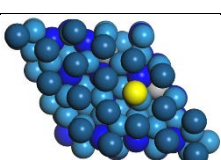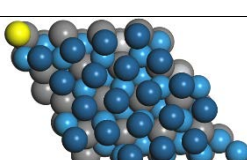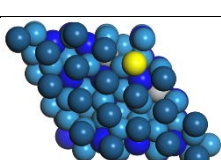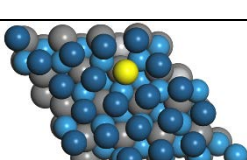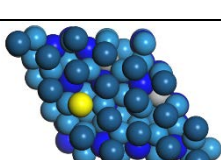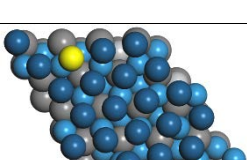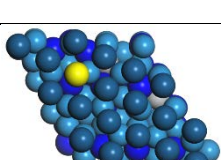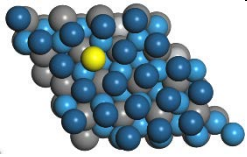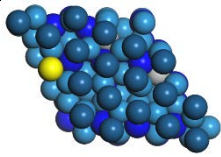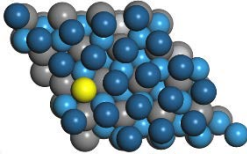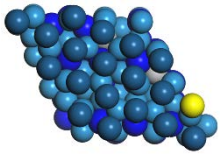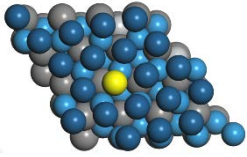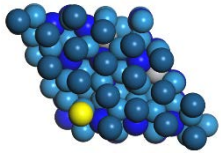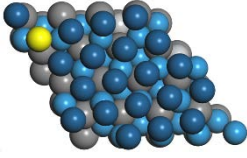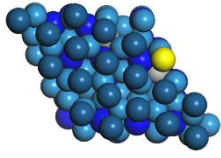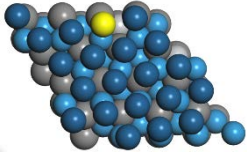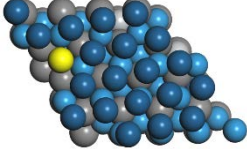
Table S4-7. d-band center of Pt atoms on 1ML Pt/TiWC, 1ML Pt/TiWN and Pt (111) continue				
8	-2.86		-3.00	
9	-2.94		-2.99	
10	-2.88		-3.06	
11	-2.76		-3.06	
12	-2.83		-2.83	
13	-2.79		-2.94	
14	-2.89		-2.95	
15	-2.76		-2.92	

Table S4-7. d-band center of Pt atoms on 1ML Pt/TiWC, 1ML Pt/TiWN and Pt (111) continue				
16	-2.80		-3.09	
17	-2.85		-2.91	
18	-2.77		-2.71	
19	-2.81		-2.80	
20	-2.84		NA	NA
21	-2.87		NA	NA

Industrial front-end condition reactivities

Table S4-26. Results for front-end condition reactions using core-shell particles, Pt_{comm} and incipient wetness impregnation Pt/W_2C.

Reaction conditions: C_2H_2 = 0.02 atm, H_2 = 0.23 atm, C_2H_4 = 0.31 atm, CH_4=0.15 atm (internal standard), and He = 0.29 atm with a gas hourly space velocity (GHSV) of ~1800 hr^{-1}.

	Temperature (K)	C_2H_2 Conversion	C_2H_4 Conversion
Pt_{comm}	371	83.1%	15.9% ± 0.2%
Pt/W$_2$C (IWI)*	378	81.5%	5.5% ± 0.2%
1ML Pt/TiWC	354	81.5%	5.4% ± 0.1%
2ML Pt/TiWC	348	82.1%	5.0% ± 0.1%
0.5ML Pt/TiWC	353	81.5%	4.7% ± 0.2%
2ML Pt/TiWN	378	85.9%	2.1% ± 0.1%
0.5ML Pt/TiWN	378	81.4%	1.0% ± 0.1%
1ML Pt/TiWN	368	83.0%	-0.3% ± 0.1%
0.5ML Pt/TiWN	379	94.5%	2.7% ± 0.3%
2ML Pt/TiWN	386	93.5%	2.6% ± 0.1%
1ML Pt/TiWN	370	95.8%	0.8% ± 0.2%

IWI: incipient wetness impregnation

Catalyst particle size pre- and post- C_2H_2 hydrogenation

The morphology of the Pt_{comm} and core-shell particles did not change after the acetylene hydrogenation reaction. Specifically, the sizes of Pt_{comm} 1.4 ± 0.5 nm, Pt/TiWC 6.2 ± 1.5 nm and Pt/TiWN 6.1 ± 1.8 nm did not change after reaction as confirmed by transmission electron microscopy (TEM) in Table S4-9 with 500 particles size counts.

Table S4-27. Volume-averaged particle size distribution from TEM measurements based on measuring 500 catalyst particles.

	Before Reaction (nm)	After Reaction (nm)
2ML Pt/TiWC	6.2±1.5	6.5±1.6
2ML Pt/TiWN	6.1±1.8	6.1±1.8
Pt_{comm}	1.4±0.5	1.7±0.7

Stability of 1ML Pt/TiWN and Pt$_{comm}$ under Industrial Condition

(a)

(b)
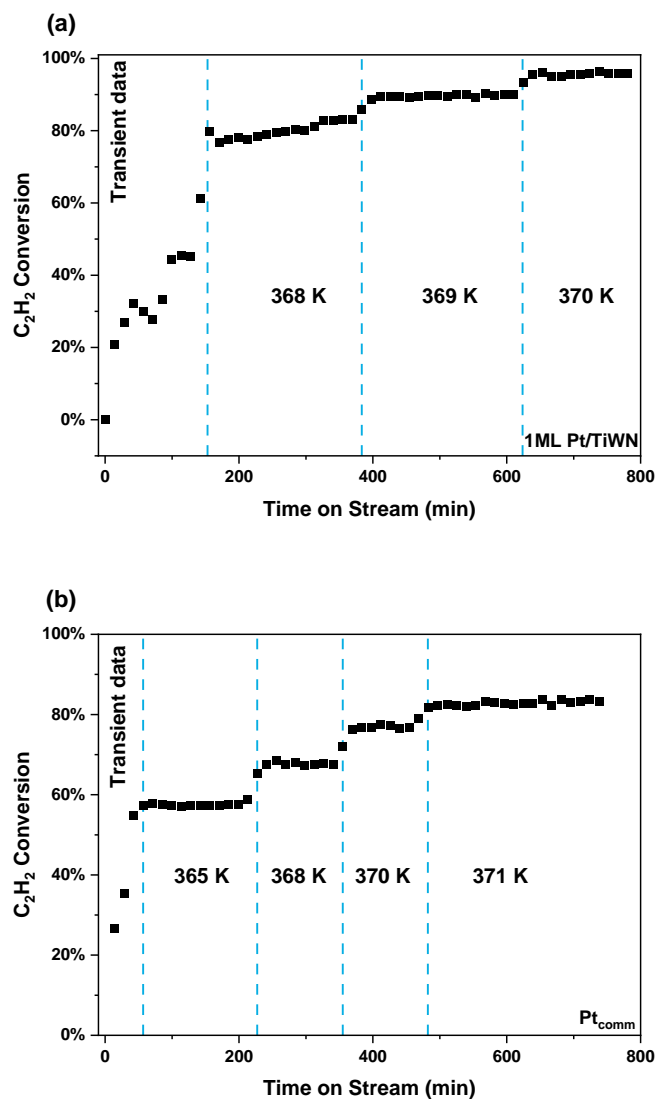
Figure S4-34. Steady-state data of 1ML Pt/TiWN core-shell and commercial Pt particles collected at different temperatures for 13 hours.

The total flow rate was 65 mL/min (5% C_2H_2/He = 20 mL/min, H_2 = 15 mL/min, C_2H_4 = 20 mL/min CH_4 = 10 mL/min (internal standard) or C_2H_2=0.02 atm, H_2=0.23 atm, C_2H_4=0.31 atm CH_4=0.15 atm (internal standard) and He=0.29 atm) (a) 1ML Pt/TiWN, reaction temperature was varied from 368 K to 370 K. Turnover number was 6300 for segment at 370 K only and 22,400 over the entire time span of the graph (b) Pt$_{comm}$, reaction temperature was varied from 365 K to 371 K. Turnover number was 5779 for the segment at 371 K only and 12,226 over the entire time span of the graph.

Gas-Phase Reactivity Testing

General Set-up

The hydrogenation experiments were carried out with C_2H_2 (Airgas, industrial grade), C_2H_4 (Airgas, grade 2.5), H_2 (Airgas, UHP grade 5), C_2H_6 (Airgas, UHP grade 5), He (Airgas, UHP grade 5) and 5% C_2H_2 diluted in He (Airgas, with part number X02HE95C200R483). C_2H_6 (Airgas, grade 2) combined with C_2H_2, C_2H_4, and C_2H_6 were used in the GC calibration.

The C_2H_2 hydrogenation performance was tested in a packed-bed, downflow reactor. A K-type thermocouple (Omega, model SCAXL-020G-12) was set inside a 3/8-inch stainless tube (inner diameter 0.305 inches). Quartz wool (~70-80 mg) was set right above the thermocouple as physical support of the catalyst bed. The reactor was mounted in a single-zone furnace (Applied Test Systems, Series 3210, 850W/115V) and the temperature was controlled by a temperature controller (Digi-Sense, model 68900-10). The gases were controlled by the Brooks mass flow controllers (GF40). Core-shell particles supported on carbon black or Pt_{comm} catalysts (~2-70 mg) was well-mixed with α-alumina (4.0 g, 100-200 mesh Sigma-Aldrich, pictures showed in Figure S4-10 and loaded on top of the quartz wool in the reactor. The catalyst bed length was around 4.6 cm. Catalysts were activated by a reduction in pure H_2 (50 mL/min) and ramped from room temperature to 473 K over 1.5 h and soaked at 473 K for ½ h. The catalysts were then cooled to the reaction temperature under H_2.
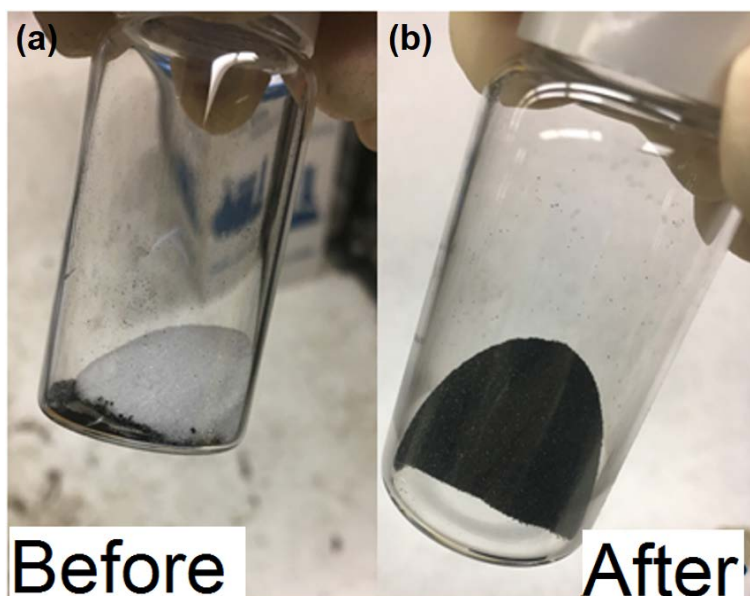
Figure S4-35. Catalyst and diluent mixture before and after shaking.

(a) Before mixing thoroughly; (b) after mixing catalyst and diluent alumina thoroughly.

For the C_2H_2 hydrogenation reaction, the total flow rate was 60 mL/min (C_2H_2 = 3 mL/min, H_2 = 12 mL/min, CH_4 = 5 mL/min (internal standard), He = 40 mL/min or C_2H_2=0.05 atm, H_2=0.20 atm, CH_4=0.08 atm (internal standard) and He=0.67 atm), reaction temperature was varied from 343 K to 388 K.

For C_2H_4 hydrogenation, the total flow rate was 60 ml/min (C_2H_4 = 5 mL/min, H_2 = 5 mL/min, CH_4 = 5 mL/min (internal standard), He = 45 mL/min or C_2H_4=0.08 atm, H_2=0.08 atm, CH_4=0.08 atm (internal standard) and He=0.75 atm), reaction temperature was 318 K.

For the industrial C_2H_2 hydrogenation, the total flow rate was 65 ml/min (5% C_2H_2/He = 20mL/min, H_2 = 15 mL/min, C_2H_4 = 20 mL/min CH_4 = 10 mL/min (internal standard) or C_2H_2=0.02 atm, H_2=0.23 atm, C_2H_4=0.31 atm CH_4=0.15 atm (internal standard) and He=0.29 atm), reaction temperature was varied from 348 K to 378 K. All product distributions were analyzed with an Agilent 6890 FID gas chromatography.

C$_2$H$_4$ Selectivity vs. Conversion and Temperature

The C$_2$H$_2$ conversion and the C$_2$H$_4$ selectivity were defined as follows:

$$C_2H_2 \text{ conversion} = \frac{C_2H_2(\text{feed}) - C_2H_2}{C_2H_2(\text{feed})}$$

Equation S4-17

$$C_2H_4 \text{ selectivity} = \frac{C_2H_4}{C_2H_2(\text{feed}) - C_2H_2}$$

Equation S4-18

No oligomer was observed from the gas chromatography and the carbon mass balance was obtained as 99%.

Kinetics Data

In addition to the reactivity test, H$_2$ and C$_2$H$_2$ order measurements were carried out for the C$_2$H$_2$ hydrogenation reaction. All these measurements were carried out in the differential regime (conversion less than 15%). C$_2$H$_2$ order and H$_2$ order were shown in Table S4-1 and Table S4-2. The core-shell had more negative C$_2$H$_2$ order dependence which indicated the C$_2$H$_2$ might bind the core-shell surface stronger and stopped further hydrogenation. The H$_2$ dependence for core-shell was more positive. From 323 K to 358 K, Pt$_{comm}$ C$_2$H$_2$ order changed from largely negative to close to 0 while core-shell particles remained almost the same. For the H$_2$ order during the same temperature range, Pt$_{comm}$ dropped from 1.2 to 1.0 while the core-shell stayed relatively constant with a slight increase.

Isotopically-labeled Semi-hydrogenation Batch Reactions

Reactivity (and selectivity) studies using isotopically-labeled hydrocarbon mixtures were performed in a gas-tight batch reactor similar to the one described by Spanjers et al.[202] The 1ML Pt/TiWN catalyst (2 mg) was mixed with 500 mg silica gel (Davisil Grade 62, 60-200 mesh, Sigma Aldrich) and 5 mg of this mixture was loaded in a quartz tube (5 mm I.D.), immobilized between two plugs of quartz wool. The reactor was evacuated to ~200 mTorr and backfilled with 6 Torr ^{12}C$_2$H$_2$ (1% in He, Airgas), 120 Torr ^{13}C$_2$H$_4$ (99.8%, Sigma Aldrich), 90 Torr H$_2$ (UHP, Praxair) and 20 Torr Ar (UHP, Praxair). Sampling was

performed through a rubber septum by a 100 µL SampleLock syringe (Hamilton Company). The syringe was purged at least twice before a gas sample was collected for each data point. The sample was analyzed on a Shimadzu QP 2010 Ultra GC-MS fitted with an Rt-Alumina BOND/KCl column. Ar was used as an internal standard to normalize any change in chromatogram peak area due to a discrepancy in injection volume between different samples. At least three samples were taken at room temperature (when reactivity is zero) to determine initial peak ratios of all the components present in the reactor. Catalytic reaction data is collected at 343 K. The isotope distribution in case of ethylene and ethane are determined through the matrix method developed by Price and Iglesia.[203] This method has been previously used in similar analyses by Spanjers et al.[202, 204] and Bui and Bhan.[205]

Heat and Mass Transfer Limitation Calculation

External Transport Limitations

Mear's criteria were used to estimate the external mass transfer.[159]

$$\frac{r_{obs}\rho_b Rn}{k_c C_b} < 0.15 \qquad\qquad \textbf{Equation S4-19}$$

where r_{obs} is the observed rate of reaction in kmol/(kg$_{cat}$*s); ρ_b is the catalyst bed density in kg/m^3 (the total weight of the catalyst bed and the volume taken up in the reactor was measured, hence void fraction was not used in this calculation); R is the catalyst particle radius in m; n is the reactant reaction rate order; k_c is the external mass transfer coefficient in m/s; C_b is the reactant bulk concentration in kmol/m^3.

k_c was calculated by assuming the Sherwood number equals to 2 when Re (Reynolds Number) is much smaller than 1 and D$_{AB}$ is the diffusivity.

$$Sh(Sherwood\ Number) = \frac{2Rk_c}{D_{AB}} = 2 \qquad\qquad \textbf{Equation S4-20}$$

Mear's external heat transfer was shown as follow.[159]

$$\frac{\left|\Delta H\right| r_{obs}\rho_b RE_a}{hR_g T_0^2} < 0.15 \qquad \textbf{Equation S4-21}$$

where ΔH is the enthalpy of reaction in kJ/kmol; E_a is the reaction activation energy in kJ/kmol; h is the external heat transfer coefficient in kW/(m^2-K); R_g is the gas constant (8.314 kJ/(kmol*K)); T_0 is the reaction temperature (373K was used).

h was calculated by assuming the Nusselt number equals to 2 when Re (Reynolds Number) is much smaller than 1.[159]

$$Nu(Nusselt\ Number) = \frac{2Rh}{D_{AB}} = 2 \qquad \textbf{Equation S4-22}$$

Table S4-28. Tabulation of Parameters for the Mear's Criteria Calculation

Symbol	Meaning & Unit	Value
r_{obs}	reaction rate (kmol/(kg$_{cat}$-s)) (highest)	3.3×10^{-4}
Re	Reynold's number	0.026
Q	flow rate (ml/min)	60
u	superficial velocity (m/s)	0.02
D	reactor inner diameter (m)	0.0077
A	reactor inner area (m^2)	4.7×10^{-5}
ρ_{gas}	gas density (kg/m^3)	0.186
ρ_b	catalyst bed density (kg/m^3) very low due to lots of diluent added	4.7
μ	gas viscosity (Pa-s)	1.91×10^{-5}
P	total pressure of the gas (Pa)	1.01×10^5
R	particle size (sieved to a mesh size 150 microns) (m)	6.4×10^{-5}
k_c	external mass transfer coefficient (m/s)	3.83
C_b	reactant bulk concentration (use H$_2$) (kmol/m^3)	6.5×10^{-3}
E_a	activation energy (kJ/kmol) (the largest one)	80000
ΔH	C$_2$H$_2$ → C$_2$H$_6$ enthalpy (kJ/kmol)	309000
n	reaction order (use H$_2$, the largest one)	1.2
h	heat transfer coefficient (kW/m^2-K)	2.27
Mear's criterion (Mass) 4.7×10^{-6} << 0.15		
Mear's criterion (Heat) 9.6×10^{-4} << 0.15		

Internal Transport Limitations

Internal mass transfer lizmitation was checked by using the Weisz-Prater criterion.[159]

$$\eta\phi^2 = \frac{r_{obs}R^2\rho_c}{D_e C_{AS}}$$

Equation S4-23

η is the dimensionless effectiveness factor; ϕ is the Thiele modulus; D_e is the effective gas-phase diffusivity in m^2/s; C_{AS} is the reactant gas concentration at the catalyst surface in kmol/m^3 which was assumed to be the same as C_b due to no external mass transfer limitation; ρ_c is the crystallite density in kg/m^3; if ϕ <<1, then $\eta \approx 1$ and ϕ can be calculated. D_e was calculated using the following equation, where D is the diffusivity, ε is the porosity; δ is the constrictivity; τ is the tortuosity. (ε =0.6, δ =0.8, τ =1.8) [160]

$$D_e = \frac{D\varepsilon\delta}{\tau}$$ **Equation S4-24**

Table S4-29. Tabulation of Parameters for the Weisz-Prater's Criteria Calculation

Symbol	Meaning & Unit	Value
r_{obs}	rate of reaction (kmol/(kg$_{cat}$-s)	3.3×10^{-4}
R	catalyst particle radius (m)	6.4×10^{-5}
D$_e$	effective diffusivity (m^2/s)	4.4×10^{-5}
ρ_c	catalyst particle density (kg/m^3)	96.1
C$_{AS}$	reactant concentration at the catalyst surface (kmol/m$^{3)}$	6.5×10^{-3}
Calculated Weisz-Prater criterion ($\eta\phi^2$)		**4.4×10^{-4} <<1**

Catalyst Synthesis

The core-shell platinum/titanium tungsten carbide nanoparticles and core-shell platinum/titanium tungsten nitride nanoparticles were synthesized through carburizing mixtures of H_2PtCl_6 and tungsten oxides encapsulated in removable silica templates.[6] Core-shell nitride samples were obtained through nitridation of the core-shell carbide sample.[3] Pt$_{comm}$ was purchased from the Premetek Company with 5wt% Pt loading supported on Vulcan XC-72 carbon black. Platinum nanoparticle supported on tungsten carbide was synthesized using the incipient wetness impregnation method. $H_2PtCl_6\cdot6H_2O$ (Strem chemical Inc, containing 38%-40% Pt) 150 mg was dissolved in 0.3 g of Milli Q water and sonicated for 1 minute. The solution was then impregnated onto 800 mg of

W$_2$C support (Sigma-Aldrich) under stirring at 333 K until all the water evaporated. The sample was then dried at 393 K oven. Prior to characterization, the sample was reduced under 100 sccm pure H$_2$ at 573 K for 3 h with a 2 K/min ramping rate. Before the reaction, the reduced sample was further reduced with 50 sccm H$_2$ at 573 K for 12 h to eliminate the surface oxygen.

Catalyst Characterization

Transmission electron microscopy (TEM) was performed on a JEOL 2010 equipped with a field emission gun (FEG) operating at 200 kV. Magnifications of obtained images ranged from 25,000× to 500,000×. Samples were prepared by dispersion in acetone and deposited onto copper grids with carbon film.

Powder x-ray diffraction (PXRD) was performed on a Bruker D8 diffractometer using Cu Kα radiation with a step size of 0.01° and step time of 0.2 s. Powder samples were placed onto zero background silicon crystal sample plate (MTI corp). Rietveld refinement is carried out using HighScore Plus software to analyze quantitatively the individual component peak contribution.

X-ray photoelectron spectroscopy (XPS) was used to analyze the surface Pt and tungsten carbide core changes for different H$_2$ pretreatments before hydrogenation reactions. PHI Versaprobe II with a monochromatic Al anode X-ray source was used to perform the XPS. The X-ray source was operated at 50 W and 15 kV. No charge correction was applied to the carbon black supported samples due to the high conductivity. Pure H$_2$ (50 sccm) flowed through a U-tube set-up where 2ML Pt/TiWN and 2ML Pt/TiWC samples were reduced at 473 K for 30 min (ramping rate 2 K/min). The core-shell particles were exposed to the reaction gas mixture C$_2$H$_2$: H$_2$: He=1: 4: 19 at 373 K for 3 h. After the reaction, the U-tube set-up was isolated by two on-off valves and transferred into a glove box. XPS samples were prepared by mounting powders onto conductive copper tape inside the glove box. Samples were exposed to air only when it was loaded into the XPS side chamber (for less than 2 min).

X-ray absorption spectroscopy (XAS) was performed at the Advanced Photon Source (APS) at Argonne National Laboratory with 10-BM-B beamline. Pt L2-edge (13,273 eV) was measured for the Pt foil, PtO2 and core-shell materials in transmission mode. The maximum wavenumber, kmax, was limited to ~11 Å-1 by the Pt L1-edge at 13,880 eV. Pt L3-edge (11,564) was not possible to extract due to the proximity to the W L2-edge (11,544 eV). Samples were measured simultaneously with a Pt foil and the energy scales were aligned by using the foil as a reference spectrum. The extended x-ray absorption fine structure parameters were fitted with Athena and Artemis software from the Demeter package and were shown in the Table S4-4 and Table S4-5 where the Table S4-4 was the material under H_2 at 300°C.[99]

Inductively coupled plasma mass spectrometry (ICP-MS) was performed on an Agilent 7900 ICP-MS. Samples with carbon black support were dissolved in aqua regia overnight and filtered through Acrodisc filter with 0.2 μm HT Tuffryn membrane. The filtrate was then diluted with 2% HNO_3 to a Pt concentration of ~100 ppb level. Samples with silica encapsulation were dissolved by mixing with a 48 wt % aqueous HF solution (Sigma-Aldrich) and aqua regia. The samples were then diluted to ~100 ppb level for the measurement. The ICP-MS results were shown in Table S4-12.

Thermogravimetric analysis (TGA) was performed on a Q500 thermal analysis system (TA Instruments). The sample was placed in a platinum holder and heated up to 423 K (10 K/min ramping rate) with 30 min of isothermal holding to get rid of moisture. The flow for this period was 5sccm N_2 only. The sample was then heated up to 1073 K with a 10 K/min ramping rate under 5 sccm of air and held at 1073 K for 10 min. The TGA results were shown in Table S4-12.

Table S4-30. Material Compositions

	Total catalyst wt%	Pt loading wt%	W:Ti mole ratio	Pt/core-shell particle wt% (not including CB)
2ML Pt/TiWC/CB	18.0%±1.7%	5.0%±0.1%	4.6:1	27.8%±2.7%
2ML Pt/TiWN/CB	18.0%±1.7%	5.0%±0.1%	4.6:1	27.8%±2.7%
1ML Pt/TiWC/CB	22.3%±1.5%	4.5%±0.3%	6.7:1	20.2%±1.9%
1ML Pt/TiWN/CB	22.3%±1.5%	4.5%±0.3%	6.7:1	20.2%±1.9%
0.5ML Pt/TiWC/CB	10.9%±0.2%	1.0%±0.1%	5.8:1	9.2%±0.9%
0.5ML Pt/TiWN/CB	10.9%±0.2%	1.0%±0.1%	5.8:1	9.2%±0.9%
Pt$_{comm}$ (From TGA)	5.3%±0.4%	5.3%±0.4%	N.A.	5.3%±0.4%
Pt$_{comm}$ (From ICP)	4.6%±0.1%	4.6%±0.1%	N.A.	4.6%±0.1%

CB indicates carbon black support

Number of sites measurements

Two methods, namely hydrogen underpotential deposition (Hupd) and CO chemisorption, were used to measure the number of active sites to calculate the site time yield (STY) and turnover frequency (TOF). CO chemisorption is typically used to measure the number of Pt active sites, but the core-shell particles possess really weak CO binding strength which hindered the ability to determine the number of surface Pt sites (Pt$_s$) at room temperature. Therefore, we used the electrochemical Hupd method (described in Figure S4-11). In order to validate both methods, the number of active sites on Pt$_{comm}$ was measured by both Hupd and CO chemisorption method. The number of exposed Pt sites obtained for the Pt$_{comm}$ was consistent between the Hupd and the CO chemisorption methods with only 3.5% difference. Hence Hupd measurement was used to measure the number of active sites.

Electrochemical measurements

A CH Instruments 627E potentiostat using BASI RDE-2 rotating disk electrode was used for the electrochemical measurements. The reference electrode was Ag/AgCl and the counter electrode was a platinum coil. The measurements were performed at room temperature. A mixture of DI water, isopropanol, Nafion ® 117 solution was used to disperse carbon black supported catalysts. The ink concentration was 4 mg catalyst per 1 mL of solution for the 5 wt % Pt_{comm}, 2-3 ML Pt/TiWC and 2-3 ML Pt/TiWN core-shell particles and 8 mg catalyst per 1 mL of solution for the 1 ML Pt/TiWC and 1 ML Pt/TiWN core-shell particles. By doing this, a comparable total surface area would be achieved (1 ML core-shell particles had about half the Pt mass loading). The working electrode was formed dropping 6 µL of the ink on freshly polished 3 mm glassy carbon disk electrodes, followed by drying. Each catalyst sample measurements were made in triplicate.

Before each measurement, the core-shell catalyst surface was pretreated in argon saturated 0.1 M $HClO_4$ solution with 100 cyclic voltammetry (CV) conditioning scans from -0.259 V to 0.716 V at 0.2 V/s scan rate with a 2500 rpm ration rate; the Pt_{comm} surface was scanned from -0.259 V to 0.916 V. Core-shell could not be conditioned at higher voltage, because the high voltage may dissolve the core. After conditioning, 6 cyclic voltammetry scans from -0.259 V to 0.716 V at 0.02 V/s scan rate without rotation were performed to calculate the Hupd surface area. The voltammetry scans were shown in Figure S4-11.
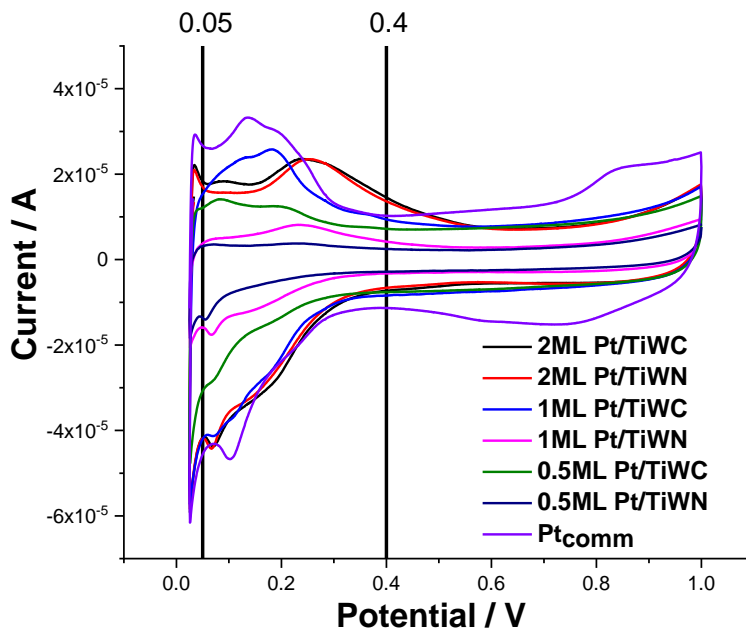
Figure S4-36. One-cycle of Cyclic Voltammetry (CV) Curve.
The area was integrated from 0.05 V to 0.4 V.

After obtaining the data, the area was integrated from 0.05 V to 0.4 V. The CV curve was the lower bound and the horizontal line passing the 0.4 V CV curve value was the upper bound. The mathematical meaning of the area was shown in the following equation.

$$Area = IV = \frac{QV}{t}$$

Equation S4-25

The area divided by the scan rate provided the total charge transferred. In order to convert the charge into a mole basis, the total charge transferred was divided by F, Faraday's constant.

$$\text{Total Charge Transfer} = \frac{Area}{ScanRate} = \frac{QV}{t} / \frac{V}{t}$$

Equation S4-26

$$\text{Mole Basis} = \frac{\text{Total Charge Transfer}}{F}$$

Equation S4-27

Chemisorption measurements

Autosorb iQ from the Quantachrome Instruments was used to measure the number of active sites for the Pt_{comm} particles. ~500 mg of 5wt% Pt_{comm} was loaded in the chemisorption cell and the cell was then loaded onto the instrument. The sample was heated at 2 K/min to 393 K under He flow and kept at 393 K for 1 h to remove moisture. After 1 h, the gas flow was switched to hydrogen and the temperature was ramped to 473 K with at a rate of 2 K/min. The sample was kept at 473 K for 2 h to fully reduce the catalyst. After reduction, the gas flow was switched back to He for 2 h followed by evacuation for 2 h while the temperature was maintained at 473 K. The sample was then cooled to 313 K for CO chemisorption. The Pt_{comm} sample measurement was made in triplicate.

The Pt_{comm} nanoparticle site number was measured both by the standard chemisorption method and the electrochemical Hupd peak integration method. The two methods have demonstrated nearly the same number of sites for Pt_{comm}, with only a 3.5% difference. The site number of the core-shell particles was only measured by the Hupd peak integration method due to the small quantities synthesized each batch.

Microcalorimetry

The uptake and heat of adsorption were measured in a combined breakthrough reactor (BTR) -differential scanning calorimetry (DSC)-mass spectrometer (MS) instrument, as shown in Figure S4-12. The DSC controlled the temperature of the catalyst bed and recorded transient heat flow, while the MS measured the concentration of the effluent gas. Catalysts were placed between two pieces of quartz wool in a quartz tube (1/4" O.D.), which were aligned with the thermopile zone of the DSC. An identical piece of quartz tubing was inserted into the reference side of the DSC. The system was purged under H_2 flow (H_2, line 2, mode A) at 30 cc/min for 20 min, followed by heating to 473 K at a ramp rate of 2 K/min and finally soaked for 2 h. The catalyst was purged with He (He, line 2, mode B) for another 4 h to remove H_2 to avoid hydrogenation of the

hydrocarbon gases (C_2H_4 or C_2H_2). The BTR was then cooled down and stabilized at 298 K before beginning the adsorption measurement.

Hydrocarbon, Ar and He were used in the adsorption process, which was conducted in pulse mode (line 1). The diluted hydrocarbon (3.59% C_2H_4 in Ar, 1.01% for C_2H_2 prediluted in He) passed through a 50 μL sample loop (line 1, mode B). For each pulse, the 10-way valve switched to mode A and He carries the dilute hydrocarbon gas within the sample loop to the BTR. After 2 min, the valve switched back to mode B and the CH filled the sample loop again for the next pulse. During the injection of hydrocarbon/Ar into the catalyst bed, C_2H_2 or C_2H_4 was captured while the Ar immediately breaks through. Simultaneously, the DSC records the heat flow due to the adsorption of the hydrocarbon. There was a 30 min interval between two consecutive pulses to allow enough time for complete adsorption and heat transfer. Catalyst samples typically saturated after a few pulses, indicated by a saturation of the hydrocarbon signal on the MS. For each pulse, the quantity of adsorbed hydrocarbon was calculated from the integration of the MS signal and the ideal gas law, and the exothermic heat released during each pulse was determined by integration of the corresponding DSC peak. The heat of adsorption was then the exothermic heat divided by the uptake.

Hydrocarbon content in each pulse was shown as follow:

$$q_{pulse} = \gamma \frac{PV}{RT} \hspace{4cm} \text{Equation S4-28}$$

where $P = 1$ atm, V is the volume of the sample loop (50 μL), R is the ideal gas constant, T is the temperature (298 K) and γ is the hydrocarbon mole fraction.

Hydrocarbon uptake during each pulse was shown below:

$$q_{uptake,i} = q_{pulse} \frac{A_{max} - A_i}{A_{max}} \hspace{3cm} \text{Equation S4-29}$$

where A_i is the area integration of the ith hydrocarbon peak on the MS signal and A_{max} is the averaged area of the hydrocarbon peaks after saturation (all hydrocarbon enters the MS).

Exothermic heat during each pulse was shown as follow:

$$Q_i = \int_{t_i}^{t_{i+1}} q(t)\, dt$$

The heat of adsorption (ΔH_i) during each pulse was shown below:

$$\Delta H_i = \frac{Q_i}{q_{uptake,i}}$$
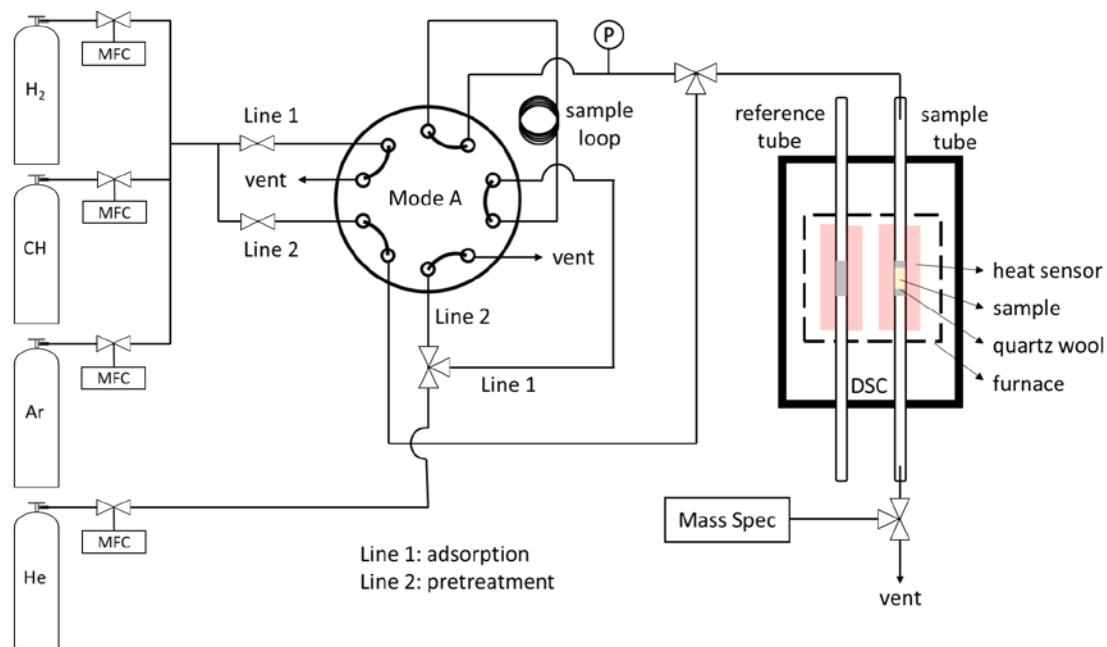
Figure S4-37. Schematic of the combined BTR-DSC-MS instrument.

Line 2 was used for H_2 pretreatment/He purging and line 1 was used for adsorption measurement. The 10-way valve as shown in the schematic is placed in mode A, while in mode B the valve rotates so each port connects to the other neighboring port. During each pulse, the CH (CH = C_2H_2 or C_2H_4)/Ar filled the sample loop in mode B, while He carries the CH/Ar in the sample loop when the valve switched back to mode A.

Density Functional Theory Calculation (DFT)

Electronic structure methods

Electronic structure calculations were performed using the Vienna ab initio simulation package (VASP) [158] The projector augmented-wave (PAW) method was used to represent the ion-core electron interactions [197]. The valence electrons were represented with a plane wave basis set with an energy cutoff of 500 eV. Nonlocal gradient corrections to the total energy were calculated using the Perdew-Burke-Ernzerhof revised for solid (PBE sol) exchange correlation functional [198]. The $4 \times 4 \times 1$ Gamma scheme was used to generate the k-point grid [206]. The structural convergence criteria were 0.05 eV Å^{-1} for all unconstrained atoms. The transition states were obtained using the climbing image nudged elastic band (CI-NEB) method by relaxing the absolute reaction tangent force below 0.05 eV/Å [207].

Adsorption energies were calculated as:

$$\Delta E_{ads} = E_{tot} - E_{sur} - E_{mol}$$ **Equation S4-32**

where E_{tot}, E_{sur} and E_{mol} indicate total energy of molecules on surfaces, the energy of bare surfaces and energy of the molecule in a vacuum, respectively.

Reaction energies ΔE_{rxn} and activation barriers ΔE_{act} were defined as the following equations

$$\Delta E_{rxn} = E_{final} - E_{initial}$$ **Equation S4-33**

where E_{final} represents the final state energy and $E_{initial}$ is the initial state energy

$$\Delta E_{act} = E_{TS} - E_{initial}$$ **Equation S4-34**

where E_{TS} means energy of transition state.

$Ti_{0.1}W_{0.9}C$ and $Ti_{0.1}W_{0.9}N_{0.5}$ surface slab

WC and W_2N bulk were built based on experimental pdf data. W_2N has the same bulk structure as WC, with half of the nitrogen atoms in WN bulk randomly deleted. After a (111) surface was cleaved from the bulk, 10% of W atoms were randomly selected to be

replaced with Ti. $Ti_{0.1}W_{0.9}C$ and $Ti_{0.1}W_{0.9}N_{0.5}$ surface slabs were then obtained by expansion to a 2 x 2 x 1 supercell with 20 Å vacuum layer. W terminated surface slabs were used to bind to the Pt top layer, which has been proved more stable when Pt atoms are adsorbed and have been applied in previous studies [208-210].

HQE process

Temperature-independent DFT models, which were applied by other researchers to construct 1ML of Pt on a WC substrate [208-213], fail to capture the surface topology resulting from a high-temperature synthetic process. Hendon et al. demonstrated the metastability of conventional 1ML coverage Pt on $Ti_{0.1}W_{0.9}C$ and introduced the Heat, Quench and Exfoliation method (HQE) to recover realistic different coverages of noble metals on $Ti_{0.1}W_{0.9}C$ [150]. Herein, we began with the same procedure and parameters to obtain 1 ML Pt on $Ti_{0.1}W_{0.9}C$ and $Ti_{0.1}W_{0.9}N_{0.5}$. We began with 2MLs of Pt (111) on $Ti_{0.1}W_{0.9}C$ and $Ti_{0.1}W_{0.9}N_{0.5}$ and performed ab initio molecular dynamics, ramping temperature from 0 to 1000 K in 0.2 K per 5 fs time steps. 5 Pt atoms in top layer fell into the second layer in direct contact with the $Ti_{0.1}W_{0.9}C$ substrate, whereas 2MLs (111) Pt on $Ti_{0.1}W_{0.9}N_{0.5}$ showed little perturbation during the heating and quenching process (Figure S4-13d). Exfoliation and optimization were performed to obtain a relaxed surface slab. The HQE process yielded an average Pt-Pt distance of 2.76 Å on $Ti_{0.1}W_{0.9}C$ and 2.98 Å on $Ti_{0.1}W_{0.9}N_{0.5}$, compared to a 2.77 Å distance for a Pt (111) slab. Average Pt-Pt distances of Pt (111) and the HQE derived 1ML Pt/TiWC are in good agreement with Hendon et al. [150]. 1ML of Pt on TiWN showed a lattice expansion experimentally to a 2.77 Å nearest neighbor, a 7.6% mismatch with the results of the HQE process.
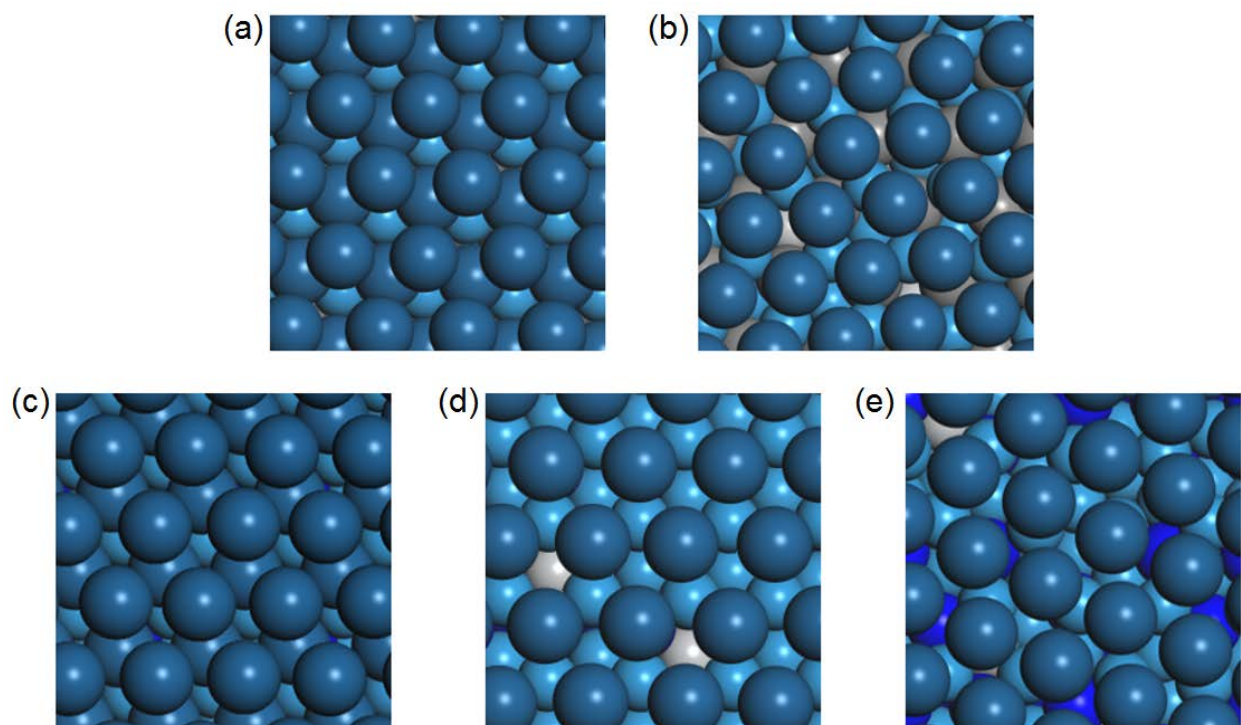
Figure S4-38. Surface configuration of Pt on TiWC and TiWN before and after HQE process.

(a) before HQE process, 2ML Pt (111) on a $Ti_{0.1}W_{0.9}C$ surface slab; (b) after HQE process, true 1 ML Pt on a $Ti_{0.1}W_{0.9}C$ surface slab, with average Pt – Pt distance of 2.76 Å; (c) before HQE process, 2ML Pt (111) on a $Ti_{0.1}W_{0.9}N_{0.5}$ surface slab; (d) after HQE process, 1 ML Pt on a $Ti_{0.1}W_{0.9}N_{0.5}$ surface slab, with average Pt – Pt distance of 2.98 Å; (e) after HQE – H process, true 1 ML Pt on a $Ti_{0.1}W_{0.9}N_{0.5}$ surface slab, with average Pt – Pt distance of 2.71 Å.

Though the HQE process can help to sample structures from 0 K, there is no guarantee that the resultant structure is the global minimum with respect to the number of Pt atoms in the first monolayer. We further ran ab initio molecular dynamic simulations with different numbers of Pt atoms in a single monolayer, ranging from 16-22 on the 2 x 2 TiWC supercell and 16-21 on the 2 x 2 TiWN supercell substrates. The temperature was set as 1000 K and maintained for 800-time steps. A reduced plane-wave basis (400 eV cutoff), and a reduced K points sampling (2 x 2 x 1) were used during ab initio molecular dynamic simulations. Then the final geometries were optimized. We evaluated the surface stability through evaluating the strength of the interaction between Pt and the substrate, which was analyzed with the differential binding energy (DBE) and integral binding energy (IBE) per surface area, as defined in the following equations.

$$DBE = E_{tot,N} - E_{tot,N-1} - E_{Pt,bulk} \qquad \textbf{Equation S4-35}$$

$$IBE = \frac{E_{tot,N} - E_{sub} - N \cdot E_{Pt,bulk}}{S} \qquad \textbf{Equation S4-36}$$

$E_{tot,N}$ and $E_{tot,N-1}$ represent total energies of a surface slab with N and N-1 Pt atoms adsorbed on TiWC or TiWN substrates. $E_{Pt,bulk}$ is the DFT energy of a single bulk Pt atom. E_{sub} is the TiWC or TiWN substrate energy. S is the surface slab area.

As shown in Figure S4-14, for 1ML Pt on TiWC, both IBE and DBE decrease, indicating greater stability as the number of Pt in the monolayer increased to 21. Adding a 22nd Pt atom in the monolayer will cost 2.10 eV energy. Also, the 22nd Pt atom will pop out from the monolayer, indicating 21 Pt atoms is the global minimum and the true monolayer on 2 X 2 $Ti_{0.1}W_{0.9}C$ substrate. As binding energies are referenced to the Pt bulk energy, negative DBE and IBE values suggest Pt - substrate interaction is stronger than the Pt cohesive energy. This suggests 1ML of Pt on the substrate is stable versus Pt agglomeration. Such strong binding of Pt to a WC substrate was reported by Vasic et al [210].

Similarly, for Pt on the TiWN surface slab, both IBE and DBE suggest 19 adsorbed Pt atoms on the 2 x 2 $Ti_{0.1}W_{0.9}N_{0.5}$ to be energetically most favorable, a significantly more dense overlayer than that found through the HQE process with an average Pt-Pt distance of 2.71 Å (Figure S4-13e). The 16 Pt atom layer, found by the HQE process, is a local minimum with respect to the number of Pt atoms.

We considered the formation of a second monolayer on both substrates by adding a second layer conformal to the minimum first monolayer and heating at 1000 K for 800-time steps, followed by DFT optimization. The integral binding energies of the 2nd layer were calculated as

$$IBE^{2nd} = \frac{E_{tot,2ML} - E_{tot,1ML} - N \cdot E_{Pt,bulk}}{S} \qquad \textbf{Equation S4-37}$$

$E_{tot,2ML}$ and $E_{tot,1ML}$ represent total energies of a surface slab with 2ML and 1ML Pt atoms adsorbed on TiWC and TiWN substrates. We found IBE^{2nd} for Pt on TiWC and TiWN are both significantly positive 0.035 eV/Å^2 and 0.016 eV/ Å^2. The 2nd layer is binding much weaklier and more unstable relative to Pt bulk formation on TiWC and TiWN. Therefore,

we can conclude that 1ML Pt atoms can well disperse on the core-shell substrates, while 2nd layer Pt is not stable relative to three-dimensional Pt growth. Herein, we use 1ML Pt/TiWC and 1ML Pt/TiWN DFT model to compare with experimental results.
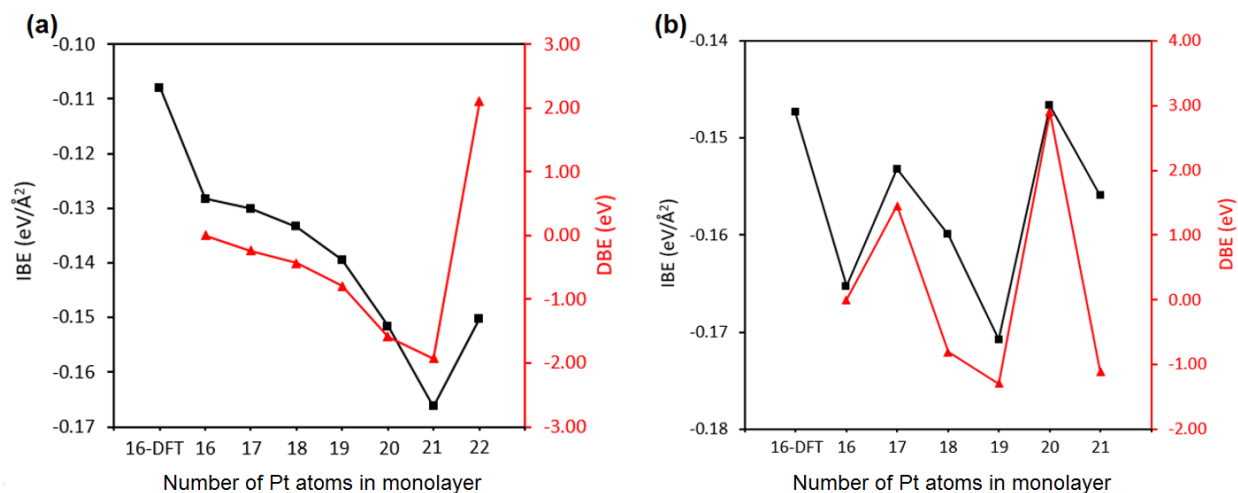
Figure S4-39. Surface Pt and Core Material Binding Energies.

a) Integral binding energy and differential binding energy of 16 – 22 Pt atoms on $Ti_{0.1}W_{0.9}C$; b) Integral binding energy and differential binding energy of 16 – 21 Pt atoms on $Ti_{0.1}W_{0.9}N_{0.5}$. 16 – DFT means 16 Pt atoms in Pt (111) configuration directly optimized by DFT without the HQE process.

C_2H_2 and C_2H_4 adsorption

Both acetylene and ethylene adsorption on Pt (111), 1ML Pt/TiWC, 1ML Pt/TiWN were studied by DFT calculations. As shown in Figure S4-15, because of the unsaturated bond character of acetylene and ethylene carbon atoms, both molecules energetically favor to evolving sp3 character of carbon atoms, resulting in acetylene adopting a hollow site with adsorption energy -2.09 eV and ethylene adsorbing at a bridge site with -1.22 eV binding strength on the Pt(111) surface. Such results agree with previous theoretical calculations [214-216] and our micro-calorimetry results. On the Pt core-shell surfaces, each Pt atoms is still six coordinated in the same layer, which will result in similar adsorption configurations of acetylene and ethylene. However, unlike Pt (111) there is no uniform alignment

between the monolayer Pt atoms and the substrate Ti, W, C, or N atoms. Thus, the substrate electronic effect on each Pt atom varies depending on the Pt position, which can be reflected from the d band center of each surface Pt atom as shown in Table S4-7. We selected several hollow and bridge sites for acetylene binding, and atop and bridge sites for ethylene adsorption. The adsorption energies can be found in Table S4-6. Figure S4-15 shows the most stable adsorption configuration from our calculations. It is clear that both acetylene and ethylene adsorption were significantly weakened compared with adsorption to Pt (111). As the Pt monolayers are compressed compared with Pt (111), the interaction between adsorbate and the Pt layer was weakened. Additionally, the interaction between the Pt monolayer and substrate caused significant d-band center down-shift compared with Pt (111). Downshift of the d-band center was shown to weaken the interaction between adsorbate and surface atoms [24, 217].
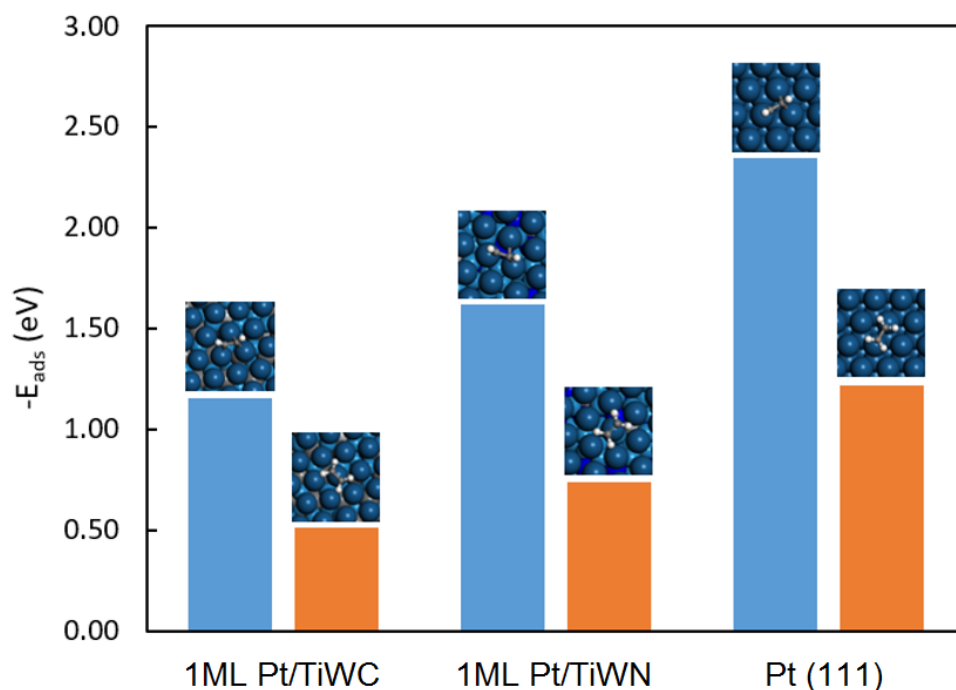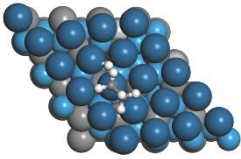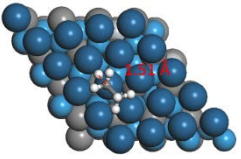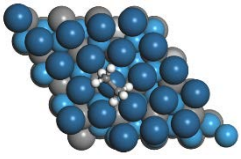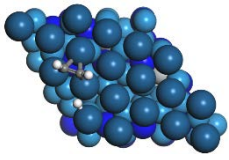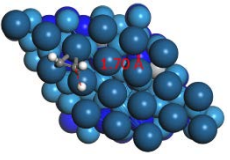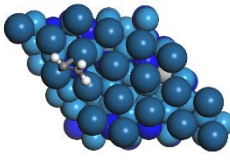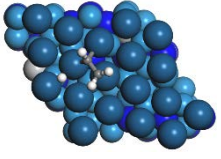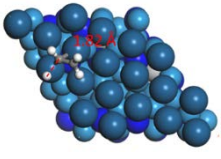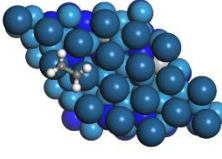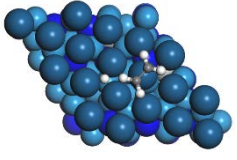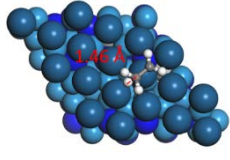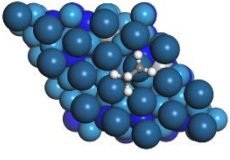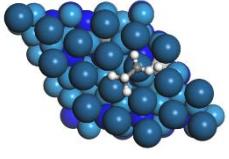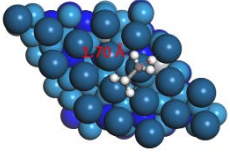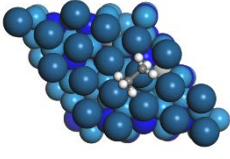
Figure S4-40. Acetylene and Ethylene Adsorption Configuration and Adsorption Energies on 1ML Pt/TiWC, 1ML Pt/TiWN and Pt (111) Surfaces.

Table S4-31. Initial, transition, and final states located by DFT for acetylene and ethylene hydrogenation on Pt (111), Pt/TiWC, and Pt/TiWN surfaces.

Catalysts	Elementary step	Reaction state		
		Initial State	Transition State	Final State
Pt(111)	$C_2H_2 + H = C_2H_3$			
	$C_2H_3 + H = C_2H_4$			
	$C_2H_4 + H = C_2H_5$			
	$C_2H_5 + H = C_2H_6$			
Pt/TiWC	$C_2H_2 + H = C_2H_3$			
	$C_2H_3 + H = C_2H_4$			
	$C_2H_4 + H = C_2H_5$			

Catalysts	Elementary step	Reaction state		
		Initial State	Transition State	Final State
Pt/TiWC	$C_2H_5 + H = C_2H_6$			
Pt/TiWN	$C_2H_2 + H = C_2H_3$			
	$C_2H_3 + H = C_2H_4$			
	$C_2H_4 + H = C_2H_5$			
	$C_2H_5 + H = C_2H_6$			

Table S4-13 Continue Initial, transition, and final states located by DFT for acetylene and ethylene hydrogenation on Pt (111), Pt/TiWC, and Pt/TiWN surfaces.

CHAPTER 5 PLATINUM/TANTALUM CARBIDE NANOPARTICLES WITH SUB-MONOLAYER SHELLS FOR METHANOL AND OXYGEN ELECTROCATALYSIS

Core-shell architectures provide opportunities to improve catalytic activities and economic feasibility of noble metal catalysts, but stability issues of core-shell materials are yet to be fully addressed in electrochemical systems. Herein, we demonstrate Pt/TaC nanoparticles as highly durable electrocatalysts for methanol oxidation and oxygen reduction, which are key reactions in direct methanol fuel cells. Owing to the oxide passivation layer with excellent stability, TaC hardly showed any sign of dissolution in fuel cell operating conditions. This enabled application of partially covered Pt/TaC nanoparticles in aqueous electrocatalysis. Participation of surface-oxidized TaC in methanol oxidation reaction resulted in significantly enhanced catalytic activities as compared to that of conventional Pt nanoparticles. The increased methanol-managing capability further led to a substantial advance in oxygen reduction performance under the presence of methanol. These results not only verify the high feasibility of Pt/TaC nanoparticles in direct methanol fuel cells but also open up opportunities to tailor catalytic properties of core-shell nanoparticles by using stable core materials that can take part in electrocatalysis and possibly modify reaction kinetics.

Introduction

Direct methanol fuel cells (DMFCs), which are operated based on methanol oxidation reaction (MOR) in anode and oxygen reduction reaction (ORR) in cathode, have been regarded as a potential power source for portable electronic devices as methanol has high energy density and is easy to store and carry.[218-220] However, sluggish kinetics of MOR and ORR are limiting the overall cell performance, while the use of platinum catalysts in both electrodes is inevitable to obtain reasonably high performances in actual devices.[219, 221-223] Therefore, enhancements in electrocatalysts, in terms of both activity and economic feasibility, are necessary for practical applications of DMFCs. Pt/transition metal carbide (TMC) core-shell nanoparticles pioneered by our group meet these

requirements, and in particular, Pt/Ti-doped WC (TiWC) catalysts manifested superior performances in MOR and ORR when compared with those of conventional Pt nanoparticles.[4, 6] Meanwhile, we recently uncovered that TiWC rapidly dissolves when it is in direct contact with an acidic electrolyte, which is unavoidable in actual DMFC operation conditions.[4]

Chemical stabilities of various TMCs have been comprehensively studied by Chen and co-workers, who verified that durability of TMCs depends on that of oxide passivation layer on the surface.[111, 224] Therefore, TMCs with parent metal that can strongly bind to oxygen are generally stable. On the other hand, because thermal carburization of oxide-based precursors is an essential step for the synthesis of TMC-based nanoparticles, strong interaction between transition metal and oxygen is unfavorable in terms of experimental feasibility. Among various transition metal carbides that are stable in acids, such as titanium, tantalum, and zirconium carbides,[225-226] tantalum carbide has relatively small oxygen binding energy while it shows a similar level of chemical stability in acid as the others.[111] Based on these understandings, it is expected that tantalum carbide is a suitable core material for Pt/TMC nanoparticles, satisfying both viability for synthesis and stability in acidic environments.

In this study, Pt/TaC core-shell nanoparticles wer synthesized for the first time and were applied as highly active and stable electrocatalysts for both MOR and ORR, targeting their potential applications in DMFCs. Synthesis of these core-shell nanoparticles was carried out by high-temperature self-assembly method developed by our group,[6] which enables atomically thin Pt monolayers (MLs) to cover nanosized TaC particles. Pt/TaC catalysts with sub-ML shell manifested superior activity in MOR compared to that of bare Pt by bifunctional effect between core and shell. In addition, Pt/TaC nanoparticles showed significantly higher ORR performance under the presence of methanol, which represents the realistic condition of DMFC cathode. Furthermore, the stability of Pt/TaC in electrochemical operation conditions was thoroughly investigated and verified by diverse analytical techniques.

Results and Discussion

Syntheses and Characterizations of Pt/TaC Nanoparticles. Procedures for the synthesis of Pt/TaC core-shell nanoparticles via high-temperature self-assembly method were summarized as a scheme in Figure 5-1. Firstly, TaO_x nanoparticles were prepared in reverse microemulsion and Pt precursor was added in a separate smaller reverse microemulsion batch serving as the shell component. Then the particles were encapsulated with silica shells and underwent thermal carburization at 970 °C in a tube furnace filled with a mixture gas of 80% H_2 and 20% CH_4, for reduction and carburization of TaO_x, respectively. In general, fully carburization of TaO_x take place when the temperature is higher than 1200°C,[116] but we could perform the carburization at a milder condition as Pt facilitates the decomposition of CH_4, which serves as the carbon source.[101-102] Pt/TaC nanoparticles were obtained by dissolving silica shell using ethanol solution containing HF and were dispersed onto carbon black supports for applications in electrocatalysis. Pt/TaC nanoparticles with four different shell thicknesses were prepared by using different amounts of Pt precursors. We used commercial carbon-supported Pt nanoparticles (20 wt.%, Premetek), which are hereafter denoted as Pt_{comm}, for comparative investigations.
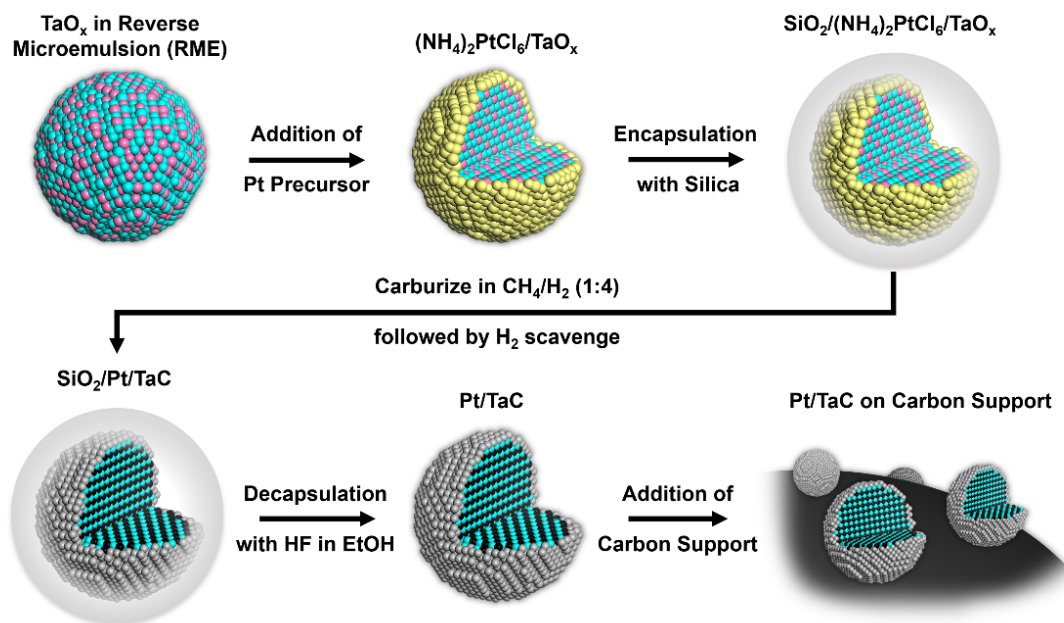
Figure 5-41. Schematic overview of synthetic procedures for carbon-supported Pt/TaC core-shell nanoparticles.
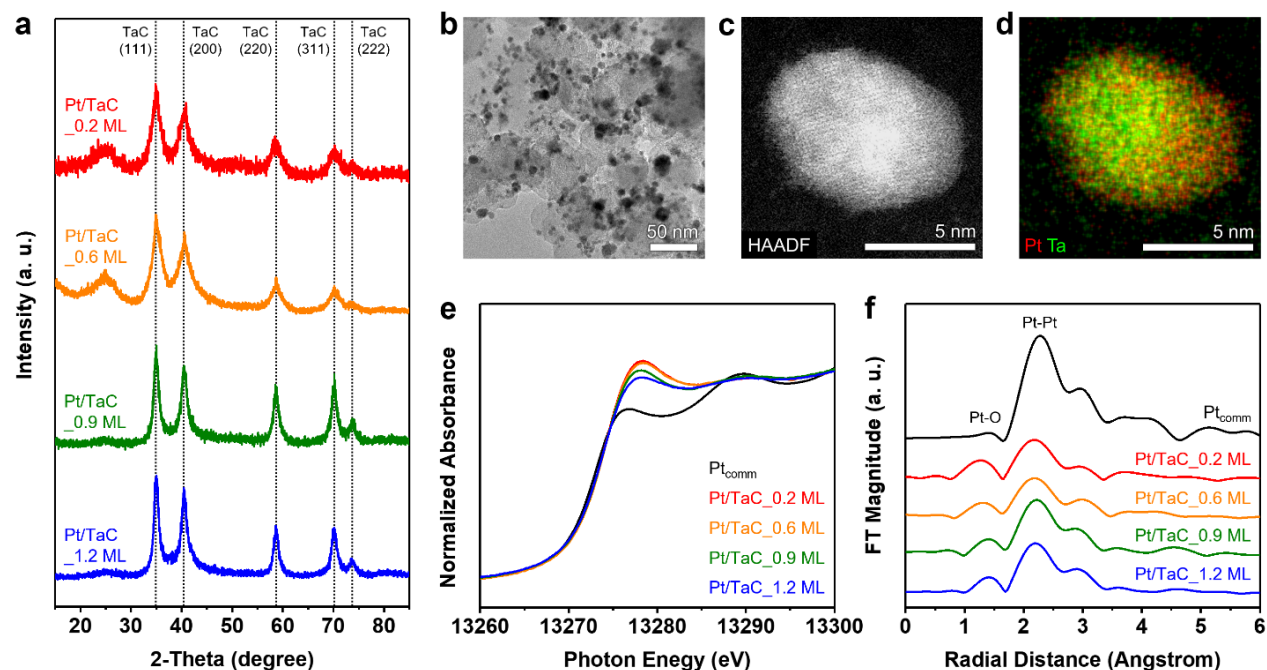
Figure 5-42. Characterization of Pt/TaC core-shell nanoparticles.

(a) PXRD patterns of Pt/TaC core-shell nanoparticles with various shell thicknesses. (b) Low-magnification TEM image of Pt/TaC_0.6 ML. (c) High-magnification STEM image of Pt/TaC_0.6 obtained by using a high-angle annular dark-field (HAADF) detector and (d) corresponding elemental map showing the locations of Pt and Ta atoms. (e) XANES and (f) k^3-weighted Fourier transform of EXAFS spectra of Pt_{comm} and Pt/TaC nanoparticles acquired at Pt L_2-edge.

From the powder X-ray diffraction (PXRD) patterns of Pt/TaC core-shell particles displayed in Figure 5-2a, signals from phase-pure cubic TaC (PDF no. 00-035-0801) were clearly observable while reflections from Pt were not projecting out. From the crystallite sizes calculated from PXRD patterns and Pt:Ta ratio obtained from inductively coupled plasma-mass spectroscopy (ICP-MS), Pt shell thicknesses of the synthesized nanoparticles were estimated as 0.2, 0.6, 0.9, and 1.2 ML, and the Pt/TaC nanoparticles were respectively named as Pt/TaC_0.2 ML, Pt/TaC_0.6 ML, Pt/TaC_0.9 ML, and Pt/TaC_1.2 ML. Morphologies of Pt/TaC were characterized by transmission electron microscopy (TEM) analysis, which clearly showed carbon-supported nanoparticles of around 5-20 nm (Figure 5-2b and Figure S5-1). In addition, the formation of core-shell configuration was confirmed by aberration-corrected scanning transmission electron microscopy (STEM) and corresponding elemental mapping acquired by energy-dispersive X-ray spectroscopy (EDX) displayed in Figure 5-2c and d, respectively.

Influences of TaC core to Pt shell electronic structures with diverse thicknesses were then investigated by using various X-ray techniques. Figure 5-2e shows X-ray absorption near edge structure (XANES) spectra of Pt_{comm} and Pt/TaC nanoparticles obtained at Pt L_2-edge. Though XANES at Pt L_3-edge is mostly measured as it gives a large amount of information on the 5d states, L_2-edge was selected because Ta L_1- and L_2-edges are located close to Pt L_3-edge; however, it is clear from diverse literatures that XANES obtained at Pt L_2-edge represents the trend of electronic structures reasonably well.[77, 227-228] It was noteworthy that the white line intensity was significantly larger in Pt/TaC as compared to that of Pt_{comm}, and it became larger as the thickness of the shell in Pt/TaC was smaller. We thoroughly discussed in a previous report that white line intensity gives information on the trend of Pt valence d-bandwidth in Pt/TMC core-shell nanoparticles when coupling matrix element of TMC's parent metal is larger than that of Pt.[99] According to the work by Hammer and Nørskov, Ta has larger coupling matrix element than Pt, and this leads to broadening of Pt d-band when the Pt and Ta hybridization takes place.[229-230] Therefore, we could expect the downshift of Pt d-band center with regard to the Fermi level, given that the d-band filling should be conserved. We cross-checked this trend by X-ray photoelectron spectroscopy (XPS) analysis, from which larger degree of positive shift of Pt 4f spectra with regard to smaller shell thickness was observed (Figure S5-2). The trend in the surface coverage of TaC core with Pt was indirectly characterized by comparing the signals from oxide and carbide in XPS Ta 4f spectra (Figure S5-3), for TaC regionally covered with Pt shell is less likely to form a native oxide layer. In order to investigate geometric characteristics of Pt shell on TaC core, extended X-ray absorption fine structure (EXAFS) analysis was carried out (Figure 5-2f). From the peaks located within the radial distance of 2 to 2.5 Å, we could notice that Pt-Pt distance in Pt/TaC was slightly smaller than that in Pt_{comm}. This was counterintuitive as the lattice parameter of face-centered cubic (fcc) Pt (0.39 nm) is smaller than that of TaC (0.44 nm), but our observation was still attributable to the different crystal structure of fcc Pt and cubic TaC. The slight decrease in Pt-Pt distance and corresponding compressive strain induced by the presence of TaC core was expected to increase the overlap between the d-orbitals of Pt and Ta, resulting in a more significant Pt d-band broadening and downshift of the d-band center. [63, 231-232]
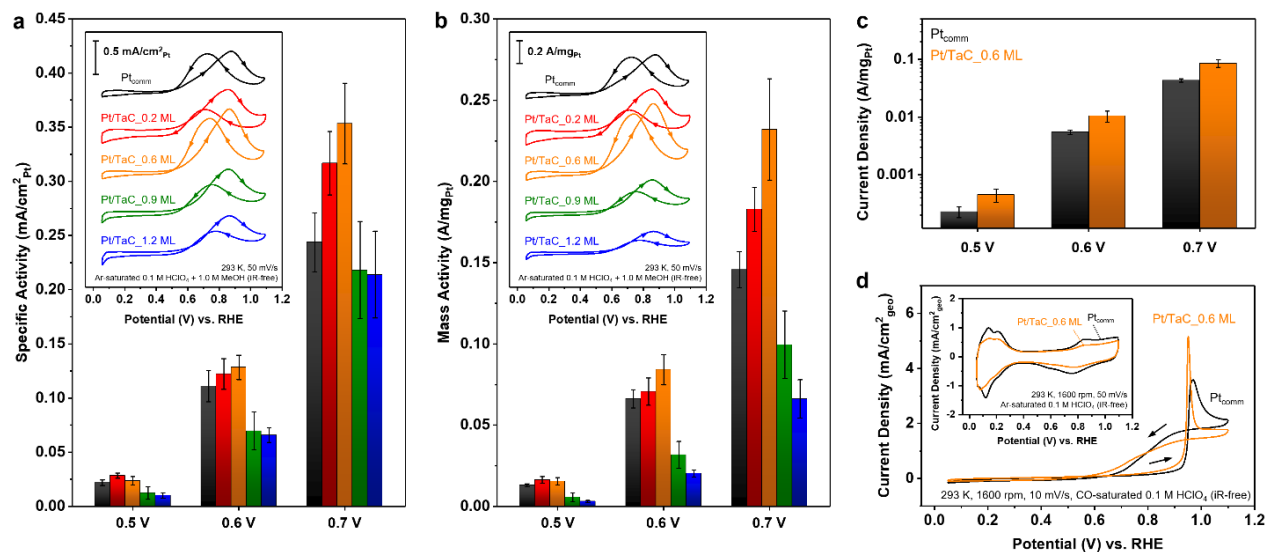
Figure 5-43. MOR electrocatalytic performance and CO bulk oxidation.

(a) specific and (b) mass MOR activities of Pt_{comm} and Pt/TaC core-shell nanoparticles obtained by MOR CV results displayed in the insets. (c) Summary of mass MOR activities of Pt_{comm} and Pt/TaC_0.6 ML from steady-state measurements at various potentials. (d) CO bulk oxidation characteristics of Pt_{comm} and Pt/TaC_0.6 ML; the inset shows CV diagrams measured without the presence of CO.

Methanol Oxidation Characteristics of Pt/TaC. Considering the potential application of Pt/TaC in anode of DMFCs, MOR performances were first characterized by cyclic voltammetry (CV) measurements in 0.1 M $HClO_4$ electrolyte containing 1.0 M methanol (insets of Figure 5-3a and b). We selected current densities at 0.5, 0.6, and 0.7 V vs. reversible hydrogen electrode (RHE; all of the electrochemical potentials are hereafter noted with regard to RHE, otherwise stated) to compare the activities, because removal of capacitive currents (by subtracting currents obtained without methanol in the electrolyte) was not viable in a potential range below 0.45 V; strong adsorption of reaction intermediates (dehydrogenated methanol, typically CO) on Pt surface led to significantly different electrochemical responses in hydrogen underpotential deposition (H_{upd}) region.[23, 232-233] Figure 5-3a and b show specific and mass activities of Pt_{comm} and Pt/TaC nanoparticles in MOR. It was noteworthy that Pt/TaC with relatively thin (0.2 ML and 0.6 ML) shell manifested higher MOR activities as compared to Pt_{comm}, while those with 0.9 ML and 1.2 ML-thick shells were inferior in performances. In 0.5 V, Pt/TaC_0.2 ML was most active, but Pt/TaC_0.6 ML had superior activity at higher potentials. Since

interferences from capacitive currents would be larger when the overall current density is smaller (i.e. at lower potentials), we selected Pt/TaC_0.6 ML as the best-performing catalysts and used it for further investigations. We additionally carried out chronoamperometry of Pt_{comm} and Pt/TaC_0.6 ML catalysts at 0.5, 0.6, and 0.7 V (Figure S5-4a and b), given that actual fuel cell devices are operated at steady-state conditions. Specific and mass activities were calculated using the current density at 10 min, and they are displayed in Figure S5-4c and Figure 5-3c, respectively. Even under steady-state operations, Pt/TaC_0.6 ML clearly manifested higher MOR activities, from which advantage of Pt/TaC core-shell nanoparticles over Pt_{comm} could be confirmed.

We then explored the origin of high MOR activity of Pt/TaC catalysts. It is known that MOR proceeds by dehydrogenation of methanol followed by CO oxidation;[234] in general, CO oxidation step is understood as the rate-limiting step on Pt surface.[235] Figure 5-3d shows CO bulk oxidation characteristics of Pt_{comm} and Pt/TaC_0.6 ML measured in CO-saturated 0.1 M $HClO_4$ electrolyte. CO oxidation on Pt/TaC_0.6 ML surface took place at earlier potential relative to that on Pt_{comm}, indicating that Pt/TaC is more capable of removing CO poisoning. In general, CO oxidation on Pt takes place by reacting with -OH group adsorbed on the surface of Pt via Langmuir-Hinshelwood mechanism, and -OH formation step limits the rate of whole CO oxidation.[236] The inset of Figure 5-3d shows the CV curves of Pt_{comm} and Pt/TaC_0.6 ML measured in Ar-saturated 0.1 M $HClO_4$ electrolyte, from which negligible difference of -OH formation property between Pt_{comm} and Pt/TaC could be observed. From these results, change in CO adsorption characteristic by the presence of TaC core could be regarded as the reason for superior MOR performance in Pt/TaC nanocatalysts; electronic interaction between TaC core and Pt shell, which presumably leads to the downshift of Pt d-band center, may lead to reduced CO adsorption strength on Pt surface and enhance the overall CO oxidation performance. We additionally obtained CO stripping results of Pt_{comm} and Pt/TaC_0.6 ML and cross-checked that Pt/TaC has a superior capability to deal with CO poisoning (Figure S5-5).

On the other hand, it was noteworthy that specific MOR activities of Pt/TaC nanoparticles with near-complete coverage of shells (0.9 ML and 1.2 ML) were similar, while both were lower than that of Pt_{comm} (Figure 5-3a). These observations show that

electronic interaction between TaC core and Pt shell alone cannot lead to an enhanced MOR performance. This implies that TaC core actively participates in the reaction, and TaC surface exposed to the electrolyte is playing a critical role in enhancing MOR activities. In MOR potential region, oxide passivation layer forms spontaneously on the surface of TaC core,[111] making the surface rich with -OH groups. In Pt/TaC with the shell thickness significantly smaller than 1 ML, CO oxidation can be facilitated by bifunctional effect[23, 237] at borders between Pt and TaC on the catalyst surface, where the reaction between -CO on Pt and -OH on passivated TaC may take place (Figure S5-6). This also matches well with the narrow CO bulk oxidation peak of Pt/TaC_0.6 relative to that of Pt_{comm}; CO oxidation potential is dependent to facets and coordination environment in Pt_{comm},[238-239] and surface border between Pt and TaC gives relatively uniform environment for CO oxidation reaction. Meanwhile, when the coverage of shell in Pt/TaC nanoparticles are close to or more than 1 ML, influence of bifunctional effect by -OH on the exposed TaC surface is not significant. However, oxidation of TaC could still occur to some extent through pinholes in Pt shell, which is analogous to our previous observations from Pt/TiWC[99] and XPS results showing the presence of native TaO_x even when the thickness of Pt shell is 1.2 ML (Figure S5-3). The oxide layer that forms between TaC and Pt decreases the overall electrical conductivity of the catalysts, which leads to the drop of electrocatalytic activities. This seems to be the origin of low MOR performances of Pt/TaC_0.9 ML and Pt/TaC_1.2 ML.
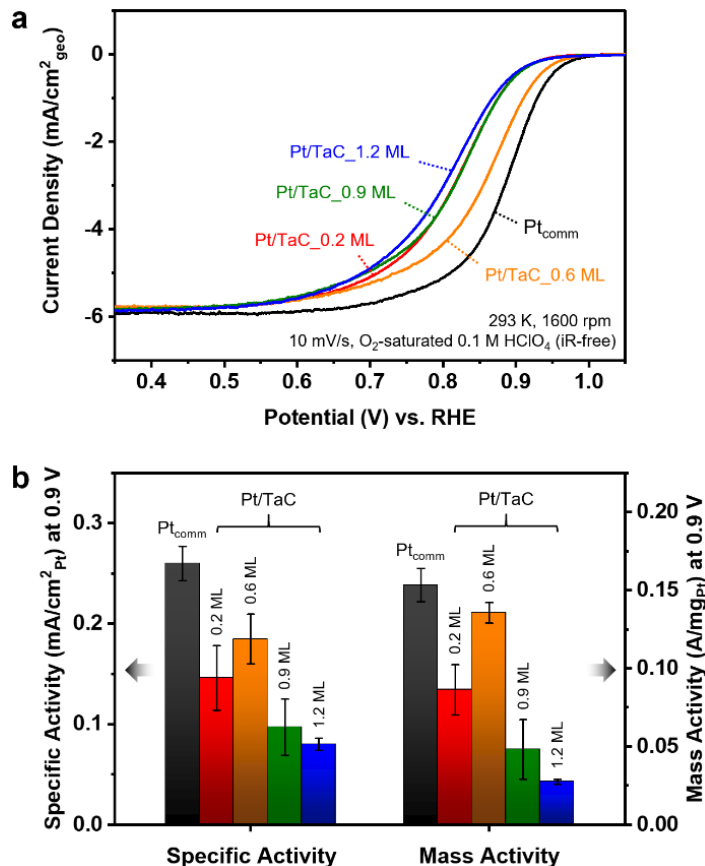
Figure 5-44. Pt$_{comm}$ and Pt/TaC ORR performance.
(a) ORR polarization curves of Pt$_{comm}$ and Pt/TaC core-shell nanoparticles with various shell thicknesses. (b) Electrocatalytic specific and mass ORR activities of Pt$_{comm}$ and Pt/TaC core-shell nanoparticles at 0.9 V.

Oxygen Reduction Characteristics and Electrochemical Stability of Pt/TaC. We then evaluated the feasibility of Pt/TaC nanoparticles in DMFC cathodes by measuring their ORR activities. Figure 5-4a shows the ORR polarization curves of Pt$_{comm}$ and Pt/TaC core-shell nanoparticles with diverse shell thicknesses. Specific and mass activities were calculated at 0.9 V by obtaining kinetic current density using the following Koutecky-Levich equation:

$$1/j = 1/j_L + 1/j_K \qquad \text{Equation 5-38}$$

where j is experimentally observed current density, j_L is the limiting current density, and j_K is the kinetic current density.[240] Figure 5-4b shows a summary of calculated activities.

148

It was notable that Pt/TaC core-shell nanoparticles were not as active as Pt_{comm} in ORR, even when the current densities were normalized by the mass of Pt. In order to figure out whether the presence of TaC is creating any difference in reaction mechanisms, ORR polarization curves were obtained under various rotation rates (Figure S5-7), and electron transfer numbers of Pt_{comm} and the best-performing Pt/TaC core-shell nanoparticles (Pt/TaC_0.6 ML) were calculated by Koutecky-Levich analysis (Figure S5-8) using the following equations:

$$j_L = B\omega^{1/2}$$ **Equation 5-39**

$$B = 0.62nFC_0(D_{O2})^{2/3}u^{-1/6}$$ **Equation 5-40**

where ω is the rotation speed, n is the number of transferred electrons, F is the Faraday constant.[240-241] C_0 is the O_2 concentration at saturated condition, D_{O2} is the diffusion coefficient of O_2, and u is the kinematic viscosity of the electrolyte. Based on the numbers in previous literatures,[241-242] we obtained identical electron transfer numbers (4.08 electrons) for both Pt_{comm} and Pt/TaC_0.6 ML, from which the lack of changes in reaction mechanisms by TaC core could be corroborated.

It was discussed above that electronic interaction between TaC and Pt leads to the downshift of the Pt d-band center, which is favorable in terms of ORR activity.[229] Among Pt/TaC catalysts, those with thinner shell was expected to have the highest specific activity, as the degree of core-shell interaction would be larger suggested by the XANES and XPS results (Figure 5-2 and Figure S5-2). On the other hand, it should be taken into account that oxidative passivation of TaC core could possibly decrease the conductivity of catalysts and reduce the accessibility of electrons from and to catalytic active sites (i.e. Pt). In this viewpoint, Pt/TaC with larger Pt coverage was expected to show higher performance. From the trend of ORR activities shown in Figure 5-4b, Pt/TaC_0.6 ML seemed to be at the optimum position as it manifested the highest performance among Pt/TaC nanoparticles. However, as mentioned above, Pt/TaC regardless of the shell thickness had inferior specific and mass activities to those of Pt_{comm}, and this was attributable to a higher degree of TaC oxidation as ORR takes place at more oxidative potential compared to MOR.
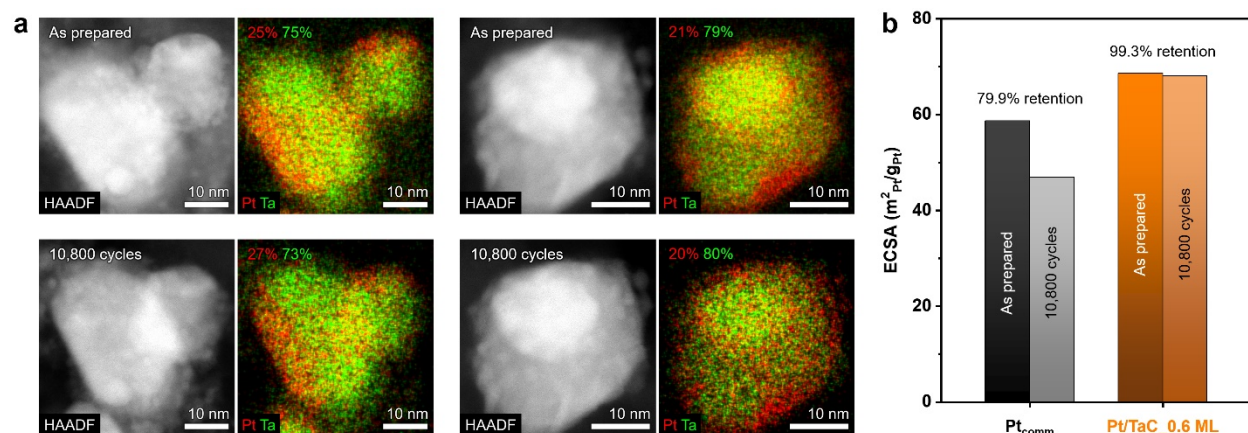
Figure 5-45. Pt/TaC Stability characterization

(a) IL-STEM images and corresponding elemental EDX mapping of Pt/TaC_0.6 before and after 10,800 ADT cycles in 0.1 M HClO₄ electrolyte within potential range of 0.4 to 1.0 V (scan rate: 1.0 V/s). (b) ECSAs of Pt_comm and Pt/TaC_0.6 before and after the ADT.

We then explored the stability of Pt/TaC regarding its applications in DMFC. Since the stability of fuel cell catalysts is mostly challenged by oxidative degradations at high potentials, we carried out various analyses in ORR condition (in 0.1 M HClO₄ electrolyte at potential range of 0.4 to 1.0 V). First, Pt/TaC_0.6 ML was characterized before and after 10,800 potential cycles by using identical location (IL)-STEM techniques with corresponding elemental EDX mappings (Figure 5-5a). It was noteworthy from the STEM images that the changes in the morphologies of non-fully covered core-shell nanoparticles were negligible even after the 10,800 potential cycles which was a great improvement from the previous Pt/TiWC core-shell particles under a similar test condition.[4] Moreover, elemental EDX mapping clearly shows that the locations of Pt and Ta did not change over long-term potential cycles, and the ratio between Pt and Ta were also retained, from which excellent stability of Pt/TaC nanoparticles could be verified. We additionally carried out comparison of stabilities of Pt/TiWC and Pt/TaC by *in situ* inductively coupled plasma-mass spectroscopy (ICP-MS) analyses and cross-checked the high durability of TaC core, as dissolution of Ta was significantly less than that of W by around three orders of magnitude during the potential cycling (Figure S5-9).

To further probe the stability, we also measured the electrochemically active surface area (ECSA) of Pt_{comm} and Pt/TaC nanoparticles before and after the long-term potential cycles (Figure 5-5b and Figure S5-10). Based on the adsorption/desorption charges in H_{upd} region, around 20% drop of ECSA was apparent in Pt_{comm}, while less than 1% decrease was observed from Pt/TaC_0.6 ML. From these results, stability of Pt shell on TaC and overall stability of Pt/TaC nanoparticles were corroborated. Meanwhile, from the CV curves of Pt_{comm} and Pt/TaC_0.6 ML before and after 10,800 potential cycles (Figure S5-10), a noteworthy difference was observable. In the case of Pt_{comm}, currents originating from adsorption and desorption of hydrogen and oxygen species were both dropped in similar ratios. On the other hand, the decrease was only apparent for Pt/TaC_0.6 ML within the potential region related to oxygen species. Moreover, shapes of H_{upd} profiles were changed in Pt/TaC_0.6 ML, which indicated that the rearrangement of Pt atoms on TaC surface took place during the potential cycles. According to the XRD results in Figure 5-2a, TaC core has cubic structure, while Pt forms fcc lattice in general. As Pt favors to form chemical bonds with metals in TMCs rather than carbon and given that there was negligible drop of ECSA (i.e. no agglomeration of Pt atoms), rearrangement of Pt into (100) facet-like arrangement might take place. We observed that decrease of ORR performance after the potential cycles were more significant in Pt/TaC than Pt_{comm} (Figure S5-11), and this could be attributed to the rearrangements of Pt atoms, as Pt (100) surface has lower ORR activity than other common low-index facets such as (111) and (110).[243-244]
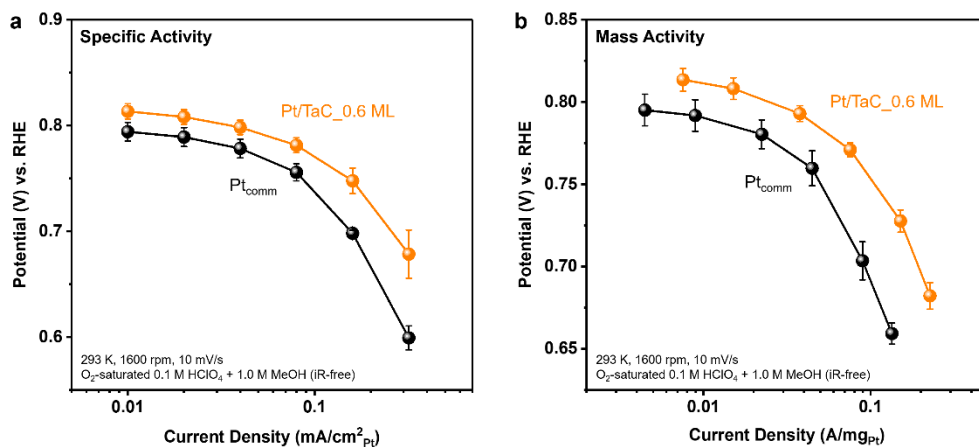
Figure 5-46. Electrocatalytic ORR activities of Pt_{comm} and Pt/TaC_0.6 ML under the presence of methanol (a) specific activities and (b) mass activities.

Oxygen Reduction Characteristics of Pt/TaC under the Presence of Methanol.
Even in most advanced DMFCs to this date, diffusion of methanol from anode to cathode through a proton-conducting membrane (mostly Nafion®) is inevitable.[245-246] This methanol crossover causes MOR to take place in the cathode, which results in mixed cathode potential and CO poisoning that lead to a significant drop of overall cell voltage.[247-248] Therefore, it is important to develop methanol-resistant ORR catalysts for DMFC cathodes; however, Pt-Ru alloy catalysts with state-of-the-art ability to manage methanol and CO are not favorable for ORR as reaction intermediates bind too weakly on its surface.[23, 249-250] Meanwhile, it was clearly observed that Pt/TaC core-shell nanoparticles are capable for the oxidation of methanol and CO owing to bifunctional enhancement at the interface between Pt and surface-oxidized TaC exposed to the electrolyte.

We investigated ORR characteristics of Pt/TaC under the presence of methanol in order to evaluate the feasibility of Pt/TaC as electrocatalysts for DMFC cathodes. Figure S5-12 shows ORR polarization curves of Pt_{comm} and Pt/TaC_0.6 ML measured in O_2-saturated 0.1 M $HClO_4$ containing 1.0 M methanol, with those obtained without methanol for comparisons. Since competition between MOR and ORR at the same catalytic site, we could not calculate activities by removing capacitive currents via subtracting the backgrounds obtained using Ar-saturated electrolyte, where active sites could be solely used for MOR. Therefore, we averaged forward and backward scans of ORR polarization curves and then calculated specific and mass activities, which are summarized in Figure 5-6a and b, respectively. Pt/TaC manifested significantly higher activities as compared to those of Pt_{comm}. This difference could be attributed to higher CO oxidation and MOR performances of Pt/TaC; since the average ratio between methanol and oxygen continuously reaching active sites would be similar in both catalysts, Pt/TaC which can manage methanol in a shorter period of time would be able to reduce larger number of oxygens per active site. As a result, Pt/TaC manifested significantly higher ORR activity than Pt_{comm} under the presence of methanol, and feasibility of Pt/TaC catalysts for both electrodes of DMFC could be clearly verified.

Conclusion

In this study, Pt/TaC core-shell nanoparticles were synthesized and applied as electrocatalysts for DMFCs, wherein MOR and ORR take place. TaC was chosen as a core material due to its high stability, which originates from the inertness of the passivating oxide layer forming on the surface. Pt/TaC nanoparticles with sub-monolayer shell thickness showed superior MOR activity to that of Pt_{comm}, as a result of the bifunctional effect induced by the participation of surface-oxidized TaC in the reaction. In addition, owing to superior MOR characteristics, Pt/TaC manifested significantly higher ORR activity than Pt_{comm} under the presence of methanol, which represents a realistic condition of DMFC cathode. The stability of Pt/TaC in electrochemical condition was also thoroughly investigated based on diverse analytical techniques. In short, the feasibility of Pt/TaC in both electrodes of DMFC could be verified by these results. We believe that Pt/TaC could serve as an early-stage platform for designing stable core-shell nanoparticles for applications in diverse electrochemical and catalytic systems, given their high versatility and wide room for further enhancements by compositional and structural engineering. Furthermore, our study opens up opportunities to tailor the property of core-shell nanoparticles by demonstrating that core materials that are sufficiently stable can take part in catalysis and modify reaction kinetics.

Experimental Section

Synthesis of Pt/TaC Core-Shell Nanoparticles. The detailed steps were described in the end of the supporting information. In general, the Pt/TaC core-shell nanoparticles were synthesized through a reverser microemulsion (RME) method combining with high temperature carburization to convert TaO_x into TaC. Silica encapsulation was emplaced to prevent nanoparticle from sintering through the carburization process. After forming the carbide @ Pt core-shell structure, silica was removed through dissolution process where hydrofluoric acid, diluted with degassed ethanol, was used.

Materials Characterizations. Crystal structure of Pt/TaC catalysts were characterized by PXRD measurements using Bruker D8. A PHI Veraprobe II equipped with an Al-Kα source was used for XPS analyses. ICP-MS measurements for quantification of Pt and Ta contents were performed on an Agilent 7900, and Perkin Elmer NexION 350X was used for the *in situ* analyses. Low-magnification TEM images were obtained with a JEOL 2010F, and IL-STEM analyses and elemental EDX mappings were performed by using FEI Titan 80-200 (ChemiSTEM) equipped with a Cs-corrector (CEOS GmbH). XANES and EXAFS spectra were measured in fluorescence mode at 8-ID (ISS) beamline of National Synchrotron Light Source II (NSLS-II) in Brookhaven National Laboratory.

Electrochemical Analysis. For the electrochemical measurements to evaluate catalytic activities, Pt_{comm} (20 wt% Pt nanoparticles on Vulcan carbon supports, Premetek) and Pt/TaC nanoparticles were dispersed in isopropanol to make catalyst inks, and Nafion was introduced as binders; the mass of added Nafion was approximately 50% that of carbon supports. Then the catalytic inks were drop-casted onto a glassy carbon rotating disk electrode (Pine Instrument), and the loadings characterized by ICP-MS were 22.37 $\mu g/cm^2$ (Pt_{comm}), 5.32 $\mu g/cm^2$ (Pt/TaC_0.2 ML), 13.24 $\mu g/cm^2$ (Pt/TaC_0.6 ML), 12.11 $\mu g/cm^2$ (Pt/TaC_0.9 ML), and 17.67 $\mu g/cm^2$ (Pt/TaC_1.2 ML) and otherwise stated. Electrochemical data were obtained by using a Biologic SP-300 potentiostat and a CH Instruments 627e potentiostat, under a standard three-electrode condition comprised of a Pt wire counter electrode and a Ag/AgCl (sat. KCl) reference electrode. All of the electrodes were pre-cycled in an Ar-saturated 0.1 M $HClO_4$ electrolyte within the potential range of 0.05 to 1.1 V at a scan rate of 100 mV/s to remove organic contaminants from the surface of catalysts. Correction of iR-drop was carried out by using the high-frequency intercept of the Nyquist plot, of which value was around 25 Ω.

Acknowledgements

Supporting Information

Figure S5-47. Low-magnification TEM images of Pt/TaC core-shell nanoparticles

(a) Pt/TaC_0.2 ML, (b) Pt/TaC_0.6 ML, (c) Pt/TaC_0.9 ML, and (d) Pt/TaC_1.2 ML.
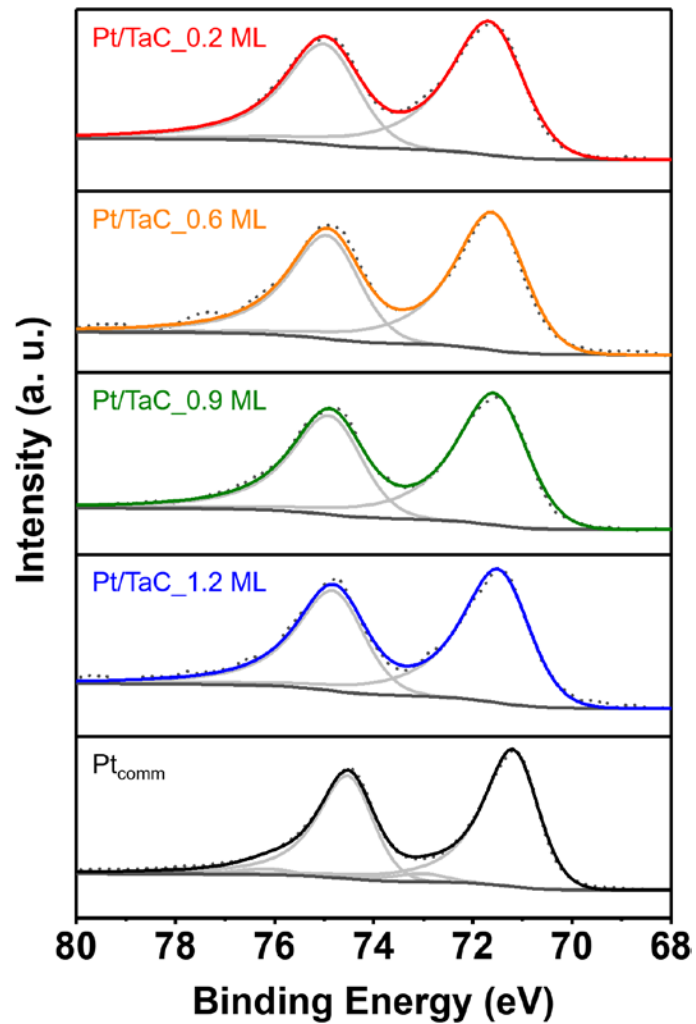
Figure S5-48. XPS Pt 4f spectra of Pt$_{comm}$ and Pt/TaC nanoparticles with various shell thicknesses.
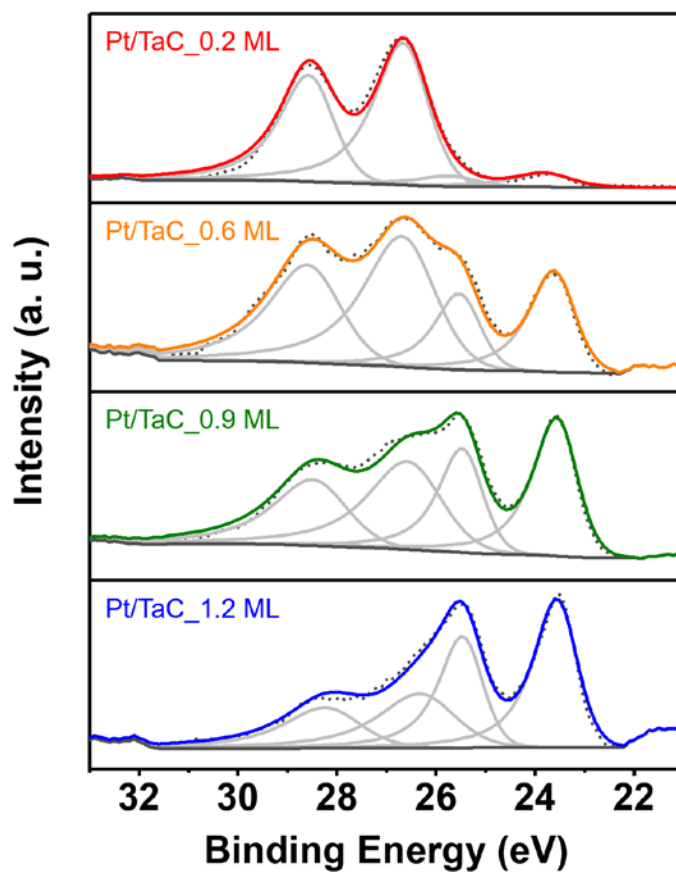
Figure S5-49. XPS Ta 4f spectra of Pt/TaC nanoparticles with various shell thicknesses.

Two peaks on lower binding energy positions are signals from Ta carbide, and those with higher binding energy positions originate from Ta oxide.
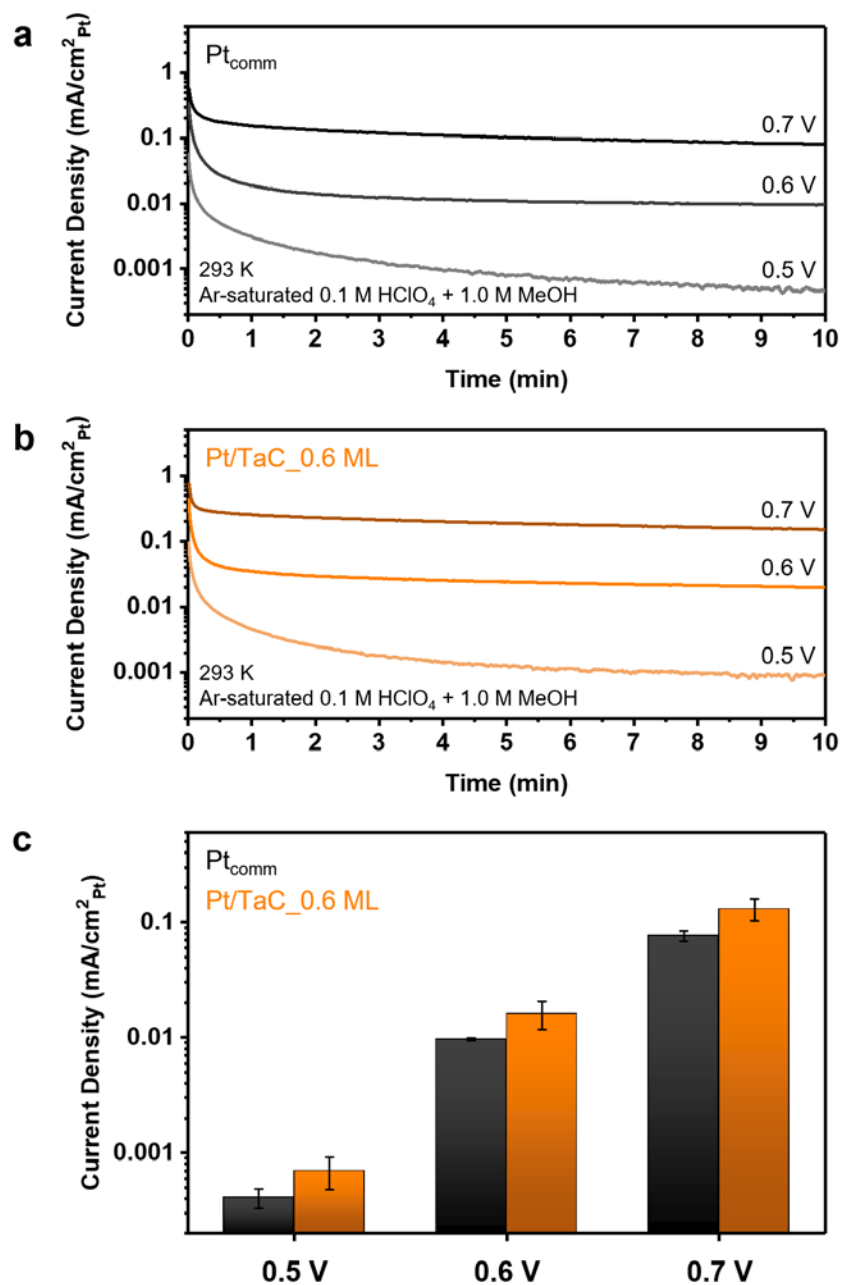
Figure S5-50. Pt$_{comm}$ and Pt/TaC for MOR stability performance

(a,b) ECSA-normalized MOR current densities of (a) Pt$_{comm}$ and (b) Pt/TaC_0.6 ML from steady-state measurement at various potentials. (c) Summary of ECSA-normalized MOR current densities in (a) and (b) at 10 min.
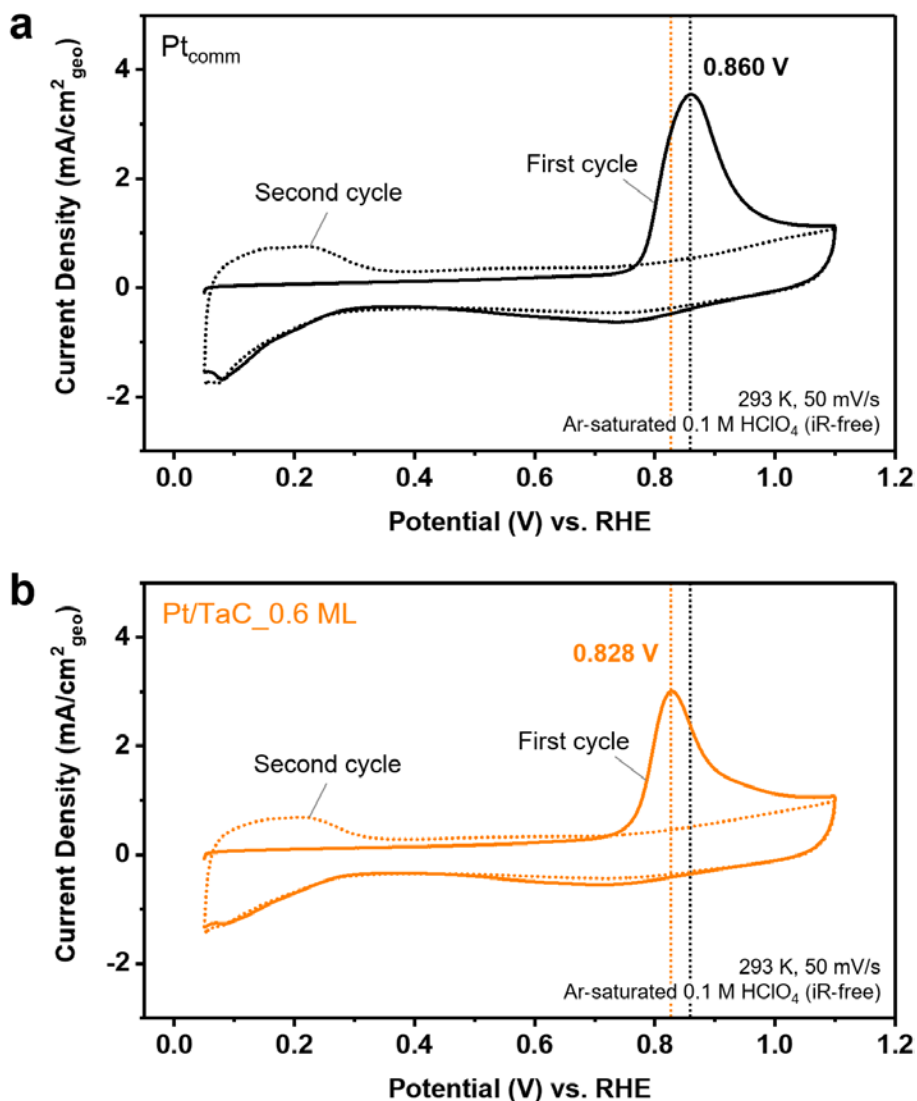
Figure S5-51. CO stripping results

(a) Pt$_{comm}$ and Pt/TaC_0.6 ML obtained after adsorption of CO on the surface. Peak potentials of CO stripping currents were 0.860 and 0.828 V for Pt$_{comm}$ and Pt/TaC_0.6 ML, respectively.

Supporting Note: For the CO stripping measurements, 0.05 V was applied to the catalysts in CO-saturated 0.1 M HClO$_4$ electrolyte for 10 min for adsorption of CO on Pt sites. Then Ar was purged into the electrolyte for 20 min to remove excess CO, and CO stripping currents were acquired in Ar-saturated condition.
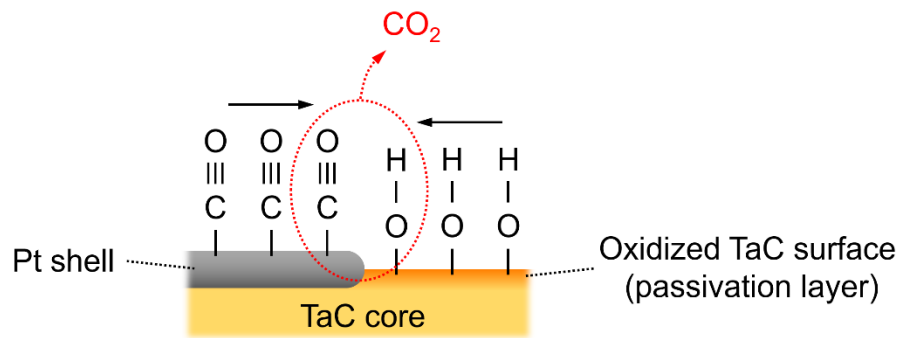
Figure S5-52. Schematic illustration of Langmuir-Hinshelwood CO oxidation taking place at the interface between Pt shell and surface-oxidized TaC core that is exposed to the electrolyte.
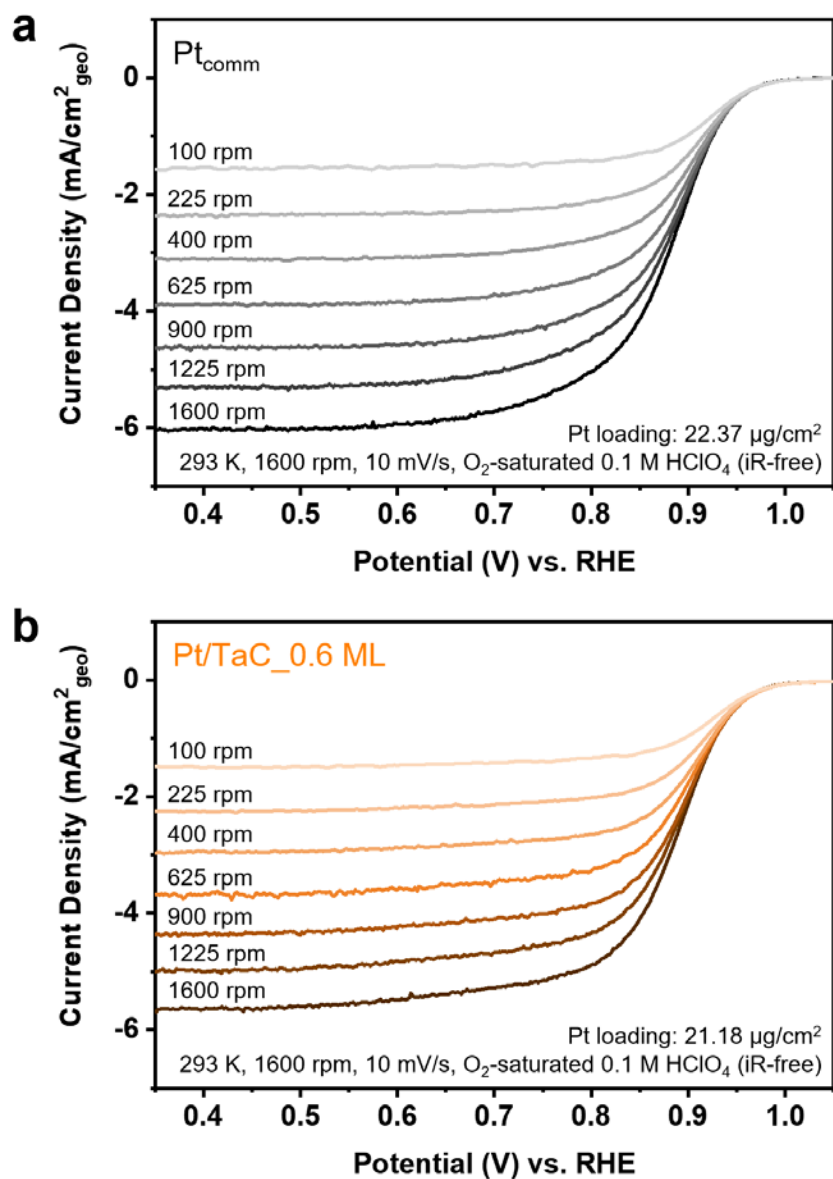
Figure S5-53. ORR polarization curves

(a) Pt_comm and (b) Pt/TaC_0.6 ML measured at various ration speeds.
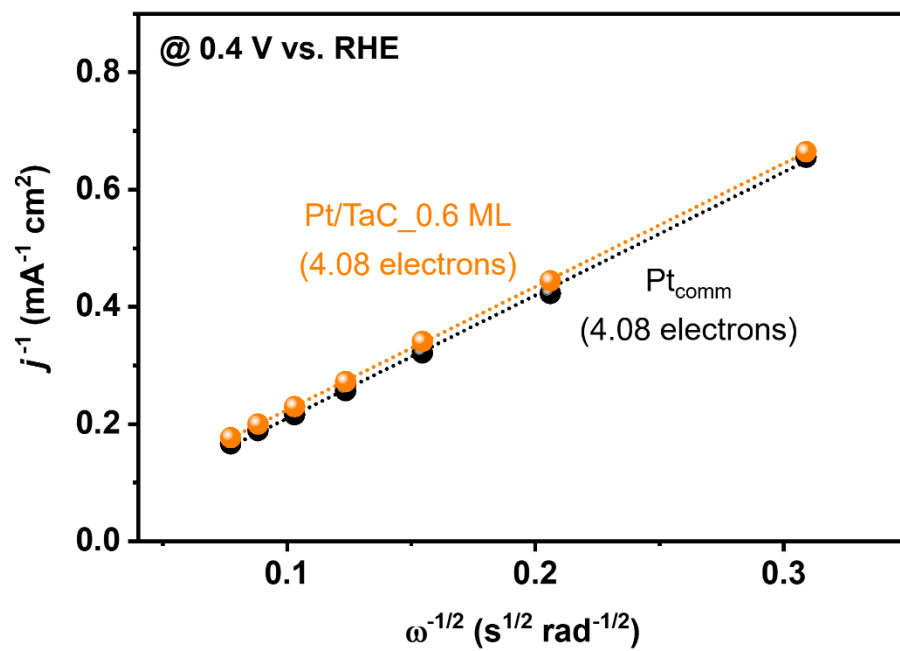
Figure S5-54. Koutecky-Levich plots of Pt_{comm} and Pt/TaC_0.6 ML.

Electron transfer number calculated for ORR was 4.08 for both catalysts.
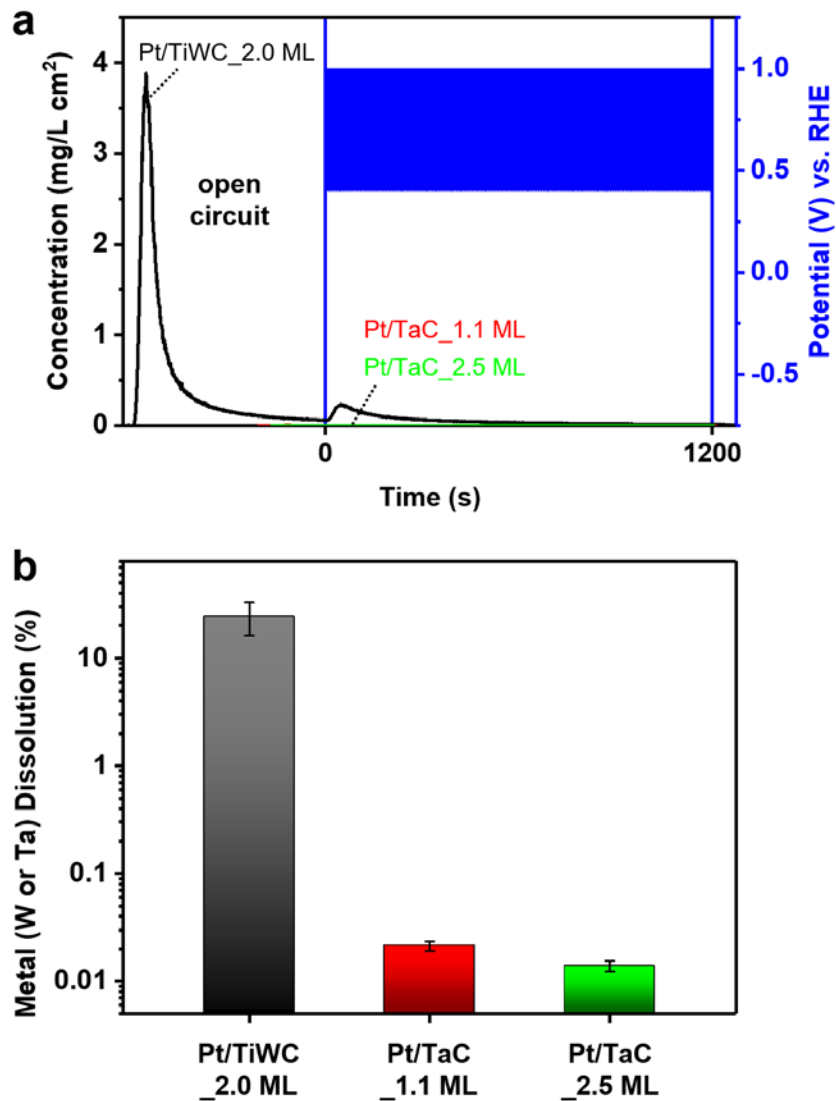
Figure S5-55. *In-situ* ICP-MS results.

(a) Time-transient concentrations of dissolved W or Ta measured by in situ ICP-MS. After the saturation of W or Ta dissolution at open circuit condition, 1,000 potential cycles between 0.4 and 1.0 V were carried out at the scan rate of 1.0 V/s. (b) Summary of the total amount of dissolved Ta or W by integrating the areas under the curves in (a).

Supporting Note: In order to compare the stability of TaC core to that of TiWC core in state-of-the-art Pt/TiWC nanoparticles with 2.0 ML-thick Pt shell,[4] we prepared Pt/TaC nanoparticles with the shell thicknesses of 1.1 ML and 2.5 ML for reasonable comparisons.
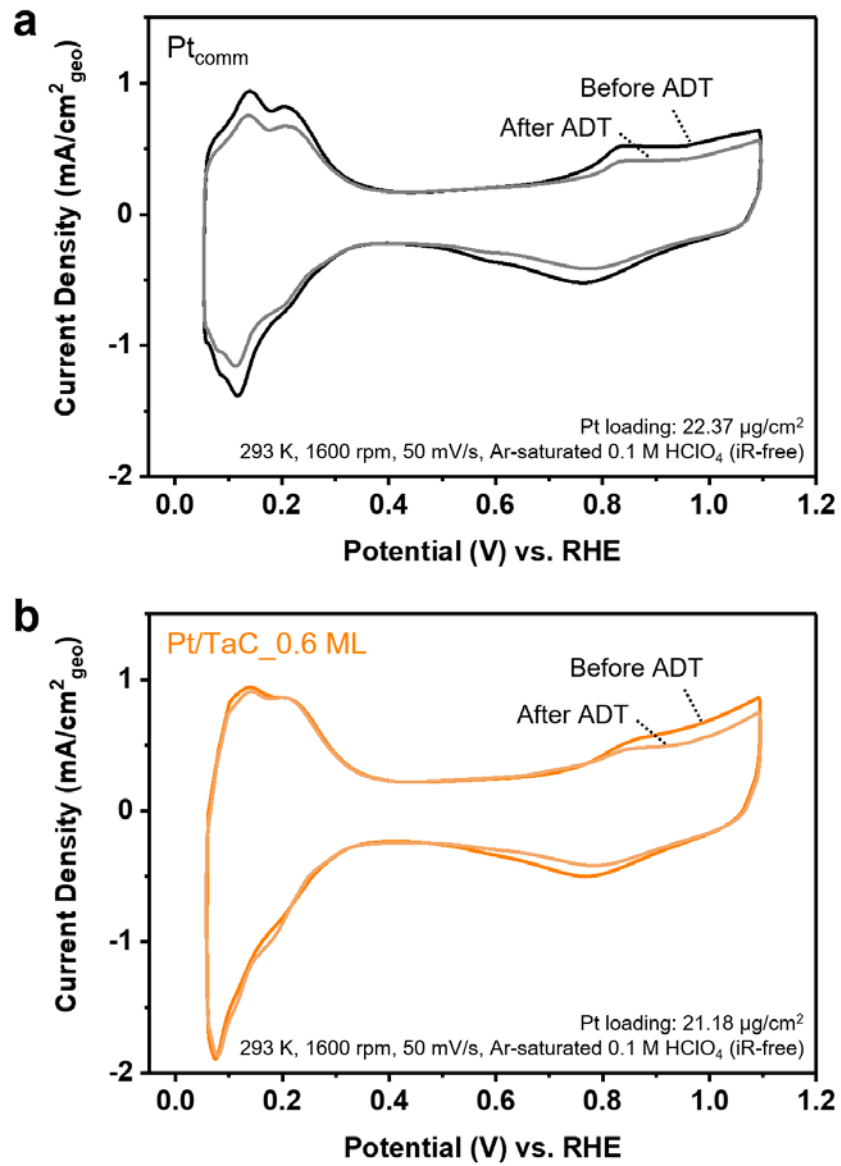
Figure S5-56. CV diagrams for stability performance

(a) Pt_comm and (b) Pt/TaC_0.6 ML before and after 10,800 cycles of ADT.
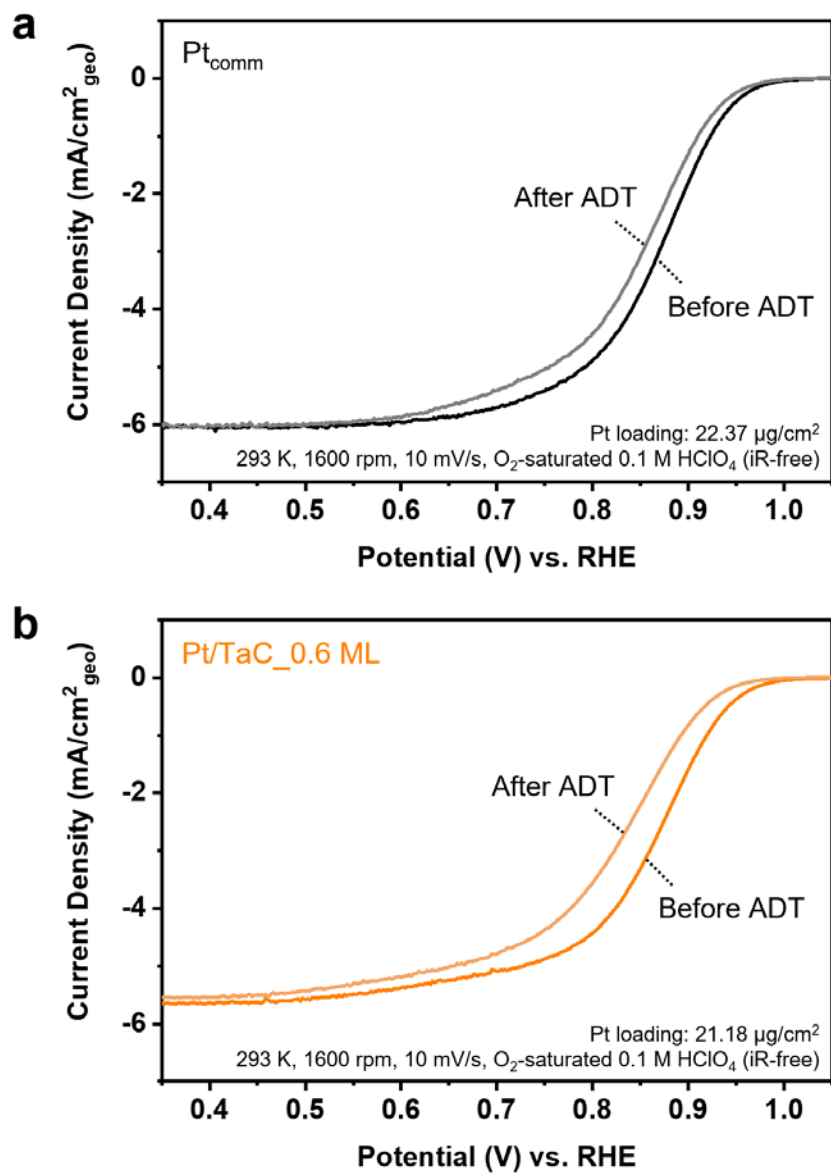
Figure S5-57. ORR polarization curves

(a) Pt_{comm} and (b) Pt/TaC_0.6 ML before and after 10,800 cycles of ADT.
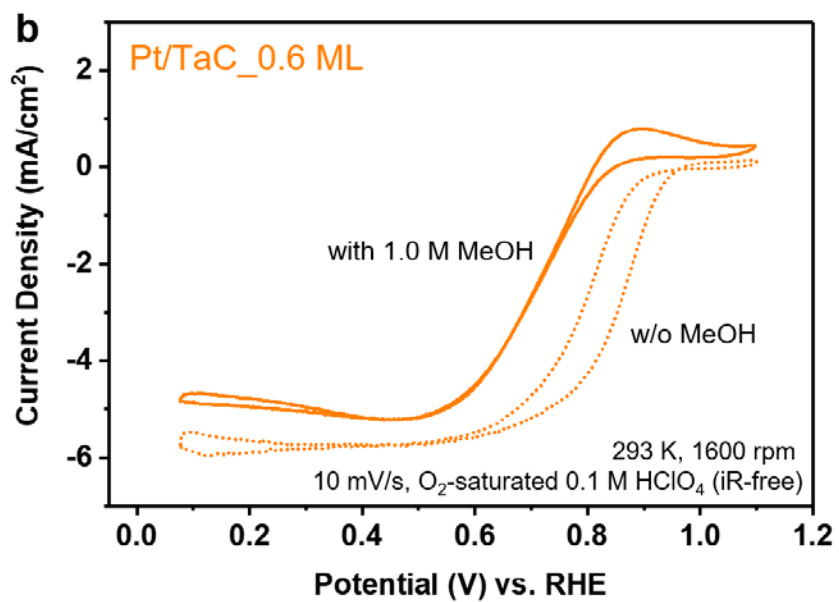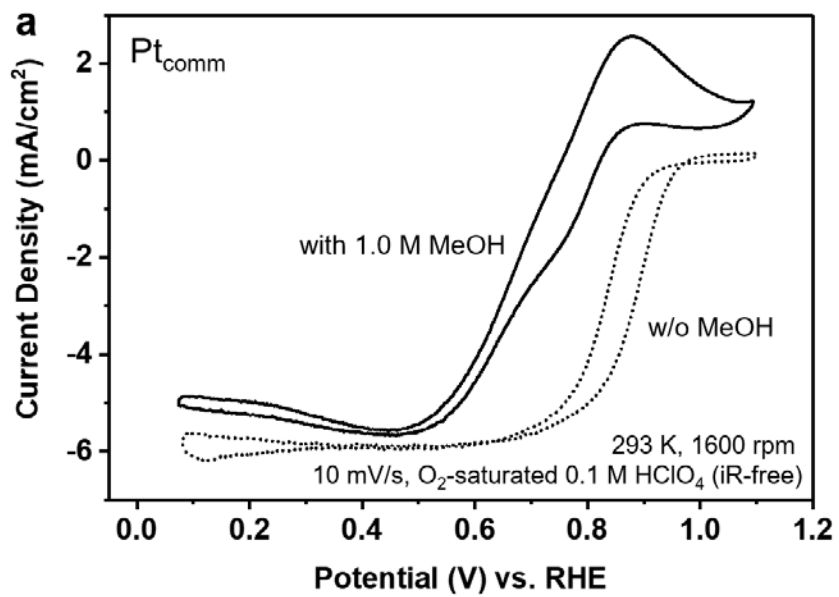
Figure S5-58. ORR CV curves

(a) Pt_{comm} and (b) Pt/TaC_0.6 ML obtained with and without 1.0 M methanol in 0.1 M $HClO_4$ electrolyte.

Reverse microemulsion (RME) synthesis of oxide nanoparticles

The RME was prepared by mixing 54 mL Brij-L4® surfactant (Sigma-Aldrich) with 240 mL n-heptane (VWR), then stirred till transparent. 7.8 mL DI water (18.2 MΩ·cm) was mixed with 1.4 mL concentrated NH_4OH solution (Sigma-Aldrich), then injected into the previous described heptane-Brij transparent mixture. The RME mixture was then sonicated for 10 minutes to ensure small aqueous phases to be well dispersed. Then 1.5 mL tantalum isopropoxide (TaIPO, Alfa Aesar) was diluted with 100 mL anhydrous heptane inside the glovebox. The mixture was then injected into the RME as fast as possible to minimize hydrolysis in air. The RME mixture was left stirring for 4 hours to ensure complete hydrolysis of the alkoxide precursors to form corresponding oxides.

A separate RME containing H_2PtCl_6 precursor was prepared with 46 mL n-heptane (VWR), 7.2 mL Brij-L4® surfactant (Sigma-Aldrich) and 50~120 mg of H_2PtCl_6 (Strem Chemical) dissolving in 1 mL MiliQ water (18.2 MΩ·cm). The small RME batch was sonicated 10 minutes before adding dropwise into the big RME. Tetraethyl orthosilicate (TEOS, Sigma-Aldrich) was added 4 hours after the Pt precursor added. The whole system was left stirring for 16.5 hours before precipitating out with 300 mL methanol (Sigma-Aldrich). The solid was recovered by decanting, centrifugation, washing with acetone and drying under vacuum.

Carburization

The previously obtained solid was heated in a tube furnace up to 970-990 °C at a ramping rate of 2 °C min^{-1} under 120 sccm H_2 and 30 sccm CH_4 flow. The temperature was held at 970 °C -990 °C for 7 hours then ramped to 1020-1090 °C with a ramping rate 2 °C min^{-1} with only 120 sccm H_2 flowing as the scavenge step. This step was held for 1~3 hours. The system was then cooled to room temperature under a pure H_2 atmosphere. Encapsulated core-shell nanoparticles were passivated with 1% O_2/ 99%N_2 for 2 hours. The samples were measured by XRD to confirm the carbide phase formation then stored in a glovebox.

Dissolution of silica shell

210 µL or 270 µL (depends on the carburization temperatures) of 48 wt% aqueous HF solution (Sigma-Aldrich) was diluted with 5 mL degassed ethanol (VWR) to make the dissolving solution. 30 mg of the encapsulated core-shell nanoparticles were firstly mixed with 10 mg of acid-treated carbon black (Cabot, Vulcan® XC-72r) and then silica dissolving stock solution was added into the solid mixture. The whole mixture was sonicated for 1 minute followed by shaking for 18 hours to ensure fully dissolving the silica encapsulation. The core-shell nanoparticles were then recovered by centrifugation and washed thoroughly with degassed ethanol 4 times. The powders were dried under vacuum and tested by XRD to confirm the carbide phased remained before storing in a glovebox.

CHAPTER 6 CONCLUSIONS AND OUTLOOK

Conclusions

This thesis aimed to broaden the synthesis spectrum and provide a fundamental understanding of how core tunes noble metal shell and change the shell interactions with corresponding adsorbates in different thermal catalytical and electrochemical reactions. Specifically, the core-shell synthesis spectrum was broadened from the main tungsten carbide and tungsten nitride cores to including niobium and tantalum carbide cores. The shell was also extended from pure Pt, or mainly Pt, to pure Rh, Ir.[6] These combinations were examined under XRD, TEM, ICP-MS, XPS, EDX-mapping, and some of them were examined under XAS to testify the core-shell interactions and the formation of the core-shell structure. The shell coverages and particle sizes could be controlled by loading different shell-to-core metal precursor ratios and changing carburization profiles respectively which were detailed documented in Chapter 2 Broaden the Core-Shell Synthesis Library.

The catalysts were then used in different probe reactions to demonstrate the core-shell interaction and its impact on macro-reactivities and selectivity. The first example was that Rh/NbC and Rh/TiWC had enhanced CO selectivity compared to the commercial Rh in CO_2 hydrogenation reactions with 0.2 ML Rh/TiWC featuring ~10 times higher in the CO selectivity and 18 times higher in CO STY at 300 ^oC normalized by the Rh active sites. Rh shell was found upshifting 0.3 eV in the XPS compared to the commercial Rh and the d-band of the Rh shell was lower based on the DFT calculation which indicated a lower CO binding energy which facilitated the CO desorption during the CO_2 hydrogenation. Additionally, Rh/TiWC core-shell Rh-Rh coordination number is only half that of the commercial Rh which also contributed to the enhanced CO selectivity. The details were documented in Chapter 3 Enhancement of CO Selectivity by Transition Metal Carbide Rhodium Core-Shell Nanoparticles in CO_2 Hydrogenation.

As the CO adsorbate had been shown to bind more weakly on core-shells electrochemically [3, 6], and thermal catalytically from Chapter 3, we moved to other

adsorbates, C_2H_2 and C_2H_4. We identified the TiWC and TiWN cores modulated the binding energies of alkynes and alkenes on Pt surfaces to achieve high partial alkyne hydrogenation exclusively by an electronic effect. Rigorous acetylene hydrogenation (C_2H_2: H_2=1:4) over Pt$_{comm}$, Pt/TiWC, and Pt/TiWN were performed demonstrating the superior selectivity of C_2H_4 for the core-shell particles (4 times higher). Electrochemical Hupd and conventional CO chemisorption methods were used to quantify the number of exposed Pt sites and acetylene hydrogenation turnover frequency followed the trend Pt$_{comm}$ > Pt/TiWC > Pt/TiWN. Microcalorimetry measurements were consistent with a change in the Pt electronic structure that decreased C_2H_4 binding strength, thus increasing partial hydrogenation selectivity. DFT calculations, XPS and XANES both indicated broadening of the Pt d-band and concomitant down-shifting of the d-band center. EXAFS spectroscopy identified no change in Pt-Pt distance which disentangled the geometric effect from the electric effect. The detail was documented in Chapter 4 Enhancement of Alkyne Semi-Hydrogenation Selectivity by Electronic Modification of Platinum.

After showing two thermal catalytical probe reaction examples, the core-shell platform was used in the direct methanol fuel cell application to tackle the real-world energy problem. In Chapter 5 Platinum/Tantalum Carbide Nanoparticles with Sub-Monolayer Shells for Methanol and Oxygen Electrocatalysis, Pt/TaC core-shells with varied Pt shell thickness were tested for the MOR and methanol interfered ORR. The result indicated the 0.57 ML Pt/TaC had superior MOR activity and less methanol affected ORR activity compared to the Pt$_{comm}$. Pt shell XPS 4f peak would upshift and the Pt L_2 edge XANES had larger white-line intensity than the Pt foil both of which indicated the Pt d-band in Pt/TaC was broadened and Pt d-band center was downshifted. Hence the CO intermediate did not poison the Pt/TaC surface as intensively as Pt$_{comm}$. Moreover, unlike the non-fully covered Pt/TiWC core dissolving under ORR condition,[4] Pt/TaC core was stable after 10800 0.4-1.0 V cycles. After 10800 0.4-1.4 V cycles, the TaC core still existed even though the Pt shell was dissolved.

Limitations

Even though this work has demonstrated a few breakthroughs from the previous core-shell system, there are still limitations that need to be overcome.

First and foremost, the mass activity of Pt/TaC in ORR was not as good as the Pt/TiWC or Pt/TiWN counterparts. This could be owing to Pt embedding inside the TaC core which needs to be liberated out. This is supported by smaller ECSA for the Pt/TaC than Pt/TiWC or Pt/TiWN. Another hypothesis was the TaC core forced Pt to form (100) facet which was the least active facet in the ORR. Secondly, the onset potential and Pt mass activity of Pt/TaC in MOR was not as favorable as the state-of-art PtRu catalyst. Based on the CO bulk oxidation reaction result, CO adsorption on Pt/TaC was less favored than the Pt_{comm} but the normal CV scan also indicated the OH adsorption was not as favored on the core-shell. This suggested the lack of OH adsorption was one of the reasons limiting the better MOR performance.

Besides the reactivity, the scalability of core-shell synthesis remained an issue. By scaling up the synthesis, core-shell catalysts can be used for thermal catalytic reactions, yet it would take a long time to generate enough samples for a complete data set, therefore it will be difficult for commercial purposes. The scalability challenge was due to the use of the reverse microemulsion method and also the involvement of HF to de-capsulate silica shell. However, if not using the silica protection, the noble metal shell would sinter and form larger stand-alone noble metal particles that defeated the purpose of the core-shell structure.

Additionally, it was found to be difficult to control the shell coverage approaching 1ML or even higher for some core-shell platforms, such as Rh/TiWC. The addition of Rh precursor to some extent would induce the formation of W_2C phases which made it hard to have a full ML Rh coverage. For other core-shell systems, noble metal coverage more than 2-3 ML appeared to be challenging as stand-alone noble metal particles would show up in the XRD which defeated the purpose of the core-shell structure.

Outlook

The future directions can be divided into two main parts. One is to improve the current system, specifically on the synthesis of core-shell platform to solve the existing problems. The other one is to apply the core-shell system in other reactions.

Improving the core-shell synthesis

There are at least two aspects can be done in the future to improve the core-shell synthesis. The first one is to add heteroatoms in the shell to harvest the bifunctionality on the shell surface. From the discussion in Chapter 5, the lack of OH on the Pt/TaC surface was one reason that the core-shell did not perform as well as the state-of-art PtRu catalyst.[23, 251] Additionally, the previous work for the PtRu/TiWC core-shell also exhibited a similar on-set potential with the state-of-art PtRu catalyst and a much better noble metal mass activity owing to the core-shell structure.[6] Inspired by this, adding a second element Ru in the Pt/TaC shell would very likely to increase the catalyst specific and mass activity. One can take one step further in this route by introducing a third element in the shell. For example, Pt_7Ru_2Fe nanowires possess a higher MOR and formic acid oxidation reaction (FAOR) activity compared to binary Pt_7Ru_3 and Pt_7Fe_3 catalysts.[252] Other examples are PtRuCo, PtRuNi, PtRuSn, PtRuMo, and PtRuTe catalysts which all exhibit a better CO tolerance hence a better activity towards MOR.[253-255] As the core-shell Pt/TaC itself already has good CO tolerance, adding a third component in the shell may be able to amplify the effect even further.

In addition to the activity boost, the other direction to improve the synthesis is to reduce the synthesis difficulty. One possible direction is to minimize the carburization temperature which is a critical step to avoid the silica encapsulation as lower temperature (<500°C) will not lead to noble metal sintering if the noble metal shell is anchored on the carbide surface.[6] By avoiding the silica encapsulation, the synthesis route will then not use HF which improves the safety and applicability in the industry greatly. Normal transition metal carbides formation temperatures are usually around 800-1200 °C, which was necessary to break the C-C bonds or C-H bonds in the hydrocarbon precursors and also breaking the metal-oxygen bond in the metal oxides.[256] Additionally, the high

temperature also facilitates carbon diffuse into the oxycarbide lattice to replace the oxygen out. However, diffusion is a slow process. One natural solution to this is to shorten the diffusion distance. About 20 years ago, Johnson et al, demonstrated that various elements could be evaporated at a rate of 0.5 Å/s using an electron beam gun source.[256] By doing so, the elemental layer thickness was changed which resulted in a completer interdiffusion at relatively low temperatures. For example, TiC was observed to crystallize at 350 $^\circ$C, Mo_2C at 500 $^\circ$C, and W_2C at 600 $^\circ$C. This was a great proof-of-concept work to demonstrate that you can achieve low-temperature carburization of transition metals, yet, the electron beam gun was not a scalable way to synthesize carbide materials. More recently, Baddour et al, demonstrated they can synthesize α-MoC_{1-x} with $Mo(CO)_6$ precursors at 320 $^\circ$C. The system was able to synthesize nanosized α-MoC_{1-x} in a continuous flow manner.[257] Li et al, also reported the synthesis of scroll-type 1-D Mo_2C from pyrolysis of $Mo(CO)_6$.[258] From all these previously reported works, we can hypothesize a possibility of synthesis WC_{1-x} from $W(CO)_6$ and CrC_{1-x} from $Cr(CO)_6$ at low temperatures. Once these pristine carbide nanoparticles form, we can add noble metal precursors into the system and coat the nano-carbides to form core-shell structures.

Core-shell Rh catalyst for the hydroformylation reaction

Rh/SiO_2 catalyst was reported to be active for ethylene hydroformylation under the conditions of 180 $^\circ$C, 2 MPa with mixed gas (C_2H_4:CO:H_2:Ar = 30:40:20:10).[259] The selectivity towards hydroformylation products increased as the Rh particle size decreased which indicated the hydroformylation preferably occurred at the coordinatively unsaturated Rh atoms located at the edge and corner sites of the particle.[260] The unwanted products, CH_4 and C_2H_6, were from CO dissociative hydrogenation and ethylene hydrogenation. Mechanistically, CO dissociation and alkene adsorption on catalyst surface involves the cleavage or formation of a π-bond where the rate over terraces sites is much higher than the edge sites. The reason is mainly related to the absence of surface metal atom sharing of the dissociating atoms in edge sites.[261-262] Therefore, undercoordinated sites are essential to achieve high hydroformylation selectivity by hindering CO dissociation and unwanted alkene hydrogenation. This can be

achieved through the engineering Rh geometric structure using the core-shell platform. The work described in Chapter 3 demonstrated that the Rh-Rh coordination number was drastically decreased in Rh/TiWC system compared to Rh_{comm} under CO_2 hydrogenation reaction condition. The EXAFS results indicated the core-shell Rh had more coordinatively unsaturated Rh atoms, therefore, core-shell Rh catalysts would be ideal candidates for the ethylene hydroformylation reaction.

Here, I propose that core-shell Rh nanoparticles can be used for the ethylene hydroformylation reaction given the Rh undercoordinated sites are much more abundant than the regular Rh nanoparticles. Additionally, due to the Rh-core interaction shown in the EXAFS and XPS data, the Rh shell will very likely to remain stable on the core during reaction conditions. Moreover, the Rh-core interaction enables the Rh electron donation to the core, which is analogous to the homogenous Rh complex, where the ligands withdraw Rh electrons. A combined theoretical and experimental approach shall be used to investigate the active sites and mechanism of the hydroformylation over the core-shell Rh nanoparticles. Specifically, one should use synchrotron radiation sources based *in operando* XAS experiments to identify the Rh coordination changes over the hydroformylation reaction condition. The downstream shall be connected to an in-line GC to analyze the product formation, given the structural changes during the reaction condition. Ambient XPS experiments shall be used to probe the Rh electronic structure change before and after the introduction of CO and ethylene. These experiments will provide insights on the stability and active sites of the core-shell Rh catalysts. With the geometric and electronic structure information from the experiments, DFT can then be used to calculate the energetics of each intermediate step. Combining with the micro-kinetics modeling, one can propose the mechanism of hydroformylation over the core-shell Rh catalysts which can then be used to further optimize catalyst performances.

Core-shell Pt catalyst for the propane dehydrogenation reaction

As the shale gas technologies boomed more than a decade ago, the propane production also increased dramatically. The demand for propylene, an important industrial intermediate, also grows rapidly.[263-264] Propane dehydrogenation (PDH) is an ideal

reaction to satisfy the growing demand for propylene and also consume the increasingly produced propane from shale gas hydraulic fracking. The two major types of catalysts for the PDH reaction was chromium oxides and Pt-based bimetallic catalysts. The CrO_x based catalysts are cheaper, more selective towards propylene but less active and less stable. While the Pt-based catalysts are in general more stable and active but less selective.[58] With the benefit of stability and higher activity, combining with the core-shell structure to minimize the Pt loading, the Pt core-shell systems are considered promising in this reaction. Bimetallic Pt-based catalysts are in general more selective to propylene than a monometallic Pt and the reason was considered to be the geometric effect.[67] Additionally, a weaker propylene binding energy on the catalyst surface will result in a better propylene selectivity.[265] As the Pt/TiWC and Pt/TiWN core-shells were shown to have lower binding energy towards the C_2H_4 double bond in Chapter 4 , it is very likely the binding energy of propylene on the Pt/TiWC and Pt/TiWN are also lower. Moreover, a very recent study by Wegener et al, demonstrated the Pt-Fe intermetallic compound had a decrease in the average energy of the filled 5d states of Pt characterized by resonant inelastic X-ray scattering (RIXS), in other words, a lower d-band center.[266] As the Pt/TiWC, Pt/TiWN had downshifted d-band center based on the DFT calculation, it is very promising that these two Pt core-shell nanoparticles will have a similar propylene selectivity as the Pt-Fe intermetallic in the PDH.

REFERENCES

1.   Wei, C.; Rao, R. R.; Peng, J. Y.; Huang, B. T.; Stephens, I. E. L.; Risch, M.; Xu, Z. C. J.; Shao-Horn, Y. Recommended Practices and Benchmark Activity for Hydrogen and Oxygen Electrocatalysis in Water Splitting and Fuel Cells. *Adv Mater* **2019,** *31*.

2.   Hunt, S. T.; Milina, M.; Wang, Z. S.; Roman-Leshkov, Y. Activating Earth-Abundant Electrocatalysts for Efficient, Low-Cost Hydrogen Evolution/Oxidation: Sub-Monolayer Platinum Coatings on Titanium Tungsten Carbide Nanoparticles. *Energ Environ Sci* **2016,** *9*, 3290-3301.

3.   Garg, A.; Milina, M.; Ball, M.; Zanchet, D.; Hunt, S. T.; Dumesic, J. A.; Roman-Leshkov, Y. Transition-Metal Nitride Core@Noble-Metal Shell Nanoparticles as Highly Co Tolerant Catalysts. *Angew Chem Int Ed* **2017,** *56*, 8828-8833.

4.   Göhl, D.; Garg, A.; Paciok, P.; Mayrhofer, K. J. J.; Heggen, M.; Shao-Horn, Y.; Dunin-Borkowski, R. E.; Román-Leshkov, Y.; Ledendecker, M. Engineering Stable Electrocatalysts by Synergistic Stabilization between Carbide Cores and Pt Shells. *Nat Mater* **2020,** *19*, 287-291.

5.   Markovic, N. M.; Gasteiger, H. A.; Ross, P. N.; Jiang, X. D.; Villegas, I.; Weaver, M. J. Electrooxidation Mechanisms of Methanol and Formic-Acid on Pt-Ru Alloy Surfaces. *Electrochim Acta* **1995,** *40*, 91-98.

6.   Hunt, S. T.; Milina, M.; Alba-Rubio, A. C.; Hendon, C. H.; Dumesic, J. A.; Roman-Leshkov, Y. Self-Assembly of Noble Metal Monolayers on Transition Metal Carbide Nanoparticle Catalysts. *Science* **2016,** *352*, 974-978.

7.   Lam, C. H.; Lowe, C. B.; Li, Z. L.; Longe, K. N.; Rayburn, J. T.; Caldwell, M. A.; Houdek, C. E.; Maguire, J. B.; Saffron, C. M.; Miller, D. J.; Jackson, J. E. Electrocatalytic Upgrading of Model Lignin Monomers with Earth Abundant Metal Electrodes. *Green Chem* **2015,** *17*, 601-609.

8.   Shui, J. I.; Chen, C.; Li, J. C. M. Evolution of Nanoporous Pt-Fe Alloy Nanowires by Dealloying and Their Catalytic Property for Oxygen Reduction Reaction. *Adv Funct Mater* **2011,** *21*, 3357-3362.

9.   Lu, B. A.; Sheng, T.; Tian, N.; Zhang, Z. C.; Xiao, C.; Cao, Z. M.; Ma, H. B.; Zhou, Z. Y.; Sun, S. G. Octahedral Ptcu Alloy Nanocrystals with High Performance for Oxygen

Reduction Reaction and Their Enhanced Stability by Trace Au. *Nano Energy* **2017,** *33*, 65-71.

10.   Zhang, J.; Lima, F. H. B.; Shao, M. H.; Sasaki, K.; Wang, J. X.; Hanson, J.; Adzic, R. R. Platinum Monolayer on Nonnoble Metal-Noble Metal Core-Shell Nanoparticle Electrocatalysts for O_2 Reduction. *J Phys Chem B* **2005,** *109*, 22701-22704.

11.   Neyerlin, K. C.; Srivastava, R.; Yu, C. F.; Strasser, P. Electrochemical Activity and Stability of Dealloyed Pt-Cu and Pt-Cu-Co Electrocatalysts for the Oxygen Reduction Reaction (ORR). *J Power Sources* **2009,** *186*, 261-267.

12.   Sekol, R. C.; Li, X. K.; Cohen, P.; Doubek, G.; Carmo, M.; Taylor, A. D. Silver Palladium Core-Shell Electrocatalyst Supported on Mwnts for Orr in Alkaline Media. *Appl Catal B-Environ* **2013,** *138*, 285-293.

13.   Zheng, J. S.; Zhang, X. S.; Li, P.; Zhu, J.; Zhou, X. G.; Yuan, W. K. Effect of Carbon Nanofiber Microstructure on Oxygen Reduction Activity of Supported Palladium Electrocatalyst. *Electrochemistry Communications* **2007,** *9*, 895-900.

14.   Huang, J. J.; Zhu, N. W.; Yang, T. T.; Zhang, T. P.; Wu, P. X.; Dang, Z. Nickel Oxide and Carbon Nanotube Composite (NiO/CNT) as a Novel Cathode Non-Precious Metal Catalyst in Microbial Fuel Cells. *Biosensors & Bioelectronics* **2015,** *72*, 332-339.

15.   Lee, D. H.; Lee, W. J.; Lee, W. J.; Kim, S. O.; Kim, Y. H. Theory, Synthesis, and Oxygen Reduction Catalysis of Fe-Porphyrin-Like Carbon Nanotube. *Phys Rev Lett* **2011,** *106*.

16.   Jeon, T. Y.; Kim, S. K.; Pinna, N.; Sharma, A.; Park, J.; Lee, S. Y.; Lee, H. C.; Kang, S. W.; Lee, H. K.; Lee, H. H. Selective Dissolution of Surface Nickel Close to Platinum in Ptni Nanocatalyst toward Oxygen Reduction Reaction. *Chem Mater* **2016,** *28*, 1879-1887.

17.   Dubau, L.; Lopez-Haro, M.; Castanheira, L.; Durst, J.; Chatenet, M.; Bayle-Guillemaud, P.; Guetaz, L.; Caque, N.; Rossinot, E.; Maillard, F. Probing the Structure, the Composition and the Orr Activity of Pt3co/C Nanocrystallites During a 3422 H Pemfc Ageing Test. *Appl Catal B-Environ* **2013,** *142*, 801-808.

18.   Kim, J. H.; Cheon, J. Y.; Shin, T. J.; Park, J. Y.; Joo, S. H. Effect of Surface Oxygen Functionalization of Carbon Support on the Activity and Durability of Pt/C Catalysts for the Oxygen Reduction Reaction. *Carbon* **2016,** *101*, 449-457.

19.   Li, X. L.; Faghri, A. Review and Advances of Direct Methanol Fuel Cells (Dmfcs) Part I: Design, Fabrication, and Testing with High Concentration Methanol Solutions. *J Power Sources* **2013,** *226*, 223-240.

20.   Melaina, M. P., M Hydrogen Station Cost Estimates https://www.nrel.gov/docs/fy13osti/56412.pdf.

21.   Zhao, S. L.; Yin, H. J.; Du, L.; Yin, G. P.; Tang, Z. Y.; Liu, S. Q. Three Dimensional N-Doped Graphene/Ptru Nanoparticle Hybrids as High Performance Anode for Direct Methanol Fuel Cells. *J Mater Chem A* **2014,** *2*, 3719-3724.

22.   Huang, J. C.; Liu, Z. L.; He, C. B.; Gan, L. M. Synthesis of PtRu Nanoparticles from the Hydrosilylation Reaction and Application as Catalyst for Direct Methanol Fuel Cell. *J Phys Chem B* **2005,** *109*, 16644-16649.

23.   Lee, M. J.; Kang, J. S.; Kang, Y. S.; Chung, D. Y.; Shin, H.; Ahn, C. Y.; Park, S.; Kim, M. J.; Kim, S.; Lee, K. S.; Sung, Y. E. Understanding the Bifunctional Effect for Removal of CO Poisoning: Blend of a Platinum Nanocatalyst and Hydrous Ruthenium Oxide as a Model System. *ACS Catal* **2016,** *6*, 2398-2407.

24.   Alayoglu, S.; Nilekar, A. U.; Mavrikakis, M.; Eichhorn, B. Ru-Pt Core-Shell Nanoparticles for Preferential Oxidation of Carbon Monoxide in Hydrogen. *Nat Mater* **2008,** *7*, 333-338.

25.   Engstfeld, A. K.; Klein, J.; Brimaud, S.; Behm, R. Electrochemical Stability and Restructuring and Its Impact on the Electro-Oxidation of CO: Pt Modified Ru(0001) Electrodes. *Surf. Sci.* **2015,** *631*, 248-257.

26.   Davy, H. Viii. Some New Experiments and Observations on the Combustion of Gaseous Mixtures, with an Account of a Method of Preserving a Continued Light in Mixtures of Inflammable Gases and Air without Flame. *PHILOS T R SOC B* **1817,** *107*, 77-85.

27.   Kattel, S.; Yu, W. T.; Yang, X. F.; Yan, B. H.; Huang, Y. Q.; Wan, W. M.; Liu, P.; Chen, J. G. G. CO_2 Hydrogenation over Oxide-Supported PtCo Catalysts: The Role of the Oxide Support in Determining the Product Selectivity. *Angew Chem Int Ed* **2016,** *55*, 7968-7973.

28.   Rodriguez, J. A.; Liu, P.; Stacchiola, D. J.; Senanayake, S. D.; White, M. G.; Chen, J. G. G. Hydrogenation of CO_2 to Methanol: Importance of Metal-Oxide and Metal-Carbide Interfaces in the Activation of CO_2. *ACS Catal* **2015,** *5*, 6696-6706.

29.   Bond, G. C.; Dowden, D. A.; Mackenzie, N. The Selective Hydrogenation of Acetylene. *T Faraday Soc* **1958,** *54*, 1537-1546.

30.   Gutierrez, A.; Kaila, R. K.; Honkela, M. L.; Slioor, R.; Krause, A. O. I. Hydrodeoxygenation of Guaiacol on Noble Metal Catalysts. *Catal Today* **2009,** *147*, 239-246.

31.   Gandhi, H. S.; Graham, G. W.; McCabe, R. W. Automotive Exhaust Catalysis. *J. Catal* **2003,** *216*, 433-442.

32.   Yu, C. L.; Ge, Q. J.; Xu, H. Y.; Li, W. Z. Effects of Ce Addition on the Pt-Sn/Gamma-Al2o3 Catalyst for Propane Dehydrogenation to Propylene. *Appl Catal a-Gen* **2006,** *315*, 58-67.

33.   Rossetti, I.; Forni, L. Effect of Ru Loading and of Ru Precursor in Ru/C Catalysts for Ammonia Synthesis. *Appl Catal a-Gen* **2005,** *282*, 315-320.

34.   Norskov, J. K.; Bligaard, T.; Rossmeisl, J.; Christensen, C. H. Towards the Computational Design of Solid Catalysts. *Nat Chem* **2009,** *1*, 37-46.

35.   Rylander, P. N., *Catalytic Hydrogenation over Platinum Metals*. Academic Press: New York,, 1967; p xii, 550 p.

36.   Hall, W. K.; Lutinski, F. E. Studies of the Hydrogen Held by Solids .5. Investigation of Platinum Supported on Alumina Catalysts by Exchange with Deuterium Gas. *J. Catal* **1963,** *2*, 518-527.

37.   Toshima, N.; Yonezawa, T.; Kushihashi, K. Polymer-Protected Palladium-Platinum Bimetallic Clusters - Preparation, Catalytic Properties and Structural Considerations. *J Chem Soc Faraday T* **1993,** *89*, 2537-2543.

38.   Jones, L. C.; Gordon, M. J. Influence of Step-Edge Vs Terrace Sites on Temperature-Dependent C2h2 Hydrogenation with Ag-Doped Pt Nanoparticles. *J. Phys. Chem. C* **2012,** *116*, 23472-23476.

39.   Visser, C.; Zuidwijk, J. G.; Ponec, V. Reactions of Hydrocarbons on Palladium-Gold Alloys. *J. Catal* **1974,** *35*, 407-416.

40.   Tauster, S. J.; Fung, S. C.; Baker, R. T. K.; Horsley, J. A. Strong-Interactions in Supported-Metal Catalysts. *Science* **1981,** *211*, 1121-1125.

41.   Leviness, S.; Nair, V.; Weiss, A. H.; Schay, Z.; Guczi, L. Acetylene Hydrogenation Selectivity Control on Pdcu/Al2o3 Catalysts. *J Mol Catal* **1984,** *25*, 131-140.

42.   Durussel, P.; Feschotte, P. A Revision of the Binary System Ag-Pt. *J Alloy Compd* **1996,** *239*, 226-230.

43.   Pei, G. X.; Liu, X. Y.; Wang, A. Q.; Lee, A. F.; Isaacs, M. A.; Li, L.; Pan, X. L.; Yang, X. F.; Wang, X. D.; Tai, Z. J.; Wilson, K.; Zhang, T. Ag Alloyed Pd Single-Atom Catalysts for Efficient Selective Hydrogenation of Acetylene to Ethylene in Excess Ethylene. *ACS Catal* **2015,** *5*, 3717-3725.

44.   Xu, J.; White, T.; Li, P.; He, C. H.; Yu, J. G.; Yuan, W. K.; Han, Y. F. Biphasic Pd-Au Alloy Catalyst for Low-Temperature CO Oxidation. *J Am Chem Soc* **2010,** *132*, 10398-10406.

45.   Jin, Y. M.; Datye, A. K.; Rightor, E.; Gulotty, R.; Waterman, W.; Smith, M.; Holbrook, M.; Maj, J.; Blackson, J. The Influence of Catalyst Restructuring on the Selective Hydrogenation of Acetylene to Ethylene. *J. Catal* **2001,** *203*, 292-306.

46.   Knecht, M. R.; Weir, M. G.; Frenkel, A. I.; Crooks, R. M. Structural Rearrangement of Bimetallic Alloy Pdau Nanoparticles within Dendrimer Templates to Yield Core/Shell Configurations. *Chem Mater* **2008,** *20*, 1019-1028.

47.   Armbruster, M.; Kovnir, K.; Behrens, M.; Teschner, D.; Grin, Y.; Schlogl, R. Pd-Ga Intermetallic Compounds as Highly Selective Semihydrogenation Catalysts. *J Am Chem Soc* **2010,** *132*, 14745-14747.

48.   Jones, L. C.; Buras, Z.; Gordon, M. J. Partial Hydrogenation of C2h2 on Ag-Doped Pt Nanoparticles. *J. Phys. Chem. C* **2012,** *116*, 12982-12988.

49.   Matsubu, J. C.; Yang, V. N.; Christopher, P. Isolated Metal Active Site Concentration and Stability Control Catalytic CO_2 Reduction Selectivity. *J Am Chem Soc* **2015,** *137*, 3076-3084.

50.   Puddu, S.; Ponec, V. Effect of Ensemble Size in Hydrogenation of Benzene on Pt and Pt-Au Catalysts. *Recueil Des Travaux Chimiques Des Pays-Bas-Journal of the Royal Netherlands Chemical Society* **1976,** *95*, 255-257.

51.   Ponec, V.; Sachtler, W. M. Reactions between Cyclopentane and Deuterium on Nickel and Nickel-Copper Alloys. *J. Catal* **1972,** *24*, 250-&.

52.   Sinfelt, J. H.; Yates, D. J. C.; Carter, J. L. Catalytic Hydrogenolysis and Dehydrogenation over Copper-Nickel Alloys. *J. Catal* **1972,** *24*, 283-&.

53.   Oezaslan, M.; Hasche, F.; Strasser, P. Pt-Based Core-Shell Catalyst Architectures for Oxygen Fuel Cell Electrodes. *J Phys Chem Lett* **2013,** *4*, 3273-3291.

54.   Oezaslan, M.; Strasser, P. Activity of Dealloyed $PtCo_3$ and $PtCu_3$ Nanoparticle Electrocatalyst for Oxygen Reduction Reaction in Polymer Electrolyte Membrane Fuel Cell. *J Power Sources* **2011,** *196*, 5240-5249.

55.   Andersson, K. J.; Calle-Vallejo, F.; Rossmeisl, J.; Chorkendorff, L. Adsorption-Driven Surface Segregation of the Less Reactive Alloy Component. *J Am Chem Soc* **2009,** *131*, 2404-2407.

56.   Tao, F.; Grass, M. E.; Zhang, Y. W.; Butcher, D. R.; Renzas, J. R.; Liu, Z.; Chung, J. Y.; Mun, B. S.; Salmeron, M.; Somorjai, G. A. Reaction-Driven Restructuring of Rh-Pd and Pt-Pd Core-Shell Nanoparticles. *Science* **2008,** *322*, 932-934.

57.   Habas, S. E.; Lee, H.; Radmilovic, V.; Somorjai, G. A.; Yang, P. Shaping Binary Metal Nanocrystals through Epitaxial Seeded Growth. *Nat Mater* **2007,** *6*, 692-697.

58.   Yang, C.; Wu, Z. W.; Zhang, G. H.; Sheng, H. P.; Tian, J.; Duan, Z. L.; Sohn, H.; Kropf, A. J.; Wu, T. P.; Krause, T. R.; Miller, J. T. Promotion of Pd Nanoparticles by Fe and Formation of a Pd3fe Intermetallic Alloy for Propane Dehydrogenation. *Catal Today* **2019,** *323*, 123-128.

59.   Wang, J. X.; Inada, H.; Wu, L. J.; Zhu, Y. M.; Choi, Y. M.; Liu, P.; Zhou, W. P.; Adzic, R. R. Oxygen Reduction on Well-Defined Core-Shell Nanocatalysts: Particle Size, Facet, and Pt Shell Thickness Effects. *J Am Chem Soc* **2009,** *131*, 17298-17302.

60.   Zhang, J.; Mo, Y.; Vukmirovic, M. B.; Klie, R.; Sasaki, K.; Adzic, R. R. Platinum Monolayer Electrocatalysts for O_2 Reduction: Pt Monolayer on Pd(111) and on Carbon-Supported Pd Nanoparticles. *J Phys Chem B* **2004,** *108*, 10955-10964.

61.   Zhang, J. L.; Vukmirovic, M. B.; Sasaki, K.; Nilekar, A. U.; Mavrikakis, M.; Adzic, R. R. Mixed-Metal Pt Monolayer Electrocatalysts for Enhanced Oxygen Reduction Kinetics. *J Am Chem Soc* **2005,** *127*, 12480-12481.

62.   Naitabdi, A.; Ono, L. K.; Behafarid, F.; Roldan Cuenya, B. Thermal Stability and Segregation Processes in Self-Assembled Size-Selected Auxfe1-X Nanoparticles Deposited on TiO$_2$ (110): Composition Effects. *J Phys Chem C* **2009,** *113*, 1433-1446.

63.   Strasser, P.; Koh, S.; Anniyev, T.; Greeley, J.; More, K.; Yu, C. F.; Liu, Z. C.; Kaya, S.; Nordlund, D.; Ogasawara, H.; Toney, M. F.; Nilsson, A. Lattice-Strain Control of the Activity in Dealloyed Core-Shell Fuel Cell Catalysts. *Nat Chem* **2010,** *2*, 454-460.

64.   Sasaki, K.; Naohara, H.; Cai, Y.; Choi, Y. M.; Liu, P.; Vukmirovic, M. B.; Wang, J. X.; Adzic, R. R. Core-Protected Platinum Monolayer Shell High-Stability Electrocatalysts for Fuel-Cell Cathodes. *Angew Chem Int Ed* **2010,** *49*, 8602-8607.

65.   Henning, A. M.; Watt, J.; Miedziak, P. J.; Cheong, S.; Santonastaso, M.; Song, M. H.; Takeda, Y.; Kirkland, A. I.; Taylor, S. H.; Tilley, R. D. Gold-Palladium Core-Shell Nanocrystals with Size and Shape Control Optimized for Catalytic Performance. *Angew Chem Int Ed* **2013,** *52*, 1477-1480.

66.   Du, W. X.; Wang, Q.; Saxner, D.; Deskins, N. A.; Su, D.; Krzanowski, J. E.; Frenkel, A. I.; Teng, X. W. Highly Active Iridium/Iridium-Tin/Tin Oxide Heterogeneous Nanoparticles as Alternative Electrocatalysts for the Ethanol Oxidation Reaction. *J Am Chem Soc* **2011,** *133*, 15172-15183.

67.   Cesar, L. G.; Yang, C.; Lu, Z.; Ren, Y.; Zhang, G. H.; Miller, J. T. Identification of a Pt3Co Surface Intermetallic Alloy in Pt-Co Propane Dehydrogenation Catalysts. *ACS Catal* **2019,** *9*, 5231-5244.

68.   Kuttiyiel, K. A.; Sasaki, K.; Choi, Y. M.; Su, D.; Liu, P.; Adzic, R. R. Nitride Stabilized Ptni Core-Shell Nanocatalyst for High Oxygen Reduction Activity. *Nano Lett* **2012,** *12*, 6266-6271.

69.   Yu, S. P.; Lou, Q.; Han, K. F.; Wang, Z. M.; Zhu, H. Synthesis and Electrocatalytic Performance of Mwcnt-Supported Ag@Pt Core-Shell Nanoparticles for Orr. *Int J Hydrogen Energ* **2012,** *37*, 13365-13370.

70.   Ali, S.; Khan, I.; Khan, S. A.; Sohail, M.; Ahmed, R.; Rehman, A. U.; Ansari, M. S.; Morsy, M. A. Electrocatalytic Performance of Ni@Pt Core-Shell Nanoparticles Supported on Carbon Nanotubes for Methanol Oxidation Reaction. *J Electroanal Chem* **2017,** *795*, 17-25.

71.   Zhang, H. S.; Jin, R. H.; Yao, H.; Tang, S.; Zhuang, J. L.; Liu, G. H.; Li, H. X. Core-Shell Structured Mesoporous Silica: A New Immobilized Strategy for Rhodium Catalyzed Asymmetric Transfer Hydrogenation. *Chem Commun* **2012,** *48*, 7874-7876.

72.   Cargnello, M.; Jaen, J. J. D.; Garrido, J. C. H.; Bakhmutsky, K.; Montini, T.; Gamez, J. J. C.; Gorte, R. J.; Fornasiero, P. Exceptional Activity for Methane Combustion over Modular Pd@CeO$_2$ Subunits on Functionalized Al$_2$O$_3$. *Science* **2012,** *337*, 713-717.

73.   Adijanto, L.; Bennett, D. A.; Chen, C.; Yu, A. S.; Cargnello, M.; Fornasiero, P.; Gorte, R. J.; Vohs, J. M. Exceptional Thermal Stability of Pd@CeO$_2$ Core-Shell Catalyst Nanostructures Grafted onto an Oxide Surface. *Nano Lett* **2013,** *13*, 2252-2257.

74.   Garcia, S.; Anderson, R. M.; Celio, H.; Dahal, N.; Dolocan, A.; Zhou, J. P.; Humphrey, S. M. Microwave Synthesis of Au-Rh Core-Shell Nanoparticles and Implications of the Shell Thickness in Hydrogenation Catalysis. *Chem Commun* **2013,** *49*, 4241-4243.

75.   Fang, P. P.; Jutand, A.; Tian, Z. Q.; Amatore, C. Au-Pd Core-Shell Nanoparticles Catalyze Suzuki-Miyaura Reactions in Water through Pd Leaching. *Angew Chem Int Ed* **2011,** *50*, 12184-12188.

76.   Suzuki, A. Recent Advances in the Cross-Coupling Reactions of Organoboron Derivatives with Organic Electrophiles, 1995-1998. *Journal of Organometallic Chemistry* **1999,** *576*, 147-168.

77.   Wang, Z., Garg, A., Wang, L., He, H., Dasgupta, A., Zanchet, D., Janik, M. J., Rioux, R. M., & Román-Leshkov, Y. Enhancement of Alkyne Semi-Hydrogenation Selectivity by Electronic Modification of Platinum. *ACS Catal* **2020**.

78.   Chen, J. G. G. Carbide and Nitride Overlayers on Early Transition Metal Surfaces: Preparation, Characterization, and Reactivities. *Chem Rev* **1996,** *96*, 1477-1498.

79.   Levy, R. B.; Boudart, M. Platinum-Like Behavior of Tungsten Carbide in Surface Catalysis. *Science* **1973,** *181*, 547-549.

80.   Lee, J. S.; Oyama, S. T.; Boudart, M. Molybdenum Carbide Catalysts .1. Synthesis of Unsupported Powders. *J. Catal* **1987,** *106*, 125-133.

81.   Michalsky, R.; Zhang, Y. J.; Medford, A. J.; Peterson, A. A. Departures from the Adsorption Energy Scaling Relations for Metal Carbide Catalysts. *J Phys Chem C* **2014,** *118*, 13026-13034.

82.   Ren, H.; Humbert, M. P.; Menning, C. A.; Chen, J. G.; Shu, Y. Y.; Singh, U. G.; Cheng, W. C. Inhibition of Coking and CO Poisoning of Pt Catalysts by the Formation of Au/Pt Bimetallic Surfaces. *Appl Catal a-Gen* **2010,** *375*, 303-309.

83.   Shi, W. Y.; Yi, B. L.; Hou, M.; Jing, F. N.; Ming, P. W. Hydrogen Sulfide Poisoning and Recovery of Pemfc Pt-Anodes. *J Power Sources* **2007,** *165*, 814-818.

84.   McIntyre, D. R.; Burstein, G. T.; Vossen, A. Effect of Carbon Monoxide on the Electrooxidation of Hydrogen by Tungsten Carbide. *J Power Sources* **2002,** *107*, 67-73.

85.   Porosoff, M. D.; Yang, X. F.; Boscoboinik, J. A.; Chen, J. G. G. Molybdenum Carbide as Alternative Catalysts to Precious Metals for Highly Selective Reduction of Co2 to Co. *Angew Chem Int Ed* **2014,** *53*, 6705-6709.

86.   Lee, W. S.; Kumar, A.; Wang, Z. S.; Bhan, A. Chemical Titration and Transient Kinetic Studies of Site Requirements in Mo2c-Catalyzed Vapor Phase Anisole Hydrodeoxygenation. *ACS Catal* **2015,** *5*, 4104-4114.

87.   Lee, K. C.; Ishihara, A.; Mitsushima, S.; Kamiya, N.; Ota, K. I. Stability and Electrocatalytic Activity for Oxygen Reduction in Wc Plus Ta Catalyst. *Electrochim Acta* **2004,** *49*, 3479-3485.

88.   Oyama, S. T., *Introduction to the Chemistry of Transition Metal Carbides and Nitrides*. Springer: Dordrecht, 1996.

89.   Ono, S.; Kikegawa, T.; Ohishi, Y. A High-Pressure and High-Temperature Synthesis of Platinum Carbide. *Solid State Commun* **2005,** *133*, 55-59.

90.   Hsu, I. J.; Kimmel, Y. C.; Jiang, X. G.; Willis, B. G.; Chen, J. G. Atomic Layer Deposition Synthesis of Platinum-Tungsten Carbide Core-Shell Catalysts for the Hydrogen Evolution Reaction. *Chem Commun* **2012,** *48*, 1063-1065.

91.   Kelly, T. G.; Hunt, S. T.; Esposito, D. V.; Chen, J. G. G. Monolayer Palladium Supported on Molybdenum and Tungsten Carbide Substrates as Low-Cost Hydrogen Evolution Reaction (Her) Electrocatalysts. *Int J Hydrogen Energ* **2013,** *38*, 5638-5644.

92.   Abild-Pedersen, F.; Greeley, J.; Studt, F.; Rossmeisl, J.; Munter, T. R.; Moses, P. G.; Skulason, E.; Bligaard, T.; Norskov, J. K. Scaling Properties of Adsorption Energies for Hydrogen-Containing Molecules on Transition-Metal Surfaces. *Phys Rev Lett* **2007,** *99*.

93.   Medford, A. J.; Vojvodic, A.; Studt, F.; Abild-Pedersen, F.; Norskov, J. K. Elementary Steps of Syngas Reactions on Mo2c(001): Adsorption Thermochemistry and Bond Dissociation. *J. Catal* **2012,** *290*, 108-117.

94.   Wang, S.; Petzold, V.; Tripkovic, V.; Kleis, J.; Howalt, J. G.; Skulason, E.; Fernandez, E. M.; Hvolbaek, B.; Jones, G.; Toftelund, A.; Falsig, H.; Bjorketun, M.; Studt, F.; Abild-Pedersen, F.; Rossmeisl, J.; Norskov, J. K.; Bligaard, T. Universal Transition State Scaling Relations for (De)Hydrogenation over Transition Metals. *Phys Chem Chem Phys* **2011,** *13*, 20760-20765.

95.   Esposito, D. V.; Chen, J. G. G. Monolayer Platinum Supported on Tungsten Carbides as Low-Cost Electrocatalysts: Opportunities and Limitations. *Energ Environ Sci* **2011,** *4*, 3900-3912.

96.   Esposito, D. V.; Hunt, S. T.; Kimmel, Y. C.; Chen, J. G. G. A New Class of Electrocatalysts for Hydrogen Production from Water Electrolysis: Metal Monolayers Supported on Low-Cost Transition Metal Carbides. *J Am Chem Soc* **2012,** *134*, 3025-3033.

97.   Yan, Z. X.; Cai, M.; Shen, P. K. Nanosized Tungsten Carbide Synthesized by a Novel Route at Low Temperature for High Performance Electrocatalysis. *Sci Rep-Uk* **2013,** *3*.

98.   Upadhyaya, G. S. Materials Science of Cemented Carbides - an Overview. *Mater Design* **2001,** *22*, 483-489.

99.   Garg, A.; Goncalves, D. S.; Liu, Y. S.; Wang, Z. S.; Wang, L. X.; Yoo, J. S.; Kolpak, A.; Rioux, R. M.; Zanchet, D.; Roman-Leshkov, Y. Impact of Transition Metal Carbide and Nitride Supports on the Electronic Structure of Thin Platinum Overlayers. *ACS Catal* **2019,** *9*, 7090-7098.

100.   Hunt, S. T.; Kokumai, T. M.; Zanchet, D.; Roman-Leshkov, Y. Alloying Tungsten Carbide Nanoparticles with Tantalum: Impact on Electrochemical Oxidation Resistance and Hydrogen Evolution Activity. *J Phys Chem C* **2015,** *119*, 13691-13699.

101.   Mallens, E. P. J.; Hoebink, J. H. B. J.; Marin, G. B. An Investigation on the Reaction-Mechanism for the Partial Oxidation of Methane to Synthesis Gas over Platinum. *Catal Lett* **1995,** *33*, 291-304.

102.   Bui, P. A.; Vlachos, D. G.; Westmoreland, P. R. Catalytic Ignition of Methane/Oxygen Mixtures over Platinum Surfaces: Comparison of Detailed Simulations and Experiments. *Surf. Sci.* **1997,** *385*, L1029-L1034.

103.   Mallens, E. P. J.; Hoebink, J. H. B. J.; Marin, G. B. The Reaction Mechanism of the Partial Oxidation of Methane to Synthesis Gas: A Transient Kinetic Study over Rhodium and a Comparison with Platinum. *J. Catal* **1997,** *167*, 43-56.

104.   Agency, U. S. E. P. Fast Facts on Transportation Greenhouse Gas Emissions. https://www.epa.gov/greenvehicles/fast-facts-transportation-greenhouse-gas-emissions.

105.   Tajitsu, N. S., M Toyota Plans to Expand Production, Shrink Cost of Hydrogen Fuel Cell Vehicles. https://www.reuters.com/article/us-toyota-hydrogen/toyota-plans-to-expand-production-shrink-cost-of-hydrogen-fuel-cell-vehicles-idUSKBN1KG0Y0.

106.   Sasaki, K. K., K.A.; Adzic, R.R. Designing High Performance Pt Monolayer Core-Shell Electrocatalysts for Fuel Cells. *Current Opinion in Electrochemistry* **2020**.

107.   Wang, X.; Choi, S. I.; Roling, L. T.; Luo, M.; Ma, C.; Zhang, L.; Chi, M. F.; Liu, J. Y.; Xie, Z. X.; Herron, J. A.; Mavrikakis, M.; Xia, Y. N. Palladium-Platinum Core-Shell Icosahedra with Substantially Enhanced Activity and Durability Towards Oxygen Reduction. *Nat Commun* **2015,** *6*.

108.   Schwammlein, J. N.; Stuhmeier, B. M.; Wagenbauer, K.; Dietz, H.; Tileli, V.; Gasteiger, H. A.; El-Sayed, H. A. Origin of Superior Hor/Her Activity of Bimetallic Pt-Ru Catalysts in Alkaline Media Identified Via Ru@Pt Core-Shell Nanoparticles. *J Electrochem Soc* **2018,** *165*, H229-H239.

109.   Flynn, N. T.; Gewirth, A. A. Attenuation of Surface-Enhanced Raman Spectroscopy Response in Gold-Platinum Core-Shell Nanoparticles. *J Raman Spectrosc* **2002,** *33*, 243-251.

110.   Li, J. F.; Yang, Z. L.; Ren, B.; Liu, G. K.; Fang, P. P.; Jiang, Y. X.; Wu, D. Y.; Tian, Z. Q. Surface-Enhanced Raman Spectroscopy Using Gold-Core Platinum-Shell Nanoparticle Film Electrodes: Toward a Versatile Vibrational Strategy for Electrochemical Interfaces. *LANGMUIR* **2006,** *22*, 10372-10379.

111.   Kimmel, Y. C.; Xu, X. G.; Yu, W. T.; Yang, X. D.; Chen, J. G. G. Trends in Electrochemical Stability of Transition Metal Carbides and Their Potential Use as Supports for Low-Cost Electrocatalysts. *ACS Catal* **2014,** *4*, 1558-1562.

112.	Koc, R.; Folmer, J. S. Carbothermal Synthesis of Titanium Carbide Using Ultrafine Titania Powders. *J Mater Sci* **1997,** *32*, 3101-3111.

113.	Sen, W.; Xu, B. Q.; Yang, B.; Sun, H. Y.; Song, J. X.; Wan, H. L.; Dai, Y. N. Preparation of Tic Powders by Carbothermal Reduction Method in Vacuum. *Transactions of Nonferrous Metals Society of China* **2011,** *21*, 185-190.

114.	Yan, C. L.; Liu, R. J.; Cao, Y. B.; Zhang, C. R.; Zhang, D. K. Synthesis of Zirconium Carbide Powders Using Chitosan as Carbon Source. *Ceram Int* **2013,** *39*, 3409-3412.

115.	Li, J.; Fu, Z. Y.; Wang, W. M.; Wang, H.; Lee, S. H.; Niihara, K. Preparation of Zrc by Self-Propagating High-Temperature Synthesis. *Ceram Int* **2010,** *36*, 1681-1686.

116.	Sevast'yanov, V. G.; Simonenko, E. P.; Ignatov, N. A.; Ezhov, Y. S.; Kuznetsov, N. T. Low-Temperature Synthesis of Tac through Transparent Tantalum-Carbon Containing Gel. *Inorg Mater+* **2010,** *46*, 495-500.

117.	daSilva, V. L. S. T.; Schmal, M.; Oyama, S. T. Niobium Carbide Synthesis from Niobium Oxide: Study of the Synthesis Conditions, Kinetics, and Solid-State Transformation Mechanism. *J Solid State Chem* **1996,** *123*, 168-182.

118.	Zhang, C. F.; Beidaghi, M.; Naguib, M.; Lukatskaya, M. R.; Zhao, M. Q.; Dyatkin, B.; Cook, K. M.; Kim, S. J.; Eng, B.; Xiao, X.; Long, D. H.; Qiao, W. M.; Dunn, B.; Gogotsi, Y. Synthesis and Charge Storage Properties of Hierarchical Niobium Pentoxide/Carbon/Niobium Carbide (Mxene) Hybrid Materials. *Chem Mater* **2016,** *28*, 3937-3943.

119.	Harold, K. R. V., C. Carbon Monoxide Tolerant Platinum-Tantalum Alloyed Catalyst. 5183713, 1993.

120.	Alloyeau, D.; Ricolleau, C.; Mottet, C.; Oikawa, T.; Langlois, C.; Le Bouar, Y.; Braidy, N.; Loiseau, A. Size and Shape Effects on the Order-Disorder Phase Transition in Copt Nanoparticles. *Nat Mater* **2009,** *8*, 940-946.

121.	Barnard, A. S.; Lin, X. M.; Curtiss, L. A. Equilibrium Morphology of Face-Centered Cubic Gold Nanoparticles > 3 Nm and the Shape Changes Induced by Temperature. *J Phys Chem B* **2005,** *109*, 24465-24472.

122.	Hu, J.; Wu, L. J.; Kuttiyiel, K. A.; Goodman, K. R.; Zhang, C. X.; Zhu, Y. M.; Vukmirovic, M. B.; White, M. G.; Sasaki, K.; Adzic, R. R. Increasing Stability and Activity

of Core-Shell Catalysts by Preferential Segregation of Oxide on Edges and Vertexes: Oxygen Reduction on Ti-Au@Pt/C. *J Am Chem Soc* **2016,** *138*, 9294-9300.

123.   Baiker, A.; Kilo, M.; Maciejewski, M.; Menzi, S.; Wokaun, A.; Waugh, K. C.; Krauss, H. L.; Prins, R.; Kochloefl, K.; Holderich, W.; Hojlundnielsen, P. E.; Trimm, D. L.; Haruta, M.; Rooney, J. J. Hydrogenation of CO_2 over Copper, Silver and Gold Zirconia Catalysts - Comparative-Study of Catalyst Properties and Reaction Pathways. *New Frontiers in Catalysis, Pt B* **1993,** *75*, 1257-1272.

124.   Koeppel, R. A.; Baiker, A.; Schild, C.; Wokaun, A. Carbon-Dioxide Hydrogenation over Au/ZrO_2 Catalysts from Amorphous Precursors - Catalytic Reaction-Mechanism. *J Chem Soc Faraday T* **1991,** *87*, 2821-2828.

125.   Deng, Y. J.; Tripkovic, V.; Rossmeisl, J.; Arenz, M. Oxygen Reduction Reaction on Pt Overlayers Deposited onto a Gold Film: Ligand, Strain, and Ensemble Effect. *ACS Catal* **2016,** *6*, 671-676.

126.   Liu, P.; Norskov, J. K. Ligand and Ensemble Effects in Adsorption on Alloy Surfaces. *Phys Chem Chem Phys* **2001,** *3*, 3814-3818.

127.   Schneider, U.; Busse, H.; Linke, R.; Castro, G. R.; Wandelt, K. Interaction Properties of Molecules with Binary Alloy Surfaces. *Journal of Vacuum Science & Technology a-Vacuum Surfaces and Films* **1994,** *12*, 2069-2073.

128.   Yang, J. H.; Chen, X. J.; Yang, X. F.; Ying, J. Y. Stabilization and Compressive Strain Effect of Aucu Core on Pt Shell for Oxygen Reduction Reaction. *Energ Environ Sci* **2012,** *5*, 8976-8981.

129.   Kugler, E. L.; Boudart, M. Ligand and Ensemble Effects in the Adsorption of Carbon-Monoxide on Supported Palladium-Gold Alloys. *J. Catal* **1979,** *59*, 201-210.

130.   Garcia-Trenco, A.; Regoutz, A.; White, E. R.; Payne, D. J.; Shaffer, M. S. P.; Williams, C. K. Pdin Intermetallic Nanoparticles for the Hydrogenation of CO_2 to Methanol. *Appl Catal B-Environ* **2018,** *220*, 9-18.

131.   Xin, H. L. L.; Alayoglu, S.; Tao, R. Z.; Genc, A.; Wang, C. M.; Kovarik, L.; Stach, E. A.; Wang, L. W.; Salmeron, M.; Somorjai, G. A.; Zheng, H. M. Revealing the Atomic Restructuring of Pt-Co Nanoparticles. *Nano Lett* **2014,** *14*, 3203-3207.

132.   Cui, C. H.; Gan, L.; Heggen, M.; Rudi, S.; Strasser, P. Compositional Segregation in Shaped Pt Alloy Nanoparticles and Their Structural Behaviour During Electrocatalysis. *Nat Mater* **2013,** *12*, 765-771.

133.   Solymosi, F.; Erdohelyi, A.; Bansagi, T. Methanation of CO_2 on Supported Rhodium Catalyst. *J. Catal* **1981,** *68*, 371-382.

134.   Swalus, C.; Jacquemin, M.; Poleunis, C.; Bertrand, P.; Ruiz, P. Co2 Methanation on Rh/Gamma-Al_2O_3 Catalyst at Low Temperature: "In Situ" Supply of Hydrogen by Ni/Activated Carbon Catalyst. *Appl Catal B-Environ* **2012,** *125*, 41-50.

135.   Maroto-Valiente, A.; Rodriguez-Ramos, I.; Guerrero-Ruiz, A. Surface Study of Rhodium Nanoparticles Supported on Alumina. *Catal Today* **2004,** *93-5*, 567-574.

136.   Kwak, J. H.; Kovarik, L.; Szanyi, J. CO_2 Reduction on Supported Ru/Al2o3 Catalysts: Cluster Size Dependence of Product Selectivity. *ACS Catal* **2013,** *3*, 2449-2455.

137.   Kwak, J. H.; Kovarik, L.; Szanyi, J. Heterogeneous Catalysis on Atomically Dispersed Supported Metals: Co2 Reduction on Multifunctional Pd Catalysts. *ACS Catal* **2013,** *3*, 2094-2100.

138.   Morse, J. R.; Juneau, M.; Baldwin, J. W.; Porosoff, M. D.; Willauer, H. D. Alkali Promoted Tungsten Carbide as a Selective Catalyst for the Reverse Water Gas Shift Reaction. *Journal of CO_2 Utilization* **2020,** *35*, 38-46.

139.   Porosoff, M. D.; Kattel, S.; Li, W. H.; Liu, P.; Chen, J. G. Identifying Trends and Descriptors for Selective CO_2 Conversion to Co over Transition Metal Carbides. *Chem Commun* **2015,** *51*, 6988-6991.

140.   Dubois, J. L.; Sayama, K.; Arakawa, H. CO_2 Hydrogenation over Carbide Catalysts. *Chem Lett* **1992**, 5-8.

141.   Yao, S. Y.; Lin, L. L.; Liao, W. J.; Rui, N.; Li, N.; Liu, Z. Y.; Cen, J. J.; Zhang, F.; Li, X.; Song, L.; De Leon, L. B.; Su, D.; Senanayake, S. D.; Liu, P.; Ma, D.; Chen, J. G.; Rodriguez, J. A. Exploring Metal-Support Interactions to Immobilize Subnanometer Co Clusters on Gamma-Mo_2N: A Highly Selective and Stable Catalyst for CO_2 Activation. *ACS Catal* **2019,** *9*, 9087-9097.

142.   Trovarelli, A.; Dolcetti, G.; Deleitenburg, C.; Kaspar, J. CO_2 Hydrogenation over Platinum-Group Metals Supported on CeO_2 - Evidence for a Transient Metal-Support Interaction. *Studies in Surface Science and Catalysis* **1993,** *75*, 2781-2784.

143.   Goguet, A.; Meunier, F. C.; Tibiletti, D.; Breen, J. P.; Burch, R. Spectrokinetic Investigation of Reverse Water-Gas-Shift Reaction Intermediates over a Pt/Ceo2 Catalyst. *J Phys Chem B* **2004,** *108*, 20240-20246.

144.   Beale, A. M.; Weckhuysen, B. M. Exafs as a Tool to Interrogate the Size and Shape of Mono and Bimetallic Catalyst Nanoparticles. *Phys Chem Chem Phys* **2010,** *12*, 5562-5574.

145.   Green, A. E.; Justen, J.; Schollkopf, W.; Gentleman, A. S.; Fielicke, A.; Mackenzie, S. R. Ir Signature of Size-Selective CO_2 Activation on Small Platinum Cluster Anions, Pt-N(-) (N=4-7). *Angew Chem Int Ed* **2018,** *57*, 14822-14826.

146.   Kibata, T.; Mitsudome, T.; Mizugaki, T.; Jitsukawaa, K.; Kaneda, K. Investigation of Size-Dependent Properties of Sub-Nanometer Palladium Clusters Encapsulated within a Polyamine Dendrimer. *Chem Commun* **2013,** *49*, 167-169.

147.   Aleandri, L. E.; Bonnemann, H.; Jones, D. J.; Richter, J.; Roziere, J. Structural Investigation of Bimetallic Rh-Pt Nanoparticles through X-Ray-Absorption Spectroscopy. *J Mater Chem* **1995,** *5*, 749-752.

148.   Varga, E.; Pusztai, P.; Ovari, L.; Oszko, A.; Erdohelyi, A.; Papp, C.; Steinruck, H. P.; Konya, Z.; Kiss, J. Probing the Interaction of Rh, Co and Bimetallic Rh-Co Nanoparticles with the CeO_2 Support: Catalytic Materials for Alternative Energy Generation. *Phys Chem Chem Phys* **2015,** *17*, 27154-27166.

149.   Liu, Y. F.; Zhang, L. F.; Goltl, F.; Ball, M. R.; Hermans, I.; Kuech, T. F.; Mavrikakis, M.; Dumesic, J. A. Synthesis Gas Conversion over Rh-Mn-Wxc/Sio2 Catalysts Prepared by Atomic Layer Deposition. *ACS Catal* **2018,** *8*, 10707-10720.

150.   Hendon, C. H.; Hunt, S. T.; Milina, M.; Butler, K. T.; Walsh, A.; Roman-Leshkov, Y. Realistic Surface Descriptions of Heterometallic Interfaces: The Case of Tiwc Coated in Noble Metals. *J Phys Chem Lett* **2016,** *7*, 4475-4482.

151.   Schauermann, S.; Nilius, N.; Shaikhutdinov, S.; Freund, H. J. Nanoparticles for Heterogeneous Catalysis: New Mechanistic Insights. *Accounts of Chemical Research* **2013,** *46*, 1673-1681.

152. Kattel, S.; Liu, P.; Chen, J. G. G. Tuning Selectivity of Co2 Hydrogenation Reactions at the Metal/Oxide Interface. *J Am Chem Soc* **2017,** *139*, 9739-9754.

153. Graciani, J.; Mudiyanselage, K.; Xu, F.; Baber, A. E.; Evans, J.; Senanayake, S. D.; Stacchiola, D. J.; Liu, P.; Hrbek, J.; Sanz, J. F.; Rodriguez, J. A. Highly Active Copper-Ceria and Copper-Ceria-Titania Catalysts for Methanol Synthesis from Co2. *Science* **2014,** *345*, 546-550.

154. Koverga, A. A.; Florez, E.; Dorkis, L.; Rodriguez, J. A. Co, Co2, and H2 Interactions with (0001) and (001) Tungsten Carbide Surfaces: Importance of Carbon and Metal Sites. *J Phys Chem C* **2019,** *123*, 8871-8883.

155. Posada-Perez, S.; Vines, F.; Ramirez, P. J.; Vidal, A. B.; Rodriguez, J. A.; Illas, F. The Bending Machine: Co2 Activation and Hydrogenation on Delta-Moc(001) and Beta-Mo2c(001) Surfaces. *Phys Chem Chem Phys* **2014,** *16*, 14912-14921.

156. Hammer, B.; Norskov, J. K. Why Gold Is the Noblest of All the Metals. *Nature* **1995,** *376*, 238-240.

157. Hammer, B.; Norskov, J. K. Theoretical Surface Science and Catalysis - Calculations and Concepts. *Advances in Catalysis* **2000,** *45*.

158. Kresse, G.; Furthmuller, J. Efficiency of Ab-Initio Total Energy Calculations for Metals and Semiconductors Using a Plane-Wave Basis Set. *Comp Mater Sci* **1996,** *6*, 15-50.

159. Fogler, H. S., *Elements of Chemical Reaction Engineering*. Fifth edition. ed.; Prentice Hall: Boston, 2016; p xxxiii, 957 pages.

160. Nakshatharan, S. S.; Punning, A.; Johanson, U.; Aabloo, A. Effect of Porosity and Tortuosity of Electrodes on Carbon Polymer Soft Actuators. *J Appl Phys* **2018,** *123*.

161. Jeon, M. K.; Daimon, H.; Lee, K. R.; Nakahara, A.; Woo, S. I. Co Tolerant Pt/Wc Methanol Electro-Oxidation Catalyst. *Electrochemistry Communications* **2007,** *9*, 2692-2695.

162. Saidani, F.; Rochefort, D.; Mohamedi, M. Synthesis, Characterization of Nanostructured Rhodium Films and Their Electrochemical Behavior Towards Carbon Monoxide Oxidation. *Electrocatalysis* **2011,** *2*, 114-122.

163.   Sung, Y. E.; Thomas, S.; Wieckowski, A. Characterization of the Rh(111) Electrode by Ceels, Aes, Leed, and Voltammetry - Adsorption of (Bi)Sulfate, Perchlorate, and Carbon-Monoxide. *J Phys Chem-Us* **1995,** *99*, 13513-13521.

164.   Shao, M. H.; Peles, A.; Shoemaker, K. Electrocatalysis on Platinum Nanoparticles: Particle Size Effect on Oxygen Reduction Reaction Activity. *Nano Lett* **2011,** *11*, 3714-3719.

165.   Qiao, B. T.; Wang, A. Q.; Yang, X. F.; Allard, L. F.; Jiang, Z.; Cui, Y. T.; Liu, J. Y.; Li, J.; Zhang, T. Single-Atom Catalysis of Co Oxidation Using Pt-1/Feox. *Nat Chem* **2011,** *3*, 634-641.

166.   Bratlie, K. M.; Lee, H.; Komvopoulos, K.; Yang, P. D.; Somorjai, G. A. Platinum Nanoparticle Shape Effects on Benzene Hydrogenation Selectivity. *Nano Lett* **2007,** *7*, 3097-3101.

167.   Narayanan, R.; El-Sayed, M. A. Shape-Dependent Catalytic Activity of Platinum Nanoparticles in Colloidal Solution. *Nano Lett* **2004,** *4*, 1343-1348.

168.   Cheng, N. C.; Stambula, S.; Wang, D.; Banis, M. N.; Liu, J.; Riese, A.; Xiao, B. W.; Li, R. Y.; Sham, T. K.; Liu, L. M.; Botton, G. A.; Sun, X. L. Platinum Single-Atom and Cluster Catalysis of the Hydrogen Evolution Reaction. *Nat Commun* **2016,** *7*.

169.   Cui, X. J.; Li, W.; Ryabchuk, P.; Junge, K.; Beller, M. Bridging Homogeneous and Heterogeneous Catalysis by Heterogeneous Single-Metal-Site Catalysts. *Nat Catal* **2018,** *1*, 385-397.

170.   O'Connor, N. J.; Jonayat, A. S. M.; Janik, M. J.; Senftle, T. P. Interaction Trends between Single Metal Atoms and Oxide Supports Identified with Density Functional Theory and Statistical Learning. *Nat Catal* **2018,** *1*, 531-539.

171.   Roy, C.; Sebok, B.; Scott, S. B.; Fiordaliso, E. M.; Sorensen, J. E.; Bodin, A.; Trimarco, D. B.; Damsgaard, C. D.; Vesborg, P. C. K.; Hansen, O.; Stephens, I. E. L.; Kibsgaard, J.; Chorkendorff, I. Impact of Nanoparticle Size and Lattice Oxygen on Water Oxidation on Nifeoxhy. *Nat Catal* **2018,** *1*, 820-829.

172.   Wanjala, B. N.; Luo, J.; Loukrakpam, R.; Fang, B.; Mott, D.; Njoki, P. N.; Engelhard, M.; Naslund, H. R.; Wu, J. K.; Wang, L. C.; Malis, O.; Zhong, C. J. Nanoscale Alloying, Phase-Segregation, and Core-Shell Evolution of Gold-Platinum Nanoparticles and Their Electrocatalytic Effect on Oxygen Reduction Reaction. *Chem Mater* **2010,** *22*, 4282-4294.

173.	Jain, A.; Ramasubramaniam, A. Tuning Core-Shell Interactions in Tungsten Carbide-Pt Nanoparticles for the Hydrogen Evolution Reaction. *Phys Chem Chem Phys* **2018,** *20*, 23262-23271.

174.	Studt, F.; Abild-Pedersen, F.; Bligaard, T.; Sorensen, R. Z.; Christensen, C. H.; Norskov, J. K. On the Role of Surface Modifications of Palladium Catalysts in the Selective Hydrogenation of Acetylene. *Angew Chem Int Ed* **2008,** *47*, 9299-9302.

175.	Studt, F.; Abild-Pedersen, F.; Bligaard, T.; Sorensen, R. Z.; Christensen, C. H.; Norskov, J. K. Identification of Non-Precious Metal Alloy Catalysts for Selective Hydrogenation of Acetylene. *Science* **2008,** *320*, 1320-1322.

176.	Huang, D. C.; Chang, K. H.; Pong, W. F.; Tseng, P. K.; Hung, K. J.; Huang, W. F. Effect of Ag-Promotion on Pd Catalysts by Xanes. *Catal Lett* **1998,** *53*, 155-159.

177.	Meyer, R. J.; Zhang, Q.; Kryczka, A.; Gomez, C.; Todorovic, R. Perturbation of Reactivity with Geometry: How Far Can We Go? *ACS Catal* **2018,** *8*, 566-570.

178.	Abon, M.; Massardier, J.; Tardy, B.; Bertolini, J. C. Pt50ni50(111) Alloy and Pt(111) - Chemisorptive Properties for Acetylene and Ethylene and Catalytic Behavior for the Acetylene Selective Hydrogenation. *Surf. Sci.* **1987,** *189*, 880-885.

179.	Spiewak, B. E.; Cortright, R. D.; Dumesic, J. A. Microcalorimetric Studies of H-2, C2h4, and C2h2 Adsorption on Pt Powder. *J. Catal* **1998,** *176*, 405-414.

180.	Osswald, J.; Kovnir, K.; Armbruster, M.; Giedigleit, R.; Jentoft, R. E.; Wild, U.; Grin, Y.; Schlogl, R. Palladium-Gallium Intermetallic Compounds for the Selective Hydrogenation of Acetylene - Part Ii: Surface Characterization and Catalytic Performance. *J. Catal* **2008,** *258*, 219-227.

181.	Vincent, M. J.; Gonzalez, R. D. A Langmuir-Hinshelwood Model for a Hydrogen Transfer Mechanism in the Selective Hydrogenation of Acetylene over a Pd/Gamma-Al2o3 Catalyst Prepared by the Sol-Gel Method. *Appl Catal a-Gen* **2001,** *217*, 143-156.

182.	Sheth, P. A.; Neurock, M.; Smith, C. M. First-Principles Analysis of the Effects of Alloying Pd with Ag for the Catalytic Hydrogenation of Acetylene-Ethylene Mixtures. *J Phys Chem B* **2005,** *109*, 12449-12466.

183.	Denhartog, A. J.; Deng, M.; Jongerius, F.; Ponec, V. Hydrogenation of Acetylene over Various Group Viii Metals - Effect of Particle-Size and Carbonaceous Deposits. *J Mol Catal* **1990,** *60*, 99-108.

184.   Stuck, A.; Wartnaby, C. E.; Yeo, Y. Y.; King, D. A. Microcalorimetric Study of Ethylene on Pt(110)-(1x2). *Phys Rev Lett* **1995,** *74*, 578-581.

185.   Yeo, Y. Y.; Stuck, A.; Wartnaby, C. E.; King, D. A. Microcalorimetric Study of Ethylene Adsorption on the Pt{111} Surface. *Chem Phys Lett* **1996,** *259*, 28-36.

186.   Palfi, S.; Lisowski, W.; Smutek, M.; Cerny, S. Calorimetric Studies of Hydrocarbon Adsorption on Metal-Films .5. Hydrocarbons on Platinum. *J. Catal* **1984,** *88*, 300-312.

187.   Wang, L. X.; Al-Aufi, M.; Pacheco, C. N.; Xie, L. Y.; Rioux, R. M. Polyethylene Glycol (Peg) Addition to Polyethylenimine (Pei)-Impregnated Silica Increases Amine Accessibility During Co2 Sorption. *Acs Sustainable Chemistry & Engineering* **2019,** *7*, 14785-14795.

188.   Asplund, S. Coke Formation and Its Effect on Internal Mass Transfer and Selectivity in Pd-Catalysed Acetylene Hydrogenation. *J. Catal* **1996,** *158*, 267-278.

189.   Huang, X. H.; Xia, Y. J.; Cao, Y. J.; Zheng, X. S.; Pan, H. B.; Zhu, J. F.; Ma, C.; Wang, H. W.; Li, J. J.; You, R.; Wei, S. Q.; Huang, W. X.; Lu, J. L. Enhancing Both Selectivity and Coking-Resistance of a Single-Atom Pd-1/C3n4 Catalyst for Acetylene Hydrogenation. *Nano Res* **2017,** *10*, 1302-1312.

190.   Kelly, T. G.; Chen, J. G. Metal Overlayer on Metal Carbide Substrate: Unique Bimetallic Properties for Catalysis and Electrocatalysis. *Chem Soc Rev* **2012,** *41*, 8021-8034.

191.   Teschner, D.; Borsodi, J.; Wootsch, A.; Revay, Z.; Havecker, M.; Knop-Gericke, A.; Jackson, S. D.; Schlogl, R. The Roles of Subsurface Carbon and Hydrogen in Palladium-Catalyzed Alkyne Hydrogenation. *Science* **2008,** *320*, 86-89.

192.   Kuttiyiel, K. A.; Choi, Y.; Hwang, S. M.; Park, G. G.; Yang, T. H.; Su, D.; Sasaki, K.; Liu, P.; Adzic, R. R. Enhancement of the Oxygen Reduction on Nitride Stabilized Pt-M (M=Fe, Co, and Ni) Core-Shell Nanoparticle Electrocatalysts. *Nano Energy* **2015,** *13*, 442-449.

193.   Zhang, Q. W.; Li, J.; Liu, X. X.; Zhu, Q. M. Synergetic Effect of Pd and Ag Dispersed on Al2o3 in the Selective Hydrogenation of Acetylene. *Appl Catal a-Gen* **2000,** *197*, 221-228.

194.   Sarkany, A.; Weiss, A. H.; Guczi, L. Structure Sensitivity of Acetylene Ethylene Hydrogenation over Pd Catalysts. *J. Catal* **1986,** *98*, 550-553.

195. Mears, D. E. Diagnostic Criteria for Heat Transport Limitations in Fixed Bed Reactors. *J. Catal* **1971,** *20*, 127-&.

196. Weisz, P. B.; Prater, C. D. Interpretation of Measurements in Experimental Catalysis. *Advances in Catalysis* **1954,** *6*, 143-196.

197. Kresse, G.; Joubert, D. From Ultrasoft Pseudopotentials to the Projector Augmented-Wave Method. *Phys Rev B* **1999,** *59*, 1758-1775.

198. Perdew, J. P.; Burke, K.; Ernzerhof, M. Generalized Gradient Approximation Made Simple. *Phys Rev Lett* **1996,** *77*, 3865-3868.

199. Moreno-Castilla, C.; Alvarez-Merino, M. A.; Carrasco-Marin, F.; Fierro, J. L. G. Tungsten and Tungsten Carbide Supported on Activated Carbon: Surface Structures and Performance for Ethylene Hydrogenation. *LANGMUIR* **2001,** *17*, 1752-1756.

200. Vidick, B.; Lemaitre, J.; Leclercq, L. Control of the Catalytic Activity of Tungsten Carbides .3. Activity for Ethylene Hydrogenation and Cyclohexane Dehydrogenation. *J. Catal* **1986,** *99*, 439-448.

201. Cui, X. Z.; Zhou, X. X.; Chen, H. R.; Hua, Z. L.; Wu, H. X.; He, Q. J.; Zhang, L. X.; Shi, J. L. In-Situ Carbonization Synthesis and Ethylene Hydrogenation Activity of Ordered Mesoporous Tungsten Carbide. *Int J Hydrogen Energ* **2011,** *36*, 10513-10521.

202. Spanjers, C. S.; Held, J. T.; Jones, M. J.; Stanley, D. D.; Sim, R. S.; Janik, M. J.; Rioux, R. M. Zinc Inclusion to Heterogeneous Nickel Catalysts Reduces Oligomerization During the Semi-Hydrogenation of Acetylene. *J. Catal* **2014,** *316*, 164-173.

203. Price, G. L.; Iglesia, E. Matrix Method for Correction of Mass Spectra in Deuterium-Exchange Applications. *Industrial & Engineering Chemistry Research* **1989,** *28*, 839-844.

204. Spanjers, C. S.; Sim, R. S.; Sturgis, N. P.; Kabius, B.; Rioux, R. M. In Situ Spectroscopic Characterization of Ni1– X Znx Zno Catalysts and Their Selectivity for Acetylene Semihydrogenation in Excess Ethylene. *ACS Catalysis* **2015,** *5*, 3304--3315.

205. Bui, L.; Bhan, A. Mechanisms for Cc Bond Cleavage and Formation During Acrolein Production on a Mixed Metal Oxide Catalyst. *Applied Catalysis A: General* **2017,** *546*, 87-95.

206. Monkhorst, H. J.; Pack, J. D. Special Points for Brillouin-Zone Integrations. *Phys Rev B* **1976,** *13*, 5188-5192.

207. Henkelman, G.; Uberuaga, B. P.; Jonsson, H. A Climbing Image Nudged Elastic Band Method for Finding Saddle Points and Minimum Energy Paths. *J Chem Phys* **2000,** *113*, 9901-9904.

208. Ma, C. A.; Liu, T.; Chen, L. T. A Computational Study of H-2 Dissociation and Co Adsorption on the Pt-Ml/Wc(0001) Surface. *Appl Surf Sci* **2010,** *256*, 7400-7405.

209. Esposito, D. V.; Hunt, S. T.; Stottlemyer, A. L.; Dobson, K. D.; McCandless, B. E.; Birkmire, R. W.; Chen, J. G. G. Low-Cost Hydrogen-Evolution Catalysts Based on Monolayer Platinum on Tungsten Monocarbide Substrates. *Angew Chem Int Edit* **2010,** *49*, 9859-9862.

210. Vasic, D. D.; Pasti, I. A.; Mentus, S. V. Dft Study of Platinum and Palladium Overlayers on Tungsten Carbide: Structure and Electrocatalytic Activity toward Hydrogen Oxidation/Evolution Reaction. *Int J Hydrogen Energ* **2013,** *38*, 5009-5018.

211. Kimmel, Y. C.; Yang, L.; Kelly, T. G.; Rykov, S. A.; Chen, J. G. G. Theoretical Prediction and Experimental Verification of Low Loading of Platinum on Titanium Carbide as Low-Cost and Stable Electrocatalysts. *J Catal* **2014,** *312*, 216-220.

212. Anicijevic, D. D. V.; Nikolic, V. M.; Marceta-Kaninski, M. P.; Pasti, I. A. Is Platinum Necessary for Efficient Hydrogen Evolution? - Dft Study of Metal Monolayers on Tungsten Carbide. *Int J Hydrogen Energ* **2013,** *38*, 16071-16079.

213. Sheng, T.; Lin, X.; Chen, Z. Y.; Hu, P.; Sun, S. G.; Chu, Y. Q.; Ma, C. A.; Lin, W. F. Methanol Electro-Oxidation on Platinum Modified Tungsten Carbides in Direct Methanol Fuel Cells: A Dft Study. *Phys Chem Chem Phys* **2015,** *17*, 25235-25243.

214. Mittendorfer, F.; Thomazeau, C.; Raybaud, P.; Toulhoat, H. Adsorption of Unsaturated Hydrocarbons on Pd(111) and Pt(111): A Dft Study. *J Phys Chem B* **2003,** *107*, 12287-12295.

215. Watwe, R. M.; Spiewak, B. E.; Cortright, R. D.; Dumesic, J. A. Density Functional Theory (Dft) Studies of C-1 and C-2 Hydrocarbons Species on Pt Clusters. *J Catal* **1998,** *180*, 184-193.

216. Medlin, J. W.; Allendorf, M. D. Theoretical Study of the Adsorption of Acetylene on the (111) Surfaces of Pd, Pt, Ni, and Rh. *J Phys Chem B* **2003,** *107*, 217-223.

217. Mavrikakis, M.; Hammer, B.; Norskov, J. K. Effect of Strain on the Reactivity of Metal Surfaces. *Phys Rev Lett* **1998,** *81*, 2819-2822.

218.   Steele, B. C. H.; Heinzel, A. Materials for Fuel-Cell Technologies. *Nature* **2001,** *414*, 345-352.

219.   Tiwari, J. N.; Tiwari, R. N.; Singh, G.; Kim, K. S. Recent Progress in the Development of Anode and Cathode Catalysts for Direct Methanol Fuel Cells. *Nano Energy* **2013,** *2*, 553-578.

220.   Xia, Z. X.; Zhang, X. M.; Sun, H.; Wang, S. L.; Sun, G. Q. Recent Advances in Multi-Scale Design and Construction of Materials for Direct Methanol Fuel Cells. *Nano Energy* **2019,** *65*.

221.   Zhao, X.; Yin, M.; Ma, L.; Liang, L.; Liu, C. P.; Liao, J. H.; Lu, T. H.; Xing, W. Recent Advances in Catalysts for Direct Methanol Fuel Cells. *Energ Environ Sci* **2011,** *4*, 2736-2753.

222.   Kakati, N.; Maiti, J.; Lee, S. H.; Jee, S. H.; Viswanathan, B.; Yoon, Y. S. Anode Catalysts for Direct Methanol Fuel Cells in Acidic Media: Do We Have Any Alternative for Pt or Pt-Ru? *Chem Rev* **2014,** *114*, 12397-12429.

223.   Tong, Y. Y.; Yan, X.; Liang, J.; Dou, S. X. Metal-Based Electrocatalysts for Methanol Electro-Oxidation: Progress, Opportunities, and Challenges. *Small* **2019**.

224.   Weidman, M. C.; Esposito, D. V.; Hsu, Y. C.; Chen, J. G. Comparison of Electrochemical Stability of Transition Metal Carbides (Wc, W2c, Mo2c) over a Wide Ph Range. *J Power Sources* **2012,** *202*, 11-17.

225.   Pourbaix,M - Atlas of Electrochemical Equilibria in Aqueous Solutions. *Anti-Corrosion* **1967,** *14*, 28-&.

226.   Göhl, D.; Rueβ, H.; Schlicht, S.; Vogel, A.; Rohwerder, M.; Mayrhofer, K. J. J.; Bachmann, J.; Roman-Leshkov, Y.; Schneider, J. M.; Ledendecker, M. Stable and Active Oxygen Reduction Catalysts with Reduced Noble Metal Loadings through Potential Triggered Support Passivation. *Chemelectrochem* **2020**.

227.   Ramaker, D. E.; Mojet, B. L.; Oostenbrink, M. T. G.; Miller, J. T.; Koningsberger, D. C. Contribution of Shape Resonance and Pt-H Exafs in the Pt L-2,L-3 X-Ray Absorption Edges of Supported Pt Particles: Application and Consequences for Catalyst Characterization. *Phys Chem Chem Phys* **1999,** *1*, 2293-2302.

228. Lei, Y.; Jelic, J.; Nitsche, L. C.; Meyer, R.; Miller, J. Effect of Particle Size and Adsorbates on the L-3, L-2 and L-1 X-Ray Absorption near Edge Structure of Supported Pt Nanoparticles. *Top Catal* **2011,** *54*, 334-348.

229. Hammer, B.; Nørskov, J. K. Theoretical Surface Science and Catalysis - Calculations and Concepts. *Adv Catal* **2000,** *45*, 71-129.

230. Hammer, B.; Nørskov, J. K. Why Gold Is the Noblest of All the Metals. *Nature* **1995,** *376*, 238-240.

231. Kattel, S.; Wang, G. F. Beneficial Compressive Strain for Oxygen Reduction Reaction on Pt (111) Surface. *J Chem Phys* **2014,** *141*.

232. Lamy, C.; Leger, J. M.; Clavilier, J.; Parsons, R. Structural Effects in Electrocatalysis - a Comparative-Study of the Oxidation of Co, Hcooh and Ch3oh on Single-Crystal Pt Electrodes. *J Electroanal Chem* **1983,** *150*, 71-77.

233. Urchaga, P.; Baranton, S.; Coutanceau, C.; Jerkiewicz, G. Evidence of an Eley-Rideal Mechanism in the Stripping of a Saturation Layer of Chemisorbed Co on Platinum Nanoparticles. *LANGMUIR* **2012,** *28*, 13094-13104.

234. Gasteiger, H. A.; Markovic, N. M.; Ross, P. N. H2 and Co Electrooxidation on Well-Characterized Pt, Ru, and Pt-Ru .1. Rotating-Disk Electrode Studies of the Pure Gases Including Temperature Effects. *J Phys Chem-Us* **1995,** *99*, 8290-8301.

235. Chung, D. Y.; Lee, K. J.; Sung, Y. E. Methanol Electro-Oxidation on the Pt Surface: Revisiting the Cyclic Voltammetry Interpretation. *J Phys Chem C* **2016,** *120*, 9028-9035.

236. Lebedeva, N. P.; Koper, M. T. M.; Feliu, J. M.; van Santen, R. A. Role of Crystalline Defects in Electrocatalysis: Mechanism and Kinetics of Co Adlayer Oxidation on Stepped Platinum Electrodes. *J Phys Chem B* **2002,** *106*, 12938-12947.

237. Wang, H. S.; Abruna, H. D. Origin of Multiple Peaks in the Potentiodynamic Oxidation of Co Adlayers on Pt and Ru-Modified Pt Electrodes. *J Phys Chem Lett* **2015,** *6*, 1899-1906.

238. Lee, S. W.; Chen, S. O.; Sheng, W. C.; Yabuuchi, N.; Kim, Y. T.; Mitani, T.; Vescovo, E.; Shao-Horn, Y. Roles of Surface Steps on Pt Nanoparticles in Electro-Oxidation of Carbon Monoxide and Methanol. *J Am Chem Soc* **2009,** *131*, 15669-15677.

239.   Urchaga, P.; Baranton, S.; Coutanceau, C.; Jerkiewicz, G. Electro-Oxidation of Cochem on Pt Nanosurfaces: Solution of the Peak Multiplicity Puzzle. *LANGMUIR* **2012,** *28*, 3658-3663.

240.   Paulus, U. A.; Schmidt, T. J.; Gasteiger, H. A.; Behm, R. J. Oxygen Reduction on a High-Surface Area Pt/Vulcan Carbon Catalyst: A Thin-Film Rotating Ring-Disk Electrode Study. *J Electroanal Chem* **2001,** *495*, 134-145.

241.   Koenigsmann, C.; Zhou, W. P.; Adzic, R. R.; Sutter, E.; Wong, S. S. Size-Dependent Enhancement of Electrocatalytic Performance in Relatively Defect-Free, Processed Ultrathin Platinum Nanowires. *Nano Lett* **2010,** *10*, 2806-2811.

242.   Wang, R. Y.; Higgins, D. C.; Hoque, M. A.; Lee, D.; Hassan, F.; Chen, Z. W. Controlled Growth of Platinum Nanowire Arrays on Sulfur Doped Graphene as High Performance Electrocatalyst. *Sci Rep-Uk* **2013,** *3*.

243.   Marković, N. M.; Adžić, R. R.; Cahan, B. D.; Yeager, E. B. Structural Effects in Electrocatalysis - Oxygen Reduction on Platinum Low-Index Single-Crystal Surfaces in Perchloric-Acid Solutions. *J Electroanal Chem* **1994,** *377*, 249-259.

244.   Lopes, P. P.; Strmcnik, D.; Tripkovic, D.; Connell, J. G.; Stamenkovic, V.; Marković, N. M. Relationships between Atomic Level Surface Structure and Stability/Activity of Platinum Surface Atoms in Aqueous Environments. *ACS Catal* **2016,** *6*, 2536-2544.

245.   Heinzel, A.; Barragán, V. M. A Review of the State-of-the-Art of the Methanol Crossover in Direct Methanol Fuel Cells. *J Power Sources* **1999,** *84*, 70-74.

246.   Ahmed, M.; Dincer, I. A Review on Methanol Crossover in Direct Methanol Fuel Cells: Challenges and Achievements. *International Journal of Energy Research* **2011,** *35*, 1213-1228.

247.   Qi, Z. G.; Kaufman, A. Open Circuit Voltage and Methanol Crossover in Dmfcs. *J Power Sources* **2002,** *110*, 177-185.

248.   Jang, S.; Kim, S.; Kim, S. M.; Choi, J.; Yeon, J.; Bang, K.; Ahn, C. Y.; Hwang, W.; Her, M.; Cho, Y. H.; Sung, Y. E.; Choi, M. Interface Engineering for High-Performance Direct Methanol Fuel Cells Using Multiscale Patterned Membranes and Guided Metal Cracked Layers. *Nano Energy* **2018,** *43*, 149-158.

249.   Zhang, J. L.; Vukmirovic, M. B.; Xu, Y.; Mavrikakis, M.; Adzic, R. R. Controlling the Catalytic Activity of Platinum-Monolayer Electrocatalysts for Oxygen Reduction with Different Substrates. *Angew Chem Int Ed* **2005,** *44*, 2132-2135.

250.   Greeley, J.; Stephens, I. E. L.; Bondarenko, A. S.; Johansson, T. P.; Hansen, H. A.; Jaramillo, T. F.; Rossmeisl, J.; Chorkendorff, I.; Norskøv, J. K. Alloys of Platinum and Early Transition Metals as Oxygen Reduction Electrocatalysts. *Nat Chem* **2009,** *1*, 552-556.

251.   Huang, H. J.; Zhu, J. X.; Li, D. B.; Shen, C.; Li, M. M.; Zhang, X.; Jiang, Q. G.; Zhang, J. F.; Wu, Y. P. Pt Nanoparticles Grown on 3d Ruo2-Modified Graphene Architectures for Highly Efficient Methanol Oxidation. *J Mater Chem A* **2017,** *5*, 4560-4567.

252.   Scofield, M. E.; Koenigsmann, C.; Wang, L.; Liu, H. Q.; Wong, S. S. Tailoring the Composition of Ultrathin, Ternary Alloy Ptrufe Nanowires for the Methanol Oxidation Reaction and Formic Acid Oxidation Reaction. *Energ Environ Sci* **2015,** *8*, 350-363.

253.   Kang, D. K.; Noh, C. S.; Kim, N. H.; Cho, S. H.; Sohn, J. M.; Kim, T. J.; Park, Y. K. Effect of Transition Metals (Ni, Sn and Mo) in Pt5ru4m Alloy Ternary Electrocatalyst on Methanol Electro-Oxidation. *J Ind Eng Chem* **2010,** *16*, 385-389.

254.   Ma, S. Y.; Li, H. H.; Hu, B. C.; Cheng, X.; Fu, Q. Q.; Yug, S. H. Synthesis of Low Pt-Based Quaternary Ptpdrute Nanotubes with Optimized Incorporation of Pd for Enhanced Electrocatalytic Activity. *J Am Chem Soc* **2017,** *139*, 5890-5895.

255.   Huang, T.; Liu, J. L.; Li, R. S.; Cai, W. B.; Yu, A. S. A Novel Route for Preparation of Ptrume (Me = Fe, Co, Ni) and Their Catalytic Performance for Methanol Electrooxidation. *Electrochemistry Communications* **2009,** *11*, 643-646.

256.   Johnson, C.; Sellinschegg, H.; Johnson, D. C. Low-Temperature Synthesis of Tic, Mo2c, and W2c from Modulated Elemental Reactants. *Chem Mater* **2001,** *13*, 3876-3881.

257.   Baddour, F. G.; Roberts, E. J.; To, A. T.; Wang, L.; Habas, S. E.; Ruddy, D. A.; Bedford, N. M.; Wright, J.; Nash, C. P.; Schaidle, J. A.; Brutchey, R. L.; Malmstadt, N. An Exceptionally Mild and Scalable Solution-Phase Synthesis of Molybdenum Carbide Nanoparticles for Thermocatalytic Co2 Hydrogenation. *J Am Chem Soc* **2020,** *142*, 1010-1019.

258. Li, X. L.; Li, Y. D. Synthesis of Scroll-Type Composite Microtubes of Mo2c/Moco by Controlled Pyrolysis Mo(Co)(6). *Chem-Eur J* **2004,** *10*, 433-439.

259. Hanaoka, T.; Arakawa, H.; Matsuzaki, T.; Sugi, Y.; Kanno, K.; Abe, Y. Ethylene Hydroformylation and Carbon Monoxide Hydrogenation over Modified and Unmodified Silica Supported Rhodium Catalysts. *Catal Today* **2000,** *58*, 271-280.

260. Takasaki, S.; Koga, F.; Tanabe, S.; Ueno, A.; Kotera, Y. Particle-Size Control of Rhodium Dispersed on Silica and Its Effects on Decomposition of 1-Propanol. *Nippon Kagaku Kaishi* **1984**, 998-1004.

261. Quek, X. Y.; Guan, Y. J.; Hensen, E. J. M. Structure Sensitivity in the Hydrogenation of Unsaturated Hydrocarbons over Rh Nanoparticles. *Catal Today* **2012,** *183*, 72-78.

262. Van Santen, R. A. Complementary Structure Sensitive and Insensitive Catalytic Relationships. *Accounts of Chemical Research* **2009,** *42*, 57-66.

263. Akporiaye, D.; Jensen, S. F.; Olsbye, U.; Rohr, F.; Rytter, E.; Ronnekleiv, M.; Spjelkavik, A. I. A Novel, Highly Efficient Catalyst for Propane Dehydrogenation. *Ind Eng Chem Res* **2001,** *40*, 4741-4748.

264. Kumar, M. S.; Chen, D.; Walmsley, J. C.; Holmen, A. Dehydrogenation of Propane over Pt-Sba-15: Effect of Pt Particle Size. *Catal Commun* **2008,** *9*, 747-750.

265. Zhu, J.; Yang, M. L.; Yu, Y. D.; Zhu, Y. A.; Sui, Z. J.; Zhou, X. G.; Holmen, A.; Chen, D. Size-Dependent Reaction Mechanism and Kinetics for Propane Dehydrogenation over Pt Catalysts. *ACS Catal* **2015,** *5*, 6310-6319.

266. Wegener, E. C.; Bukowski, B. C.; Yang, D. L.; Wu, Z. W.; Kropf, A. J.; Delgass, W. N.; Greeley, J.; Zhang, G. H.; Miller, J. T. Intermetallic Compounds as an Alternative to Single-Atom Alloy Catalysts: Geometric and Electronic Structures from Advanced X-Ray Spectroscopies and Computational Studies. *Chemcatchem* **2020,** *12*, 1325-1333.

Education

Ph.D. Chemical Engineering
Massachusetts Institute of Technology, **2020**
Minor: Finance

M.S. Chemical Engineering Practice
Massachusetts Institute of Technology, **2017**

M.S. Chemical Engineering Practice
Massachusetts Institute of Technology, **2017**

B.Eng. Chemical Engineering with high distinction
University of Minnesota-Twin Cities, **2015**

B.A. Chemistry with high distinction
University of Minnesota-Twin Cities, **2015**

B.S. Mathematics with high distinction
University of Minnesota-Twin Cities, **2015**

Publications

Wang, Zhenshu, Jin Soo Kang, Daniel Göhl, Paul Paciok, Karl J. J. Mayrhofer, Marc Heggen, Rafal E. Dunin-Borkowski, Yang Shao-Horn, Marc Ledendecker, and Yuriy Román-Leshkov. "Platinum/Tantalum Carbide Nanoparticles with Sub-Monolayer Shells for Methanol and Oxygen Electrocatalysis." *In preparation.* 2020

Wang, Zhenshu, Haoran He, Danielle S. Gonçalves, Linxi Wang, Robert M. Rioux, Michael J. Janik, Daniela Zanchet, and Yuriy Román-Leshkov. "Enhancement of CO Selectivity by Transition Metal Carbide Rhodium Core-Shell Nanoparticles in CO_2 Hydrogenation." *In preparation.* 2020

Wang, Zhenshu, Aaron Garg, Linxi Wang, Haoran He, Anish Dasgupta, Daniela Zanchet, Michael J. Janik, Robert M. Rioux, and Yuriy Román-Leshkov. "Enhancement of Alkyne Semi-Hydrogenation Selectivity by Electronic Modification of Platinum." *ACS Catalysis* (2020).

Garg, Aaron, Danielle S. Goncalves, Yusu Liu, **Zhenshu Wang**, Linxi Wang, Jong Suk Yoo, Alexie Kolpak, Robert M. Rioux, Daniela Zanchet, and Yuriy Roman-Leshkov. "Impact of Transition Metal Carbide and Nitride Supports on the Electronic Structure of Thin Platinum Overlayers." *ACS Catalysis* 9, no. 8 (2019): 7090-7098.

Cai, Bin, Karthik Akkiraju, William P. Mounfield III, **Zhenshu Wang**, Xing Li, Botao Huang, Shuai Yuan, Dong Su, Yuriy Román-Leshkov, and Yang Shao-Horn. "Solid-state gelation for nanostructured perovskite oxide aerogels." *Chemistry of Materials* 31, no. 22 (2019): 9422-9429.

Iida, Takayuki, Manish Shetty, Karthick Murugappan, **Zhenshu Wang**, Koji Ohara, Toru Wakihara, and Yuriy Román-Leshkov. "Encapsulation of molybdenum carbide nanoclusters inside zeolite micropores enables synergistic bifunctional catalysis for anisole hydrodeoxygenation." *ACS Catalysis* 7, no. 12 (2017): 8147-8151.

Hunt, Sean T., Maria Milina, **Zhenshu Wang**, and Yuriy Román-Leshkov. "Activating earth-abundant electrocatalysts for efficient, low-cost hydrogen evolution/oxidation: sub-monolayer platinum coatings on titanium tungsten carbide nanoparticles." *Energy & Environmental Science* 9, no. 10 (2016): 3290-3301.

Lee, Wen-Sheng, Anurag Kumar, **Zhenshu Wang**, and Aditya Bhan. "Chemical titration and transient kinetic studies of site requirements in Mo2C-catalyzed vapor phase anisole hydrodeoxygenation." *ACS Catalysis* 5, no. 7 (2015): 4104-4114.

Lee, Wen-Sheng, **Zhenshu Wang**, Ryan J. Wu, and Aditya Bhan. "Selective vapor-phase hydrodeoxygenation of anisole to benzene on molybdenum carbide catalysts." *Journal of catalysis* 319 (2014): 44-53.

Lee, Wen-Sheng, **Zhenshu Wang**, Weiqing Zheng, Dionisios G. Vlachos, and Aditya Bhan. "Vapor phase hydrodeoxygenation of furfural to 2-methylfuran on molybdenum carbide catalysts." *Catalysis Science & Technology* 4, no. 8 (2014): 2340-2352.

Presentations

*North American Catalysis Society Meeting (**NAM 26**) 2019,* Chicago, Illinois
June 19th, 2019. Oral Presentation
Zhenshu Wang, Aaron Garg, Linxi Wang, Haoran He, Anish Dasgupta, Daniela Zanchet, Michael J. Janik, Robert M. Rioux, and Yuriy Román-Leshkov. "Electronic Properties of Pt-Coated Transition Metal Carbide and Nitride Nanoparticles"

*Gordon Research Conferences-Catalysis (**GRS**) 2018,* New London, New Hampshire
June 23, 2018. Poster Presentation
Zhenshu Wang and Yuriy Román-Leshkov. "Pt/TiWC and Pt/TiWN Core-Shell Particles for Selective Hydrogenation"

*New England Catalysis Society (**NECS**) Fall Meeting 2017,* Worchester, Massachusetts
December 12, 2017. Oral Presentation
Zhenshu Wang and Yuriy Román-Leshkov. "Selective Hydrogenation of Acetylene by Platinum Titanium Tungsten Carbide/Nitride Core-Shell Nanoparticles"

*International Precious Metals Institute (**IPMI**) 41st annual IPMI Conference 2017*, Orlando, Florida. June 11, 2017. Poster Presentation
Zhenshu Wang and Yuriy Román-Leshkov. "Transition Metal Carbide/Noble Metal Core-Shell Platform and Applications."

*International Precious Metals Institute (**IPMI**) 41st annual IPMI Conference 2017*, Orlando, Florida. June 13, 2017. Oral Presentation
Zhenshu Wang and Yuriy Román-Leshkov. "Transition Metal Carbide/Noble Metal Core-Shell Platform and Applications."

Honors and Awards

Dow Travel Award for NAM26 2019	June 2019
Chyn Duog Shiah Memorial Fellowship	Sep 2017-May 2018
Sabin Metal Ron Bleggi Student Award	May 2017
George T Walker Chemistry Scholarship	Fall 2014-Spring 2015
Golden Global Excellence Scholarship	Sep 2011-May 2015
Min (Amy) Xu and Michael Schumann Scholarship	Spring 2013